



THÈSE DE DOCTORAT
DE L'UNIVERSITÉ PSL

Préparée à Institut de Biologie de l'École Normale Supérieure

**The regulation of neuronal and synaptic
development by Catenin-delta 2**

Soutenue par

Nora M. ASSENDORP

Le 17 décembre 2021

Ecole doctorale n° 158

**Cerveau – cognition –
comportement**

Spécialité

Neurosciences

Composition du jury :

Fekrije, SELIMI Directrice de recherche, CIRB	<i>Président</i>
Corette, WIERENGA Associate Professor, Utrecht University	<i>Rapporteur</i>
Antoine, DE CHEVIGNY Chargée de recherche, Inmed	<i>Rapporteur</i>
Ethienne, HERZOG Chargée de recherche, IINS	<i>Examineur</i>
Alberto, BACCI Directeur de recherche, ICM	<i>Examineur</i>
Cécile, CHARRIER Chargée de recherche, IBENS	<i>Directeur de thèse</i>

*'Anyone can
if so inclined
be the sculptor
of their brain'*

free after

Santiago Ramon y Cajal
(1852-1934)

Résumé

Les synapses sont des nanomachines qui transfèrent, intègrent et stockent l'information dans les circuits neuronaux. Leur fonctionnement repose sur des réseaux d'interactions moléculaires dont la composition et la dynamique façonnent la transmission synaptique et l'architecture des circuits, et dont les altérations sont une cause majeure de troubles neurologiques. Un nombre croissant d'études indiquent que chez l'homme, et en particulier dans le néocortex, les synapses présentent un degré supplémentaire de spécialisation contribuant au développement et au fonctionnement de circuits complexes qui sous-tendent les capacités cognitives humaines. Dans ce travail de thèse, j'ai caractérisé le rôle de la protéine caténine delta-2 (CTNND2), un composant des complexes cadhérines/caténines exprimé essentiellement dans le cerveau. CTNND2 est liée à l'évolution humaine de par son interaction avec SRGAP2C (Slit-Robo Rho GTPase-activating protein 2C), une protéine spécifiquement humaine qui contribue notamment à l'allongement de la période de maturation synaptique chez l'homme, et les mutations de CTNND2 sont impliquées dans des troubles neurodéveloppementaux sévères. En inactivant de manière éparse CTNND2 dans les neurones pyramidaux de la couche 2/3 du cortex somatosensoriel de souris, nous avons montré que CTNND2 opère à la fois aux synapses excitatrices et inhibitrices in vivo. Chez les souris jeunes, la déficience en CTNND2 accélère le développement des synapses excitatrices, perturbe l'équilibre excitation/inhibition et augmente l'excitabilité neuronale intrinsèque, ce qui illustre une rupture des mécanismes de rétrocontrôle homéostatique. Cette phase d'hyperexcitabilité et d'hyperexcitation juvénile est suivie, chez l'adulte, d'une perte de connections synaptiques prématurée compatible avec la diminution de l'activité corticale, l'altération des processus mnésiques et cognitifs et la dégénérescence progressive des dendrites observés dans d'autres études. L'analyse du réseau d'interactions de CTNND2 à l'aide d'un crible protéomique nous a permis de mieux comprendre comment CTNND2 régulait le développement des synapses excitatrices, des synapses inhibitrices et l'excitabilité neuronale. Elle a également mis en évidence un lien étroit avec d'autres métronomes du développement synaptique dont les mutations accélèrent la maturation synaptique dans certaines formes d'autisme et de déficiences intellectuelles. Ainsi, CTNND2 est une protéine synaptique au carrefour du développement neuronal, de la neurodégénérescence et de l'évolution humaine qui détermine la temporalité de la synaptogénèse, limite l'excitabilité et conditionne le maintien à long-terme des structures neuronales.

Summary

Synapses are nanomachines that transfer, integrate and store information in brain circuits. Their function relies on molecular interaction networks whose composition and dynamics shape synaptic transmission and circuit architecture, and whose alterations are a prominent cause of neurological disorders. A growing body of evidence indicates that synapses specialized in humans, especially in the human neocortex, which contributes to the formation and function of complex circuits that underlie human cognitive abilities. During my doctoral work, I characterized the role of catenin delta-2 (CTNND2), a component of cadherin/catenin complexes that is mainly expressed in the brain. CTNND2 is linked to human evolution through its interaction with SRGAP2C (Slit-Robo Rho GTPase-activating protein 2C), a human-specific protein that contributes to the protraction of the period of synaptic maturation in the human brain, and its mutations are involved in severe neurodevelopmental disorders. Using sparse inactivation of CTNND2 in layer 2/3 pyramidal neurons of the mouse somatosensory cortex, we demonstrate that CTNND2 operates at both excitatory and inhibitory synapses *in vivo*. In young mice, CTNND2 deficiency accelerates the development of excitatory synapses, disrupts the balance between excitation and inhibition, and increases intrinsic neuronal excitability, which illustrates a failure of homeostatic feedback mechanisms. The phase of juvenile hyperexcitability and hyperexcitation is followed by a premature loss of synaptic connections in adult mice, which is compatible with the progressive degeneration of dendrites and with memory and cognitive impairments observed in other studies. Proteomic analysis of CTNND2 interaction network provided critical insights into CTNND2 function in the regulation of excitatory synapses, inhibitory synapses and neuronal excitability. It also uncovered a close link with other metronomes of synaptic development whose mutations in autism and intellectual disabilities accelerate synaptic maturation. Thus, CTNND2 is a synaptic protein at the crossroad of neurodevelopment, neurodegeneration and human evolution that determines the timing of synaptogenesis, limits excitability and is necessary for the long-term maintenance of neuronal structures.

Publications

Fossati M, Assendorp N, Gemin O, Colasse S, Dingli F, Arras G, Loew D, Charrier C (2019) Trans-Synaptic Signaling through the Glutamate Receptor Delta-1 Mediates Inhibitory Synapse Formation in Cortical Pyramidal Neurons. *Neuron*. 104(6):1081-1094.e7. doi: 10.1016/j.neuron.2019.09.027.

Gemin O, Serna P, Zamith J, Assendorp N, Fossati M, Rostaing P, Triller A, Charrier C (2021) Unique properties of dually innervated dendritic spines in pyramidal neurons of the somatosensory cortex uncovered by 3D correlative light and electron microscopy. *PLoS Biol* 19(8): e3001375. <https://doi.org/10.1371/journal.pbio.3001375>

In preparation

Assendorp N, Depp M, Fossati M, Dingli F, Loew D, Charrier C. CTNND2 moderates synaptic excitation and neuronal excitability during postnatal development in the neocortex.

TABLE OF CONTENTS

Résumé	3
Summary	4
Publications	5
 CHAPTER 1 – GENERAL INTRODUCTON	 9
<i>CHAPTER 1.1 The brain and neuronal communication</i>	<i>11</i>
<i>CHAPTER 1.2 The cortex</i>	<i>13</i>
 CHAPTER 2 – SYNAPSES	 21
<i>CHAPTER 2.1 Synaptic ultrastructure and transmission</i>	<i>24</i>
<i>CHAPTER 2.2 Synapse development</i>	<i>32</i>
<i>Chapter 2.3 Synapse Evolution</i>	<i>37</i>
 CHAPTER 3 – CELL ADHESION MOLECULES AT SYNAPSES	 43
<i>Chapter 3.1 Synaptic cell adhesion molecules</i>	<i>45</i>
<i>Chapter 3.2 Cell adhesion molecules in synapse development</i>	<i>47</i>
<i>Chapter 3.3 Cell adhesion molecules shape synapse function</i>	<i>49</i>
<i>Chapter 3.4 Cadherin-catenin complexes at the synapse</i>	<i>51</i>
 AIM OF THIS THESIS	 59
 CHAPTER 4 – CTNND2 moderates synaptic excitation and neuronal excitability during postnatal development in the neocortex.	 61
<i>INTRODUCTION</i>	<i>65</i>
<i>RESULTS</i>	<i>66</i>
<i>DISCUSSION</i>	<i>75</i>
<i>MATERIALS AND METHODS</i>	<i>77</i>
 CHAPTER 5 – Perspectives	 87
 REFERENCES	 93
 Supplementary	 111
<i>Figure S1</i>	<i>113</i>
<i>Figure S2</i>	<i>114</i>
<i>Figure S3</i>	<i>115</i>
<i>TABLE S1</i>	<i>116</i>
 ANNEX 1	 125
ANNEX 2	126

CHAPTER 1 – GENERAL INTRODUCTON

CHAPTER 1.1 The brain and neuronal communication

The nervous system enables animals to receive and respond to environmental cues in a coordinated manner. In vertebrates, the computational center of the nervous system is the brain. The cell type central to this computational power are neurons, which specialize to integrate and relay information and to subsequently generate an appropriate response. In the brain there is a multitude of neuronal subtypes, each characterized either by having a defined class of neurotransmitter or through distinct morphological, molecular or functional characteristics. The largest functional difference between neuronal subtypes is arguably found between excitatory and inhibitory neurons (the latter often referred to as interneurons), that respectively enhance or inhibit activity in other cells.

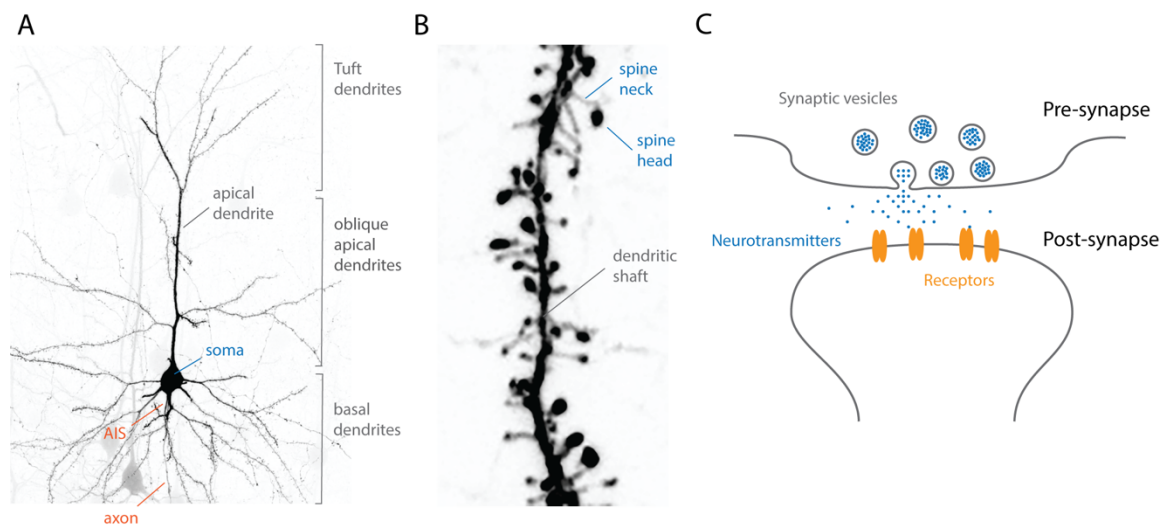


FIGURE 1 Neuron, dendrite and synapse morphology. (A) Adult layer 2/3 cortical pyramidal neuron electroporated with a fluorescent filler. Labels indicate different cellular compartments. Cortical pyramidal neurons typically have a main apical dendrite that extends towards the cortical surface but bifurcates before it reaches layer 1 to form the *tuft*. Basal dendrites originate from the cell body or *soma* and branch extensively. A single axon projects from the soma downwards and branches extensively to reach multiple target areas in the brain. The somato-dendritic and axonal compartments are separated by the axon initial segment (AIS). Note that the axon continues outside the image and some of the dendrites were cut during sample preparation. (B) A segment of an oblique apical dendrite with dendritic spines protruding from the dendritic shaft. The spine head is connected to the shaft via a spine neck of variable thickness. Various spine morphologies illustrate spine diversity. (C) Schematic illustration of a chemical synapse. The pre-synapse contains vesicles filled with neurotransmitters which fuse with the pre-synaptic membrane to release the neurotransmitters into the synaptic cleft. Here they bind to post-synaptic receptors which induces a postsynaptic response

All neuronal subtypes have in common that they are highly polarized cells with a cell body or soma from which multiple dendrites and a single axon protrude (Figure 1A). The soma and dendrites together form the somato-dendritic compartment that receives and integrates information, whereas the axon functions as a sender. Dendrites can be highly branched and morphologically complex but

only extend locally from the soma. The axon can project locally but also to distant targets within the nervous system and it branches extensively within its target areas. The somato-dendritic and axonal compartment of the cell are separated by the axon initial segment (AIS) which is located at the start of the axon (Figure 1A). This segment acts (1) as a barrier for intracellular transport and thus strongly contributes to cellular polarization and (2) as site of action potential initiation. Action potentials (APs) are strong, rapid and transitory changes of the cell's membrane potential that propagate along the axonal cell membrane. They form an all-or-nothing output signal generated by the neuron in response to integrated inputs it receives. As such AP generation is heavily regulated through for instance specific inhibition of the AIS and down-regulation of neuronal *intrinsic excitability*, its likelihood to fire and AP in response to a given stimulus.

Neurons are highly interconnected with one another and form complex functional networks via synapses. Synapses are intercellular junctions that mediate neuronal communication through synaptic transmission. In the central nervous system (CNS) two classes of synapses coexist: (1) electrical synapses, in which signals are transmitted in the form of ion currents that flow from one neuron to another via gap junctions, protein complexes that physically connect the cytoplasm of two cells; and (2) chemical synapses, that essentially are transcellular multimolecular machineries (Figure 1C). On one cell, the presynaptic compartment or *pre-synapse* is filled with vesicles containing neurotransmitters and highly specialized to release a chemical signal (neurotransmitter) in response to action potentials (Südhof, 2012). This pre-synapse is closely opposed to the post-synaptic compartment or *post-synapse* on the other cell, separated only by a narrow and protein dense *synaptic cleft* between the two membranes. During synaptic transmission, neurotransmitters are released from the pre-synapse into the cleft and activate receptors that are located on the postsynaptic cell membrane. This leads to a local influx of ions and thus a change of voltage across the membrane of the receiving cell. The vast majority of chemical synapses connect the axon of one neuron with the dendrite of another (*axo-dendritic* synapses). Most pre-synapses are situated all along the length of an axon forming varicosities or *en passant boutons*. Post-synapses on the receiving cell are located either on dendritic spines (small protrusions of the dendritic membrane (Figure 1B)), the dendritic shaft, the membrane of the soma (*axo-somatic* synapses) or, in the case of *axo-axonal* synapses, the axon initial segment.

At any given time, a neuron receives a vast multitude of synaptic signals. These signals are integrated by amplitude, polarity and timing at different scales: the post-synaptic compartment, within a dendrite and within the larger somato-dendritic compartment. If the integrated signal adds up to reach the AP threshold, the neuron fires an action potential and thus transmits the information to other cells within its network. Neuronal excitability and synaptic transmission thus form the basis of neural communication and consequently brain function, behavior and cognition.

CHAPTER 1.2 The cortex

The brain processes information from the environment through the creation of representations of the world and subsequently using these representations to produce perception and behavior. For that, separate regions of the brain have distinct functional specializations but are interconnected to form complex processing pathways. The neocortex, for instance, is the region which coordinates sensory perception, motor planning and association processing, enabling animals to perform complex tasks and giving us humans our unique cognitive abilities. Within the cortex, sensory modalities (e.g. somatosensory vs auditory or visual) are anatomically segregated into distinct areas (Brodmann, 1909) (Figure 2A). Yet the cellular organization between areas is broadly similar, suggesting the existence of a *canonical cortical circuit* or organizational theme employing similar strategies to process multiple types of sensory information (Harris and Shepherd, 2015; Jabaudon, 2017).

The cortex is radially organized into six histologically distinct layers, formed by varying densities of highly specialized neuronal subtypes (Fig. 2A+D). *Excitatory projection neurons* constitute about 80% of the neurons in the cortex and send their axons to distal targets. They are classified according to their axonal innervation pattern and further subdivided based on regional and laminar location or morphological characteristics (Greig et al., 2013; Harris and Shepherd, 2015) (Figure 2D). For instance, layer 2/3 pyramidal neurons (*pyramidal* because of the shape of their soma) of the somatosensory cortex are *intratelencephalic projecting neurons* (IT; telencephalon: neocortex + basal ganglia) (Harris and Shepherd, 2015). Their axons primarily innervate cortical targets including the same functional area in the contralateral hemisphere (Figure 2A), enabling bilateral integration of information (Greig et al., 2013; Harris and Shepherd, 2015).

Excitatory projection neurons are interconnected in an excitatory cortical circuit (Figure 2B) that mediates information flow through the cortex and is modulated by local inhibitory circuits as well as intricate long-range feedback circuits (Jabaudon, 2017). Briefly, sensory information from the periphery is relayed by the thalamus mostly to cortical Layer 4. Layer 4 granular cells form the main entry point into the cortical circuit and act as a gateway. Within the cortex, sensory information is then integrated with other cortical and subcortical inputs, predominantly by layer 2/3 pyramidal neurons. Principal neurons of Layer 5 are the main output neurons of the cortical circuit and send their axon into subcerebral regions like the spinal cord (Figure 2A+B), relaying integrated information to initiate behavior. (Jabaudon, 2017)

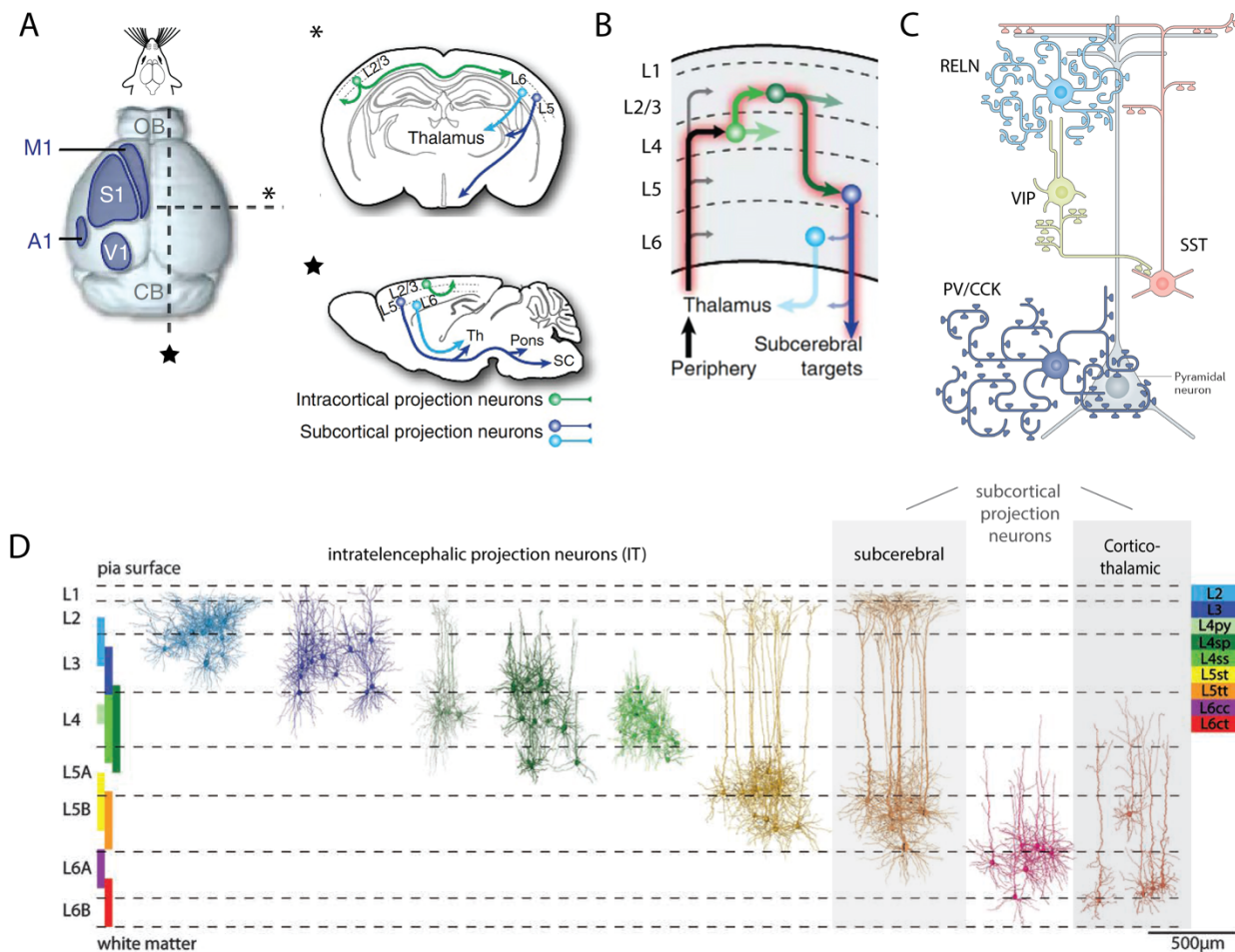


FIGURE 2 Organization and neuronal subtypes of the cortex. (A) Schematic representation of the mouse cortex. Left: the different sensory modalities occupy distinct areas of the neocortex, here the primary areas per modality are indicated on the left hemisphere. A1: primary auditory cortex; M1: primary motor cortex; S1: primary somatosensory cortex; V1: primary visual cortex. Right: Coronal (*) and sagittal (★) views of long range axonal pathways of 3 classes of projection neurons. Layer 2/3 (L2/3, green) pyramidal neurons project within the cortex to the same or contralateral hemisphere. Deep layer projection neurons target subcortical areas such as the thalamus (corticothalamic neurons, Layer 6, blue) and subcerebral targets as the hindbrain or spinal cord (corticospinal neurons, Layer 5, purple). (B) Simplified schematic of the excitatory cortical circuits. Sensory information from the periphery is relayed by the thalamus to the cortex. Thalamic axons innervate the granular layer 4 which forms the gateway to the neocortical circuit. Layer 2/3 neurons integrate sensory information with other thalamic and cortical inputs. Output neurons in layer 5 project to subcortical or subcerebral targets. (C) Cortical interneuron diversity and pyramidal cell innervation. Distinct interneurons show targeting specificity and create local inhibitory circuits. The pyramidal cells somatic region is targeted by parvalbumin (PV) or cholecystikinin (CCK) expressing neurons. Chandelier cells target the AIS. Somatostatin (SST) interneurons innervate the dendritic domain. Vasoactive intestinal peptide (VIP) synapse onto other interneurons. Reelin (RELN) positive cells use volume transmission to induce slow inhibition in superficial layers. (D) Morphology of excitatory neurons of the somatosensory cortex. Pyramidal cells (L2/3, L4, L5) have a main apical dendrite that reaches layer 1 where it branches extensively (tuft). Layer 4 star pyramidal cells have apical dendrites but lack the tuft. Similarly, the apical dendrite of Layer 6 neurons lacks the tuft and only extends into L4/5. Layer 4 spiny stellate cells lack the apical dendrite altogether. Classifying according to their axonal projections: intratelencephalic projection neurons (IT) project their axons within the cortex and basal ganglia; subcortical projection neurons (L5) project to subcerebral targets and cortical thalamic neurons (L6) projecting to the thalamus. (Adapted from A-B (Jabaudon, 2017), C (Wamsley and Fishell, 2017) and D (Oberlaender et al., 2012a))

At each step of the excitatory cortical circuit, the information flow is gated, shaped and modulated by local inhibitory circuits (Roux and Buzsáki, 2015). These are formed by a diverse population of interneurons, that are traditionally broadly classified by their expression of at least one of the following neurochemical markers: parvalbumin (PV), somatostatin (SST), cholecystokinin (CCK), vasoactive intestinal peptide (VIP) and reelin (RELN). Interneurons exhibit crucial control over cortical excitation through processes such as feedforward and feedback inhibition (mediated by CCK⁺, PV⁺ and SST⁺ interneurons respectively), dis-inhibition mediated by VIP-expressing cells (targeting other interneurons) and slow-acting volume inhibition induced by non-synaptic neurotransmitter release from RELN⁺ cells (Huang and Paul, 2019; Wamsley and Fishell, 2017). An important characteristic of cortical inhibitory circuits is the subcellular specificity by which distinct interneuron subtypes target excitatory pyramidal neurons (Fig 2C) (Wamsley and Fishell, 2017). Somata of pyramidal neurons are innervated by PV⁺ or CCK⁺ basket cells, whereas the AIS is specifically targeted by chandelier cells and the dendritic compartments are targeted by SST- and RELN-expressing interneurons (reviewed in Huang & Paul, 2019).

Cortical network activity, and thus cortical processing, depends on the interplay of excitation to propagate neuronal firing and inhibition to limit and shape propagation in time and space (Borg-Graham et al 1998; Salinas and Sejnowski 2000, Wang 2001; Haider et al 2006). This is commonly referred to as *excitatory-inhibitory (E/I) balance* (also called E/I ratio), a term which is somehow controversial as *balance* usually implies equal magnitudes, which does not apply here. For lack of a better word, the term is used to describe the relative levels of excitation and inhibition both on the neuronal network level and on the level of single neurons. On the single-neuron level it can refer to the relative numbers of synapses or the relative magnitudes of individual excitatory and inhibitory inputs (Froemke, 2015). Acute experimental manipulations of the global E/I ratio that selectively decrease either inhibition or excitation result in a shift of cortical activity to a hyperexcitable (epileptiform) or silent (comatose) state (Sanchez-Vives et al., 2010; Yizhar et al., 2011), thus demonstrating the importance of the E/I balance for cortical function.

Cortical development

The formation of cortical circuits involves the generation of cortical cells from progenitors, their migration and morphogenesis (i.e., extension of axon and dendrites) and subsequent establishment of connectivity (i.e., synapse formation) (Figure 3A 1-4). These processes are governed by intrinsic (e.g., differential gene expression) and extrinsic (e.g., input from thalamocortical afferents and spontaneous neuronal activity) factors that shape cortical circuits far into postnatal development (Greig et al., 2013; Jabaudon, 2017; López-Bendito and Molnár, 2003; Silva et al., 2019). Corticogenesis starts with the expansion of the neuroepithelium by symmetric divisions of neuroepithelial stem cells (NESCs). Around embryonic day (E) 11.5 in mice and post-conception week (pcw) 8 in humans, radial glia cells (RG) derive from this founder population of NESCs and form the ventricular zone, where they will divide asymmetrically to self-renew and give rise to outer radial glia (oRG; cell bodies in the subventricular zone), intermediate progenitors and excitatory neurons (Figure 3A). Already at this early stage, morphogen gradients regulate the expression of transcription factors that pattern the distinct cortical areas (Cadwell et al., 2019).

Excitatory cortical neurons are born successively between E10 and 18.5 in mice (pcw8 and pcw24 in humans) (Farhy-Tselnicker and Allen, 2018; Klingler et al., 2021). They are produced through asymmetric division of RG (direct neurogenesis) or from intermediate progenitors and outer RG (indirect neurogenesis) that reside in the subventricular zone (SVZ) (Figure 3A). Newborn neurons then proceed to populate the cortical plate in an inside-out manner with early-born neurons forming the deep layers and later-born neurons migrating past them to progressively form the superficial layers (Gilmore and Herrup, 1997). For this radial migration (Figure 3A-2) neurons use radial glia processes that span the cortical plate as scaffolds (Götz et al., 2002; Kriegstein and Alvarez-Buylla, 2009). While migrating, they acquire their axon-dendrite polarization (Xu et al., 2015) and begin to develop morphologically (neuritogenesis; see Figure 3A-3; reviewed in (Barnes and Polleux, 2009; Cadwell et al., 2019).

In parallel to excitatory neuronal migration and maturation, once excitatory neurogenesis is complete (P0 in rodents), radial glia switch from a neurogenic to a gliogenic differentiation program and differentiate to astrocytes (Kriegstein and Alvarez-Buylla, 2009; Noctor et al., 2008). Newborn astrocytes retain proliferative potential and expand in numbers well into postnatal development until they are evenly distributed across the cortical layers and areas, each occupying their own non-overlapping space by the fourth postnatal week (Ge et al., 2012). (Farhy-Tselnicker and Allen, 2018)

A Excitatory neurogenesis and migration

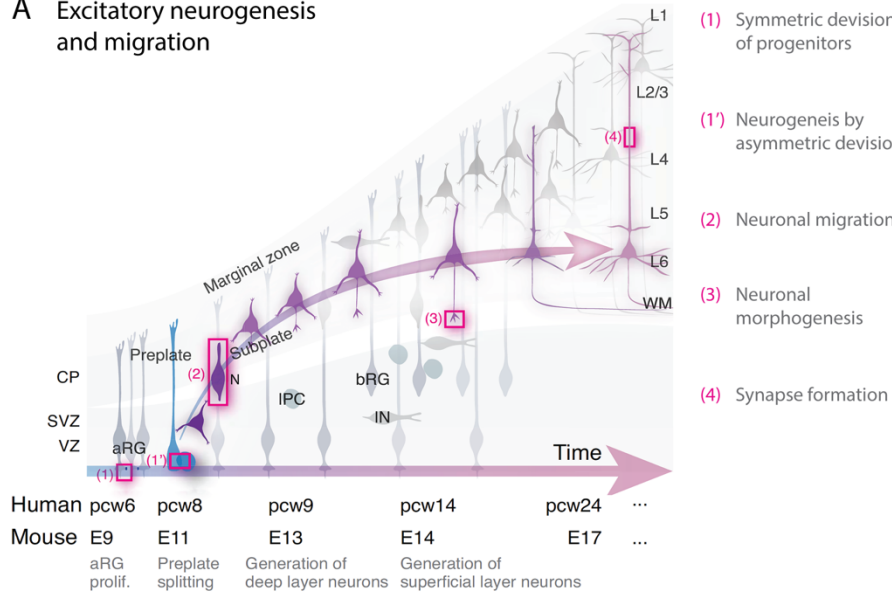
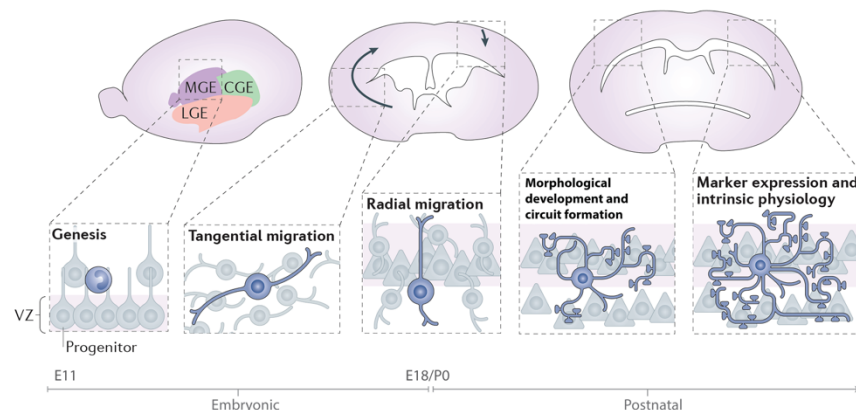


FIGURE 3 Cortical development. (A) Summary of cortical excitatory neurogenesis, migration and maturation. Cortical excitatory neurons are born in an inside out manner (deep layer neurons first, upper layer neurons later) from progenitors lining the ventricular zone (1'). They migrate radially along aRG processes into the cortical plate (2) and morphologically develop once they have reached their final position (3). Neuronal morphogenesis, synaptogenesis (4) and refinement of connectivity extend into postnatal development. Here a deep layer cortical neuron can be followed through its development (arrow). CP, cortical plate; (S)VZ, (sub)ventricular zone; E, embryonic day; pcw, post-conception week; a/bRG, apical/basal radial glia; N, neuron; IN, interneuron; WM, white matter. (adapted from Klingler et al., 2021) (B) Cortical interneurons are generated from stem cells in the medial ganglionic eminence (MGE) and the caudal ganglionic eminence (CGE) and migrate tangential into the cortical plate. This is followed by radial migration to populate the developing cortical layers where upon reaching their final position during postnatal development, they establish their distinct morphology and synaptic contacts. In parallel their transcriptional identity and physiological attributes are acquired (adapted from Wamsley & Fishell, 2017).

B Inhibitory neurogenesis and migration



In contrast to excitatory neurons and astrocytes, cortical interneurons are formed from progenitors in one of three proliferative zones that line the ventricles - the medial, caudal and lateral ganglionic eminences (MGE, CGE and LGE, respectively) - and migrate tangentially into the cortical plate between E11 and P0, where they disperse radially to populate the nascent cortical layers (Fishell and Kepecs, 2020; Wamsley and Fishell, 2017) (Figure 3B). Upon reaching their target location, interneurons mature, are recruited into cortical circuits, and their diversity becomes evident through distinct morphologies, connectivity and marker expression pattern (Figure 2C + 3B). (Silva et al., 2019; Wamsley and Fishell, 2017)

In the first weeks of postnatal development (in rodents), cortical neurons begin to establish connectivity. The formation of functional cortical circuits require axons to find their way to their appropriate target area (*axon guidance* – for a comprehensive review see Chédotal, 2019), the

connection of appropriate synaptic partners (*synapse specificity* – see chapter 2 and 3), the assembly of functional synapses (*synaptogenesis* – see chapter 2) and their *maturation* and subsequent activity-dependent circuit *refinement* (see chapter 2). Like the formation of cortical layers, circuit formation also follows an inside-out gradient. This is reflected by the successive critical periods of circuit refinement in deep cortical layers vs upper layers (e.g., in the rodent somatosensory cortex P4 and P16 are correlated with the end of the critical periods for structural plasticity of thalamocortical inputs to layer IV and that of lateral connections between layer II/III pyramidal neurons respectively (Erzurumlu and Gaspar, 2012)). Generally, the inside-out manner of development means that during postnatal development various stages of neuronal and circuit development co-exist and thus could be differentially affected by environmental stimuli (Crair and Malenka, 1995; Fox and Wong, 2005; Jabaudon, 2017; Oberlaender et al., 2012b).

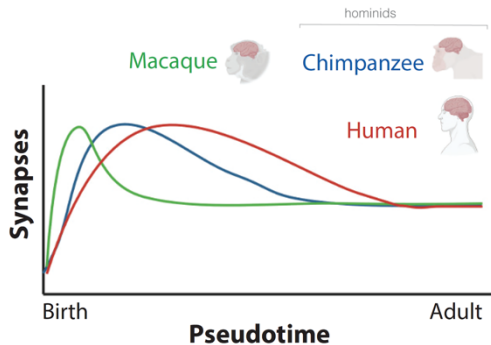


FIGURE 4 Heterochrony of human cortical development. Synapse formation and circuit refinement is protracted in hominids and even more in humans, relative to life span and in absolute duration (to enable comparison here indicated as pseudo time). (adapted from Libé-Philippot & Vanderhaeghen, 2021)

Humans, compared to other species, display *heterochrony* of cortical development: while overall the processes of cortical formation are conserved, in humans they span over a different timescale (Figure 4) (reviewed in Iwata & Vanderhaeghen, 2020; Libé-Philippot & Vanderhaeghen, 2021). This is most evident in the protracted maturation of cortical neurons and glia cells, that results in *neoteny*, the retention of juvenile traits over longer time-scales (Petanjek et al., 2011; Sousa et al., 2017). In humans, maturation of cortical neurons, including morphogenesis and synapse development, take up several years instead of months in macaque or weeks in mice (Huttenlocher, 1979; Petanjek et al., 2011). This is also reflected in a protracted gene expression profile of genes involved in synaptogenesis (Liu et al., 2012; Zhu et al., 2018b). Even when human neurons are transplanted as single cells in a mouse brain, they follow their own prolonged developmental timeline (Linaro et al., 2019), suggesting the involvement of neuron-intrinsic mechanisms governing their developmental timing. The protracted development has been proposed to play a major role in the development of human cognitive abilities, as it allows for extended critical periods of plasticity and thus for more environmental influence on brain development (Bufill et al., 2011; Sherwood and Gomez-Robles,

2017). Interestingly, altered developmental time courses seem to be a part of the pathophysiology of neurodevelopmental disorders such as autism spectrum disorders (ASD) and schizophrenia (Forrest et al., 2018).

CHAPTER 2 – SYNAPSES

CHAPTER 2 Synapses

The term *synapse* was first introduced in 1897 by Charles Sherrington to re-name what Santiago Ramón y Cajal had called *nervous articulations* and defined as a structure through which neurons could communicate without being continuous (Foster and C.S Sherrington, 1897; Sotelo, 2020). Cajal also postulated that the dendritic protrusions, which came to be known as dendritic *spines*, were points of contact between two neurons that facilitate diverse connections with axons from many different sources. But the existence of chemical synapses (and its presence on spines) was unambiguously demonstrated only in the 1950s using electron microscopy (Palay, 1956). These early anatomical studies also first described the structure that chemical synapses across different nervous tissue have in common: The closely opposed vesicle-filled pre-synaptic terminal and the post-synaptic membrane, separated only by a narrow synaptic cleft (Palay, 1956). Today we know that, although there is a common theme to the architecture of chemical synapses, they are highly structurally and molecularly diverse. Functionally, chemical synapses can be subdivided into two general classes: excitatory and inhibitory synapses. Within both classes, synapses are further identified based on the identity of pre- and post-synaptic cells, the neurotransmitters used, their subcellular localization, their molecular composition and organization or their electrophysiological properties. Here I will introduce the two broad subclasses relevant for this thesis, namely glutamatergic excitatory and GABAergic inhibitory synapses, which are also arguably the most studied synaptic subtypes and form the majority of synapses in the cortex.

On principal cells of the mature mammalian cortex, GABAergic inhibitory synapses are found on the dendritic shaft, the cell body, the AIS as well as on dendritic spines (van Versendaal and Levelt, 2016; Villa et al., 2016). In contrast, the vast majority of glutamatergic excitatory synapses are formed between axons and *dendritic spines*, small actin-rich protrusions from the dendritic shaft (see Figure 1B) (Yuste and Bonhoeffer, 2004). Spines are composed of a bulbous head that is connected to the shaft by a narrow neck (Arellano et al., 2007; Harris and Weinberg, 2012) and can exhibit a large range of variability in size and shape from thin filopodia like spines to spines with a thin neck but a large spine head that are called *mushroom spines* (Berry and Nedivi, 2017; Runge et al., 2020). Spines compartmentalize biochemical and electrical synaptic signals, with the neck acting as diffusional barrier that isolates the spine head from its parent dendrite (Adrian et al., 2017; Alvarez and Sabatini, 2007; Tønnesen et al., 2014; Yasuda, 2017). In addition, spine necks are thought to filter the electrical component of synaptic signals and amplify spine head depolarization (Harnett et al., 2012; Tønnesen and Nägerl, 2016; Yuste, 2013) (but see Popovic et al., 2015; Takasaki & Sabatini, 2014). The introduction of two-photon microscopy for live *in vivo* neuroimaging in the 90s (Denk and Svoboda, 1997) has revealed that spines exhibit an incredible capacity for structural

remodeling even in the mature nervous system (Grutzendler et al., 2002; Trachtenberg et al., 2002). Most spines are dynamic throughout the life of an animal, exhibiting changes in size, shape or even complete turnover in response to the animal's experience and environment (reviewed in Holtmaat and Svoboda, 2009; Runge et al., 2020). Changes in spine size, shape and lifetime can be used to investigate changes in synaptic strength or maturation (reviewed in Berry & Nedivi, 2017 & Bhatt et al., 2009 and see below).

In addition to the post-synaptic specialization, spines can contain various intracellular organelles as well as ribosomes and endosomes enabling local protein synthesis and membrane and receptor trafficking respectively (Bailey et al., 2015). Some spines also harbor an inhibitory postsynaptic specialization. These spines, termed dually innervated spines, exist especially in the upper layers of the cortex (Kubota et al., 2007) and host about 40% of inhibitory synapses in basal dendrites (Gemin et al., 2021). The presence of an inhibitory specialization further reinforces signal compartmentalization in these spines (see Annex 2; Gemin et al., 2021)

CHAPTER 2.1 Synaptic ultrastructure and transmission

Synaptic transmission at both excitatory and inhibitory synapses is operated and tightly regulated by the molecular machineries of the pre-synapse, synaptic cleft and post-synapse acting in concert (Figure 5A). While pre-synaptic organization and composition is canonical, postsynaptic membranes are highly diverse (Boyken et al., 2013; Südhof, 2012)

The pre-synaptic active zone

On the presynaptic side, action potentials trigger the release of synaptic vesicles containing neurotransmitters. The type of neurotransmitter released depends on presynaptic cell type and the expression of distinct synthesizing enzymes and vesicular transporters that load the transmitter into the synaptic vesicles. Vesicle exocytosis is restricted to a small pre-synaptic membrane domain called the *active zone*, where a subset of vesicles, the *readily releasable vesicles*, are docked to the membrane (Kaesler and Regehr, 2017). Fusion of vesicles with the pre-synaptic membrane is executed by SNARE proteins and triggered by Ca^{2+} influx and binding to synaptotagmin upon action potential arrival (Jahn and Fasshauer, 2012). Central to the pre-synaptic machinery are RIM and Munc13 proteins that localize to sites of vesicle fusion where they are essential to the priming and docking of synaptic vesicles (Figure 5B) (Augustin et al., 1999; Kaesler and Regehr, 2017; Schoch et al., 2002; Tang et al., 2016; Varoqueaux et al., 2002) and RIM proteins tether Ca^{2+} channels to release sites via RIM binding proteins (Acuna et al., 2015; Han et al., 2011; Hibino et al., 2002). Other components of the active zone such as the large multidomain proteins Bassoon and Piccolo,

Synapsins, the ELKS family members and Liprin- α are thought to have scaffolding as well as regulatory functions (Schoch and Gundelfinger, 2006; Südhof, 2012). In addition, many other proteins, including cytoskeletal elements and adaptors, trans-membrane proteins - exemplified by Neurexins (Südhof, 2017) - and ion channels are present at, though not necessarily restricted to, the active zone (Boyken et al., 2013). (Figure 5B)

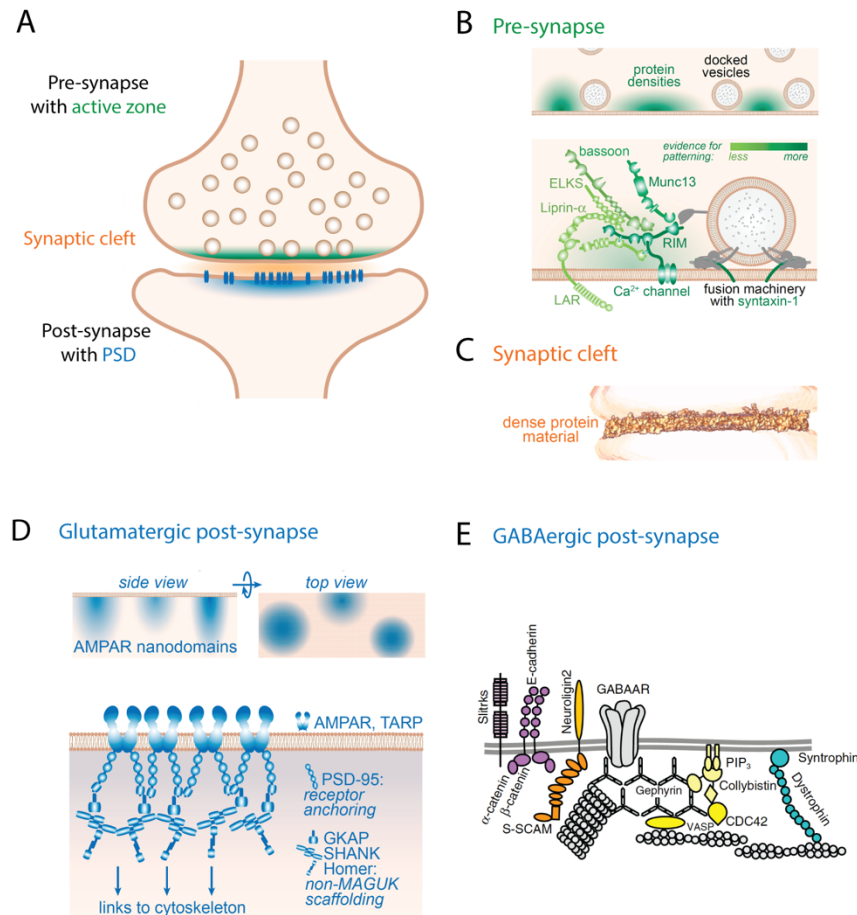


FIGURE 5 The protein machinery of chemical synapses. (A) Overview of a chemical synapse with the pre-synaptic machinery or active zone in green, the synaptic cleft machinery in orange and the post-synaptic density highlighted in blue. Note that here the post-synapse is depicted on a dendritic spine, as it is the case for the majority of excitatory synapses. Inhibitory post-synapses however can be formed on the dendritic shaft, spines (and spine neck) or the membrane of the soma and AIS. (B) Patterning (top) and molecular components (bottom) of the presynaptic active zone. Color code from light to dark indicate the evidence for patterning. (C) Side view of the protein complex of the synaptic cleft. Composition and function of the synaptic cleft machinery will be discussed in the following chapter. (D) Excitatory glutamatergic post-synapse: (Top) Patterning of the PSD seen from the side and the top and (bottom) schematic illustration of the molecular composition of the PSD. The excitatory PSD is layered vertically with receptors and transmembrane proteins intracellularly linking to a PDZ scaffold that in turn links to signaling proteins and the cytoskeleton. (E) Inhibitory GABAergic post-synapse: Receptors and cell adhesion molecules dynamically interact with the hexagonal gephyrin lattice that in turn mediates the interaction with signaling proteins and the cytoskeleton. (adapted from Arendt, 2020; Biederer et al., 2017)

The synaptic cleft

The second compartment of the synapse is the *synaptic cleft* – the 24nm wide extracellular space between the pre- and post-synaptic membrane (Lučić et al., 2005) (Figure 5C). Despite its name, the cleft is not empty but a rather protein-rich environment that contains extracellular matrix, secreted proteins and cell adhesion molecules (CAMs) that form trans-synaptic interactions (Burette et al., 2012; Gray, 1959; Lučić et al., 2005; Yuzaki, 2018; Zuber et al., 2005). Interactions occurring in the cleft are thought to have the ability to modulate and instruct synapse development, maturation and function (De Wit and Ghosh, 2016). I will discuss CAMs and their role at excitatory and inhibitory synapses in more detail in Chapter 3.

The post-synaptic density

On the post synaptic side, the *post synaptic density* (PSD) is positioned opposite of the presynaptic active zone (Figure 5A). There is considerable variation in composition between the PSDs of different synapse types and the overall molecular compositions of excitatory and inhibitory PSDs is profoundly different (Boyken et al., 2013; Moss and Smart, 2001; Sanes and Lichtman, 2001). Yet, all post-synapses have some organizational principles in common: they all use adhesion based differentiation (see chapter 3) and scaffold-based assembly of receptors and signalling proteins into tightly packed molecular machineries that rely on transient interactions (reviewed in Choquet and Triller, 2013; Fritschy et al., 2012; Okabe, 2007; Sheng and Hoogenraad, 2007; Sheng and Kim, 2011). An emerging idea based on recent *in vitro* biochemical studies (Feng et al., 2019; Milovanovic and De Camilli, 2017) suggest that PSD machineries may be best understood as membrane-less organelles or condensates that form through multivalency driven liquid-liquid phase separation (Figure 6) (Chen et al., 2020). With reference to the membrane, they are organized in three dimensions: Individual components of the PSD are differentially positioned perpendicularly to the cell membrane, forming a laminar organization with receptors and adhesion proteins at the surface, scaffold proteins beneath and signalling proteins facing the cytosolic side and linking to the cytoskeleton (reviewed in Sheng & Kim, 2011). Some PSD components also exhibit distinct lateral subsynaptic distributions forming so called *nanodomains* within the post-synapse (see upper panel Figure 5 B+D) (MacGillavry et al., 2013; Pennacchietti et al., 2017; Specht et al., 2013). At both excitatory and inhibitory synapses, pre- and post-synaptic nanodomains can align trans-synaptically, creating *nanocolumns* across the synaptic cleft (reviewed in Biederer et al., 2017) which are thought to ensure efficiency of synaptic transmission as they align post-synaptic receptors with vesicle release sites (Biederer et al., 2017; Tang et al., 2016). Importantly, the number and size of nanodomains vary between synapses and are subject to change in response to activity (reviewed in Biederer et al., 2017). Excitatory and inhibitory post-synapses have further in common that they are highly dynamic and undergo continuously remodelling over the timescale of minutes to days (Choquet and Triller, 2013). The abundance, activity, distribution

and mobility of the individual PSD components are dynamically regulated by post-translational modifications (particularly phosphorylation), local translation, protein degradation and alterations in protein synthesis as well as targeted trafficking to and from the synapse (Choquet and Triller, 2013; Holt et al., 2019; Sheng and Hoogenraad, 2007). Cytosolic components diffuse in and out of the PSD at varying rates and transmembrane proteins, including receptors, diffuse between synaptic and extra-synaptic compartment of the membrane (Choquet and Triller, 2013). The dynamic nature of the synapse not only allows for the turnover and recycling of its molecular components but also for dynamic scaling of synaptic strength in response to activity, generally referred to as *synaptic plasticity*. At the post-synapse, plasticity can be expressed through a vast array of molecular mechanisms (reviewed in Alvarez-Castelao & Schuman, 2015; Citri & Malenka, 2008; Spence & Soderling, 2015; Woolfrey & Dell'Acqua, 2015) that ultimately lead to changes in the number, distribution or biophysical properties of post-synaptic receptors (Diering and Huganir, 2018). These can coincide with changes in structural parameters (*structural plasticity*; e.g., change in spine, bouton or PSD size) during *long term plasticity*. Thereby the area of the PSD is proportional to its number of receptors (Nusser et al., 1997). As a result, synaptic strength correlates with PSD size and spine head volume (Holler et al., 2021).

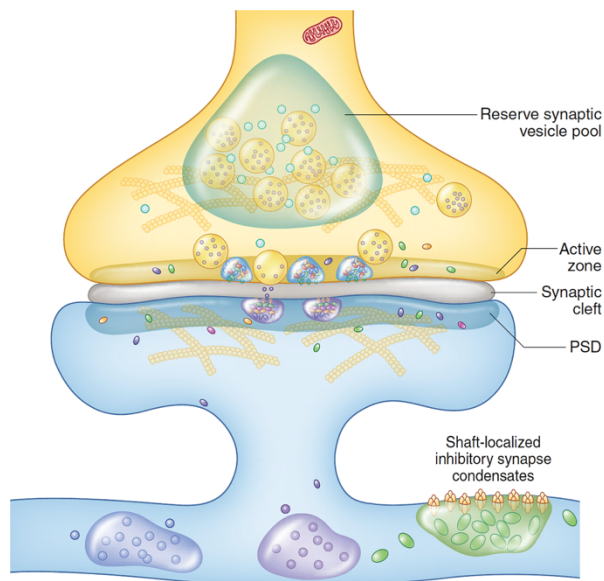


FIGURE 6 Biological condensates at the synapse. In the pre-synapse, liquid-liquid phase separation may play a role in clustering of the reserved pool of synaptic vesicles as well as active zone formation. Additionally, PSD and dendritic shaft may also contain various condensed protein assemblies. As biological condensates may have different compositions, they can spatially segregate protein clusters with distinct functions, e.g., inhibitory and excitatory post-synaptic condensates. (adapted from Chen et al., 2020)

Excitatory post-synaptic densities

On principal cells, excitatory post-synapses (Figure 5D) are localized to the head of dendritic spines and their PSD consists of a dense and rich network of interacting proteins formed by protein-protein interactions (Kim and Sheng, 2004). Glutamate released into the synaptic cleft acts upon ionotropic and metabotropic glutamate receptors (iGluRs and mGluRs respectively). Whereas mGluRs are G-protein-coupled receptors that have a role in various intracellular signal transduction pathways, iGluRs are ligand-gated ion channels and the main actors of excitatory synaptic transmission. iGluRs can be subdivided into N-methyl-D-aspartate (NMDA) receptors, α -amino-3-hydroxy-5methylisoxazole-4-propionate-type glutamate receptors (AMPA) and kainate receptors (KARs). During basal synaptic transmission, AMPARs are the main charge carriers, permitting the influx mainly of sodium ions upon glutamate binding and thus inducing fast depolarization of the postsynaptic membrane (Reiner and Levitz, 2018). NMDARs on the other hand are blocked by extracellular Mg^{2+} at resting membrane potential which is released when the post-synaptic membrane is depolarized. Additionally, NMDAR signalling requires co-agonist binding. NMDARs can therefore act as *coincidence detectors* opening only once all conditions (membrane depolarization and agonist binding) are met. When open, NMDARs are non-selective cation channels allowing the influx of Ca^{2+} and Na^{2+} ions and the flow of K^{+} ions out of the cells. NMDAR mediated Ca^{2+} influx and the intracellular signalling it triggers, is critical for *synaptic plasticity*, the activity dependent change in synaptic strength (Reiner and Levitz, 2018). In addition to the glutamate receptors, various types of cell adhesion molecules, receptor tyrosine kinases, ion channels and G-protein-coupled receptors localize to the post-synaptic membrane and participate in post-synaptic signalling (Stefen et al., 2016).

Receptor and transmembrane protein surface expression and lateral distribution is inter-dependently regulated through their intra- and extracellular interactions (Fossati and Charrier, 2021). Intracellular scaffold proteins contain multiple protein-protein interaction domains that accommodates parallel interactions and enable them to form the dense protein network of the PSD (Figure 7) (Sheng and Kim, 2011). At mature glutamatergic PSDs the core scaffold is formed by postsynaptic density protein 95 (PSD-95), guanylate kinase-associated protein (GKAP), SH3-domain and ankyrin-repeat domain protein (SHANK) and Homer (Sheng and Kim, 2011), which *in vitro* have been demonstrated to condensate together by phase separation (Zeng et al., 2018). Scaffold proteins can be represented by various family members and splice variants which is thought to contribute to synapse diversity (Sheng and Hoogenraad, 2007). PSD-95, which belongs to the membrane-associated guanylate kinase protein family (MAGUKs), provides direct binding sites to neurotransmitter receptors and many adhesion proteins (Sheng and Kim, 2011; Won et al., 2017). Interestingly, the number of PSD-95 largely exceeds receptor and CAM numbers in the PSD (Sheng and Hoogenraad, 2007), suggesting that during baseline transmission ample scaffold *s/ots* are unfilled which provides the means for fast up or down scaling of AMPAR numbers during synaptic plasticity (Opazo et al., 2012).

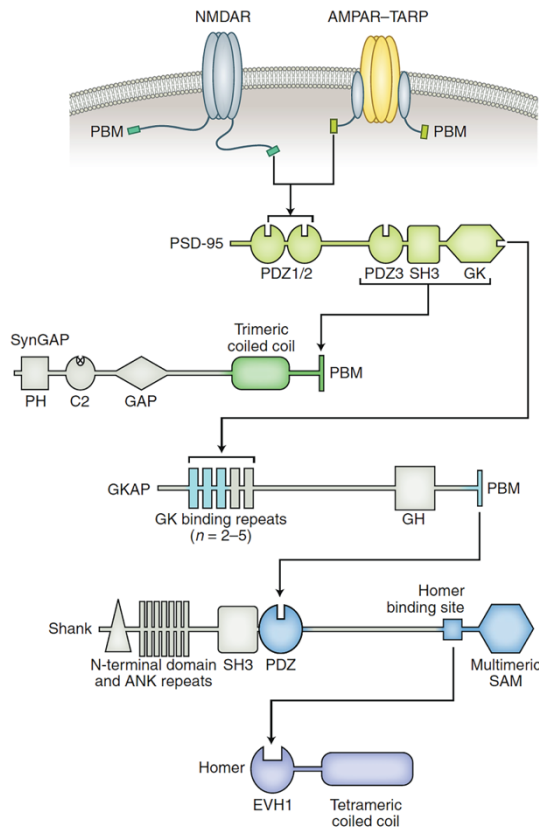


FIGURE 7 Domain organizations and interactions of core excitatory PSD components. Schematic depiction of multivalent protein-protein interactions between core PSD proteins that mediate phase separation under physiological conditions *in vitro*. Repeating domains or protein-protein interaction motifs on the different components increase network valency. (adapted from Chen et al., 2020)

Scaffold proteins recruit various cytoplasmic signalling proteins to the PSD such as kinases, phosphatases and small GTPases, which regulate actin dynamics, as well as their effectors, GTP-exchange factors (GEFs) and GTPase activating proteins (GAPs) (Sheng and Kim, 2011). Of these, CaMKII α/β and the Ras/Rab1 GTPase activating protein SYNGAP1 are especially abundant at the PSD. The two CaMKII isoforms are Ca²⁺/calmodulin dependent kinases that are regulated by autoinhibition and best studied for their role in *synaptic plasticity*, where NMDAR dependent activation of CaMKII is at the beginning of signalling cascades that lead to the expression of long term potentiation (Herring and Nicoll, 2016). Together CaMKII α and β are by far the most abundant proteins of the excitatory post-synapse, exceeding PSD95 by a ten-fold (Sheng and Hoogenraad, 2007). SYNGAP1 is comparable in numbers to PSD-95 family members (Sheng and Hoogenraad, 2007) with which it condensate *in vitro* in a phosphorylation dependent manner (Zeng et al., 2018). SYNGAP1 operates within a complex network of signalling cascades that ultimately regulates synaptic strength at baseline and following neuronal activity (Gamache et al., 2020). Both SYNGAP1 and CaMKII α translocate in and out of dendritic spines in a synapse activity dependent manner (Araki et al., 2015; Merrill et al., 2005; Strack et al., 1997). Importantly, although SHANK and SYNGAP are core components of the PSD, their mutation actually increases excitation (Aceti et al., 2015; Clement et al., 2012; Peixoto et al., 2016, 2019; Rumbaugh et al., 2006), showing that they function as negative

regulators of excitatory transmission and illustrating how excitatory synapses have a build-in capacity for auto-regulation.

Inhibitory post-synaptic densities

In contrast to excitatory synapses, the postsynaptic specializations of GABAergic inhibitory synapses (Figure 4E) appears less elaborate (Sheng and Kim, 2011), but is also less understood (Chiu et al., 2019). The main neurotransmitter receptors at inhibitory post-synapses in the brain are γ -aminobutyric acid (GABA) type A receptors (GABA_AR). Functionally, GABA_AR act as ligand-gated ion channels that mediate inhibitory currents carried mainly by chloride (Farrant and Nusser, 2005). GABAergic transmission is shaped by transmembrane auxiliary subunits of GABA_AR as well as by intracellular interaction with the proteins of the inhibitory PSD. Over the last decade auxiliary subunits such as Lhfp14/GAHLR and Shisa7 have been described to regulate receptor trafficking and modulate their functional properties (Han et al., 2021; Wu et al., 2019; Yamasaki et al., 2017). Intracellularly, Gephyrin has been identified as the main component of the inhibitory scaffold, interacting directly with GABA_A receptors, trapping it to the synaptic membrane (Groeneweg et al., 2018; Kneussel and Betz, 2000; Tyagarajan and Fritschy, 2014). Gephyrin molecules cluster to form a sub-membranous scaffold, similar in form to a hexagonal lattice (Figure 4E) (Saiyed et al., 2007). Gephyrin clustering and its interaction with receptors, is intricately regulated by phosphorylation (Battaglia et al., 2018; Niwa et al., 2019; Pizzarelli et al., 2020; Tyagarajan et al., 2011a). Gephyrin further undergoes other posttranslational modification among which palmitoylation, that allows for plasma membrane anchoring and is thought to stabilize gephyrin scaffolds at synaptic membranes. Preventing gephyrin palmitoylation leads to mis-localized clusters of gephyrin outside of synapses (Dejanovic et al., 2014). While gephyrin unquestionable forms the predominant scaffold, S-SCAM (synaptic scaffolding molecule; or MAGI-2, membrane associated guanylate kinase inverted-2) is a second *bona fide* scaffold protein at inhibitory synapses (Sumita et al., 2007). Interestingly, S-SCAM also localizes to excitatory synapses where it interacts with transmembrane AMPAR receptor regulatory protein (TARP), GKAP, the cell adhesion molecule neuroligin1 and other excitatory PSD components (Danielson et al., 2012b, 2012a). Similarly, at inhibitory synapses S-SCAM interacts with the inhibitory CAM neuroligin2 (NLgn2) and links it to the dystroglycan complex (or dystrophin-glycoprotein complex; DGC) and the immunoglobulin superfamily member IgSF9b (Woo et al., 2013). In hippocampal neurons, IgSF9b seems to localize in a separate subsynaptic domains than the GABAR/gephyrin/NLgn2 complex which suggests that S-SCAM may form a bridge between functionally distinct subdomains of the inhibitory synapse post-synapse (Woo et al., 2013). Another, more recent addition to the list of possible inhibitory scaffolds are InSyn1 and InSyn2, previously unknown proteins that were identified in a proximity screen of gephyrin (Uezu et al., 2016). Interestingly, deletion of InSyn1 specifically affects the distribution of dystroglycan complex (and vice

versa (Uezu et al., 2019)) but not of gephyrin at inhibitory synapses (Uezu et al., 2016). How the DGC-InSyn1 complex relates to the gephyrin scaffold is however still largely unknown.

Furthermore, various proteins that link the inhibitory scaffold to the cytoskeleton and intracellular signalling have been identified (Chiu et al., 2013; Pizzarelli et al., 2020). Among them, the Rho-GEF collybistin is probably best characterized. Collybistin directly binds Gephyrin (Kins et al., 2000; Papadopoulos et al., 2007) and can mediate its localization to the membrane through interaction with the $\alpha 1$ subunit of GABA_AR, Nlgn2 or through direct lipid binding (which is regulated by collybistin autoinhibition) (Kins et al., 2000; Papadopoulos et al., 2007; Reddy-Alla et al., 2010; Soykan et al., 2014). It is further involved in the remodelling of the subsynaptic cytoskeleton via the small Rho GTPase Cdc42 (Tyagarajan et al., 2011b; Xiang et al., 2006). However, the collybistin knock-out has no obvious phenotype in the cortex (Papadopoulos et al., 2007). Other gephyrin binding partners such as the actin-associated proteins profilin and VASP/Mena (Giesemann et al., 2003) are thought to regulate the anchoring of the scaffold to the cytoskeleton. This anchoring is crucial for PSD stability as pharmacological disruption of either F-actin or microtubules decreases the levels of gephyrin and receptors at synapses and increases receptor mobility (as shown for GlyR in Charrier et al., 2006).

It is noteworthy, that several inhibitory PSD components show only relatively subtle and often selective phenotypes when depleted: Nlgn2, despite being present at virtually all inhibitory synapses, only affects perisomatic synapses when depleted in hippocampal neurons (Poulopoulos et al., 2009). GluD1, a member of the glutamate receptor delta family, localizes to, and is required for the formation of, inhibitory synapses between SST⁺ interneurons and layer 2/3 cortical pyramidal neurons (see **annex 1**; Fossati et al., 2019). Similarly, Slit3, a newly recognized CAM at inhibitory synapses, when depleted, showed specific loss of subpopulations of inhibitory synapses in the hippocampus (Takahashi et al., 2012). This illustrates that although there has been considerable progress to our knowledge of inhibitory post-synapses in recent years (Krueger-Burg et al., 2017), we are only starting to understand the molecular diversity underlying different inhibitory synapse subtypes.

For both excitatory and inhibitory synapses, the emerging picture from studies of their proteome over the last two decades, is one of a high degree of molecular diversity and a vast functional and structural synaptic diversity that arises from combinatorial expression of synaptic proteins (Grant and Fransén, 2020; Nusser, 2018). However, a comprehensive proteomic descriptions of specific synapse types is still lacking, even though first steps towards a systematic mapping of synaptic diversity are being taken (Cizeron et al., 2020; Curran et al., 2021; Zhu et al., 2018a). Studies like these will considerably aid our understanding of circuit function in health and disease.

CHAPTER 2.2 Synapse development

Synaptogenesis of excitatory and inhibitory synapses in the rodent cortex occurs in early postnatal development. Both synapse types are generated at a high rate that peaks around P14 (Blue and Parnavelas, 1983a, 1983b; Gonzalez-Lozano et al., 2016; Li et al., 2010) and generates an excess of synapses. This developmental synapse formation is genetically determined as demonstrated by the formation of the majority of synapses when neurotransmitter release is blocked (Sando et al., 2017; Sigler et al., 2017; Verhage et al., 2000). A large proportion of the newly formed synapses are subsequently eliminated or *pruned* during the activity-dependent refinement of cortical circuits. Synapse numbers stabilize between P21 and P28 at adult levels (Figure 8) (Blue and Parnavelas, 1983a, 1983b; Li et al., 2010).

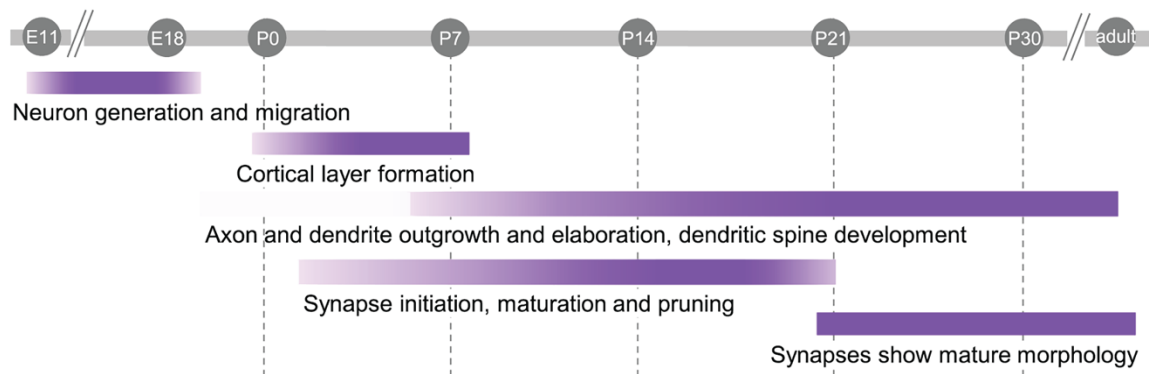


FIGURE 8 Developmental timeline in mice. Key developmental processes in the rodent cortex from embryonic stages to the end of the first month of life. Processes are represented as a colored bar, with the gradient in color intensity marking the beginning, peak, and end of the process. (adapted from Farhy-Tselnicker & Allen, 2018)

Spinogenesis

Excitatory synapse formation on principal cells is initiated by the formation of contacts between filopodia extending from dendrites and axon segments of the pre-synaptic cell. An important aspect of excitatory synapse development is therefore *spinogenesis*, the formation of dendritic spines prior to (or partially concurrent with) synapse formation. Immature dendrites form highly mobile filopodia that are functional precursors of spines (reviewed in Okabe, 2020; Runge et al., 2020). These filopodia are mostly transient structures and only a small fraction will contact an axon to form nascent synapses and subsequently differentiate into spines (Knott et al., 2006; Okabe et al., 2001). How filopodia formation is initiated and directed is however largely unclear. Extrinsic signals such as brain-derived neurotrophic factor (BDNF) signaling (Ji et al., 2005) or the local release of neurotransmitters (Kwon

and Sabatini, 2011; Oh et al., 2016) are thought to be important, as well as the interplay between membrane lipids and actin nucleation factors (Saarikangas et al., 2010), including GTPase signaling and the clustering of the membrane-associated signaling Bin/amphiphysin/Rvs (BAR)-domain proteins (reviewed in Hotulainen & Saarikangas, 2016; Okabe, 2020). BAR-domain proteins are multidomain scaffolding proteins that bind phosphoinositides (in particular PI(4,5)P₂ and PI(3,4,5)P₃) via a slightly curved lipid binding interface formed by their BAR domains and further contain domains that enable them to act in actin cytoskeleton remodeling (Carlson et al., 2011; Coutinho-Budd et al., 2012; Mattila et al., 2007). Clustering of these proteins, probably induced by the formation of phosphoinositides containing lipid rafts (Hotulainen and Saarikangas, 2016), results in membrane curvature (Coutinho-Budd et al., 2012; Mattila et al., 2007). Thereby, inverse (I)-BAR and inverse Fes-Cip1 homology (IF)-BAR proteins, such as in respectively the Missing-in-Metastasis (MIM) proteins and in slit-robo GTPase activation (SRGAP) proteins, promote negative, concave curvatures of the membrane and are involved in the formation of protrusions from the plasma membrane (Coutinho-Budd et al., 2012; Mattila et al., 2007). In cultured neurons, both the expression levels of SRGAP3 and MIM positively correlate with the density of filopodia formed (Carlson et al., 2011; Saarikangas et al., 2015). MIM accumulation was shown to occur prior to actin polymerization at the site of filopodia outgrowth (Saarikangas et al., 2015). These observations strongly implicate BAR-domain proteins in the initiation of filopodia formation. However, the upstream signaling events, despite the likely involvement of BDNF and glutamate, remain little understood (Hotulainen and Saarikangas, 2016; Okabe, 2020).

Synapse formation and maturation

Formation of both inhibitory and excitatory synapses is generally thought to involve the following sequential phases: (1) The establishment of an initial contact between appropriate synaptic partners. (2) The assembly of pre- and post-synaptic machineries to form nascent synapses and subsequently (3) synaptic specification or maturation (Figure 9) (Südhof, 2018). Key to the formation of nascent synapses are so called *synaptic organizers*, cell adhesion molecules (CAMs) (Südhof, 2018) or secreted neuronal or glial proteins (Farhy-Tselnicker and Allen, 2018; Yuzaki, 2018), that ensure appropriate connectivity (*synapse specificity*) during the formation of initial contacts and coordinate bidirectionally the assembly of synaptic machinery (see chapter 3; reviewed in Südhof, 2018, 2021). Generally, synapse assembly is thought to be facilitated by co-trafficking of synaptic components from the soma to the synapse. For example, SAP102 and NMDA receptors (Sans et al., 2005; Washbourne, 2015; Washbourne et al., 2002, 2004) as well as PSD-95, GKAP and Shank (Gerrow et al., 2006) are known to be co-trafficked as preassembled packages and inserted into synapses

together. However, the signaling pathways that initiate synapse assembly remain poorly understood and might vary between specific synapses and the trans-synaptic organizers present.

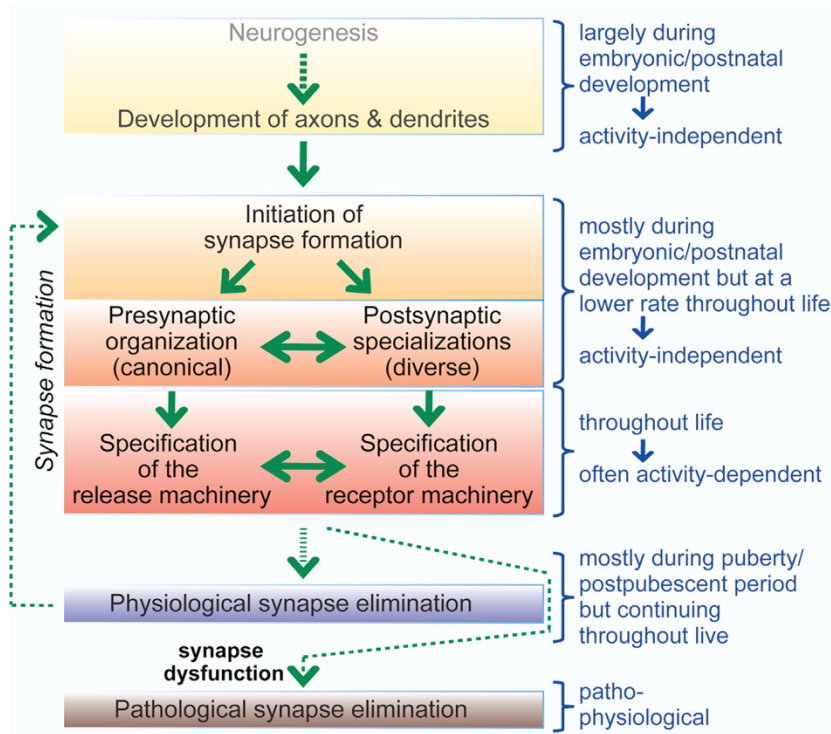


FIGURE 9 Synapse formation. During cortical development, neurons are generated, migrate, and grow short- and long-range axons and extensive dendritic trees. Initial synaptic contacts are mostly generated during development in the early postnatal period, although de novo synaptogenesis can occur throughout life. Nascent synapses are initially silent and gradually assemble pre- and postsynaptic machineries, mature and become functionally specified. Specification of synaptic function is likely an activity-dependent process that takes place continuously as a result of synaptic plasticity. Physiological synapse elimination is a key part of activity- and experience-dependent circuit refinement following synapse formation but also, at a low level, continues throughout life. Aberrant synapse development and pathological elimination are hallmark of neurodevelopmental and/or neurodegenerative disorders. (adapted from Südhof, 2018)

Newly formed excitatory synapses are initially functionally silent and convert into active synapses over time through the incorporation of AMPAR (Hanse et al., 2013). The conversion from silent to active synapses is promoted by astrocytes through the secretion of Gpc4 and 6 which recruit GluA1 to nascent synapses (Allen et al., 2012). GluA1 containing AMPAR are permeable to Ca^{2+} -ions and thus allow for high levels of synaptic plasticity (Henley and Wilkinson, 2016). Subsequently, at specific times in each cortical layer and promoted by astrocyte-secreted Chordin-like 1 (Blanco-Suarez et al., 2018), a switch from calcium-permeable to GluA2-containing calcium-impermeable AMPARs occurs and contributes to the maturation and stabilization of excitatory synapses (Brill and Huguenard, 2008; Gonzalez-Lozano et al., 2016; Kumar et al., 2002). The AMPAR subunit shift is also reflected in the expression pattern of AMPAR subunits *in vivo*: cortical GluA1 expression peaks during the first postnatal week and then remains constant throughout adulthood (Gonzalez-Lozano et al., 2016; Martin et al., 1998), while the expression of GluA2 increases only around P14 (Brill and Huguenard, 2008; Gonzalez-Lozano et al., 2016) coincident with synapse maturation. Similarly, NMDARs are developmentally regulated and the GluN2A/GluN2B ratio increases during development through activity- or experience-dependent regulation (reviewed in Yashiro & Philpot, 2008). The shift in NMDAR subunits allows for further AMPAR incorporation in the synapse, which is initially restricted

by GluN2B expression (Gray et al., 2011; Hall et al., 2007). The PSD95 protein family also sees an early expression of SAP102 that gradually declines and is replaced by PSD95 coincident with synapse maturation and spine stabilization (Lambert et al., 2017; Petralia et al., 2005; Zheng et al., 2011). Together this shows that the maturation of excitatory synapses is intricately orchestrated by astrocytes and involves structural and functional changes that are intimately related to the generation of a mature profile of post-synaptic receptors and neurotransmission.

Similarly, the expression of inhibitory synapse proteins increases in early postnatal development (Gonzalez-Lozano et al., 2016) and a shift in GABA_AR subunit expression can be observed, where the $\alpha 3$ subunit is expressed at birth and is replaced by $\alpha 1$ during development (Laurie et al., 1992; Taketo and Yoshioka, 2000). However, the role of the early expression of $\alpha 3$ containing receptor expression for the formation and function of individual inhibitory synapses remains unclear. Likewise, although astrocytes and their secreted factors are known to induce the formation of both excitatory and inhibitory synapses in culture, their precise involvement in inhibitory synapse formation and maturation remains to be elucidated (reviewed in Farhy-Tselnicker and Allen, 2018).

Activity-dependent circuit refinement

After the period of intense synapse formation in early postnatal development, cortical circuits undergo periods of experience- and activity-dependent refinement that include the elimination or *pruning* of excess or inappropriate synaptic connections and the maturation and stabilization of remaining synapses. These *critical periods* of enhanced circuit plasticity tune the circuit to best represent environmental stimuli and are under precise, circuit-specific temporal control (Hensch, 2005; Wilton et al., 2019). For instance, the critical period at L4-L2/3 synapses ranges from P11 to P13, while that of L2/3-L2/3 opens at P13 and closes around P16 (Erzurumlu and Gaspar, 2012; Wen and Barth, 2011). Even though the onset and length of critical periods are strongly influenced by the maturation of GABAergic interneurons (reviewed in Hensch, 2005; Marín, 2016), the molecular signaling pathways underlying critical periods are still an active area of research. Importantly, early hyperactivity or an elevated E/I ratio disrupts critical period plasticity and is thought to contribute to cognitive and behavioral impairment observed in neurodevelopmental disorders such as autism spectrum disorder and schizophrenia (Krol and Feng, 2018; Marín, 2016; Sun et al., 2018).

An important aspect of developmental circuit refinement is physiological elimination of synapses. Synapse elimination and the processes that govern it are best understood in systems other than the cortex, including the cerebellum (Kano and Hashimoto, 2009; Uesaka and Kano, 2018), the neuromuscular junction (Sanes and Lichtman, 1999) and retinal inputs in the visual system (reviewed in Chen and Regehr, 2000). On the one hand cell-intrinsic mechanisms such as the activation of the ubiquitin-proteasome system or expression of repulsive cues like semaphorins have been demonstrated to play a role in developmental synapse elimination (reviewed in Riccomagno and

Kolodkin, 2015), while on the other hand neuron-glia interactions are also thought to be heavily implicated, with the impairment of astrocyte or microglia function leading to profound pruning deficits (reviewed in Wilton et al., 2019).

Synapses are not only made and eliminated developmentally, but remain highly dynamic in mature circuits where they undergo activity-dependent changes in efficacy and morphology but also continuously turn over. Thus, while most neurons and their long-range axonal and dendritic structures are stable in the mature brain, their synaptic connections are often not. In the cortex, based on live-imaging of spines, approximately 40% of excitatory synapses are thought to have a short life span and turn-over every 5 days, while 60% remain stable throughout life (Attardo et al., 2015). Interestingly, in the hippocampus, spine turn-over seems to be a lot higher with nearly 100% of spines turning over every 2 weeks (Attardo et al., 2015; Pfeiffer et al., 2018), thereby likely reflecting the function of the hippocampus – in contrast to the cortex – as a highly dynamic structure designed to encode and process new memories, but not as a long-term repository of information (Frankland and Bontempi, 2005). Similarly, inhibitory synapses are subject to dynamic turn-over throughout life, being assembled and removed repeatedly at varying rates (Villa et al., 2016; Wierenga, 2017). Especially, inhibitory synapses on dually innervated spines (DiS) seem to exhibit extensive turn-over that is in stark contrast to the stable nature of the excitatory synapse on the same spines and could thus provide flexible and input-specific gating of excitatory transmission (Villa et al., 2016 and see also annex 2 Gemin et al., 2021). *De novo* synapse formation and circuit refinement in response to activity are thus prevalent in adults – albeit at different rates in different brain area's - and is thought to be essential for continued learning in adulthood (Kasai et al., 2010). However, whether the molecular mechanisms here are the same as during developmental synaptogenesis remains unclear.

Chapter 2.3 Synapse Evolution

Evolution of the vertebrate synapse

Across the animal kingdom, we find a large diversity of synapses that generally use similar organizational and development themes, which suggests common evolutionary origins. It is likely that the pre- and post-synaptic machineries have separate evolutionary origin: The presynaptic vesicle release machinery is also used by unicellular organisms to release chemicals into their environment and thus likely emerged through modification of this machinery (Arendt, 2020; Emes and Grant, 2012). By contrast, the evolutionary history of the post-synapse seems to be more complex. It has been postulated that the post-synapse has developed from a combination of signalling machineries that over the course of evolution have been co-opted into synaptic function (Arendt, 2020; Emes and Grant, 2012). Support for this is coming from comparative genomic and proteomic studies across evolutionary distant species, that show that most of the postsynaptic proteome was present in unicellular eukaryotes and some even in early prokaryotes, both predating the emergence of synapses and neurons in metazoans (Ryan and Grant, 2009) (Figure 10). So are structural features of ligand-gated ion channels (Bocquet et al., 2007), including the glutamate binding domain (Janovjak et al., 2011), conserved between present day vertebrates and prokaryotes and homologs of PSD95, Homer and Shank as well as CaMKII (Alié and Manuël, 2010; Sakarya et al., 2007) can be found in choanoflagellates, unicellular eukaryotes and close relatives of animals (Burkhardt and Sprecher, 2017). Together suggesting the presence of a simple receptor-to-transcriptome signalling pathways the common ancestor with prokaryotes and an extension of the postsynaptic proteome in early eukaryotes (Figure 10) (Emes and Grant, 2012). It is likely that synaptic proteins initially were functionally diverse and gradually co-opted into a *proto-synapse* (Emes and Grant, 2012). Once co-opted into the early metazoan synapses, postsynaptic proteins subsequently increased in number and evolved along the different animal lineages (Figure 10) (Burkhardt and Sprecher, 2017; Emes and Grant, 2012). In the vertebrate lineage, two whole genome duplications occurred approximately 550 million years ago (mya) (Figure 10) (Van De Peer et al., 2009) and led to what is called *vertebrate expansion* of the synaptic proteome. Generally, gene duplication are known to allow for rapid diversification as there is a relief of selective pressure through the duplication (Hurles, 2004). This is very dramatically illustrated by these whole genome duplications which multiplied the components of the synaptic proteome and ultimately produced greater diversity through sub-functionalization of the paralogs created (Grant, 2016). For example, while invertebrates possess a homolog of PSD95 called *disc large* (Dlg), the vertebrate PSD95 family includes four members (inlet Figure 10). Within this protein family the first whole genome duplication is thought have permitted a functional separation of the paralogs. Deletion of SAP97 and PSD95 in mice cause severe phenotypes (non-viable and strong learning impairment respectively), while the PSD93 and SAP102 KOs have relatively mild impairments

in complex learning tasks (Nithianantharajah et al., 2013). Interestingly, the vertebrate expansion pre-dates the emergence of large and anatomically diverse nervous systems of vertebrates and likely was instrumental for the generation of synapse diversity and concomitant neuronal and brain region diversity we see today in vertebrates (Ryan and Grant, 2009).

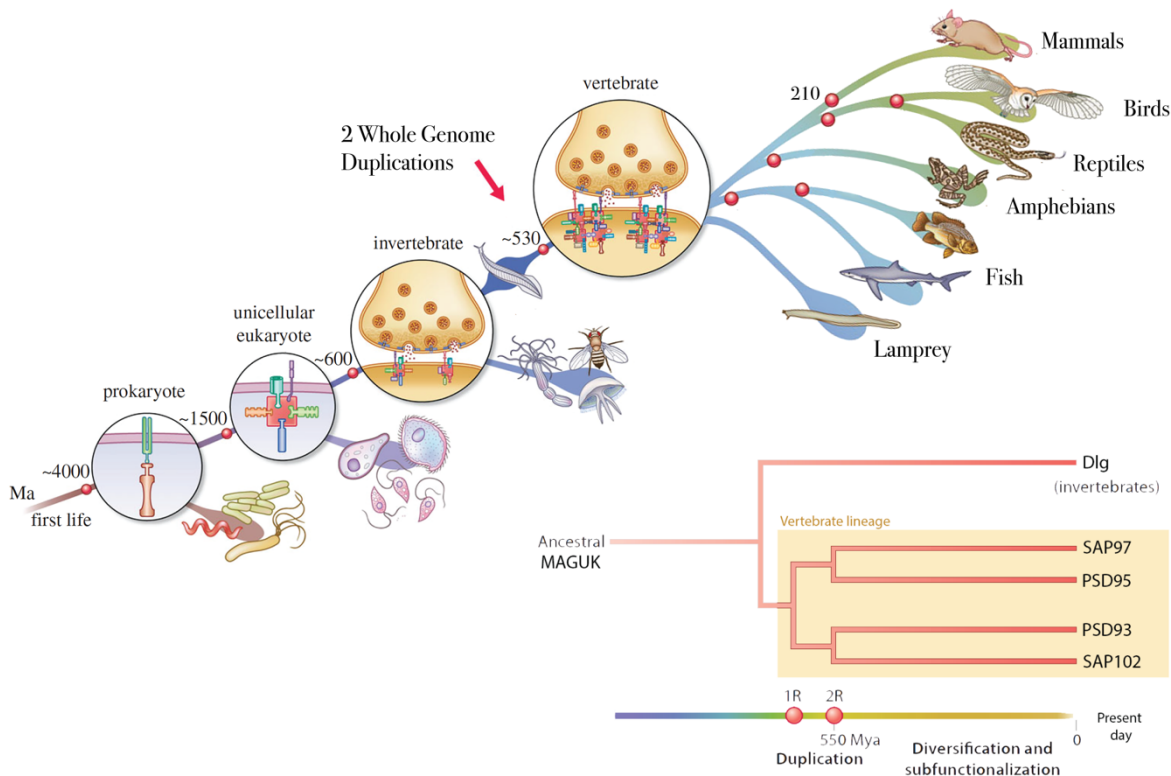


FIGURE 10 Molecular evolution of the synapse. Early versions of the postsynaptic proteins arose in prokaryotes and unicellular eukaryotes, were coopted into synapses and evolved into invertebrate and vertebrate synaptic machineries. The red arrow indicates the two genome duplications that lead to the vertebrate expansion in the synaptic proteome approximately 550 mya. **(Below)** Evolutionary tree of the vertebrate MAGUK protein family. The two sequential whole genome duplications (1R and 2R) resulted in the four vertebrate paralogs SAP-97, PSD95, PSD-93 and SAP102 followed by functional and structural diversification of each protein. Following duplication, the accumulation of sequence diversity in each paralog resulted in functional and structural diversification of each protein. Genome duplication similarly increased the complexity of many other PSP gene families in vertebrates. (adapted from Emes & Grant, 2012; Grant, 2016)

It is further noteworthy that to date we know a lot less about the evolutionary history of inhibitory synapses. On the one hand the inhibitory pre-synapse are essentially the same as that of other synapse types (except for transmitter synthesizing enzymes and vesicular transporters) which suggests a common origin and subsequent diversification in neuron types (Arendt, 2020). In line with this are various reports of co-transmission in vertebrates (reviewed in Tritsch et al., 2016). On the other hand, the inhibitory post-synapse is vastly different from excitatory PSDs (see above) and are thought to have originated separately, possibly as modulatory synapses onto otherwise glutamate responsive neurons (Arendt, 2020). Here as well, the pleiotropic nature of gephyrin (functioning both

as inhibitory postsynaptic scaffold in neurons and as enzyme within the molybdenum cofactor biosynthesis in astrocytes and other tissues (Tyagarajan and Fritschy, 2014)) hints towards a co-opting of the protein into synaptic function over the course of evolution.

Human synapse evolution

While the synaptic proteome is overall conserved among vertebrates (Grant, 2016), human synapses show specificities that are likely to contribute to the human specific cognitive abilities. Compared to non-human primates, human cortical synapses are more numerous, with human layer 2/3 cortical neurons exhibiting more elaborate dendritic trees (Deitcher et al., 2017; Mohan et al., 2015) and an increased number and density of dendritic spines and synapses per cell (Benavides-Piccione et al., 2002; DeFelipe et al., 2002; Elston et al., 2001). They mature over a protracted timescale (Petanjek et al., 2011) and seem to follow distinct learning rules during plasticity (Mansvelder et al., 2019). But what are the molecular underpinnings of these human-specific traits? One likely mechanism is the change in spatiotemporal expression of synaptic genes through altered transcriptomic regulation mediated by changes in noncoding DNA, microRNAs and human accelerated regions (HARs; of which 30% are predicted as enhancers) (Sousa et al., 2017), but also changes in the coding sequence of synaptic proteins are likely implicated. A specific focus in recent years has been on large segmental genome duplication that include known neuronal genes and occurred in the human lineage during the divergence from the chimpanzee lineage (Dennis and Eichler, 2016; Sudmant et al., 2010). Among these human-specific genes, the SLIT-ROBO-Rho-GTPase 2 (SRGAP2) paralogs (Figure 11) have been extensively studied in the lab (Charrier et al., 2012; Fossati et al., 2016) and remains the only humans specific duplication implicated at synapses so far. The ancestral SRGAP2A is highly expressed in the developing brain of all mammals (Bacon et al., 2009; Guerrier et al., 2009) and underwent a series of duplications in the human lineage giving rise to three human specific paralogs SRGAP2B, C and D (Dennis et al., 2012). Out of the paralogs, SRGAP2C became rapidly fixed in the human genome (Dennis et al., 2012) and is thus likely functionally relevant in humans. SRGAP2C expresses a truncated protein that corresponds to the F-BAR domain of SRGAP2A in which the last 49 c-terminal amino acids are replaced by 7 unique amino acids (Figure 11) (Dennis et al., 2012). When SRGAP2C is expressed in mouse cortical pyramidal neurons *in vivo*, this leads to the emergence of human-specific synaptic traits, including increased synaptic density and protracted synaptic maturation of both excitatory and inhibitory synapses (preserving the E/I ratio) (Charrier et al., 2012; Fossati et al., 2016). Interestingly, SRGAP2C expression phenocopies the constitutive knockout of *Srgap2a*, suggesting that it functions as a dominant negative paralog (Charrier et al., 2012). The truncated SRGAP2C F-BAR domain retained its ability to dimerize with the F-BAR domain of SRGAP2A, thereby targeting the heterodimer for proteolytic degradation (Schmidt et al., 2019).

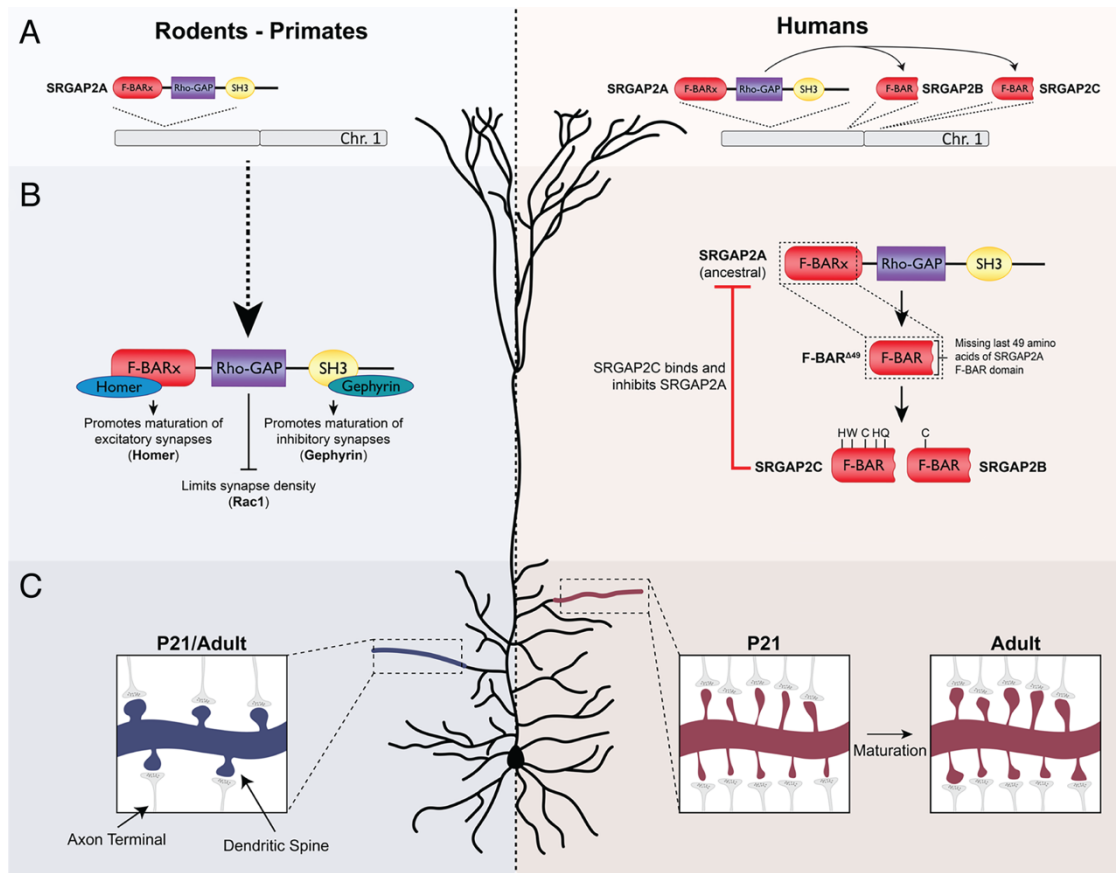


FIGURE 11 The human specific duplications of SRGAP2A. (A) The ancestral SRGAP2A, present in all mammals, was specifically duplicated in the human lineage to form human paralogs SRGAP2B and SRGAP2C. (B) SRGAP2A contains three distinct protein domains and promotes the maturation of excitatory synapses and inhibitory synapses through an interaction with Homer1 and gephyrin respectively. Through its Rho-GAP domain and Rac1, SRGAP2A limits synapse density. In humans, the partial duplication of SRGAP2A generated a truncated protein, that lacks the last C-terminal 49 amino acids of the F-BAR. A second duplication and subsequent sequence diversification led to the human-specific paralogs SRGAP2B and SRGAP2C. Binding of SRGAP2C to SRGAP2A inhibits all functions of SRGAP2A. (D) Expressing SRGAP2C in rodent cortical neurons results in the emergence of human-like characteristics of synapse development: the increase in synaptic density and protracted synaptic maturation. (adapted from Schmidt et al., 2019)

Understanding how the (partial) inhibition of SRGAP2A leads to the emergence of human traits thus requires the understanding SRGAP2A function and interaction network at synapses. So far we know that during synapse development, SRGAP2A acts a negative regulator of excitatory and inhibitory synapse density through its Rac1-specific GAP domain, promoting their maturation through its ability to bind both Homer1 at excitatory synapses and Gephyrin at inhibitory synapses with its class II EVH1 binding domain embedded in its F-BAR domain and its SH3 domain respectively (Figure 11) (Charrier et al., 2012; Fossati et al., 2016; Guez-Haddad et al., 2015; Okada et al., 2011). Further investigating the interaction network of SRGAP2 and other human-specific mutation will contribute to our understanding of human-specific regulations of synapse and has the potential to provide further insights in the pathophysiology of, and human vulnerability to, neurological disorders.

CHAPTER 3 – CELL ADHESION MOLECULES AT SYNAPSES

Chapter 3.1 Synaptic cell adhesion molecules

Cell adhesion molecules (CAMs; also called synaptic adhesion molecules or SAMs) are embedded in the synaptic membranes and an integral part of the synaptic cleft machinery. Generally, CAMs are tethered to membranes either by transmembrane segments or a GPI-anchor. They mediate cell-cell adhesion via extracellular interactions and, in the case of transmembrane CAMs, bind intercellularly to scaffolding and signaling proteins as well as the cytoskeleton. Neurons express a great diversity of CAMs from a large number of protein families (Figure 12) (Südhof, 2018, 2021). The most extensively studied among these are: Neurexins and neuroligins, cadherins and proto-cadherins, leucine rich repeat transmembrane proteins (LRRTMs), SynCAMs, Ephrin/Eph-Receptors, and teneurins (reviewed in Dalva et al., 2007; de Wit & Ghosh, 2014; De Wit & Ghosh, 2016; Südhof, 2018, 2021). Each of the CAM protein families exhibit substantial molecular diversity, which arises either through the large size of the underlying gene family (e.g., cadherins) or through alternative splicing of a more limited number of genes (e.g., neurexin). Together this gives rise to a staggering number of total cell adhesion molecules, most of which remain to be characterized with regard to their expression pattern and putative role at synapses (Rudenko, 2017; Südhof, 2018).

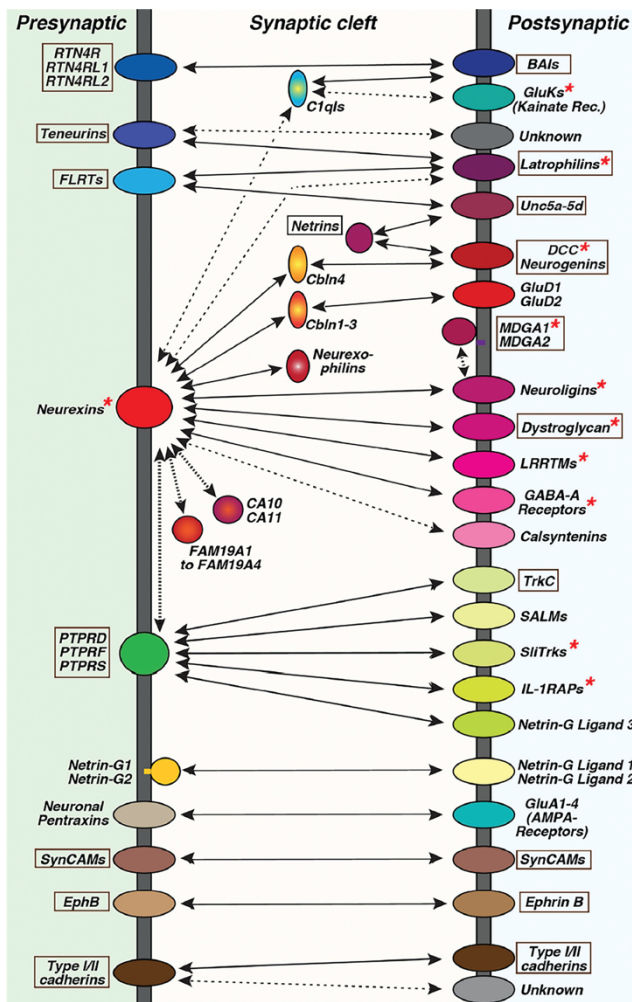


Figure 12 Overview of CAM families and their putative interactions at the synapse. Schematic representation of CAM interaction at synapses. Arrows depict physical interactions and are grouped per protein family without addressing member or isoform specific interactions. * indicates genetic association with neuro-psychiatric disorders. 'Boxed' CAMs are also implicated in developmental functions unrelated to synapses. (adapted from Südhof, 2021)

Originally, understanding of CAMs at the synapse was limited to their adhesive function, providing a structural link between pre- and post-synapse. This was typically assessed through their ability to aggregate cells in cell-based assays, combined with pull down in synaptic fraction, as well as synaptic localization in electron or light microscopy. In addition, CAMs were thought to have a dedicated trans-synaptic partner, with the typical example being pre-synaptic neurexins interacting with post-synaptic neuroligins (Song et al., 1999). However, over the last decade this view has been challenged and dramatically expanded to a more nuanced view, in which some CAMs can have multiple partners in *cis* and *trans* (reviewed in Chamma & Thoumine, 2018; De Wit & Ghosh, 2016a; Rudenko, 2017; Südhof, 2021) giving rise to a complex synaptic cleft interaction network that involves considerable cross-talk between adhesive systems (Figure 12) (Südhof, 2018). Neurexins (NRXs), for instance, are now known to interact with a wide array of structurally diverse partners across the synaptic cleft, depending on the expression of neurexin splice variants, which likely contributes to the specification of synapses (Gomez et al., 2021; Südhof, 2017). *Cis*-interactions of CAMs are often regulatory in nature: promoting, inhibiting or modulating the strength of *trans* interactions. For example, the *cis* binding of the GPI-anchored protein MDGA1 to neuroligin2 (NLGN2) inhibits the *trans* NLGN2-NRX interaction (Gangwar et al., 2017). Some CAMs extracellularly interact with proteins that are secreted by neurons (e.g., cerebellins and pentraxins) or glia (e.g., Hevin) and can serve as extracellular scaffolds, trapping CAMs or neurotransmitter receptors at the synapse (reviewed in Yuzaki, 2018). At cerebellar excitatory synapses, Cerebellin1 (Cbln1) secreted from the axon bridge postsynaptic glutamate receptor delta 2 (GluD2) and presynaptic neurexin to form a trans-synaptic interaction required for the maintenance and the plasticity of synapses formed onto Purkinje cells by parallel fibers (Matsuda et al., 2010; Uemura et al., 2010). A similar interaction *triad* spanning the synaptic cleft is formed at cortical inhibitory synapses by GluD1, Cbln4 and presynaptic neurexins (see **annex 1**; Fossati et al., 2019). Therefore trans-synaptic interactions can be mediated by proteins other than canonical CAMs, like glutamate receptors (Fossati and Charrier, 2021) or metabotropic g-protein coupled receptors (GPCRs) such as Latrophilins and BAI1s (reviewed in Südhof, 2018a, 2021; and see Kakegawa et al., 2015; Sando & Südhof, 2021; Sigoillot et al., 2015), thereby further adding to the myriad of possible interactions in the synaptic cleft.

Chapter 3.2 Cell adhesion molecules in synapse development

Trans-synaptic cell adhesion has been recognized early on to play key roles during the different stages of synapse development (Figure 13) (Favuzzi and Rico, 2018; Jang et al., 2017; Kim et al., 2021; Südhof, 2018, 2021; Yuzaki, 2018). CAMs and their secreted interaction partners mediate the establishment of initial cell-cell contacts and formation of nascent synapses by serving as cell-cell recognition tags, permissive adhesion substrates or repulsive signals, that specify cellular and sub-cellular connectivity in concert with guidance cues (Sanes and Zipursky, 2020). They act as synaptogenic nucleating factors (also referred to as synaptic organizers), inducing the clustering of pre- and post-synaptic machineries to promote synapse differentiation and maturation. Even in later stages of synapse development, CAMs are thought to be involved in the activity-dependent stabilization and elimination of synapses and thus refinement of circuits (Südhof, 2021). Throughout development, specific CAMs might have all or just a subset of these functions, and different CAMs likely work in concert to form individual synapses and shape specific synaptic properties. For example, the combinatorial expression of protocadherins that exhibit very strict isoform binding specificity in their homophilic trans interactions, is thought to aid target selections by providing a molecular recognition code and aiding self-avoidance during early synaptic development without having synapse inducing properties themselves (reviewed in De Wit & Ghosh, 2016; Lefebvre et al., 2012; Sanes & Zipursky, 2020; Takeichi, 2007).

Whether or not a protein has synaptogenic properties can be tested with co-culture assays, where distinct CAM are expressed in non-neuronal cells (e.g., COS and HEK cells) to assess their ability to form a pre- or post-synaptic differentiation in co-cultured neurons. Pioneering studies demonstrated that expression of neuroligin1 in non-neuronal cells could induce neuronal pre-synaptic differentiation in co-cultured neurons (Scheiffele et al., 2000), while heterologous expression of neurexin can induce the differentiation of GABAergic and glutamatergic postsynaptic membrane (Graf et al., 2004).

To date, most of the synaptic CAMs identified (Figure 12) have been tested similarly and nearly all have been shown to be capable of inducing heterologous synapse formation (reviewed in De Wit & Ghosh, 2016; Südhof, 2018). However, when assessed through genetic depletion *in vivo*, very few actually seem to be required for synapse formation on a large scale (reviewed in Südhof, 2021). For example, the deletion of latrophilins or BAI isoforms in mice produces a severe decrease in the formation of specific synapses in the hippocampus, cerebellum and olfactory bulb (Sando and Südhof, 2021; Sigoillot et al., 2015). In contrast, neurexin deletions lead to little synapse loss *in vivo* but impair synaptic transmission through either impaired per-synaptic Ca^{2+} -channel recruitment (Luo et al., 2020) or impaired endocannabinoid signaling (Anderson et al., 2015) depending on the cellular context. This illustrates that, even though most of the individual CAMs might not be required for

synapse formation or maintenance *in vivo*, they play a key role in synapse maturation, serving as synapse organizers and conferring synapse-specific properties (Südhof, 2021) (see below).

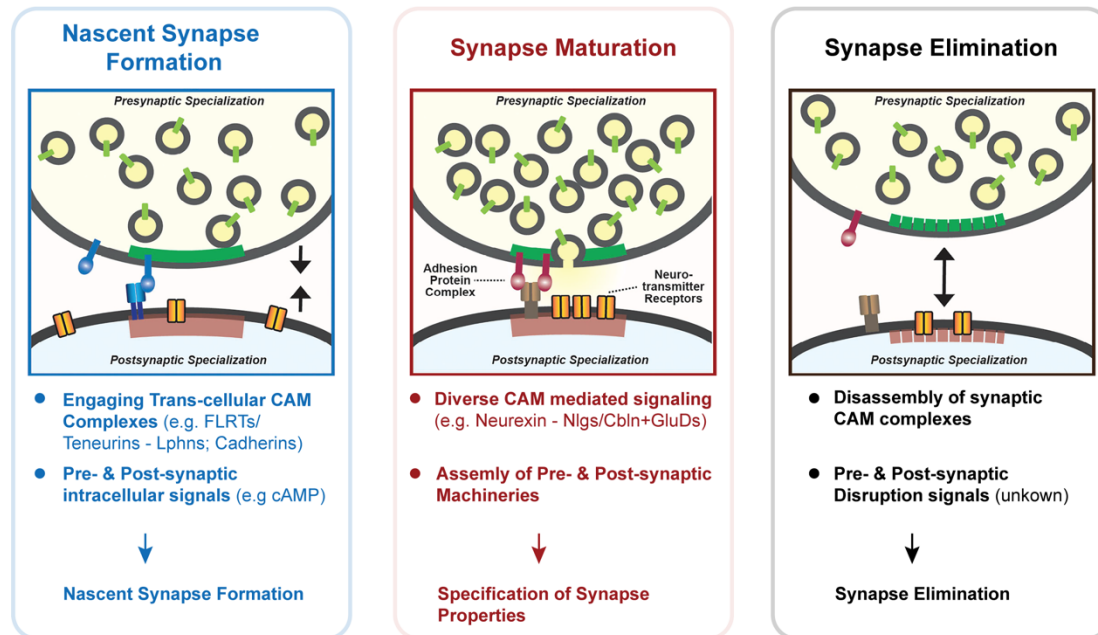


FIGURE 13 CAM function in synapse development. Schematic of nascent synapses (left), mature synapses (center), and synapses elimination (right). At nascent synapses, CAMs such as latrophilins establish initial cell-cell contact and initiate signaling cascades that lead to synapse formation. Subsequently CAMs organize synapse assembly and shape synaptic properties to promotes synapse maturation. During activity dependent refinement of circuits, synapse elimination is likely mediated by a weakening of CAM interactions leading to a disruption of synaptic processes. (adapted from Südhof, 2021).

Taken together with the promiscuity of synapse formation in co-culture assays, the lack of synapse formation phenotypes for most CAMs suggests that individual synapses are formed and shaped by multiple CAMs acting in concert. Therefore, the challenge therefore remains to unravel the exact combinatorial code and the choreography of specific trans-synaptic interactions acting during the development of discrete neural circuits. This will require comprehensive spatiotemporal transcriptomic, proteomic and cell or circuit-specific gene expression studies throughout development, combined with rigorous functional studies *in vivo*. In a *tour de force*, Rico and colleagues used transcriptomics to identify cell surface and secreted proteins selectively expressed by specific subtypes of cortical interneurons during the peak of synaptogenesis (Favuzzi et al., 2019). Their study significantly advanced our understanding of the molecular code that determines the specificity, cellular (inhibitory neuron subtype) and subcellular (dendritic, perisomatic, AIS), of inhibitory connectivity onto cortical pyramidal neurons. Recent development in proteomic approaches (e.g. proximity biotinylation, cell-surface profiling, synaptosome-specific proteomics) also open new perspective to understand the wiring of synaptic connections (e.g., Allen & Eroglu, 2017; Apóstolo & de Wit, 2019; J. Li et al., 2020; Schreiner et al., 2017; Spence et al., 2019; Takano & Soderling, 2021; Xu et al., 2021). Another major challenge will be to understand the signaling pathways activated by

distinct CAMs to induce and specify the assembly and the functional properties of synapses (but see Fossati et al., 2019; Sando & Südhof, 2021).

Chapter 3.3 Cell adhesion molecules shape synapse function

Many of the synaptic CAMs are persistently expressed in the mature nervous system. CAM interactomes are multi-molecular, trans-synaptic complexes that in addition to extracellular partners include a wide array of intracellular interactors including scaffold proteins, intracellular signaling proteins and ion channels. For example, at inhibitory post-synapses Neuroligin 2 (NLGN2) forms a complex with collybistin, gephyrin and other proteins that anchor GABA_AR at the synapse and regulate GABAergic transmission (Ali et al., 2020; Krueger-Burg et al., 2017). CAM complexes like these function as structural links, stabilizing protein machineries both on pre- and post-synaptic sides and as bi-directional trans-synaptic signaling complexes, making CAMs crucial actors in orchestrating synapse structure, function and plasticity throughout the life of a synapse (reviewed in Jang et al., 2017; Shinoe & Goda, 2015; Südhof, 2018a; Yamagata et al., 2003). As cleft spanning organizers of synaptic molecular content, CAMs are thought to be prime candidates for instructing the (sub)-synaptic alignment of pre- and post-synaptic machineries (Biederer et al., 2017; Haas et al., 2018). Indeed, several CAMs (e.g., N-cadherin (Elste and Benson, 2006), cadherin-10 (Smith et al., 2017), EphB2 and SynCAM1 (Perez de Arce et al., 2015)) exhibit distinct distributions within synaptic membranes. Loss of a trans-synaptic interaction can lead to mis-alignment of active zones and PSDs, as shown for remaining parallel fiber-Purkinje cell synapses of Cbln1 KO mice (Hirai et al., 2005). In addition, persistent CAM expression is likely to be required for the regulation of synaptic turnover (Attardo et al., 2015; Kasai et al., 2010) in much the same fashion as synapse formation and circuit refinement is during development (see above).

During plasticity, modulation of adhesion (and thus CAM complexes) is needed to allow for structural plasticity to occur, to trans-synaptically communicate structural changes and to subsequently stabilize the structural changes that express plasticity. That requires reorganization of the synaptic cleft evident in the changes in the number of synaptically localized CAMs during plasticity paradigms: For instance, cadherin (Bozdagi et al., 2000) and neuroligin (Schapitz et al., 2010) numbers at synaptic membranes are increased after LTP expression. Synaptic activity induced accumulation or reduction in CAM numbers at synaptic membranes are the result of altered stability of interactions or targeted trafficking to and from the synapse regulated by posttranslational modifications. For instance, the increase in neuroligin1 numbers at excitatory PSDs is mediated by CAMKII phosphorylation of their cytoplasmic tails (Bemben et al., 2014) and also levels of presynaptic β -neurexin1 at inhibitory synapses rises in response to neural activity due to an increase in stability (or suppressed dynamics) at the pre-synaptic membrane (Fu and Huang, 2010). Other changes upon

activity, such as the re-organization or establishment of synaptic nanocolumns are also thought to be mediated by CAMs (Biederer et al., 2017).

Several CAMs including neuroligin1 (Peixoto et al., 2012) and N-cadherin (Restituito et al., 2011) are known substrates of extracellular proteases that cleave off their extracellular domain in an NMDAR dependent manner (Peixoto et al., 2012; Suzuki et al., 2012). The proteolytic cleavage of CAMs – also referred to as *ectodomain shedding* – disrupts trans-synaptic interactions and releases the cleaved ectodomain as a bio-active fragment (Shinoe and Goda, 2015). Although irreversible, shedding is thought to be highly regulated and seems to affect only a sub-population of synaptic CAMs (Restituito et al., 2011), thus providing the means for a rapid decrease in adhesion that is sufficient to enable the expression of plasticity as it for instance allows for a higher receptor mobility and thus reorganization of the synaptic membrane (Shinoe and Goda, 2015). CAMs also have the potential to influence functional properties of synapses through direct interaction with receptors or involvement in the initiation of intracellular signaling cascades that lead to the expression of plasticity. For example, postsynaptic EphBs bind and modulate the activity of NMDARs, interact with AMPARs and induce kinase-dependent changes in dendritic spine morphology (reviewed in Hruska & Dalva, 2012)

Ultimately, proper synaptic adhesion and transsynaptic signaling by CAMs is crucial to brain function which is illustrated by the implication of CAM dysfunction in various neurological and neuropsychiatric disorders in humans (Chowdhury et al., 2021; Taylor et al., 2020). Yet, despite advances in genomics and proteomics enabling the analysis of cell type-specific repertoires, mapping the enormous molecular diversity of CAMs, their combinatorial expression and distinct effects on synapses remains a challenge (Südhof, 2018; De Wit and Ghosh, 2016).

Chapter 3.4 Cadherin-catenin complexes at the synapse

The cadherin superfamily is a large, highly evolutionary conserved protein family that encompasses over 100 members and is generally subdivided into major cadherins (including classic cadherins), protocadherins and cadherin-related proteins (Gul et al., 2017). With a few exceptions, all cadherins are single-spanning transmembrane proteins with variable numbers of cadherin repeats in their extracellular domain. Via these domains they engage in trans-cellular Ca^{2+} dependent and preferentially homophilic interactions that are essential to various processes including cell-cell adhesion and recognition, tissue morphogenesis and integrity (reviewed in Hirano & Takeichi, 2012), as illustrated by the implication of cadherin dysregulation in a variety of metastatic cancers (Hirohashi, 1998; Kaszak et al., 2020; Kourtidis et al., 2017; Mendonsa et al., 2018).

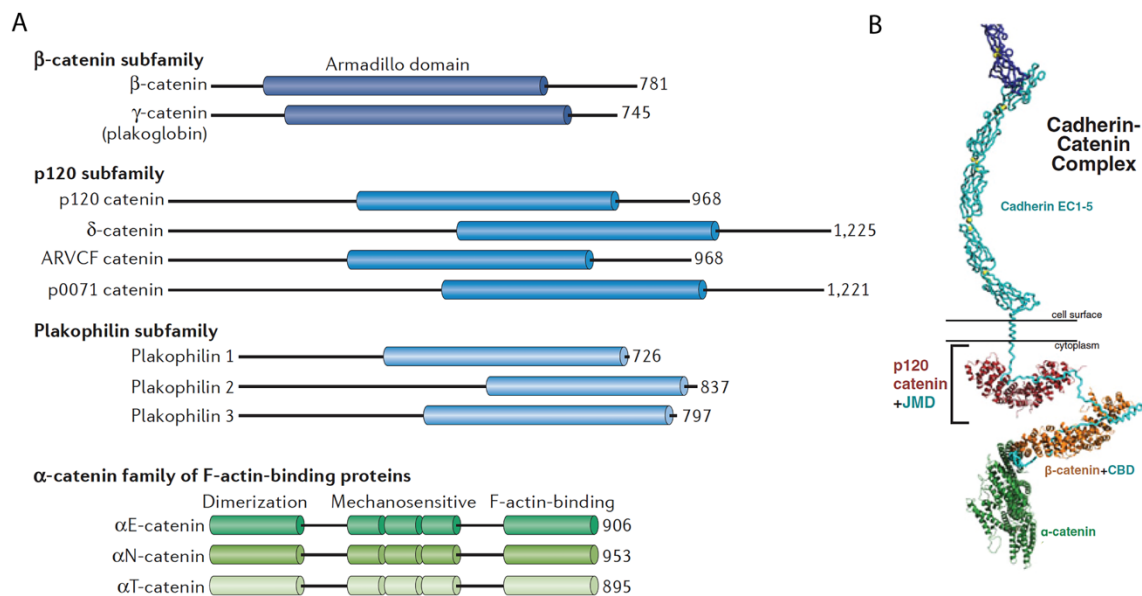


FIGURE 14 Cadherin/catenin complex. (A) An overview of vertebrate catenins. Most vertebrates have 12 genes that encode different types of catenins which can be subdivided into beta-catenins, p120 subfamily of catenins, Plakophilins and alpha-catenins. beta-catenins, p120-catenins and plakophilins are Armadillo-repeat domain proteins (depicted here in a grossly simplified form in different shades of blue). The number of armadillo-repeats varies between 9-12 depending on the catenin (each repeat is 42 amino acids in length). Armadillo repeats mediate various protein-protein interactions including Cadherin binding. Additionally, several of these catenins harbor other protein-protein interaction domains that are not depicted here, such as PDZ binding motive or coiled-coil domains, nuclear localization and export sequences as well as sequences that are responsive to canonical WNT signaling. The last family of catenins are the F-actin binding proteins alpha-catenins that are structurally very different to the other catenins harboring a dimerization, mechanosensitive and F-actin binding domain. The N-terminal dimerization domain engages mutually exclusive with beta-catenin (heteromeric) or alpha-catenin (homomeric). (B) Model of the cadherin-catenin complex. p120 catenins, beta-catenin and (indirectly) alpha-catenins associate with classical cadherins. Thereby beta-catenin interacts with the distal cytoplasmic tail of cadherin. Alpha catenin family members indirectly bind to cadherins through beta-catenin (or plakoglobin, not depicted here) and thereby link cadherins to the actin cytoskeleton. The four p120 catenins (including CTNND2) bind in a competitive manner to the juxtamembrane domain of cadherins. EC: ectodomain, JMD: juxtamembrane domain, CBD: catenin binding domain. (adapted from Ishiyama et al., 2010)

The subfamily of type I and II classic cadherins comprises 18 members in humans (type I: Cdh1-4 and Cdh15; type II: Cdh5-12, Cdh18-20, Cdh22 and Cdh24) and includes the prototypical E-cadherin (CDH1) as well as N-cadherin (CDH2), which has been extensively studied in the neuronal context (reviewed in Hirano & Takeichi, 2012). Classic cadherins are characterized by five extracellular cadherin repeats (EC domains) and a highly conserved intracellular domain that binds members of the catenin protein family to form F-actin linked cell adhesion complexes termed cadherin-catenin complexes (Figure 14) (Takeichi, 2007; Takeichi M., 1988). A key characteristic of these complexes is that the adhesion strength they provide can be readily modified either by virtue of relatively weak extracellular interactions and changes in calcium levels or by flexible intracellular interactions with, or mediated by, catenins that can be regulated by post-translational modifications (Brigidi and Bamji, 2011). Based on sequence homology, catenins are subdivided into 4 subfamilies named after representative members: α -catenin, β -catenins, p120-catenins and plakophilins (Figure 14A). Plakophilins preferentially interact with desmosomal cadherins and are thus not thought to be a part of the cadherin-catenin complex, however they are included here because they are so closely related to p120 catenins that they are sometimes classified together under the umbrella name δ -catenins (Gul et al., 2017). Among the catenins, members of the β -catenin and p120-catenin subfamilies contain armadillo (ARM) domains that directly bind to the cytoplasmic tail of cadherins, whereas α -catenins are F-actin binding proteins that are structurally related to vinculin and rely on β -catenin for cadherin association (reviewed in Gul et al., 2017; Han & Yap, 2013). In vertebrates, the α -catenin subfamily consists of α E-, α N- and α T-catenins, where E designates epithelial, N neuronal and T testis. They form a heterodimer with β -catenin (that constitutively binds the extended cytoplasmic tail of classic cadherins, Figure 14B) and at the same time either directly or indirectly (via other actin binding proteins) interacts with actin filaments (Desai et al., 2013), thus forming a bridge between the cadherin-complex and the actin cytoskeleton. In addition, unbound α -catenin homodimers have a strong affinity with F-actin and are thought to suppress Arp2/3 mediated actin polymerization (reviewed in Takeichi, 2018). Both α -catenin in complex with β -catenin and cadherins, as well as α -catenin homodimers are needed for stable and strong cadherin mediated cell adhesion (Bianchini et al., 2015). The β -catenin subfamily consists of β -catenin and γ -catenin (also called plakoglobin or junction plakoglobin/JUP). In mammals, β -catenin exerts dual functions in cell adhesion and signaling. Besides its structural role in cadherin-catenin complex, where it is required for trans-interactions of cadherins (Benson and Tanaka, 1998), β -catenin is key for the canonical Wnt/ β -catenin signaling pathway, an important signaling cascade regulating, for example, cell fate decisions in development. Briefly, in response to WNT, cytoplasmic β -catenin accumulates and translocates to the nucleus, where it interacts with transcription factors to modulate gene expression (reviewed in Valenta et al., 2012). The second member of the vertebrate β -catenin subfamily, γ -catenin, does not seem to have

a nuclear signaling function, but in contrast to β -catenin, strongly interacts with desmosomal cadherins and is essential for the formation of desmosomes (reviewed in Hirano & Takeichi, 2012). The p120 catenin subfamily comprises four members: p120 catenin (δ 1-catenin or CTNND1), ARVCF (armadillo repeat gene deleted in velocardiofacial syndrome), CTNND2 (δ 2-catenin, δ -catenin, NPRAP or neurojungin) and p0071, also known as plakophilin-4 (PKP4). In contrast to β -catenin, that has 12 ARM repeats, p120 catenin family members have only nine ARM repeats, that are interrupted by a 60 amino-acid linker between the 5th and 6th ARM repeat (Ishiyama and Ikura, 2012). This structure enables them to bind to a juxtamembrane domain within the cytoplasmic tail of cadherins (Figure ZC1B) and thereby regulate the stability of cadherin complexes by preventing cadherin endocytosis (Cadwell et al., 2016; Ishiyama et al., 2010; Tai et al., 2007). CTNND2, ARVCF and p0071, unlike p120 catenin, have a C-terminal PDZ-binding domain (Arikkath and Reichardt, 2008; Laura et al., 2002; Yuan et al., 2015). In addition, all four members are thought to modulate actin through the regulation of Rho family GTPases and p120-catenin has been shown to interact with and regulate the microtubule cytoskeleton. (reviewed in Kourtidis et al., 2013; McCrea & Park, 2007)

The cadherin-catenin complex in synapse development

In the developing nervous system, cadherin-based adhesion is thought to play diverse roles at various developmental stages, including neural tube and neuroepithelial layer formation, cell migration, axon pathfinding, neuronal morphogenesis and circuit formation (for comprehensive reviews see Friedman et al., 2015; Hirano & Takeichi, 2012). Particularly, cadherin function in circuit formation is well described. Most type I Cadherins (including N-Cadherin) are broadly expressed in the CNS (Hirano and Takeichi, 2012; Redies, 2000), whereas type II Cadherins show distinct and partially overlapping expression patterns across brain areas, and their combinatorial expression contributes to neuronal circuit development by providing a general adhesion code of distinct brain areas (Figure 15A) (reviewed in Chowdhury et al., 2021; Sanes & Zipursky, 2020). This code was long thought to mostly rely on homophilic trans-recognition of cadherins (Hirano and Takeichi, 2012). However, type II classic cadherins have been shown to also engage in heterophilic trans-interactions with varying binding affinities, creating specificity subgroups that are thought to further complexify the adhesion code (Brasch et al., 2018). The biological role of these heterophilic interactions, however, have so far been little explored (but see Basu et al., 2017; Brasch et al., 2018). To date, one of the best-elucidated examples of circuit organization mediated by cadherins is the direction-sensitive circuit of the mouse retina, where appropriate connectivity is established by combinatorial expression of CHD6-10 and CHD18 (Duan et al., 2018; Sanes and Zipursky, 2020). CHD6 deletion in mice also impairs axon-target matching for a subset of retinal ganglion cell whose axons overshoot their normal target in subcortical visual nuclei and instead innervate inappropriate visual nuclei (Osterhout et al., 2011), illustrating how targeting of long-range connectivity can be regulated by Cadherins. It has to be noted

though, that despite their function in target recognition, cadherins have been shown to have no synaptogenic function themselves (Scheiffele et al., 2000). Instead, they are thought to provide permissive adhesion necessary for initial contact and synapse formation (Figure 15B), illustrated by the need of cadherin presence for the synaptogenic function of Neuroligin1, SynCAM1 and LRRTM2 (Aiga et al., 2011; Stan et al., 2010; Yamagata et al., 2018).

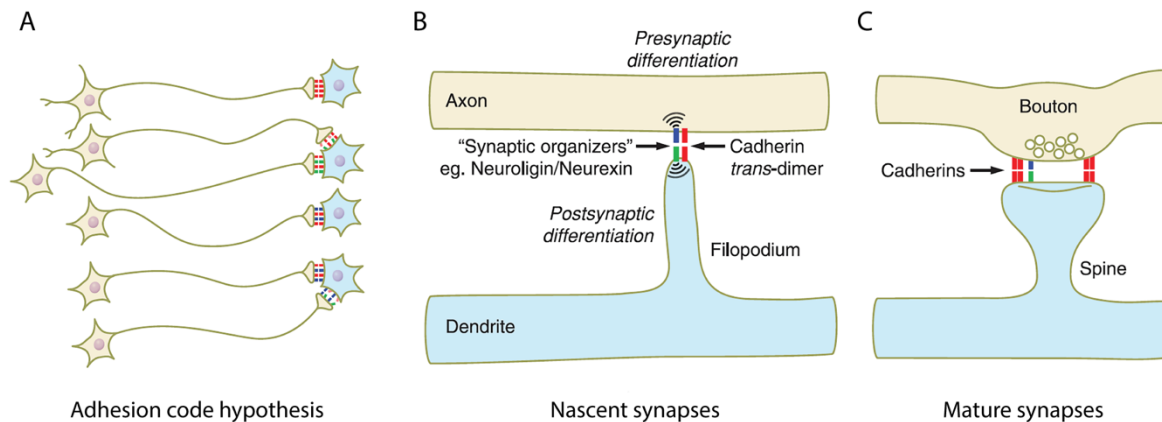


FIGURE 15 **Cadherin/catenin complex in synapse development.** (A) Cadherin adhesion code hypothesis. Each neuron expresses a specific set of cadherins, providing an *adhesion code*. Through the preferential homophilic and selective heterophilic trans-interaction of cadherins, synaptic partner selection is restricted. The cadherin code is thought to provide area specificity of synaptic targeting. (B) Classical cadherins in synapse formation. Cadherins mediate initial contacts between dendritic filopodia and axons followed by synapse assembly mediated by synaptogenic CAMs. (C) In mature synapses cadherins are accumulated at the outer rim of the synapse. (adapted from Hirano & Takeichi, 2012)

Cadherin-adhesion is further thought to play a crucial role in spine morphogenesis and spine stability. Cadherin signaling confers structural stability to developing spines or filopodia and promotes spine maturation by locally slowing down actin turnover and thereby increasing F-actin accumulation (also called a *cadherin clutch*) (Chazeau et al., 2015). In accordance with this, spine motility is abnormally increased in the absence of α -catenin (Abe et al., 2004). Furthermore, disruption of the cadherin-catenin complex in hippocampal cultures either reduces spine density or interferes with spine maturation (Mendez et al., 2010; Okuda et al., 2007; Saglietti et al., 2007; Togashi et al., 2002), while overexpression of some members of the complex increased spine density and/or promoted spine maturation (Abe et al., 2004; Mendez et al., 2010; Yu and Malenka, 2004). CTNND2, a protein almost exclusively expressed in the brain, has also been implicated in the development of dendritic spines but with contrasting results (e.g., Arikath et al., 2009; Matter et al., 2009; Turner et al., 2015; Yuan et al., 2015, but see Yuan & Arikath, 2017).

Cadherin-catenin complex in synapse function

Once synapses have formed, cadherin-catenin complexes localize at or adjacent to the PSD and active zone (Figure 15C) (Elste and Benson, 2006; Smith et al., 2017; Uchida et al., 1996). N-cadherins can interact in cis and trans with GluA2-containing AMPARs, which is thought to stabilize AMPAR in the postsynaptic membrane and proposed to promote spine morphogenesis (Saglietti et al., 2007). In line with this, increasing cadherin function by inhibiting N-cadherin internalization increases mEPSC frequency (Murase et al., 2002; Tai et al., 2007). Some of the catenins (β -catenin and CTNND2) have also been shown to directly bind to excitatory scaffold proteins (Ide et al., 1999; Jones et al., 2002; Nishimura et al., 2002; Yuan et al., 2015). However, at this point it is unclear how cadherin-catenin complexes regulate synaptic transmission, as functional studies have produced diverging results. *In vitro* studies in hippocampal neurons have shown that interfering with the cadherin-catenin complex reduces mEPSC amplitude (Okuda et al., 2007) or decreases mEPSC frequency and pre-synaptic vesicle release probability, either with (Saglietti et al., 2007) or without (Vitureira et al., 2012) affecting spine density. Postsynaptic β -catenin, independent of N-Cadherin, has furthermore been demonstrated to be required for trans-synaptic homeostatic scaling of transmission (Okuda et al., 2007; Vitureira et al., 2012). Interestingly, post-synaptic β -catenin or N-cadherin overexpression is not sufficient to significantly increase excitatory synaptic transmission (Okuda et al., 2007; Vitureira et al., 2012). By contrast, in upper layer cortical neurons *in vivo* (or *ex vivo*), pre-synaptic, but not post-synaptic β -catenin gain of function (through the expression of a degradation-resistant β -catenin mutant) increases spine density and glutamatergic synaptic transmission (Li et al., 2017). In the same cells, late embryonic knock-out of β -catenin lead to reduced mEPSC frequency at P21 but not at earlier developmental timepoints (Li et al., 2017). So far it is not known if these discrepancies depend on differences between *in vitro* and *in vivo* experiments and/or between hippocampal and cortical neuron specificities.

Synaptic activity, in turn, has been demonstrated to affect cadherin-catenin complexes (reviewed in Arikath & Reichardt, 2008; Friedman et al., 2015; Hirano & Takeichi, 2012; Tai et al., 2008). Upon strong synaptic activity, cadherins temporarily re-localize from the periphery of the synapse to the center (Yam et al., 2013) and their synaptic accumulation increases along with the association of α -catenin, β -catenin and CTNND2 with the complex (Abe et al., 2004; Brigidi et al., 2014; Murase et al., 2002). β -catenin has been shown to locally redistribute to active spines from neighboring spines and to promote spine growth of active and shrinkage of inactive spines in a cadherin-dependent manner, suggesting activity-dependent inter-spine competition of cadherin-catenin complexes (Bian

et al., 2015). Furthermore, the sensitivity of cadherins to extracellular calcium has the potential to modulate their adhesive properties and lead to decreased adhesion upon strong synaptic activity (Tai et al., 2008). Similarly, extracellular proteolysis of N-cadherin by matrix metalloproteinases decreases cadherin-adhesion and allows spine enlargement during LTP (Monea et al., 2006; Uemura et al., 2006). Activity-dependent cleavage of the cytosolic tail of cadherin might also be important in this context (Uemura et al., 2006). Notably, mice carrying a conditional deletion of N-cadherin in hippocampal neurons cannot maintain LTP nor the spine head enlargement following potentiation, suggesting that N-cadherin is required for the stabilization of structural changes following plasticity (Bozdagi et al., 2010; Mendez et al., 2010). The interaction between CTNND2 and N-cadherin likely plays an important role here. In hippocampal neurons *in vitro*, increased binding of CTNND2 to cadherin in response to enhanced activity is required for activity-induced stabilization of N-cadherin at synapses, spine enlargement and insertion of AMPARs into the synaptic membrane (Brigidi et al., 2014). Conversely, enhanced endocytosis of N-cadherin has been implicated in LTD (Tai et al., 2007, 2008).

Together, the data summarized here paint a picture of cadherins and catenins as multifunctional proteins involved in cell adhesion and signaling in brain development and function. The loss of function of a number of cadherin-catenin complex members, such as CTNND2 and α 2-catenin as well as several type II cadherins with more restricted expression during development (CDH7,8,9,10,12,15 and 18), have been linked to neurodevelopmental disorders, thus underscoring the importance of this complex for brain development and function (Hirano and Takeichi, 2012; Pagnamenta et al., 2011; Redies et al., 2012; Turner et al., 2015).

So far, most studies have focused on major members of the neuronal cadherin-catenin complex and have been carried out in dissociated hippocampal neurons in culture. Therefore, a lot of the molecular complexity and cell-specific differences have received relatively little attention. However, different compositions of the cadherin-catenin complex are actually likely to exhibit different behaviors. For example, CDH8 but not N-cadherin is selectively removed from hippocampal synapses upon activity (Huntley et al., 2012). Catenins add another layer of complexity because it can be difficult to discern which aspects of their loss or gain of function phenotype rely on cell adhesion and which do not. In addition, cadherins and catenins have mostly been studied at excitatory synapses, keeping their function at inhibitory synapses little explored. We know that N-cadherin is selectively lost from GABAergic synapses during hippocampal development while catenin expression persists (Benson and Tanaka, 1998), suggesting that other cadherins take over. In line with this, the deletion of some cadherins specifically affects GABAergic synapse development (Mossink et al., 2021; Nikitczuk et al.,

2014) and cadherin 10 localizes to both excitatory and inhibitory synapses in the cortex and remarkably affects both synapse types in opposite direction when depleted (Smith et al., 2017). Together, this data suggests a role for cadherins and catenins much beyond the regulation of synaptic excitation, and shows that despite more than three decades of research into cadherins we are only beginning to understand the physiological roles of cadherin-adhesion in synapse development and function.

AIM OF THIS THESIS

In the lab we are interested in the human specific regulation of molecular pathways in synapse development and function in the neocortex. We aim to elucidate fundamental principles that are common to all mammals and uncover regulations that are specific to human synapses. The human-specific duplication of SRGAP2, a gene implicated in synapse development and function, forms an entry point here. The focus of this thesis is on one of the major partners of SRGAP2 that we have identified in a proteomic screen and that is implicated in neurological disorder in humans: Catenin- δ 2 (CTNND2).

With this thesis I aim to

- describe the role of CTNND2 in the development and maintenance of cortical synapses
- assess CTNND2 in neuronal and synaptic function
- elucidated the social network of CTNND2 at synapses to provide a mechanistic understanding of CTNND2 function in neurons
- contribute to a better understanding of the implication of CTNND2 in human neurodevelopmental disorders and neurodegeneration

CHAPTER 4 – CTNND2 moderates synaptic excitation and neuronal excitability during postnatal development in the neocortex.

CTNND2 moderates synaptic excitation and neuronal excitability during postnatal development in the neocortex.

Nora Assendorp¹, Marine Depp¹, Matteo Fossati^{1,2}, Florent Dingli³, Damarys Loew³ and Cécile CHARRIER¹

¹ Institut de Biologie de l'ENS (IBENS), Ecole Normale Supérieure, CNRS, INSERM, Université PSL, 75005 Paris, France

² Institute of Neuroscience - CNR Via Vanvitelli 32, 20129 Milano & Humanitas Clinical and Research Center Via Manzoni 56, 20089 Rozzano (MI), Italy

³ Mass Spectrometry and Proteomic facility, Institut Curie, 75005 Paris, France

MANUSCRIPT IN PREPARATION

ABSTRACT

Vulnerability to neurodevelopmental disorders increased during human evolution. Yet little is known about the molecular pathways that link evolution and brain diseases. Here we identified catenin delta-2 (CTNND2) as a binding partner of SRGAP2C, a human-specific protein that slows down synaptic maturation and increases cortical connectivity. CTNND2 is a cadherin-binding protein whose mutations cause intellectual disability in the Cri-du-Chat syndrome and severe autism. Using sparse in utero manipulations of layer 2/3 cortical pyramidal neurons, we demonstrate that CTNND2 deficiency disrupts excitation/inhibition coordination and increases neuronal excitability in juvenile mice, and then leads to precocious synapse loss during adulthood. Proteomic analysis highlighted a core postsynaptic complex that constrains excitatory activity during the period of synaptic maturation. Thus, CTNND2 is a multifunction protein at the crossroad of neurodevelopmental disorders and human evolution, whose loss of function causes a failure of neuronal homeostasis and whose interaction with SRGAP2C might contribute to human synaptic neoteny and long-term persistence.

INTRODUCTION

During human evolution, cortical pyramidal neurons have specialized to mature over longer time scales, receive a greater number of synaptic inputs, and integrate more information (Benavides-Piccione et al., 2002; DeFelipe, 2011; Elston et al., 2001; Eyal et al., 2016; Gidon et al., 2020; Huttenlocher, 1979; Kalmbach et al., 2018; Lourenço and Bacci, 2017; Mansvelder et al., 2019; Mohan et al., 2015; Petanjek et al., 2011; Sousa et al., 2017; Szegedi et al., 2016; Testa-Silva et al., 2010, 2014). Despite the increased density of synapses formed along dendrites (Benavides-Piccione et al., 2002; Elston et al., 2001), the ratio between the number of excitatory and inhibitory synapses (E/I ratio) is overall stable across species (DeFelipe, 2011), and E/I alterations are a primary cause of human neurodevelopmental disorders (Forrest et al., 2018; Mullins et al., 2016; Nelson and Valakh, 2015; Tang et al., 2021). Thus, the mechanisms that control the E/I ratio and neuronal excitability are under strong evolutionary pressure. We reasoned that investigating molecular pathways linked to human evolution could highlight crucial mechanisms of neuronal homeostasis and improve our understanding of the human brain and its diseases.

A key mechanism of evolutionary innovation is gene duplication (Ohno, 1970) which can affect gene dosage or create new genes with unique function as a result of partial duplication, gene fusion or following the accumulation of mutations in the duplicate. Among the few human-specific genes that have been identified (Fortna et al., 2004; Libé-Philippot and Vanderhaeghen, 2021; Sudmant et al., 2010), SRGAP2C is thus far unique in its implication in synaptic development and connectivity (Charrier et al., 2012; Fossati et al., 2016; Schmidt et al., 2019, 2021). SRGAP2C is the product of large segmental duplications that occurred about 3.3-2.4 million years ago, at a time that coincides with the emergence of the genus *Homo* (Dennis et al., 2012, 2017). It encodes a truncated copy of the ancestral protein SRGAP2A, a postsynaptic protein conserved in mammals that localizes to excitatory and inhibitory synapses and promotes their maturation (Charrier et al., 2012; Fossati et al., 2016). SRGAP2C antagonizes the function of SRGAP2A, and thereby delays synaptic maturation and increases synaptic density (Charrier et al., 2012; Fossati et al., 2016; Schmidt et al., 2019), two features that characterize human cortical pyramidal neurons compared to mouse or monkey neurons (Benavides-Piccione et al., 2002; Elston et al., 2001; Huttenlocher, 1979; Petanjek et al., 2011). Thus far, the cellular and molecular pathways regulated by SRGAP2 proteins remain largely unknown.

In the present study, we identify catenin delta-2 (CTNND2) as a binding partner of the human-specific protein SRGAP2C. CTNND2 belongs to the delta subfamily of the catenin superfamily and is a component of the cadherin-catenin complex. It was first identified in a yeast-2-hybrid screen as a binding partner of presenilin-1 (PS1) (Zhou et al., 1997), the most frequently mutated gene in familial Alzheimer's disease. *CTNND2* is implicated in the Cri du Chat syndrome, where its hemizygous loss causes intellectual disability (ID) (Medina et al., 2000). Point mutations in *CTNND2* have also been implicated in severe forms of autism spectrum disorders (ASD) (Turner et al., 2015) and in epilepsy

(Van Rootselaar et al., 2017). In mice, *ctnnd2* mutation impairs synaptic plasticity and memory (Israely et al., 2004), and leads to progressive degeneration of dendritic and synaptic structures in adult mice (Matter et al., 2009). CTNND2 has also been implicated in the development of excitatory synapses and dendritic spines, the postsynaptic site of excitatory synapses in pyramidal neurons, but with contrasting results (e.g. Arikath et al., 2009; Matter et al., 2009; Turner et al., 2015; Yuan et al., 2015, but see Yuan & Arikath, 2017). By sparsely depleting CTNND2 in vivo in layer 2/3 pyramidal neurons of the somatosensory cortex, we demonstrate that CTNND2 is a multifunction protein that operates at excitatory synapses, at inhibitory synapses and in the control of neuronal intrinsic excitability. In juvenile mice, CTNND2 depletion enhances excitatory synaptic transmission, disrupts a subset of inhibitory synapses and causes hyperexcitability. Later in adult mice, CTNND2 inactivation leads to a precocious loss of synapses. Proteomic and functional analyses further indicate that CTNND2 forms a complex with the inhibitory postsynaptic organizer gephyrin and is required for the synaptic recruitment of synGAP1, a major excitatory postsynaptic protein that limits synaptic excitation and whose mutation in neurodevelopmental disorders shares important pathophysiological features with CTNND2 (Aceti et al., 2015; Clement et al., 2012; Michaelson et al., 2018; Rumbaugh et al., 2006).

RESULTS

CTNND2 is a binding partner of the human-specific protein SRGAP2C.

The inhibition of ancestral SRGAP2A by human-specific SRGAP2C provides a unique framework to investigate SRGAP2 molecular network using proteomic approaches in mice (Figure 16A). We isolated protein complexes enriched in synaptic membranes using subcellular fractionation from postnatal day (P)15 mouse brains, performed co-immunoprecipitation using anti-SRGAP2 antibodies and identified SRGAP2A partners in maturing synapses using liquid chromatography tandem MS (LC-MS/MS)-based proteomics (Figure 16B). We identified CTNND2 among the 10% most enriched proteins relative to their molecular weight in SRGAP2A complexes, among known partners such as SRGAP3, SRGAP1 and homer1 (Coutinho-Budd et al., 2012; Fossati et al., 2016) (Figure 16C). CTNND2 encodes a 132 kDa protein expressed almost exclusively in the brain and most highly in the cortex (<https://gtexportal.org/home/gene/CTNND2>) whose expression peaks during postnatal development (Ho et al., 2000). It contains a N-terminal coiled-coil domain, 10 armadillo repeats, which mediates binding to cadherins, and a C-terminal tail containing a PDZ binding motif (Figure 16D). Using co-immunoprecipitation in heterologous HEK cells, we found that CTNND2 directly interacts not only with SRGAP2A but also with the human-specific protein SRGAP2C (Figure 16E). CTNND2 implication in brain diseases and human-specific molecular networks suggested a key role in neurons and at synapses.

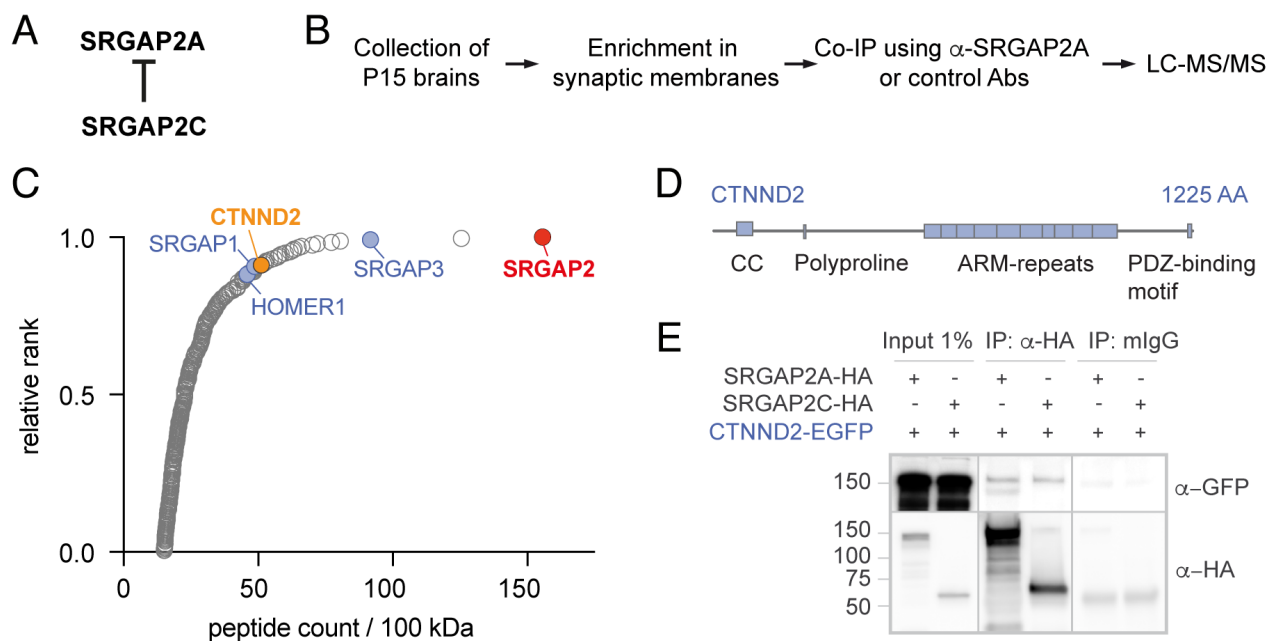


FIGURE 16 CTNND2 is a main interactor of SRGAP2 at synapses. (A) Human-specific SRGAP2C inhibits SRGAP2A. (B) Schematic of the experimental workflow used for mass spectrometry analysis. CoIP, co-immunoprecipitation; α -, anti-; LC-MS/MS, liquid chromatography followed by tandem mass spectrometry. (C) Graph illustrating the most abundant partners of SRGAP2 identified in LC-MS/MS depending on their relative rank (1 = most abundant; 0 = least abundant) and the number of peptides detected per 100 kDa (Only proteins with > 15 peptide per 100 kDa are represented). (D) CTNND2 protein domain structure. (E) CTNND2-GFP co-immunoprecipitates with HA-tagged SRGAP2A and human specific SRGAP2C in HEK cells.

CTNND2 promotes inhibitory synapse formation but limits spine density in juvenile mice

Despite CTNND2 implication in cognitive function and brain disorders, its subcellular localization in neurons remains elusive. Using immunocytochemistry in dissociated cortical neurons cultured for 18 days in vitro (DIV), we found that endogenous CTNND2 forms clusters associated with the vast majority of excitatory synapses labelled with PSD-95 ($79\% \pm 4\%$, Figure 17A-B). Remarkably, CTNND2 was also accumulated in a large fraction of inhibitory synapses labelled with gephyrin ($67\% \pm 3\%$, Figure 17A-B). This dual localization is atypical: excitatory and inhibitory synapses are built of almost distinct sets of proteins (Krueger-Burg et al., 2017; Sheng and Kim, 2011; Tyagarajan and Fritschy, 2014) and only few postsynaptic proteins have been shown to localize or operate at both types of synapses in the same neurons (Budreck and Scheiffele, 2007; Fossati et al., 2016; Moon et al., 2008; Smith et al., 2017). These proteins are in pole position for excitation/inhibition coordination. Therefore, we decided to assess the function of CTNND2 at both types of synapses. To that aim, we designed shRNAs that prevent the expression of all CTNND2 isoforms, (shCtnnd2, Figure S1), which so far has not been possible using mutant mouse lines (Israely et al., 2004; discussed in Figure S1).

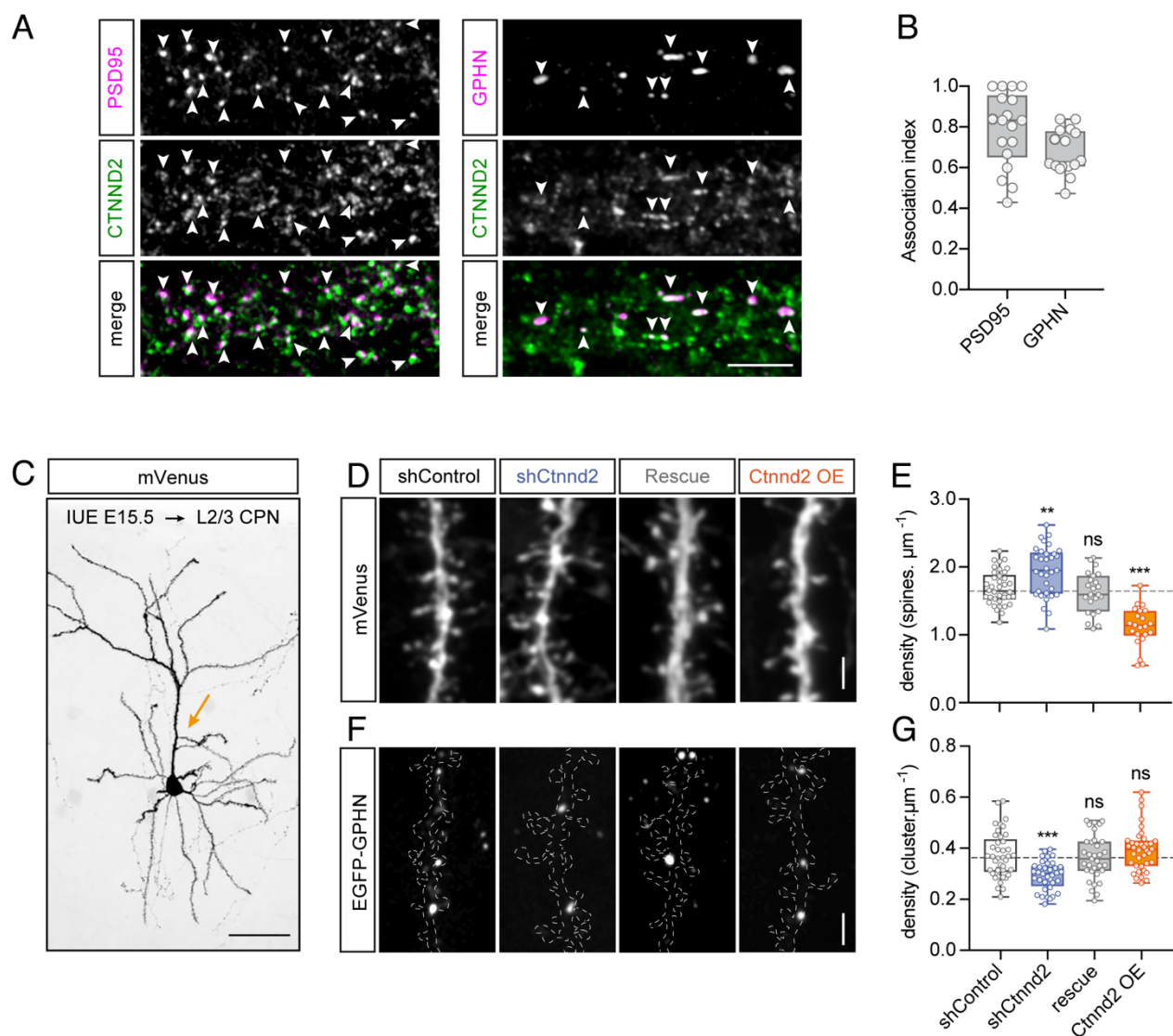


FIGURE 17 CTNND2 regulates excitatory and inhibitory synapses in opposite direction. (A) Confocal images of primary cortical neurons cultured for 18 days *in vitro* immunostained for endogenous CTNND2 and the excitatory or inhibitory postsynaptic markers PSD95 and Gephyrin (GPHN). CTNND2 clusters associates with the majority of PSD95 and Gephyrin clusters (arrowheads). Scale bar: 5 μm . (B) Boxplot with individual datapoints showing the fraction of PSD95 or Gephyrin clusters associated with CTNND2 (association index). $N_{\text{PSD95}} = 18$; $N_{\text{GPHN}} = 16$ cells. (C) *In utero* electroporation (IUE) at embryonic day 14.5-15.5 allows the sparse targeting of layer 2/3 cortical pyramidal neurons (L2/3 CPN). Arrow indicates oblique apical dendrites. Scale bar: 50 μm . (D) Representative segments of dendrites expressing shControl, shCtnnd2, shCtnnd2 together with an shCtnnd2-resistant CTNND2* (rescue), or overexpressing CTNND2 (Ctnnd2 OE) along with mVenus in juvenile mice (P21-P23). Scale bar: 2 μm . (E) Quantifications of dendritic spine density in the conditions described in D. $N_{\text{shControl}} = 38$; $N_{\text{shCtnnd2}} = 33$; $N_{\text{Rescue}} = 23$; $N_{\text{Ctnnd2 OE}} = 22$ dendrites (1 dendrite per cell was analyzed). Dashed line indicates median of shControl condition. (F-G) Same as D-E but for gephyrin clusters in neurons expressing tdTomato to visualize neuronal contour (outlined by dashed lines) and EGFP-GPHN to visualize Gephyrin clusters. $N_{\text{shControl}} = 41$; $N_{\text{shCtnnd2}} = 36$; $N_{\text{Rescue}} = 33$; $N_{\text{Ctnnd2 OE}} = 38$. ns: $p > 0.05$; **: $p < 0.01$ and ***: $p < 0.001$, one-way ANOVA followed by Tukey's multiple comparisons test.

To assess the function of CTNND2 at excitatory synapses *in vivo*, we used cortex-directed *in utero* electroporation (IUE) at embryonic days (E) 14.5 – 15.5 (Figure 17C), which allows the sparse genetic manipulation of layer 2/3 cortical pyramidal neurons (CPNs). We co-expressed shRNAs with the

fluorescent protein mVenus to visualize neuronal morphology and dendritic spines, which can be used as proxy for excitatory synapses (Harris and Stevens, 1989; Holler et al., 2021), and quantified spine density in oblique apical dendrites in the somatosensory cortex using high-resolution confocal microscopy. In juvenile mice (postnatal day (P) 21), CTNND2-depleted neurons exhibited a higher density of dendritic spines than neurons expressing a control shRNA ($114.6\% \pm 3.8\%$ of shControl; Figure 17D-E). Normal spine density was rescued by co-electroporating shCtnnd2 with an shRNA-resistant *ctnnd2* variant ($96 \pm 3.7\%$ of control) and CTNND2 overexpression reduced spine density ($59 \pm 4\%$ of control; Figure 17D-E), indicating that CTNND2 limits spine density. To examine the consequences of *ctnnd2* knock-down (KD) on inhibitory synapses, we electroporated low levels of fluorescent (EGFP-tagged) gephyrin, along with a soluble red fluorescent protein to visualize neuronal morphology (Figure 17F). This approach has been shown to reliably label inhibitory synapses without affecting synaptic development or function (Chen et al., 2012; Fossati et al., 2016; Gemin et al., 2021; van Versendaal et al., 2012). In contrast to dendritic spines, CTNND2 depletion decreased the density of gephyrin clusters ($78.8 \pm 2.5\%$ of control, Figure 17F-G). Normal density was rescued by co-expression of the shRNA-resistant construct ($98 \pm 4\%$ of control). CTNND2 overexpression did not significantly increase gephyrin cluster density, although a trend was observed ($105 \pm 3.7\%$; Figure 17F-G). Morphological parameters of dendritic spines and gephyrin clusters did not differ between the conditions (data not shown). These results indicate that CTNND2 is required for the formation and maintenance of some inhibitory synapses and that the loss of CTNND2 has opposite effect on excitatory and inhibitory synapses.

CTNND2 depletion increases spine density in juveniles but leads to spine loss in adults

Since CTNND2 has been implicated in both neurodevelopmental and neurodegenerative disorders (Lu et al., 2016; Medina et al., 2000; Van Rootselaar et al., 2017; Turner et al., 2015), we hypothesized that the consequences of CTNND2 inactivation could vary over time. We examined the consequences of *Ctnnd2* knockdown at two other developmental time points: P10, which corresponds to the peak of synaptogenesis, and P77, when mice have reached adulthood (Figure 18A). In control mice, the density of dendritic spines strongly increased between P10 and P21 (from 0.49 ± 0.03 to 1.69 ± 0.04 spine. μm^{-1}) and then remained stable in adults (1.68 ± 0.08 spine. μm^{-1} , Figure 18B). In *Ctnnd2*-KD neurons, spine density was similar to control at P10 (0.53 ± 0.03 spine. μm^{-1}). The increase in spine density between P10 and P21 was faster than in control neurons, and overshoot control level by P21. In adult mice however, spine density in *Ctnnd2*-KD neurons was lower than in juvenile neurons and adult control neurons $81.5\% \pm 3.6\%$ of control, Figure 18B), suggesting a premature loss of synapses. These results reconcile previous observations from other groups that CTNND2 limits spine density in young neurons (Arikath et al., 2009; Brigidi et al., 2014) and is required for the maintenance of dendrites and dendritic spines in adult mice (Matter et al., 2009). Together, they suggest that CTNND2

deficiency leads to an initial phase of hyperexcitation and hyperconnectivity followed by synapse degeneration.

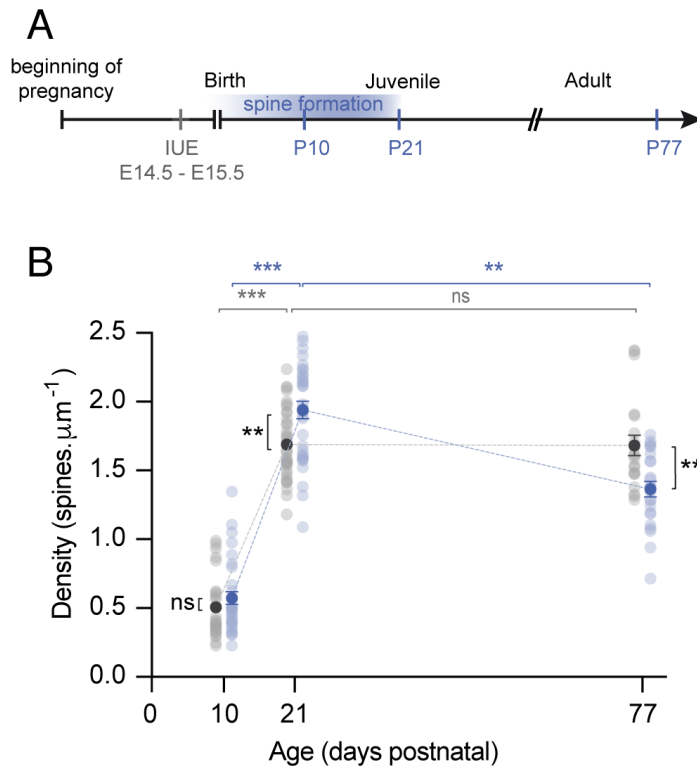


FIGURE 18 CTNND2 deficiency increases spine density in juveniles but leads to spine loss in adults. (A) Experimental workflow of the "longitudinal" analysis of dendritic spine density at P10, P21 and P77 in control and CTNND2-deficient L2/3 CPNs. IUE: in utero electroporation. (B) Quantification of spine density over time in either control condition (gray) or *Ctnnd2* KD (blue). Light colored points represent individual dendrites (1 dendrite per cell was analyzed), dark colored points are the mean \pm SEM. $N_{(\text{control}, \text{P10})} = 21$, $N_{(\text{control}, \text{P21})} = 38$, $N_{(\text{control}, \text{P77})} = 20$, $N_{(\text{shCtnnd2}, \text{P10})} = 31$, $N_{(\text{shCtnnd2}, \text{P21})} = 33$, $N_{(\text{shCtnnd2}, \text{P77})} = 24$. ns: $p > 0.05$; **: $p < 0.01$ and ***: $p < 0.001$; comparison between conditions at the same timepoint: unpaired t-tests with welch correction; comparison within conditions between timepoints: Kruskal-Wallis test with Dunn's multiple comparison test.

Loss of CTNND2 increases the E/I ratio and intrinsic excitability in juvenile mice

We further investigated what happens at the juvenile stage, when the excess of dendritic spines and the deficit in gephyrin clusters likely disrupts neuronal function. To test the physiological consequences of CTNND2 inactivation on synaptic transmission, we performed whole-cell patch-clamp recording in acute brain slices (P16-P20; Figure 19B) and compared synaptic transmission in electroporated *Ctnnd2*-depleted neurons versus neighboring non-electroporated control neurons (Figure 19A). We first examined miniature excitatory and inhibitory postsynaptic currents (mEPSCs and mIPSCs, respectively). Loss of CTNND2 strongly increased the frequency of mEPSCs ($140\% \pm 12\%$ of control, Figure 19C) without modifying their amplitude ($108\% \pm 6\%$ of control, Figure 3D). Together with the faster rise in spine density between P10 and P21, this suggests accelerated synaptic formation and maturation leading to excessive excitatory activity. On the other hand, mIPSC amplitude and frequency were not affected by *Ctnnd2* KD ($115 \pm 12\%$ and $102 \pm 11\%$ of control respectively, Figure 19E-F). These results contrast with the deficit in gephyrin clusters in oblique apical dendrites of CTNND2-deficient neurons. Since whole-cell patch clamp recordings mainly sample proximal synapses, these results suggest that CTNND2 function in inhibition could be restricted to subtypes of distal inhibitory synapses.

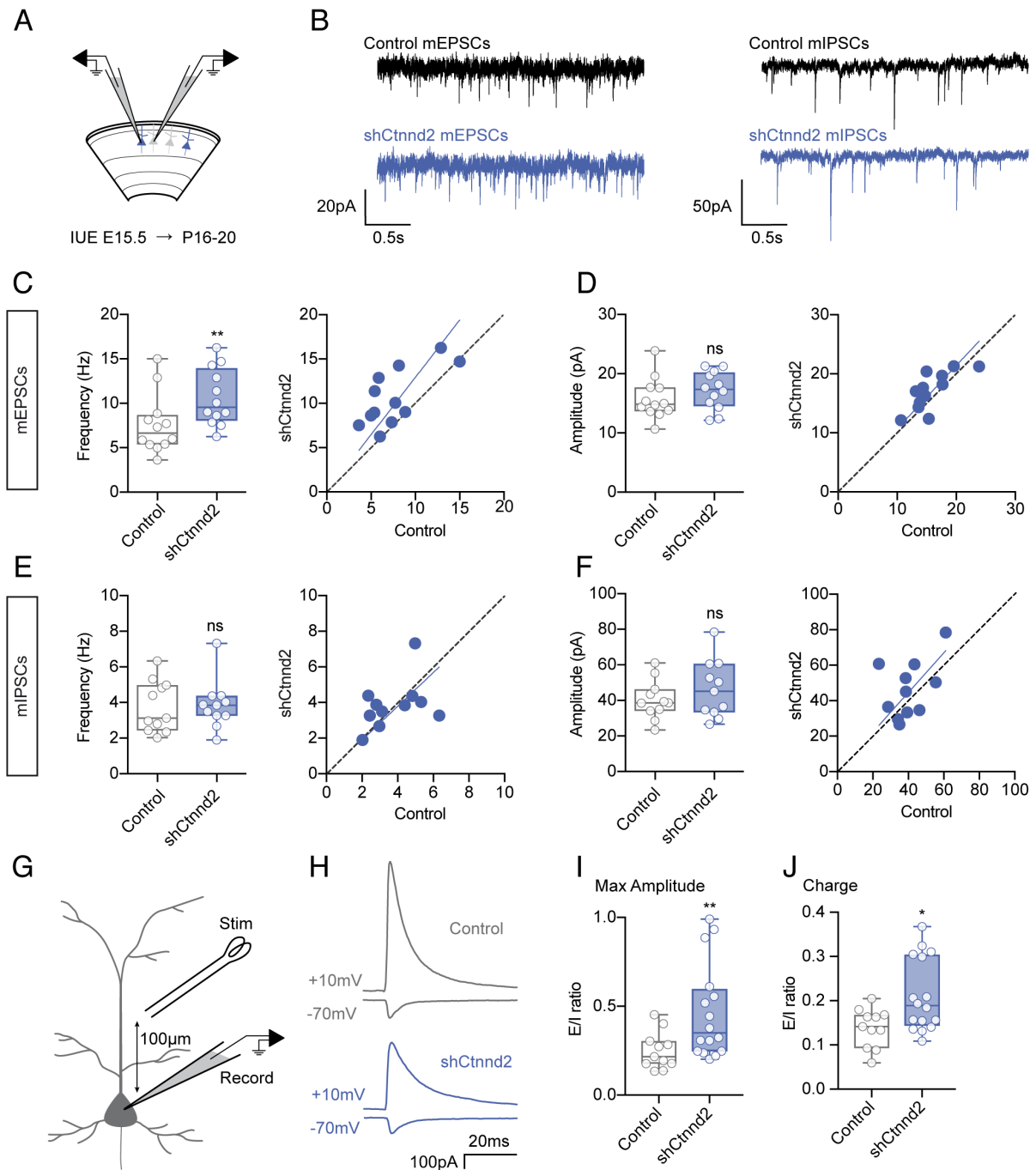


FIGURE 19 Loss of CTNND2 increases the E/I ratio in CPNs. (A) Schematic: recording of electroporated layer 2/3 CPN expressing tdTomato and the shRNA against CTNND2 (blue) following in utero electroporation (IUE) and neighboring non-electroporated control cells (gray) in acute brain slices from juvenile mice. (B) Representative traces of mEPSC and mIPSC recordings in control and shCtnnd2 electroporated neurons. (C) Quantification of mEPSC frequency per cell and Scatterplots (boxplot, right) or mean value from single pairs (scatterplot, right) in which electroporated shCtnnd2 and control were recorded from the same slice. N = 12 in both conditions. (D) Same as C Quantification but for mEPSC amplitude. (E - F) Same as (C-D) from mIPSCs. N = 11 in both conditions. (G) Evoked postsynaptic currents were recorded in layer 2/3 CPNs by placing a stimulation electrode approximately 100 μ m above the cell body along the apical dendrite. (H) Representative traces of eIPSCs and eEPSCs for a control cell and an shCtnnd2 expressing neuron. (I - J) E/I ratio calculated using the maximum amplitude (I) or the synaptic charge (J). $N_{\text{control}} = 11$ and $N_{\text{shCtnnd2}} = 16$ cells. ns: p > 0.05; *: p < 0.05 and **: p < 0.01, t-test (C-F) or Mann-Whitney test (I-J).

To directly measure the ratio between excitatory and inhibitory transmission (E/I ratio) in oblique apical dendrites, we placed a stimulation electrode $\sim 100\ \mu\text{m}$ along the main apical dendrite (Figure 19G) and adjusted the stimulation strength to evoke a response of approximately 150 pA. We then recorded evoked excitatory and inhibitory post synaptic currents (eEPSC and eIPSC) by clamping the cell at -70 mV and +10 mV, respectively (Figure 19H). CTNND2 depletion strongly increased the E/I ratio compared to control neurons (185% of maximum current amplitude in control neurons and 152% of control synaptic charge over 50ms, Figure 19I-J). By contrast, neither the ratio between AMPA receptor- and NMDA receptor-mediated synaptic transmission (AMPA/NMDA ratio), nor the paired pulse ratio were affected by CTNND2 depletion in postsynaptic neurons (Figure S2).

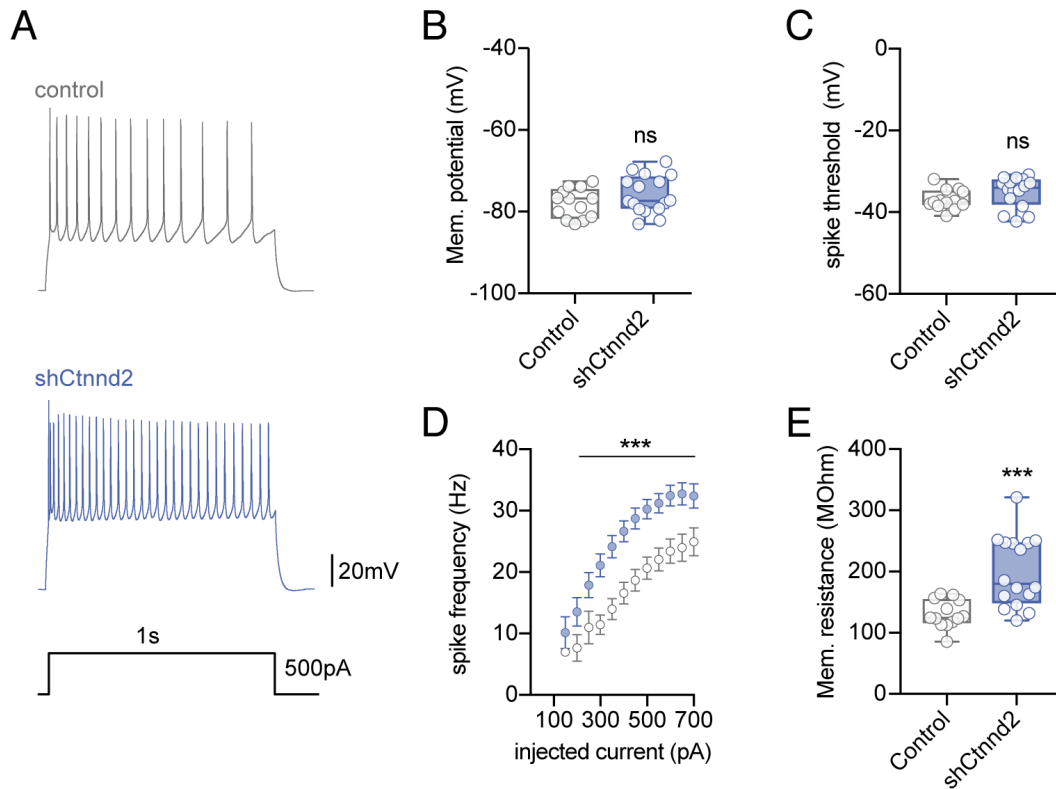


FIGURE 20 Depletion of CTNND2 increases the intrinsic excitability of CPNs. (A) Representative traces of action potentials evoked with a 500pA current step in whole cell current clamp recordings in control (grey) and ctnnd2-deficient neurons (shCtnnd2, blue). (B-E) Quantification of resting membrane (mem.) potential, spike threshold, spike frequency depending on current injection (mean \pm SEM) and membrane resistance in control (grey) and shCtnnd2 expressing neurons (blue). $N_{\text{control}} = 13$ cells, $N_{\text{shCtnnd2}} = 16$ cells. ns: $p > 0.05$; **: $p < 0.01$ and ***: $p < 0.001$, t-test.

Increases in E/I ratio are sometimes compensated by a decrease in neuronal intrinsic excitability to preserve network activity (Nelson and Valakh, 2015). To test how *Ctnnd2* KD affects intrinsic neuronal properties, we performed current-clamp recordings and injected depolarizing current steps of 50 pA intervals to evoke action potentials (Figure 20A), or a current ramp to determine the spike threshold.

Although the resting membrane potential (V_m) and spike threshold (Th) did not differ between control and KD neurons (Figure 20B: $V_{mControl} = -78 \pm 1$ mV, $V_{mshCtnnd2} = -76 \pm 1$ mV, Figure 20C: $Th_{Control} = -37 \pm 1$ mV, $Th_{shCtnnd2} = -35 \pm 1$ mV), CTNND2 deficiency strongly increased the frequency of action potential firing compared to control neurons ($162 \pm 8\%$ of control for 500 pA current injection, Figure 20D-E), reflecting a rise in membrane resistance ($152 \pm 11\%$ of control, Figure 20F). None of these intrinsic excitability parameters were significantly changed when non-electroporated control neurons were compared to neurons electroporated with a control shRNA (Figure S3). Collectively, our results indicate that CTNND2 deficiency causes homeostatic failure in cortical juvenile neurons, increasing synaptic excitation, decreasing inhibitory synapse number and ramping up intrinsic excitability.

SynGAP1 and gephyrin are two of the main partners of CTNND2

How does CTNND2 operate in the juvenile brain? To address this question, we performed a proteomic screen aimed at identifying CTNND2 social network at the synapse. We purified synaptic membranes from P15 mouse brains using subcellular fractionation, performed co-immunoprecipitation using either an anti-CTNND2 antibody or control immunoglobulins (IgGs), and identified CTNND2 partners using LC-MS/MS (Figure 21A). Using a label-free semiquantitative approach based on the normalized spectral abundance factor, we identified 322 proteins detected with at least 5 peptides and significantly enriched in CTNND2 immuno-precipitates (Table S1). Among these, 238 proteins (excluding known mitochondrial contaminants) were at least 4-fold enriched or exclusively detected in CTNND2 complexes (Figure 21B) and 58 proteins were annotated for biological processes at the synapse in SYNGO (SYNaptic Gene Ontologies database (Koopmans et al., 2019)) (Figure 21C). The most represented processes included synapse organization and assembly, trans-synaptic interactions, chemical synaptic transmission, regulation of neurotransmitter receptor level at synapses and regulation of plasma membrane potentials, which is consistent with our morphological and physiological results (Figure 21C). More specifically, members of the Cadherin/catenin superfamily were highly represented among the main partners of CTNND2 (Figure 21B+D; Table S1), which was expected. CTNND2 was also found in complex with other proteins involved in cell-cell interactions, especially EphA4, and, albeit in lower amounts, neuroligin 3, neuroligin 4I, neurexin 1 or IgSF8 (Figure 21D), suggesting widespread implication at cell-cell contacts. In agreement with the role of CTNND2 in neuronal excitability, potassium/sodium hyperpolarization-activated cyclic nucleotide-gated channels (HCN1-4) and their accessory subunit Pex5l (Lewis et al., 2009; Santoro et al., 2004) were highly represented among CTNND2 partners. However, the two most striking partners of CTNND2 were the excitatory postsynaptic protein SynGAP1 and the inhibitory scaffolding protein gephyrin, which were among the most abundant proteins in CTNND2 protein complexes (Figure 21B+D). Glutamatergic AMPA, NMDA and metabotropic receptor subunits, as well as GABAergic (Gagrb2) neurotransmitter receptor subunits were also found in complex with CTNND2, but in lower amounts

(Figure 17D, Table S1). These data support the notion that CTNND2 operates and localizes at both excitatory and inhibitory synapses.

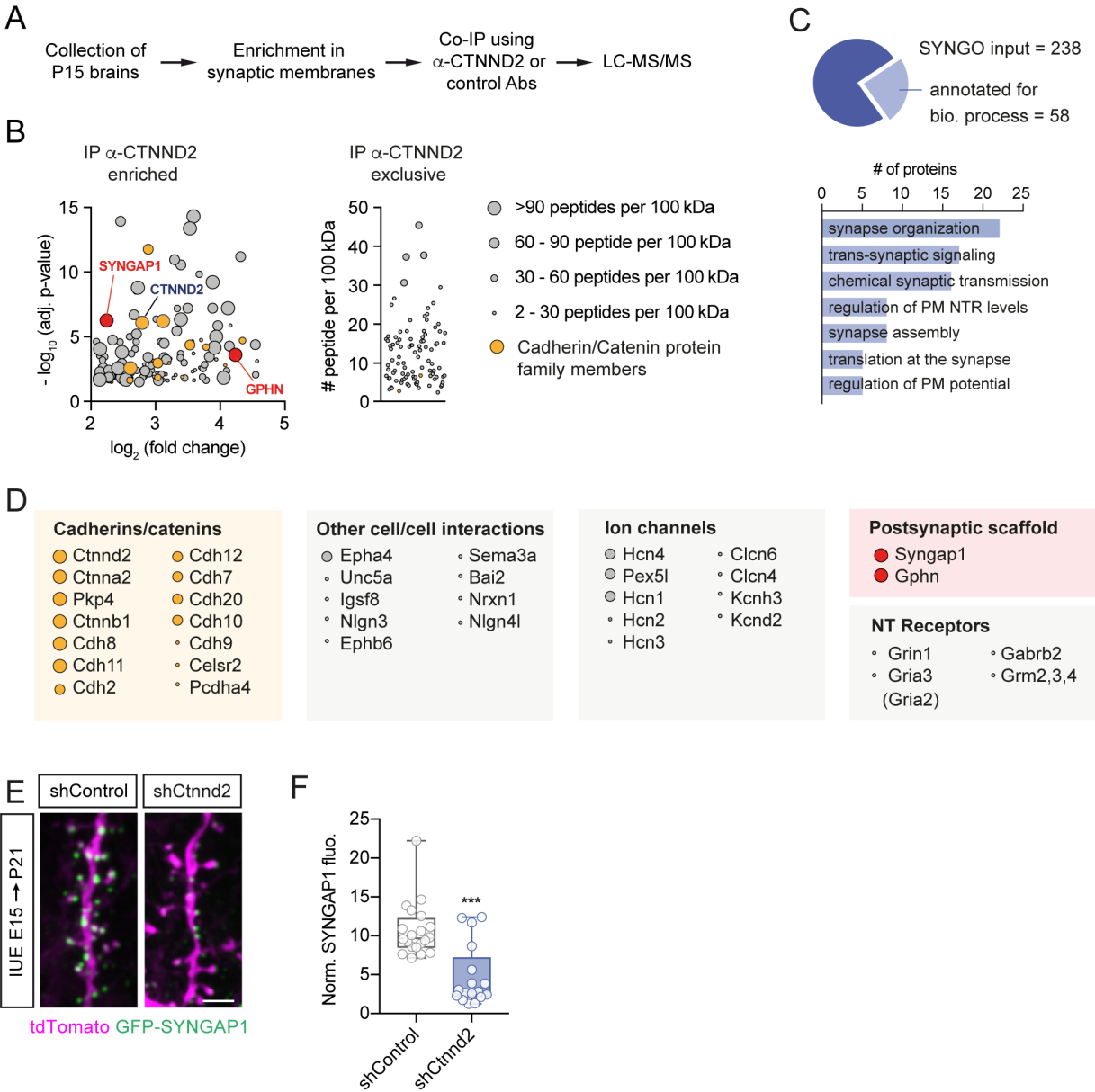


FIGURE 21 CTNND2 interacts with key proteins of excitatory and inhibitory synapses. (A) Schematic of the experimental workflow used for mass spectrometry analysis. (B) Relative distribution and abundance of proteins enriched in CTNND2 immunoprecipitates. Only proteins that were at least 4-fold enriched in CTNND2 vs control IP and whose p-value was < 0.05 based on three independent experiments are displayed. Cadherins and Catenins are shown in orange, Syngap1 and Gephyrin are in red. (C) SYNGO gene ontology analysis of CTNND2 partners identified in LC-MS/MS. (D) Classes of proteins and individual components standing out in CTNND2 protein complexes. Although not included in (B) due to our stringent threshold, GluA2 was also abundant in CTNND@ complexes. (3-fold enrichment, $p = 0.007$, 32 peptides / 100 kDa, Table S1). (E) Representative oblique dendritic segments of juvenile L2/3 CPNs expressing TdTomato and SYNGAP1-GFP together with either shControl or the shCtnnd2 following in utero electroporation (IUE). (G) Quantification of SYNGAP1-GFP accumulation in dendritic spines. The fluorescence of SYNGAP1-GFP clusters was normalized TdTomato signals $N_{\text{control}} = 17$ dendrites, $N_{\text{shCtnnd2}} = 20$ dendrites (1 dendrite per cell was analyzed), ***: $p < 0,001$, Mann-Whitney test.

As mentioned before, Gephyrin is the main component of inhibitory postsynaptic scaffolds (Krueger-Burg et al., 2017; Tyagarajan and Fritschy, 2014). It provides the skeleton for the formation of dendritic inhibitory post-synapses and the recruitment of other major proteins such as GABA_A receptors, Neuroligin 2 or collybistin. Therefore, CTNND2 might promote the formation of some dendritic inhibitory synapses (Figure 17F-G) through direct interaction with gephyrin. SynGAP1 is one of the most abundant proteins of excitatory PSDs (Sheng and Hoogenraad, 2007). It is a GTPase-activating protein for Ras and Rap (Gamache et al., 2020) and its major isoform synGAP1 α directly binds to PSD95, which is thought to limit the number of slots available for the recruitment of AMPA receptors (Gamache et al., 2020; Walkup et al., 2016). *Syngap1* haploinsufficiency accelerates excitatory synaptic maturation in mice (Clement et al., 2012) and, in humans, account for up to 1% of non-syndromic ID (Gamache et al., 2020). Like CTNND2, SynGAP1 acts as a brake on synaptic transmission and its loss of function strongly increases the frequency of mEPSCs in juvenile neurons (Rumbaugh et al., 2006). To assess the interplay between CTNND2 and SynGAP1, we co-electroporated *in utero* SynGAP1-GFP along with tdTomato and either shCtnnd2 or shControl, and we analyzed SynGAP1 distribution in oblique apical dendrites of layer 2/3 CPNs at P21. We found that CTNND2 deficiency led to a dramatic loss of synGAP1 in dendritic spines ($44 \pm 9\%$ of control, Figure 21F+G), indicating that CTNND2 is required for the synaptic accumulation of SynGAP1 in these neurons. Together these data provide important insights into the mechanisms underlying the dual role of CTNND2 at excitatory and inhibitory synapses, and its implication in the control of neuronal excitability.

DISCUSSION

We have shown that CTNND2 is a binding partner of the human-specific protein SRGAP2C that accumulates at synapses. During postnatal development, CTNND2 slows excitatory synaptogenesis, limits excitation and dampens intrinsic excitability in layer 2/3 CPNs. CTNND2 is also required for the formation of a subpopulation of inhibitory synapse, likely by mediating the recruitment of the postsynaptic organizer gephyrin at contact sites with specific subtypes of interneurons. As a consequence, CTNND2 deficiency increased spine density and excitatory synaptic transmission, decreased inhibitory synapse density and ramped up neuronal excitability, uncovering a pivotal role of CTNND2 in balancing excitation and inhibition and maintaining neuronal homeostasis. Remarkably, excitatory hyperconnectivity in juvenile *ctnnd2*-deficient neurons was only temporary. The consequences of CTNND2 inactivation on spine density reversed as mice aged and reached adulthood, so that adult *ctnnd2*-deficient neurons had less spines than adult control neurons. Our results are consistent with previous studies performed in young neurons *in vitro* (Arikkath et al., 2009; Brigidi et al., 2014 but see Arikkath, 2009) and with the progressive retraction of dendrites and dendritic spines in adult mice carrying a CTNND2 mutation (Matter et al., 2009). The parallel between

the cellular phenotypes observed in adult mice following sparse *ctnnd2* knockdown (here) and global *ctnnd2* mutation in a mouse model (Matter et al., 2009) indicate that CTNND2 function in the cortex is mostly postsynaptic and cell autonomous. In mice carrying a *ctnnd2* mutation, synaptic and dendritic retraction is associated with deficits in cortical responsiveness and cognition (Israely et al., 2004; Matter et al., 2009) and might be signs of neurodegeneration (Lu et al., 2016; Matter et al., 2009). This hypothesis is supported by evidence that presenilin1 mutations implicated in familial Alzheimer's disease increase the processing of CTNND2 (Kim et al., 2006; Lu et al., 2016; Matter et al., 2009; Zhou et al., 1997). Together, these data indicate that CTNND2 is required to limit excitation and excitability during synaptic maturation, and to ensure long-term maintenance of synaptic and neuronal structures. Future experiments will determine whether spine loss in adult neurons results from developmental excitotoxicity or if it is independent.

Biphasic developmental perturbations with early hyperactivity and faster synaptogenesis followed by adult hypofunction have been observed with other major excitatory postsynaptic proteins involved in ASD and ID: SynGAP1 and Shank3. SynGAP1 is present in high abundance in excitatory PSDs, with a near stoichiometric ratio to PSD-95 (Sheng and Hoogenraad, 2007). Its haploinsufficiency is highly penetrant and causes ID, ASD and epilepsy (Kilinc et al., 2018). In the cortex, *Syngap1* mutation accelerates dendritic spine maturation and increases spine density in a narrow time window during postnatal development (Aceti et al., 2015). However in adult mice, cortical pyramidal neurons show decreased dendritic branching and synaptic density, associated with deficits in sensory processing (Michaelson et al., 2018). Shank3 is a postsynaptic scaffolding protein that self-assembles with Homer, GKAP and PSD-95 through phase separation to form the core of excitatory postsynaptic densities and connect neurotransmitter receptors on the plasma membrane to the actin cytoskeleton (Chen et al., 2020). Shank3 haploinsufficiency leads to Phelan-McDermid syndrome and is strongly associated with idiopathic autism (Krol and Feng, 2018). In mouse corticostriatal circuits, shank3 deficiency leads to early hyperactivity and precocious synaptic maturation. Excitatory synaptic activity normalizes by P30 and then reverses so that adult mice exhibit decreased corticostriatal drive, decreased spine density and decreased mEPSC frequency (Krol and Feng, 2018; Peça et al., 2011; Peixoto et al., 2016, 2019). *SHANK2* mutation has also been shown to induce early hyperconnectivity in human cortical excitatory neurons derived ASD patients (Zaslavsky et al., 2019). Importantly, we show that SynGAP1 is a major partner of CTNND2 at synapses and that CTNND2 is required for the synaptic recruitment of SynGAP1. CTNND2 has also been shown by others to interact with Shank3 (other shank proteins have not been tested), and CTNND2 abundance in the PSD is decreased in *shank3* knock-out mice (Hassani Nia et al., 2020). Therefore, CTNND2 deficiency implies loss of synaptic SynGAP1, and reduced levels of Shank may also decrease CTNND2 and SynGAP1 synaptic accumulation. This supports a model in which CTNND2, SynGAP1 and Shank form a core protein complex that shapes the developmental trajectory of synapses.

In the human neocortex, the developmental trajectory of synapses is extremely protracted but the metronome remains poorly understood (Charrier et al., 2012; Fossati et al., 2016; Liu et al., 2012; Zhu et al., 2018b). We have previously shown that the human-specific protein SRGAP2C regulates the timing of synaptic development, in part by regulating its parental copy SRGAP2A and decelerating the assembly of the Homer-based excitatory postsynaptic scaffold (Charrier et al., 2012; Fossati et al., 2016). The interaction between CTNND2 and the human-specific protein SRGAP2C opens new perspective to understand how synaptic development is adjusted in humans at the core of postsynaptic scaffolds. It also suggests that the disruption of synaptic regulations specific to humans might contribute to the pathogenesis of neurodevelopmental disorders.

MATERIALS AND METHODS

Animals

All animals were handled according to French and EU regulations (directive 2010/63, decree 2013-118). Authorization references were #1530-2015082611508691v3 and #29476 2021020311595454v5, delivered by the French Ministry of Research after evaluation by the Comité d’Ethique en Experimentation Animale n°005. In utero electroporations were performed on pregnant Swiss females at E14.5-15.5 (Janvier labs) and electroporated offspring was used for experiments at varying postnatal timepoints (P10, P15-23 and P77) without consideration for their sex. Primary cultures were prepared from timed pregnant C57BL/6J or Swiss mice at E17.5-E18.5 (Janvier labs). Mice were maintained in a 12 hr light/dark cycle with unlimited access to food and water.

Primary neuronal cultures

Primary cultures of cortical neurons were performed as previously described (Fossati et al., 2016) with few modifications. Briefly, mouse cortices from E18.5 embryos were dissected, dissociated and neurons were plated on glass coverslips coated with poly-D-ornytine (80 µg/ml, Sigma) in MEM (Gibco) supplemented with sodium pyruvate (1 mM), L-glutamine (2 mM) and 10% horse serum. This medium was exchanged 2-3 hours after plating with Neurobasal (Gibco) supplemented with L-glutamine (2 mM), B27 (1X) and penicillin (2.5 units/ml) - streptomycin (2.5 µg/ml). Until use, every 5 days one third of the medium was changed and the cells were maintained at 37°C and 5% CO₂. Unless otherwise indicated, all products were from Thermo Fisher Scientific.

Cell lines

HEK293T (CRL-1573 from ATCC) cells were cultured according to suggested protocols. Cells were maintained in DMEM (GIBCO) supplemented with 10% fetal bovine serum (GIBCO) and 1% Penicillin-

Streptomycin (GIBCO) at 37°C, 5% CO₂. They were passaged by trypsin/EDTA digestion (GIBCO) upon reaching confluency with a maximum of 25 passages.

Plasmids for protein expression

All plasmids for protein expression *in utero* have a pCAG backbone driving protein expression under the CAG promoter. pCAG EGFP-GPHN was previously described (Fossati et al., 2016) and was used to visualize inhibitory synapses. pCAG SRGAP2A-HA and pCAG SRGAP2C-HA were previously described (Charrier et al., 2012; Fossati et al., 2016). For pCAG CTNND2-EGFP, CTNND2 cDNA was obtained from Horizon (Clone IMAGE 40080647; Insert sequence: BC111837) subcloned by PCR and inserted in pCAG between HindIII and AgeI; pCAG CTNND2-Myc was created through digestion of pCAG CTNND2-EGFP between AgeI and NotI to remove the GFP and insertion of the DNA cassette containing 3xMYC with compatible ends; For rescue experiments, four silent point mutations were introduced in *ctnnd2* (c3242a_a3243t_g3244c_c3245t) to resist to shRNA-mediated knockdown (mutant named *Ctnnd2**). For pCAG SYNGAP-EGFP, SYNGAP1 was amplified from cDNA (Horizon; ORFeome Collab. Hs SYNGAP1 ORF w/o Stop Codon; Clone IMAGE: 100015293; insert sequence: BC148357) and inserted into pCAG between BsrGI and NotI.

shRNA plasmids

To express shRNAs, we used the previously described pH1SCV2 and pH1SCTdT2 vectors (Charrier et al., 2012; Fossati et al., 2016) in which the H1 promoter drives the expression of the shRNA and a CAG promoter that of either mVenus (pH1SCV2) or TdTomato (pH1SCTdT2). mVenus was used for dendritic spine analysis. pH1SCTdT2 was used in patch clamp experiments, and along with pCAG EGFP-GPHN in morphology experiments to analyze inhibitory synapse densities. The control shRNA (shControl) was described previously (Charrier et al., 2012). To target *Ctnnd2* we inserted the following seed sequences into the shRNA vectors: shCtnnd2#1 5'-GCAGTGAGATCGATAGCAAGA-3' and shCtnnd2#2 5'-GGGAAATGATCAGCCTCAAAG-3'. Both shRNAs were used in spine density analysis at P21 and no difference was observed between them. In all the other experiments, we used shCtnnd2#2. The mutant *Ctnnd2** is resistant against shCtnnd2#2. If not otherwise indicated shCtnnd2#2 was used in experiments.

Lentiviral plasmids and Lentivirus production

To knockdown mouse *Ctnnd2* with lentivirus, we used a lentiviral vector expressing shRNA under a H1 promoter and GFP under a synapsin promoter, as previously described (Fossati et al., 2019). For production, HEK293T cells were co-transfected with the lentiviral vector expressing the shRNAs and three plasmids together comprising the lentiviral packaging system. 48h after transfection, the viral

supernatant was collected and ultracentrifuged at 4°C at 25,000 g for 2h. Viral pellets were resuspended in sterile PBS, aliquoted and stored at -80°C.

shRNA validation

shRNAs were validated in HEK293T cells on exogenously expressed CTNND2 and on endogenous *ctnnd2* in primary cultures of cortical neurons. Briefly, for validation in a heterologous system, HEK293T cells were co-transfected using Jet-Prime (Polyplus Transfection #POL114-07) according to the manufacturer protocol with either MYC tagged CTNND2 or CTNND2* together with the shRNAs targeting CTNND2 or a control shRNA at a 1:2 ratio. Two days after transfection, cells were collected and lysed in RIPA buffer (150 mM NaCl, 1.0% NP-40, 0.5% sodium deoxycholate, 0.1% SDS, 50 mM Tris, pH 8.0, Sigma-Aldrich) and further processed for western blot analysis of the relative protein expression levels. For the knockdown validation on endogenous *ctnnd2*, primary cultures of cortical neurons were infected at 4 days in vitro (DIV4) with lentiviruses carrying shCtnnd2#2 or a control shRNA. Infected cultures as well as a non-infected control were harvested at DIV21 and lysed in RIPA buffer under agitation for 1h at 4°C and further processed for western blot analysis (see below).

In utero electroporation

In utero electroporation (IUE) was performed as previously described (Fossati et al., 2016; Meyer-Dilhet and Courchet, 2020). Pregnant Swiss females at E14.5-15.5 (Janvier labs) were anesthetized with isoflurane (3.5% for induction and 1.5-2.5% during the surgery; ISO-VET Piramal Critical Care) and subcutaneously injected with 0.1 mg/kg of buprenorphine for analgesia. The uterine horns were exposed after laparotomy to enable injection of endotoxin-free DNA mix into one ventricle of the mouse embryos. The injected embryos were then electroporated with 4 pulses of 40 V for 50 ms at 500 ms intervals delivered by tweezer-type platinum disc electrodes (5 mm-diameter, Sonidel) and a square wave electroporator (ECM 830, BTX). The volume of injected DNA mix was adjusted depending on the experiments. Plasmids were used at the following concentrations: shRNA vectors: 0.5 µg/µl (adults) or 1 µg/µl (young animals; P10-P23); Ctnnd2 or shRNA-resistant Ctnnd2*: 1 µg/µl; EGFP-GPHN: 0.3 µg/µl, SYNGAP-EGFP, SRGAP2C-HA and PSD95-FingR GFP 0.7 µg/µl.

Confocal imaging

Immunocytochemistry

After 18 days in vitro (DIV), cultured cortical neurons were fixed for 15 min at room temperature using 4% (w/v) paraformaldehyde in PBS and incubated for 30 min in blocking buffer containing 0.3% Triton X100 and 3% BSA (Sigma) in PBS to permeabilize the cells and block nonspecific staining. Subsequently, cells were incubated for 1h in primary antibody, rinsed extensively, and incubated 45

min in secondary antibodies diluted in blocking buffer. Coverslips were mounted on slides with Vectashield (Vector Laboratories). Primary antibodies were mouse anti-Gephyrin. (mAb7a, Synaptic System, 1:300), mouse anti-PSD95 (clone K28/43, Neuromab, 1:200) and rabbit anti-Ctnnd2 (Abcam #ab184917; 1:500). Secondary antibodies were anti-rabbit Alexa-488 (Invitrogen; 1:500) and anti-mouse Cy3 (Jackson ImmunoResearch, 1:500).

Perfusion and slice preparation

Electroporated mice were sacrificed at the indicated age by terminal transcardial perfusion of 4% paraformaldehyde (Electron Microscopy Sciences) in PBS as described previously (Fossati et al., 2019). Unless otherwise indicated, 100 μ m coronal brain sections were obtained using a vibrating microtome (Leica VT1200S, Leica Micro- systems). Sections were mounted on slides in Vectashield.

Confocal image acquisition

Confocal images were acquired in 1024x1024 mode using either Leica TCS SP8 scanning confocal microscope controlled by the LAFAS software and equipped with a tunable white laser and hybrid detectors (Leica Microsystems) or Nikon A1R HD25 scanning confocal microscope controlled by NIS Elements and equipped with an LU-N4/N4S 4-laser unit including 405nm, 488nm, 561nm and 640nm lasers. On the Leica TCS SP8, we used a 10X PlanApo objective (NA 0.45) to identify electroporated neurons and acquire low magnification images and a 100X HC-PL APO, NA 1.44 CORR CS objective to acquire higher magnification images and z-stacks of dendrites. On the Nikon microscope, we used the following objectives: Plan Apo Lambda 10x Air NA 0.45 (MRD00105) and SR HP Plan Apo Lambda S 100x Silicone NA 1.35 (MRD73950). Z-stacks were acquired with 150nm spacing and a zoom of x 1.24. Images were blindly acquired and analyzed.

Confocal image analysis

In immunocytochemistry experiments, the association of CTNND2 with Gephyrin or PSD95 was analyzed using ICY v1.9.9.1 (de Chaumont et al., 2012). Regions of interest were manually drawn around dendrites and clusters in each channel were detected using the spot detector plugin (Olivo-Marin, 2002) of ICY. Then the association between channels was assessed with SODA 2-channel colocalization protocol (Lagache et al., 2018) using the synaptic markers as reference channel (radius set to 1.5x the max. feret diameter). The fraction of synaptic marker clusters associated with a cluster of CTNND2 was defined as association index.

In brain slices, dendritic spines and Gephyrin cluster densities were quantified in oblique dendrites originating from the apical trunk using Fiji (Schindelin et al., 2012; <https://fiji.sc/>). Only dendrites that were largely parallel to the plane of the slice and acquired from sections of comparable rostro-caudal

position were analyzed (no more than 1 dendrite per neuron). The density of dendritic spines and gephyrin clusters along dendrites was calculated as described before (Charrier et al., 2012; Fossati et al., 2016). Gephyrin cluster and spine densities were quantified over a minimal dendritic length of 50 μm starting from the object closest to the branchpoint with the main apical dendrite. The length of the dendritic segment was measured on the z projection. To assess SYNGAP1 levels in spines, ROIs were manually drawn around dendrites and SYNGAP1 clusters were detected using the ICY spot detector plugin. Fluorescence intensity of SYNGAP1 was normalized to local filler intensity and compared between conditions.

Ex vivo electrophysiology

Slice preparation

Following in utero electroporation, juvenile (postnatal day 16-20) swiss mice were anesthetized with isoflurane (ISO-VET, Piramal Critical Care), decapitated and brains were quickly removed. For inhibitory and excitatory miniature post-synaptic miniature currents (mIPSCs and mEPSCs, respectively) and intrinsic excitability recordings brains were subsequently placed in ice-cold (4°C) cutting solution containing (in mM): 85 NaCl, 64 sucrose, 25 glucose, 2.5 KCl, 1.2 NaH₂PO₄, 24 NaHCO₃, 0.5 CaCl₂, and 7 MgCl₂, saturated with 95% O₂ and 5% CO₂ (pH 7.3–7.4). Acute coronal slices were cut using the 7000 smz-2 vibratome (Campden Instrument). Slices recovered at room temperature in oxygenated artificial cerebrospinal fluid (ACSF) containing (in mM): 125 NaCl, 2.5 KCl, 2 CaCl₂, 1 MgCl₂, 1.2 NaH₂PO₄, 24 NaHCO₃, and 25 glucose (pH 7.4) for at least 30 min. For electrophysiological recordings, slices were transferred to a submerged recording chamber and continuously perfused at 33–34°C with oxygenated ACSF at a rate of 4-5 ml/min.

For E/I and AMPA/NMDA ratio as well as paired pulse ratio recordings the cutting solution contained (in mM): 83 NaCl, 2.5 KCl, 3.3 MgSO₄, 1 NaH₂PO₄, 22 Glucose, 72 Sucrose, 0.5 CaCl and the extracellular solution contained (in mM): 119 NaCl, 2.5 KCl, 1.3 MgSO₄, 1.3 NaH₂PO₄, 20 Glucose, 26 NaHCO₃, 2.5 CaCl.

Electrophysiological recordings

Whole-cell voltage or current clamp recordings were acquired from visually identified electroporated or non-electroporated layer 2/3 cortical pyramidal neurons of the somatosensory cortex. For all electrophysiological experiments an IR-DIC microscope (Olympus) was used, equipped with a 4X objective (UPlanFL, NA 0.13) as well as a 40X water immersion objective (LUMPlan FI/IR, NA 0.8), 2 automated manipulators (Patchstar, Scientifica) and a ORCAFlash 4.0LT camera (Hamamatsu). Signals were recorded with a Multiclamp 700B Amplifier (Axon instruments), Axon Digidata 1550 (Axon Instruments) and pClamp 10 software (Axon instruments). Borosilicate glass pipettes were pulled to have a resistance of 3-7M Ω . mIPSCs and mEPSCs were recorded at a holding potential of

-60 mV in the presence of 0.5 μ M TTX. mIPSCs were isolated by adding NBQX (10 μ M) and D-AP5 (50 μ M) to the ACSF and by using a high chloride intracellular solution containing (in mM): 150 KCl, 1.5 MgCl₂, 10 HEPES, 1 EGTA, 2 NaATP, 0.5 NaGTP (pH adjusted to \pm 7.3 with KOH). mEPSCs were isolated using gabazine (10 mM). For mEPSCs recordings as well as intrinsic excitability recordings the following intracellular solution was used, containing (in mM): 144 K-gluconate, 7 KCl, 10 HEPES, 1 EGTA, 1.5 MgCl₂, 2 NaATP, 0.5 NaGTP, (pH adjusted to \pm 7.3 with KOH). To record intrinsic excitability cells were held in current clamp mode at resting potential and injected with 1s step currents from -100 pA to +1000 pA with 50 pA increments to assess spike frequency. Current ramps from 0-1000 pA over 1s were used to probe the action potential threshold. E/I ratio, PPR ratio and AMPA/NMDA ratio were recorded with the following intracellular solution (in mM; previously described in Adesnik & Scanziani, 2010): 115 CsMeSO₃, 8 NaCl, 10 HEPES, 0.3 NaGTP, 4 MgATP, 0.3 EGTA, 5 QX-314, 10 BAPTA (pH adjusted to \pm 7.3). For all three types of recordings a stimulation electrode was placed approximately 100 μ m up the apical dendrite and synaptic transmission evoked at 10 s intervals. For the E/I ratio and PPR recordings the neuron was clamped at -70 mV, the reversal potential of inhibitory synaptic transmission, and subsequently at +10 mV, the reversal potential of excitatory synaptic, to record 10 sweeps of eEPSCs and eIPSCs, respectively. Reversal potentials were validated in a few cells with 10 μ M NBQX and 10 μ M Gabazine respectively. The E/I ratio was calculated from the average peak currents or integrated currents (charge) per holding potential. For the paired pulse ratio, peak currents at both holding potentials were recorded in response to two sequential stimulations with a 50 ms interval (10 sweeps). The AMPA/NMDA ratio was recorded in the presence of 10 mM Gabazine and is defined as the peak of the EPSC at -70 mV over the amplitude of the EPSC at +40 mV 50 ms after stimulation (5 sweeps per holding potential). In all recordings, access and input resistance were monitored by applying 5 mV hyperpolarizing steps of current. All toxins were obtained from Abcam, salts and other reagents from Sigma Aldrich if not otherwise indicated.

Electrophysiological data analysis

Voltage and Current clamp data were sampled at 10 kHz and filtered at 2 kHz. All traces were analyzed using pClamp 10.0 (Molecular Devices). Miniature currents were analyzed over 1 min-periods. Overlapping events were excluded from amplitude analysis. Evoked currents were averaged over 10 (E/I ratio and PPR) or 5 sweeps (A/N ratio) and quantified over 50 or 100 ms after stimulation, respectively. Sweeps with a di-synaptic response or noise interference were excluded from averaging. The E/I ratio was calculated from either the maximum amplitude or integrated currents over 50ms (charge) per holding potential. The paired pulse ratio of IPSC and EPSC was calculated from the maximum amplitude of currents per holding potential. The AMPA/NMDA ratio is defined as the peak of the EPSC at -70 mV over the amplitude of the EPSC at +40 mV 50 ms after stimulation. Cells

showing >20% change in access and input resistance upon application of 5 mV hyperpolarizing steps of current were excluded from the analysis.

Biochemistry experiments

Co-Immunoprecipitation in HEK cells

Transfected HEK cell were lysed in 10 mM Tris/Cl pH7.5, 150 mM NaCl, 0.5 mM EDTA and 0.5% Igepal and the protein concentration was determined. From each condition, 0.8-1 mg of total protein was diluted in binding buffer containing 0.05% Igepal, 10 mM Tris/Cl (pH 7.5), 150 mM NaCl, 0.5 mM EDTA and protease inhibitors as well as 25 µl of antibody-conjugated magnetic beads. Depending on the experiment GFP- or HA-conjugated magnetic beads were used (GFP-trap from Chromotek or Pierce anti-HA magnetic beads (Thermo Fisher #88837) respectively). Samples were incubated with the beads for 2h at 4°C. After extensive washes, the beads were resuspended in Laemmli buffer and bound proteins were released by boiling (5min 95°C). Samples were subjected to western blot analysis. Inputs correspond to 15 µg of proteins.

Western blotting

Western blotting was performed using precast gels, electrophoresis and transfer chambers from BioRAD according to standard procedures. The following primary antibodies were used: rabbit anti-HA (Cell Signalling #3724S, 1:1000), rabbit anti-GFP (Thermo Fisher Scientific #A11122, 1:2,000), mouse anti-Myc (Cell Signaling Technology #2276, 1:1,000), mouse anti-Ctnnd2 (Abcam #ab54578, 1:1000), rabbit anti-Ctnnd2 (Abcam #ab184917; 1:1000), and mouse anti-actin (Sigma Aldrich, #MAB1501R, 1:5000). Donkey anti-mouse or anti-rabbit HRP-conjugated secondary antibodies were used at a 1:10,000 dilution (Jackson ImmunoResearch #711-035-150 and #711-035-152 respectively). Protein visualization was performed by chemiluminescence using LumiLight western blotting (Roche) and ImageQuant 800 (GE Healthcare).

Subcellular fractionation and co-immunoprecipitation

Subcellular fractionation was performed from Swiss P15 mouse brains as previously described (Fossati et al., 2019). All steps were performed at 4°C. Briefly, brains were homogenized in ice-cold HEPES-buffered sucrose (0.32 M sucrose, 4 mM HEPES pH 7.4, 5 mM EDTA, 5 mM EGTA, protease inhibitor cocktail, from Sigma) using a motor driven glass-teflon homogenizer. The homogenate was centrifuged at 3,000g for 15min. The resulting supernatant was centrifuged at 38,400 g for 15 min, yielding the crude synaptosomal pellet. The pellet was then subjected to hypo-osmotic shock and centrifuged at 38,400 g for 20 min. The resulting pellet was lysed for 1 h using HEPES-buffered NaCl (100 mM NaCl, 4mM HEPES pH 7.4, 5mM EDTA, 5mM EGTA, protease inhibitor cocktail)

supplemented with 1% CHAPS (Sigma) and centrifuged at 100,000 g for 1h. The corresponding supernatant is referred to as synaptic fraction or synaptic membranes. Protein concentration was measured using BCA assay (Pierce) and protein samples were subjected to immunoprecipitation. Co-immunoprecipitation was performed using antibodies covalently cross-linked to protein G magnetic beads (Pierce). 36 µg of rabbit anti-CTNND2 or anti-SRGAP2 (directed against the F-BAR domain) antibody, or total rabbit IgG in control condition, were incubated for 1h at room temperature and cross-linked with 20 mM DMP (dimethylpimelimidate, Pierce) in 0.2 M Sodium Borate pH 9. After 30min, the reaction was blocked for 1h with 0.2 M Ethanolamine (pH 8). Eventual unbound antibody molecules were washed out by incubating the beads for 5 min in 0.1 M glycine (pH 3). The efficiency of cross-linking was checked by running samples on polyacrylamide 4%–15% gradient gels (Biorad) followed by Comassie Blue staining. 1 mg of total proteins from purified synaptic membranes were diluted in a HEPES-NaCl buffer containing (in mM): 20 HEPES pH 7.4, 150 NaCl, 5 EDTA, 5 EGTA and protease inhibitor cocktail supplemented with 1% CHAPS and incubated overnight at 4°C with antibody-coupled magnetic beads. The beads were rinsed 3 times using HEPES-NaCl buffer supplemented with 0.1% CHAPS and further washed 3 times in a buffer containing 20 mM HEPES (pH 7.4) and 150mM NaCl. The samples were then subjected to mass spectrometry analysis (see below).

Mass spectrometry

Proteomics analysis was performed as previously described (Fossati et al., 2019). Proteins bound to magnetic beads were washed twice with 100 µL of 25 mM NH₄HCO₃ and on-beads digested with 200 ng of trypsin/LysC (Promega) for 1 h in 100 µL of 25 mM NH₄HCO₃ at room temperature. The peptides were loaded onto an C18 StageTips (Fossati et al., 2019) for desalting and eluted using 40/60 MeCN/H₂O + 0.1% formic acid. Mass spectrometry measurement was performed on an Orbitrap Fusion Tribrid mass spectrometer (Thermo Scientific) coupled online to an RSLCnano system (Ultimate 3000, Thermo Scientific) and with a top speed DDA method using higher-energy C-trap collisional dissociation (HCD) fragmentation analyzed in the linear ion trap in rapid mode. The mass spectrometry proteomics data will be deposited to the ProteomeXchange Consortium via the PRIDE (Vizcaíno et al., 2016) before submission. For protein identification, data were searched against the *Mus musculus* (Mouse) UniProt database using Sequest^{HT} through proteome discoverer (version 2.1). Enzyme specificity was set to trypsin and a maximum of two missed cleavage site were allowed. Oxidized methionine, N-terminal acetylation, and carbamidomethyl cysteine were set as variable modifications. Maximum allowed mass deviation was set to 10 ppm for monoisotopic precursor ions and 0.6 Da for MS/MS peaks. The resulting files were further processed using myProMS (Pouillet et al., 2007) v3.9.3. FDR calculation used Percolator and was set to 1% at the peptide level for the whole study.

Proteomics analysis: label-free quantification

Label free quantification was performed by peptide Extracted Ion Chromatograms (XICs) computed with MassChroQ version 2.2.1 (Valot et al., 2011). For protein quantification, XICs from proteotypic and non-proteotypic peptides shared between compared conditions (TopN matching), no missed cleavages and all modification, charge states and sources were used. Global MAD normalization was applied on the total signal to correct the XICs for each biological replicate (n=3). To estimate the significance of the change in protein abundance, a statistical test based on a linear model adjusted on peptides and biological replicates was performed and p-values were adjusted with a Benjamini-Hochberg FDR procedure. Protein with at least five total peptides in all replicates, a 4-fold enrichment and an adjusted p-value < 0.05 were considered significantly enriched in sample comparison. Unique proteins were considered with at least 5 total peptides in all replicates.

Gene ontology analysis

Gene ontology analysis was performed using the SYNGO database (<https://syngoportal.org/>) (Koopmans et al., 2019) for all proteins with more than 5 peptide hits, 4-fold enrichment in CTNND2-immunoprecipitates and a p-value >0.05.

Statistical analysis

Statistical analyses were performed with Prism 7 (GraphPad Software). Data are obtained from a minimum of three independent experiments. For in utero electroporations data were obtained from at least three experiments or three animals from two independent litters. For statistical analysis, normality of the distributions was assessed using the D'Agostino-Pearson normality test. In case of normal distributions, we used paired or unpaired Student's t test or one-way analysis of variance followed by Tukey's post hoc test. Non-normal distributions were assessed using the non-parametric Mann-Whitney test, paired Wilcoxon test, or Kruskal-Wallis test followed by Dunn's multiple comparison test. In boxplots, whiskers correspond to the minimal and maximal values. Other data represent mean \pm sem. Sample size and statistical tests are reported in each main and supplementary figure. The significance threshold was placed at $p < 0.05$ (NS= $p > 0.05$; * = $p < 0.05$, ** = $p < 0.01$; *** = $p < 0.001$).

REFERENCES

Please note that the manuscript references are included in the main reference section.

CHAPTER 5 – Perspectives

CHAPTER 5 – Perspectives

The focus of this project is on CTNND2, a member of the neuronal cadherin-catenin complex whose mutation is implicated in neurological disorders in human and, as we have shown here, a partner of SRGAP2A and its human-specific paralog SRGAP2C. I have characterized the effect of the loss of CTNND2 function in layer 2/3 pyramidal neurons of the somatosensory cortex in mice and shown that CTNND2 is a multi-functional protein implicated in the development of both excitatory and inhibitory synapses, the regulation of intrinsic neuronal excitability and spine maintenance in adults. CTNND2 localizes to and interacts with core proteins of both inhibitory and excitatory PSDs among which gephyrin and SynGAP1. These interactions likely mediate CTNND2 function at synapses, and we demonstrated that CTNND2 is required for SynGAP1 localization in dendritic spines. Our finding that depletion of CTNND2 can lead to both an increase in the E/I ratio in juveniles and premature loss of synapses in adult mice contributes to our understanding how CTNND2 dysfunction in humans can both be implicated in neuro-developmental diseases and neurodegeneration.

However, there are still several open questions, and some aspects of CTNND2 function remain elusive. For one, we don't know how the different aspects of CTNND2 phenotype relate to one another. Is the increase in excitation and intrinsic excitability in juvenile mice causal to the premature spine loss in adults, or is CTNND2 independently needed to maintain synapse numbers? Assessing this requires the separation of the CTNND2 loss of function phenotype in time. To this end, we have introduced the shRNA targeting CTNND2 in a vector that drives expression upon tamoxifen-induced cre-recombination, which will allow us to induce CTNND2 depletion after synapse development. These experiments are ongoing and will give us further opportunity to explore the loss of function phenotype in adults. At what age does the synapse loss manifest? Is the spine loss we see in our model linked to degeneration of dendrites, as shown in adult CTNND2 mutant mice (Matter et al., 2009), or even to pathological neuronal cell death? It would further be interesting to investigate whether it is possible to alleviate the phenotypes we see through the postnatal expression of our shRNA-resistant CTNND2 construct. Would such a recovery be restricted in time, similar to what has been demonstrated for SynGAP1 and Shank3 reintroductions (reviewed in Krol and Feng, 2018)?

Generally, regarding the molecular mechanism underlying CTNND2 function, it is important to further explore the possibility that CTNND2, SYNGAP1 and SHANK contribute to a common signaling pathway at excitatory synapses, which is disrupted in neurological disorders. Moreover, the decrease in inhibitory synapses we see in juveniles is likely mediated through direct interaction of CTNND2 with gephyrin. In order to gain a better understanding of CTNND2 function at either synapse subtype as well as their mutual relationships, decoupling the influence of CTNND2 on excitatory and inhibitory synapses would be ideal. This could be done through the generation of a mutant CTNND2 that specifically disrupt either gephyrin or SynGAP interaction. Unfortunately, our considerable efforts in

that direction have thus far been unsuccessful. Alternatively, live imaging in organotypic slices to observe both spine and gephyrin cluster dynamics and their response to CTNND2 loss might also be beneficial to our understanding of the influence of CTNND2 on excitatory and inhibitory synapse development.

One aspect of CTNND2 that we have not yet looked into is its role as a part of the neuronal cadherin-catenin complex. In contrast to CTNND2 loss, loss of N-Cadherin in development has been shown to decrease excitatory synaptic transmission (Saglietti et al., 2007; Vitureira et al., 2012) and thus argues for a N-cadherin independent function of CTNND2 at excitatory synapses. However, we cannot exclude an implication of these interactions completely, nor any potential implication of other classical cadherins. As classical cadherins are thought to provide an adhesion code during synapse formation (see chapter 3 and reviewed in Hirano and Takeichi, 2012), such interactions would be especially interesting in regard to a possible synapse specificity of CTNND2 function in the formation of inhibitory synapses. Interestingly, the cadherin binding site is largely conserved between p120 catenin family members and a mutation specifically disrupting the interaction has been described for p120 catenin (Ishiyama et al., 2010). Introducing this mutation into CTNND2 thus could specifically disrupt the interaction with cadherins and would allow us to assess cadherin adhesion implication within the CTNND2 loss of function phenotype. Furthermore, although the relevance for this study is currently unknown, catenins in general and thus also CTNND2 are becoming more broadly recognized to be implicated in the regulation of gene transcription (reviewed in McCreia and Gottardi, 2016).

In humans, CTNND2 mutations have been implicated in a severe form of autism spectrum disorder (ASD) (Turner et al., 2015). Utilizing our model to carry out gene replacement experiments in which we express the autism mutation of CTNND2 could provide further insight in the specific pathophysiology of CTNND2. Relevant in this regard are also the interactions between CTNND2 and human-specific genes, as several lines of evidence indicate that synapses have specialized in humans (reviewed in i.a., Lourenço and Bacci, 2017; Sousa et al., 2017) and fully understanding CTNND2 pathophysiology will require a better understanding of the context it is operating in. A start in that direction would be to investigate the regulation of CTNND2 by human-specific genes like SRGAP2C or FRMPD2B in our model. This has the potential to contribute to our understanding of the human vulnerability to brain disease.

*'Unfortunately,
nature seems unaware
of our intellectual need
for convenience,
for unity
and often takes delight
in complication
and diversity'*

free after

Santiago Ramon y Cajal
(1852-1934)

REFERENCES

References

- Abe, K., Chisaka, O., Van Roy, F., and Takeichi, M. (2004). Stability of dendritic spines and synaptic contacts is controlled by α -catenin. *Nat. Neurosci.* 7, 357–363.
- Aceti, M., Creson, T.K., Vaissiere, T., Rojas, C., Huang, W.C., Wang, Y.X., Petralia, R.S., Page, D.T., Miller, C.A., and Rumbaugh, G. (2015). Syngap1 haploinsufficiency damages a postnatal critical period of pyramidal cell structural maturation linked to cortical circuit assembly. *Biol. Psychiatry* 77, 805–815.
- Acuna, C., Liu, X., Gonzalez, A., and Südhof, T.C. (2015). RIM-BPs Mediate Tight Coupling of Action Potentials to Ca^{2+} -Triggered Neurotransmitter Release. *Neuron* 87, 1234–1247.
- Adesnik, H., and Scanziani, M. (2010). Lateral competition for cortical space by layer-specific horizontal circuits. *Nature* 464, 1155–1160.
- Adrian, M., Kusters, R., Storm, C., Hoogenraad, C.C., and Kapitein, L.C. (2017). Probing the Interplay between Dendritic Spine Morphology and Membrane-Bound Diffusion. *Biophys. J.* 113, 2261–2270.
- Aiga, M., Levinson, J.N., and Bamji, S.X. (2011). N-cadherin and neuroligins cooperate to regulate synapse formation in hippocampal cultures. *J. Biol. Chem.* 286, 851–858.
- Ali, H., Marth, L., and Krueger-Burg, D. (2020). Neuroligin-2 as a central organizer of inhibitory synapses in health and disease. *Sci. Signal.* 13.
- Alié, A., and Manuël, M. (2010). The backbone of the post-synaptic density originated in a unicellular ancestor of choanoflagellates and metazoans. *BMC Evol. Biol.* 10.
- Allen, N.J., and Eroglu, C. (2017). Cell Biology of Astrocyte-Synapse Interactions. *Neuron* 96, 697–708.
- Allen, N.J., Bennett, M.L., Foo, L.C., Wang, G.X., Chakraborty, C., Smith, S.J., and Barres, B.A. (2012). Astrocyte glypicans 4 and 6 promote formation of excitatory synapses via GluA1 AMPA receptors. *Nature* 486, 410–414.
- Alvarez-Castelao, B., and Schuman, E.M. (2015). The regulation of synaptic protein turnover. *J. Biol. Chem.* 290, 28623–28630.
- Alvarez, V.A., and Sabatini, B.L. (2007). Anatomical and physiological plasticity of dendritic spines. *Annu. Rev. Neurosci.* 30, 79–97.
- Anderson, G.R., Aoto, J., Tabuchi, K., Földy, C., Covy, J., Yee, A.X., Wu, D., Lee, S.J., Chen, L., Malenka, R.C., et al. (2015). β -Neurexins Control Neural Circuits by Regulating Synaptic Endocannabinoid Signaling. *Cell* 162, 593–606.
- Apóstolo, N., and de Wit, J. (2019). Compartmentalized distributions of neuronal and glial cell-surface proteins pattern the synaptic network. *Curr. Opin. Neurobiol.* 57, 126–133.
- Araki, Y., Zeng, M., Zhang, M., and Huganir, R.L. (2015). Rapid Dispersion of SynGAP from Synaptic Spines Triggers AMPA Receptor Insertion and Spine Enlargement during LTP. *Neuron* 85, 173–189.
- Arellano, J.I., Benavides-Piccione, R., DeFelipe, J., and Yuste, R. (2007). Ultrastructure of Dendritic Spines: Correlation Between Synaptic and Spine Morphologies. *Front. Neurosci.* 1, 131–143.
- Arendt, D. (2020). The Evolutionary Assembly of Neuronal Machinery. *Curr. Biol.* 30, R603–R616.
- Arikkath, J. (2009). Regulation of dendrite and spine morphogenesis and plasticity by catenins. *Mol. Neurobiol.* 40, 46–54.
- Arikkath, J., and Reichardt, L.F. (2008). Cadherins and catenins at synapses: roles in synaptogenesis and synaptic plasticity. *Trends Neurosci.* 31, 487–494.
- Arikkath, J., Peng, I.-F., Ng, Y.G., Israely, I., Liu, X., Ullian, E.M., and Reichardt, L.F. (2009). Delta-catenin regulates spine and synapse morphogenesis and function in hippocampal neurons during development. *J. Neurosci.* 29, 5435–5442.
- Attardo, A., Fitzgerald, J.E., and Schnitzer, M.J. (2015). Impermanence of dendritic spines in live adult CA1 hippocampus. *Nature* 523, 592–596.
- Augustin, I., Rosenmund, C., Südhof, T.C., and Brose, N. (1999). Munc13-1 is essential for fusion competence of glutamatergic synaptic vesicles. *Nature* 400, 457–461.
- Bacon, C., Endris, V., and Rappold, G. (2009). Dynamic expression of the Slit-Robo GTPase activating protein genes during development of the murine nervous system. *J. Comp. Neurol.* 513, 224–236.
- Bailey, C.H., Kandel, E.R., and Harris, K.M. (2015). Structural components of synaptic plasticity and memory consolidation. *Cold Spring Harb. Perspect. Biol.* 7, 1–29.
- Barnes, A.P., and Polleux, F. (2009). Establishment of axon-dendrite polarity in developing neurons. *Annu. Rev. Neurosci.* 32, 347–381.

- Basu, R., Duan, X., Taylor, M.R., Martin, E.A., Muralidhar, S., Wang, Y., Gangi-Wellman, L., Das, S.C., Yamagata, M., West, P.J., et al. (2017). Heterophilic Type II Cadherins Are Required for High-Magnitude Synaptic Potentiation in the Hippocampus. *Neuron* 96, 160–176.e8.
- Battaglia, S., Renner, M., Russeau, M., Côme, E., Tyagarajan, S.K., and Lévi, S. (2018). Activity-dependent inhibitory synapse scaling is determined by gephyrin phosphorylation and subsequent regulation of GABAA receptor diffusion. *ENeuro* 5, 1–20.
- Bemben, M.A., Shipman, S.L., Hirai, T., Herring, B.E., Li, Y., Badger, J.D., Nicoll, R.A., Diamond, J.S., and Roche, K.W. (2014). CaMKII phosphorylation of neuroligin-1 regulates excitatory synapses. *Nat. Neurosci.* 17, 56–64.
- Benavides-Piccione, R., Ballesteros-Yáñez, I., DeFelipe, J., and Yuste, R. (2002). Cortical area and species differences in dendritic spine morphology. *J. Neurocytol.* 31, 337–346.
- Benson, D.L., and Tanaka, H. (1998). N-cadherin redistribution during synaptogenesis in hippocampal neurons. *J. Neurosci.* 18, 6892–6904.
- Berry, K.P., and Nedivi, E. (2017). Spine Dynamics: Are They All the Same? *Neuron* 96, 43–55.
- Bhatt, D.H., Zhang, S., and Gan, W.B. (2009). Dendritic spine dynamics. *Annu. Rev. Physiol.* 71, 261–282.
- Bian, W.J., Miao, W.Y., He, S.J., Qiu, Z., and Yu, X. (2015). Coordinated Spine Pruning and Maturation Mediated by Inter-Spine Competition for Cadherin/Catenin Complexes. *Cell* 162, 808–822.
- Bianchini, J.M., Kitt, K.N., Gloerich, M., Pokutta, S., Weis, W.I., and Nelson, W.J. (2015). Reevaluating α E-catenin monomer and homodimer functions by characterizing E-cadherin/ α E-catenin chimeras. *J. Cell Biol.* 210, 1065–1074.
- Biederer, T., Kaeser, P.S., and Blanpied, T.A. (2017). Transcellular Nanoalignment of Synaptic Function. *Neuron* 96, 680–696.
- Blanco-Suarez, E., Liu, T.F., Kopelevich, A., and Allen, N.J. (2018). Astrocyte-Secreted Chordin-like 1 Drives Synapse Maturation and Limits Plasticity by Increasing Synaptic GluA2 AMPA Receptors. *Neuron* 100, 1116–1132.e13.
- Blue, M.E., and Parnavelas, J.G. (1983a). The formation and maturation of synapses in the visual cortex of the rat. I. Qualitative analysis. *J. Neurocytol.* 12, 599–616.
- Blue, M.E., and Parnavelas, J.G. (1983b). The formation and maturation of synapses in the visual cortex of the rat. II. Quantitative analysis. *J. Neurocytol.* 12, 697–712.
- Bocquet, N., Prado De Carvalho, L., Cartaud, J., Neyton, J., Le Poupon, C., Taly, A., Grutter, T., Changeux, J.P., and Corringer, P.J. (2007). A prokaryotic proton-gated ion channel from the nicotinic acetylcholine receptor family. *Nature* 445, 116–119.
- Boyken, J., Grønborg, M., Riedel, D., Urlaub, H., Jahn, R., and Chua, J.J.E. (2013). Molecular profiling of synaptic vesicle docking sites reveals novel proteins but few differences between glutamatergic and GABAergic synapses. *Neuron* 78, 285–297.
- Bozdagi, O., Shan, W., Tanaka, H., Benson, D.L., and Huntley, G.W. (2000). Increasing numbers of synaptic puncta during late-phase LTP: N-cadherin is synthesized, recruited to synaptic sites, and required for potentiation. *Neuron* 28, 245–259.
- Bozdagi, O., Wang, X. Bin, Nikitczuk, J.S., Anderson, T.R., Bloss, E.B., Radice, G.L., Zhou, Q., Benson, D.L., and Huntley, G.W. (2010). Persistence of coordinated long-term potentiation and dendritic spine enlargement at mature hippocampal CA1 synapses requires N-cadherin. *J. Neurosci.* 30, 9984–9989.
- Brasch, J., Katsamba, P.S., Harrison, O.J., Ahlsén, G., Troyanovsky, R.B., Indra, I., Kaczynska, A., Kaeser, B., Troyanovsky, S., Honig, B., et al. (2018). Homophilic and Heterophilic Interactions of Type II Cadherins Identify Specificity Groups Underlying Cell-Adhesive Behavior. *Cell Rep.* 23, 1840–1852.
- Brigidi, G.S., and Bamji, S.X. (2011). Cadherin-catenin adhesion complexes at the synapse. *Curr. Opin. Neurobiol.* 1–7.
- Brigidi, G.S., Sun, Y., Beccano-Kelly, D., Pitman, K., Mobasser, M., Borgland, S.L., Milnerwood, A.J., and Bamji, S.X. (2014). Palmitoylation of δ -catenin by DHHC5 mediates activity-induced synapse plasticity. *Nat. Neurosci.* 17, 522–532.
- Brill, J., and Huguenard, J.R. (2008). Sequential changes in AMPA receptor targeting in the developing neocortical excitatory circuit. *J. Neurosci.* 28, 13918–13928.
- Brodmann, K. (1909). Vergleichende Lokalisationslehre der Großhirnrinde.
- Budreck, E.C., and Scheiffele, P. (2007). Neuroligin-3 is a neuronal adhesion protein at GABAergic and glutamatergic synapses. *Eur. J. Neurosci.* 26, 1738–1748.
- Buñill, E., Agustí, J., and Blesa, R. (2011). Human neoteny revisited: The case of synaptic plasticity. *Am. J. Hum. Biol.* 23, 729–739.
- Burette, A.C., Lesperance, T., Crum, J., Martone, M., Volkman, N., Ellisman, M.H., and Weinberg, R.J. (2012). Electron tomographic analysis of synaptic ultrastructure. *J. Comp. Neurol.* 520, 2697–2711.
- Burkhardt, P., and Sprecher, S.G. (2017). Evolutionary origin of synapses and neurons – Bridging the gap. *BioEssays* 39, 1–10.
- Cadwell, C.M., Su, W., and Kowalczyk, A.P. (2016). Cadherin tales: Regulation of cadherin function by endocytic membrane trafficking. *Traffic* 17, 1262–1271.

- Cadwell, C.R., Bhaduri, A., Mostajo-Radji, M.A., Keefe, M.G., and Nowakowski, T.J. (2019). Development and Arealization of the Cerebral Cortex. *Neuron* 103, 980–1004.
- Carlson, B.R., Lloyd, K.E., Kruszewski, A., Kim, I.H., Rodriguez, R.M., Heindel, C., Faytell, M., Dudek, S.M., Wetsel, W.C., and Soderling, S.H. (2011). WRP/srGAP3 facilitates the initiation of spine development by an inverse F-BAR domain, and its loss impairs long-term memory. *J. Neurosci.* 31, 2447–2460.
- Chamma, I., and Thoumine, O. (2018). Dynamics, nanoscale organization, and function of synaptic adhesion molecules. *Mol. Cell. Neurosci.* 91, 95–107.
- Charrier, C., Ehrensperger, M.V., Dahan, M., Lévi, S., and Triller, A. (2006). Cytoskeleton regulation of glycine receptor number at synapses and diffusion in the plasma membrane. *J. Neurosci.* 26, 8502–8511.
- Charrier, C., Joshi, K., Coutinho-Budd, J., Kim, J.E., Lambert, N., De Marchena, J., Jin, W.L., Vanderhaeghen, P., Ghosh, A., Sassa, T., et al. (2012). Inhibition of SRGAP2 function by its human-specific paralogs induces neoteny during spine maturation. *Cell* 149, 923–935.
- de Chaumont, F., Dallongeville, S., Chenouard, N., Hervé, N., Pop, S., Provoost, T., Meas-Yedid, V., Pankajakshan, P., Lecomte, T., Le Montagner, Y., et al. (2012). Icy: an open bioimage informatics platform for extended reproducible research. *Nat. Methods* 9, 690–696.
- Chazeau, A., Garcia, M., Czöndör, K., Perrais, D., Tessier, B., Giannone, G., and Thoumine, O. (2015). Mechanical coupling between transsynaptic N-cadherin adhesions and actin flow stabilizes dendritic spines. *Mol. Biol. Cell* 26, 859–873.
- Chédotal, A. (2019). Roles of axon guidance molecules in neuronal wiring in the developing spinal cord. *Nat. Rev. Neurosci.* 20, 380–396.
- Chen, C., and Regehr, W.G. (2000). Developmental remodeling of the retinogeniculate synapse. *Neuron* 28, 955–966.
- Chen, J.L., Villa, K.L., Cha, J.W., So, P.T.C., Kubota, Y., and Nedivi, E. (2012). Clustered Dynamics of Inhibitory Synapses and Dendritic Spines in the Adult Neocortex. *Neuron* 74, 361–373.
- Chen, X., Wu, X., Wu, H., and Zhang, M. (2020). Phase separation at the synapse. *Nat. Neurosci.* 23, 301–310.
- Chiu, C.Q., Lur, G., Morse, T.M., Carnevale, N.T., Ellis-Davies, G.C.R., and Higley, M.J. (2013). Compartmentalization of GABAergic inhibition by dendritic spines. *Science* (80-.). 340, 759–762.
- Chiu, C.Q., Barberis, A., and Higley, M.J. (2019). Preserving the balance: diverse forms of long-term GABAergic synaptic plasticity. *Nat. Rev. Neurosci.* 20, 272–281.
- Choquet, D., and Triller, A. (2013). The dynamic synapse. *Neuron* 80, 691–703.
- Chowdhury, D., Watters, K., and Biederer, T. (2021). Synaptic recognition molecules in development and disease (Elsevier Inc.).
- Citri, A., and Malenka, R.C. (2008). Synaptic plasticity: Multiple forms, functions, and mechanisms. *Neuropsychopharmacology* 33, 18–41.
- Cizeron, M., Qiu, Z., Koniaris, B., Gokhale, R., Komiyama, N.H., Fransén, E., and Grant, S.G.N. (2020). A brainwide atlas of synapses across the mouse life span. *Science* (80-.). 369, 270–275.
- Clement, J.P., Aceti, M., Creson, T.K., Ozkan, E.D., Shi, Y., Reish, N.J., Almonte, A.G., Miller, B.H., Wiltgen, B.J., Miller, C.A., et al. (2012). Pathogenic SYNGAP1 Mutations Impair Cognitive Development by Disrupting Maturation of Dendritic Spine Synapses. *Cell* 151, 709–723.
- Coutinho-Budd, J., Ghukasyan, V., Zylka, M.J., and Polleux, F. (2012). The F-BAR domains from srGAP1, srGAP2 and srGAP3 regulate membrane deformation differently. *J. Cell Sci.* 125, 3390–3401.
- Crair, M.C., and Malenka, R.C. (1995). A critical period for long-term potentiation at thalamocortical synapses. *Nature* 375, 325–328.
- Curran, O.E., Qiu, Z., Smith, C., and Grant, S.G.N. (2021). A single-synapse resolution survey of PSD95-positive synapses in twenty human brain regions. *Eur. J. Neurosci.* 54, 6864–6881.
- Dalva, M.B., McClelland, A.C., and Kayser, M.S. (2007). Cell adhesion molecules: Signalling functions at the synapse. *Nat. Rev. Neurosci.* 8, 206–220.
- Danielson, E., Zhang, N., Metallo, J., Kaleka, K., Shin, S.M., Gerges, N., and Lee, S.H. (2012a). S-SCAM/MAGI-2 is an essential synaptic scaffolding molecule for the GluA2-containing maintenance pool of AMPA receptors. *J. Neurosci.* 32, 6967–6980.
- Danielson, E., Metallo, J., and Lee, S.H. (2012b). Role of TARP interaction in S-SCAM-mediated regulation of AMPA receptors. *Channels (Austin)*. 6, 393–397.
- DeFelipe, J. (2011). The evolution of the brain, the human nature of cortical circuits, and intellectual creativity. *Front. Neuroanat.* 5, 1–17.
- DeFelipe, J., Alonso-Nanclares, L., and Arellano, J.I. (2002). Microstructure of the neocortex: Comparative aspects. *J. Neurocytol.* 31, 299–316.

- Deitcher, Y., Eyal, G., Kanari, L., Verhoog, M.B., Atnekeng Kahou, G.A., Mansvelder, H.D., De Kock, C.P.J., and Segev, I. (2017). Comprehensive Morpho-Electrotonic Analysis Shows 2 Distinct Classes of L2 and L3 Pyramidal Neurons in Human Temporal Cortex. *Cereb. Cortex* 27, 5398–5414.
- Dejanovic, B., Semtner, M., Ebert, S., Lamkemeyer, T., Neuser, F., Lüscher, B., Meier, J.C., and Schwarz, G. (2014). Palmitoylation of Gephyrin Controls Receptor Clustering and Plasticity of GABAergic Synapses. *PLoS Biol.* 12, 1–16.
- Denk, W., and Svoboda, K. (1997). Photon upmanship: Why multiphoton imaging is more than a gimmick. *Neuron* 18, 351–357.
- Dennis, M.Y., and Eichler, E.E. (2016). Human adaptation and evolution by segmental duplication. *Curr. Opin. Genet. Dev.* 41, 44–52.
- Dennis, M.Y., Nuttle, X., Sudmant, P.H., Antonacci, F., Graves, T.A., Nefedov, M., Rosenfeld, J.A., Sajjadian, S., Malig, M., Kotkiewicz, H., et al. (2012). Evolution of human-specific neural SRGAP2 genes by incomplete segmental duplication. *Cell* 149, 912–922.
- Dennis, M.Y., Harshman, L., Nelson, B.J., Penn, O., Cantsilieris, S., Huddleston, J., Antonacci, F., Penewit, K., Denman, L., Raja, A., et al. (2017). The evolution and population diversity of human-specific segmental duplications. *Nat. Ecol. Evol.* 1, 1–10.
- Desai, R., Sarpal, R., Ishiyama, N., Pellikka, M., Ikura, M., and Tepass, U. (2013). Monomeric α -catenin links cadherin to the actin cytoskeleton. *Nat. Cell Biol.* 15, 261–273.
- Diering, G.H., and Hugarir, R.L. (2018). The AMPA Receptor Code of Synaptic Plasticity. *Neuron* 100, 314–329.
- Duan, X., Krishnaswamy, A., Laboulaye, M.A., Liu, J., Peng, Y.R., Yamagata, M., Toma, K., and Sanes, J.R. (2018). Cadherin Combinations Recruit Dendrites of Distinct Retinal Neurons to a Shared Interneuronal Scaffold. *Neuron* 99, 1145–1154.e6.
- Elste, A.M., and Benson, D.L. (2006). Structural basis for developmentally regulated changes in cadherin function at synapses. *J. Comp. Neurol.* 495, 324–335.
- Elston, G.N., Benavides-Piccione, R., and DeFelipe, J. (2001). The pyramidal cell in cognition: a comparative study in human and monkey. *J. Neurosci.* 21, 1–5.
- Emes, R.D., and Grant, S.G.N. (2012). Evolution of synapse complexity and diversity. *Annu. Rev. Neurosci.* 35, 111–131.
- Erzurumlu, R.S., and Gaspar, P. (2012). Development and critical period plasticity of the barrel cortex. *Eur. J. Neurosci.* 35, 1540–1553.
- Eyal, G., Verhoog, M.B., Testa-Silva, G., Deitcher, Y., Lodder, J.C., Benavides-Piccione, R., Morales, J., Defelipe, J., de Kock, C.P.J., Mansvelder, H.D., et al. (2016). Unique membrane properties and enhanced signal processing in human neocortical neurons. *Elife* 5, 1–18.
- Farhy-Tselnicker, I., and Allen, N.J. (2018). Astrocytes, neurons, synapses: A tripartite view on cortical circuit development. *Neural Dev.* 13, 1–12.
- Farrant, M., and Nusser, Z. (2005). Variations on an inhibitory theme: Phasic and tonic activation of GABA A receptors. *Nat. Rev. Neurosci.* 6, 215–229.
- Favuzzi, E., and Rico, B. (2018). Molecular diversity underlying cortical excitatory and inhibitory synapse development. *Curr. Opin. Neurobiol.* 53, 8–15.
- Favuzzi, E., Deogracias, R., Marques-Smith, A., Maeso, P., Jezequel, J., Exposito-Alonso, D., Balia, M., Kroon, T., Hinojosa, A.J., Maraver, E.F., et al. (2019). Neurodevelopment: Distinct molecular programs regulate synapse specificity in cortical inhibitory circuits. *Science* (80-.). 363, 413–417.
- Feng, Z., Chen, X., Zeng, M., and Zhang, M. (2019). Phase separation as a mechanism for assembling dynamic postsynaptic density signalling complexes. *Curr. Opin. Neurobiol.* 57, 1–8.
- Fishell, G., and Kepecs, A. (2020). Interneuron Types as Attractors and Controllers. *Annu. Rev. Neurosci.* 43, 1–30.
- Forrest, M.P., Parnell, E., and Penzes, P. (2018). Dendritic structural plasticity and neuropsychiatric disease. *Nat. Rev. Neurosci.* 19, 215–234.
- Fortna, A., Kim, Y., MacLaren, E., Marshall, K., Hahn, G., Meltesen, L., Brenton, M., Hink, R., Burgers, S., Hernandez-Boussard, T., et al. (2004). Lineage-specific gene duplication and loss in human and great ape evolution. *PLoS Biol.* 2, 937–954.
- Fossati, M., and Charrier, C. (2021). Trans-synaptic interactions of ionotropic glutamate receptors. *Curr. Opin. Neurobiol.* 66, 85–92.
- Fossati, M., Pizzarelli, R., Schmidt, E.R., Kupferman, J. V., Stroebel, D., Polleux, F., and Charrier, C. (2016). SRGAP2 and Its Human-Specific Paralog Co-Regulate the Development of Excitatory and Inhibitory Synapses. *Neuron* 91, 356–369.
- Fossati, M., Assendorp, N., Gemin, O., Colasse, S., Dingli, F., Arras, G., Loew, D., and Charrier, C. (2019). Trans-Synaptic Signaling through the Glutamate Receptor Delta-1 Mediates Inhibitory Synapse Formation in Cortical Pyramidal Neurons. *Neuron* 104, 1081–1094.e7.

- Foster, M., and C.S Sherrington (1897). A textbook of physiology, part three: The central nervous system (MacMillan & Co Ltd, London).
- Fox, K., and Wong, R.O.L. (2005). A comparison of experience-dependent plasticity in the visual and somatosensory systems. *Neuron* 48, 465–477.
- Frankland, P.W., and Bontempi, B. (2005). The organization of recent and remote memories. *Nat. Rev. Neurosci.* 6, 119–130.
- Friedman, L.G., Benson, D.L., and Huntley, G.W. (2015). Cadherin-based transsynaptic networks in establishing and modifying neural connectivity. *Curr. Top. Dev. Biol.* 112, 415–465.
- Fritschy, J.M., Panzanelli, P., and Tyagarajan, S.K. (2012). Molecular and functional heterogeneity of GABAergic synapses. *Cell. Mol. Life Sci.* 69, 2485–2499.
- Fromme, R.C. (2015). Plasticity of cortical excitatory-inhibitory balance. *Annu. Rev. Neurosci.* 38, 195–219.
- Fu, Y., and Huang, Z.J. (2010). Differential dynamics and activity-dependent regulation of α - and β -neurexins at developing GABAergic synapses. *Proc. Natl. Acad. Sci. U. S. A.* 107, 22699–22704.
- Gamache, T.R., Araki, Y., and Huganir, R.L. (2020). Twenty years of synap research: From synapses to cognition. *J. Neurosci.* 40, 1596–1605.
- Gangwar, S.P., Zhong, X., Seshadrinathan, S., Chen, H., Machius, M., and Rudenko, G. (2017). Molecular Mechanism of MDGA1: Regulation of Neuroligin 2:Neurexin Trans-synaptic Bridges. *Neuron* 94, 1132–1141.e4.
- Ge, W.P., Miyawaki, A., Gage, F.H., Jan, Y.N., and Jan, L.Y. (2012). Local generation of glia is a major astrocyte source in postnatal cortex. *Nature* 484, 376–380.
- Gemin, O., Serna, P., Zamith, J., Assendorp, N., Fossati, M., Rostaing, P., Triller, A., and Charrier, C. (2021). Unique properties of dually innervated dendritic spines in pyramidal neurons of the somatosensory cortex uncovered by 3D correlative light and electron microscopy.
- Gerron, K., Romorini, S., Nabi, S.M., Colicos, M.A., Sala, C., and El-Husseini, A. (2006). A preformed complex of postsynaptic proteins is involved in excitatory synapse development. *Neuron* 49, 547–562.
- Gidon, A., Zolnik, T.A., Fidzinski, P., Bolduan, F., Papoutsis, A., Poirazi, P., Holtkamp, M., Vida, I., and Larkum, M.E. (2020). Dendritic action potentials and computation in human layer 2/3 cortical neurons. *Science* (80-.). 367, 83–87.
- Giesemann, T., Schwarz, G., Nawrotzki, R., Berhörster, K., Rothkegel, M., Schlüter, K., Schrader, N., Schindelin, H., Mendel, R.R., Kirsch, J., et al. (2003). Complex formation between the postsynaptic scaffolding protein gephyrin, profilin, and Mena: A possible link to the microfilament system. *J. Neurosci.* 23, 8330–8339.
- Gilmore, E.G., and Herrup, K. (1997). Cortical development: Layers of complexity. *Curr. Biol.* 7, 231–234.
- Gomez, A.M., Traunmüller, L., and Scheiffele, P. (2021). Neurexins: molecular codes for shaping neuronal synapses. *Nat. Rev. Neurosci.* 22, 137–151.
- Gonzalez-Lozano, M.A., Klemmer, P., Gebuis, T., Hassan, C., Van Nierop, P., Van Kesteren, R.E., Smit, A.B., and Li, K.W. (2016). Dynamics of the mouse brain cortical synaptic proteome during postnatal brain development. *Sci. Rep.* 6, 1–15.
- Götz, M., Hartfuss, E., and Malatesta, P. (2002). Radial glial cells as neuronal precursors: A new perspective on the correlation of morphology and lineage restriction in the developing cerebral cortex of mice. *Brain Res. Bull.* 57, 777–788.
- Graf, E.R., Zhang, X., Jin, S.X., Linhoff, M.W., and Craig, A.M. (2004). Neurexins induce differentiation of GABA and glutamate postsynaptic specializations via neuroligins. *Cell* 119, 1013–1026.
- Grant, S.G.N. (2016). The molecular evolution of the vertebrate behavioural repertoire individual behavioural responses was articulated in the nineteenth century. *Philos. Trans. R. Soc. B Biol. Sci.* 371, 0–8.
- Grant, S.G.N., and Fransén, E. (2020). The Synapse Diversity Dilemma: Molecular Heterogeneity Confounds Studies of Synapse Function. *Front. Synaptic Neurosci.* 12, 1–8.
- Gray, E. (1959). Electron Microscopy of Synaptic Contacts on Dendrite Spines of the Cerebral Cortex. *Nature* 183, 1592–1593.
- Gray, J.A., Shi, Y., Usui, H., During, M.J., Sakimura, K., and Nicoll, R.A. (2011). Distinct Modes of AMPA Receptor Suppression at Developing Synapses by GluN2A and GluN2B: Single-Cell NMDA Receptor Subunit Deletion In Vivo. *Neuron* 71, 1085–1101.
- Greig, L.C., Woodworth, M.B., Galazo, M.J., Padmanabhan, H., and Macklis, J.D. (2013). Molecular logic of neocortical projection neuron specification, development and diversity. *Nat. Rev. Neurosci.* 14, 755–769.
- Groeneweg, F.L., Trättnig, C., Kuhse, J., Nawrotzki, R.A., and Kirsch, J. (2018). Gephyrin: a key regulatory protein of inhibitory synapses and beyond. *Histochem. Cell Biol.* 150, 489–508.
- Grutzendler, J., Kasthuri, N., and Gan, W.B. (2002). Long-term dendritic spine stability in the adult cortex. *Nature* 420, 812–816.

- Guerrier, S., Coutinho-Budd, J., Sassa, T., Gresset, A., Jordan, N.V., Chen, K., Jin, W.L., Frost, A., and Polleux, F. (2009). The F-BAR Domain of srGAP2 Induces Membrane Protrusions Required for Neuronal Migration and Morphogenesis. *Cell* 138, 990–1004.
- Guez-Haddad, J., Sporny, M., Sasson, Y., Gevorkyan-Airapetov, L., Lahav-Mankovski, N., Margulies, D., Radzimanowski, J., and Opatowsky, Y. (2015). The Neuronal Migration Factor srGAP2 Achieves Specificity in Ligand Binding through a Two-Component Molecular Mechanism. *Structure* 23, 1989–2000.
- Gul, I.S., Hulpiau, P., Saeys, Y., and van Roy, F. (2017). Evolution and diversity of cadherins and catenins. *Exp. Cell Res.* 358, 3–9.
- Haas, K.T., Compans, B., Letellier, M., Bartol, T.M., Grillo-Bosch, D., Sejnowski, T.J., Sainlos, M., Choquet, D., Thoumine, O., and Hosy, E. (2018). Pre-post synaptic alignment through neuroligin-1 tunes synaptic transmission efficiency. *Elife* 7, 1–22.
- Hall, B.J., Ripley, B., and Ghosh, A. (2007). NR2B signaling regulates the development of synaptic AMPA receptor current. *J. Neurosci.* 27, 13446–13456.
- Han, S.P., and Yap, A.S. (2013). An α -catenin déjà vu. *Nat. Cell Biol.* 15, 238–239.
- Han, W., Shepard, R.D., and Lu, W. (2021). Regulation of GABAARs by Transmembrane Accessory Proteins. *Trends Neurosci.* 44, 152–165.
- Han, Y., Kaeser, P.S., Südhof, T.C., and Schneggenburger, R. (2011). RIM determines Ca²⁺ channel density and vesicle docking at the presynaptic active zone. *Neuron* 69, 304–316.
- Hanse, E., Seth, H., and Riebe, I. (2013). AMPA-silent synapses in brain development and pathology. *Nat. Rev. Neurosci.* 14, 839–850.
- Harnett, M.T., Makara, J.K., Spruston, N., Kath, W.L., and Magee, J.C. (2012). Synaptic amplification by dendritic spines enhances input cooperativity. *Nature* 491, 599–602.
- Harris, K.D., and Shepherd, G.M.G. (2015). The neocortical circuit: Themes and variations. *Nat. Neurosci.* 18, 170–181.
- Harris, K.M., and Stevens, J.K. (1989). Dendritic spines of CA1 pyramidal cells in the rat hippocampus: Serial electron microscopy with reference to their biophysical characteristics. *J. Neurosci.* 9, 2982–2997.
- Harris, K.M., and Weinberg, R.J. (2012). Ultrastructure of synapses in the mammalian brain. *Cold Spring Harb. Perspect. Biol.* 4, 7.
- Hassani Nia, F., Woike, D., Martens, V., Klüssendorf, M., Hönck, H.H., Harder, S., and Kreienkamp, H.J. (2020). Targeting of δ -catenin to postsynaptic sites through interaction with the Shank3 N-terminus. *Mol. Autism* 11, 1–17.
- Henley, J.M., and Wilkinson, K.A. (2016). Synaptic AMPA receptor composition in development, plasticity and disease. *Nat. Rev. Neurosci.* 17, 337–350.
- Hensch, T.K. (2005). Critical period plasticity in local cortical circuits. *Nat. Rev. Neurosci.* 6, 877–888.
- Herring, B.E., and Nicoll, R.A. (2016). Long-Term Potentiation: From CaMKII to AMPA Receptor Trafficking. *Annu. Rev. Physiol.* 78, 351–365.
- Hibino, H., Pironkova, R., Onumere, O., Vologodskaia, M., Hudspeth, A.J., and Lesage, F. (2002). RIM binding proteins (RBPs) couple Rab3-interacting molecules (RIMs) to voltage-gated Ca²⁺ channels. *Neuron* 34, 411–423.
- Hirai, H., Pang, Z., Bao, D., Miyazaki, T., Li, L., Miura, E., Parris, J., Rong, Y., Watanabe, M., Yuzaki, M., et al. (2005). Cbln1 is essential for synaptic integrity and plasticity in the cerebellum. *Nat. Neurosci.* 8, 1534–1541.
- Hirano, S., and Takeichi, M. (2012). Cadherins in brain morphogenesis and wiring. *Physiol. Rev.* 92, 597–634.
- Hirohashi, S. (1998). Inactivation of the E-cadherin-mediated cell adhesion system in human cancers. *Am. J. Pathol.* 153, 333–339.
- Ho, C., Zhou, J., Medina, M., Goto, T., Jacobson, M., Bhide, P.G., and Kosik, K.S. (2000). δ -Catenin is a nervous system-specific adherens junction protein which undergoes dynamic relocalization during development. *J. Comp. Neurol.* 420, 261–276.
- Holler, S., Köstinger, G., Martin, K.A.C., Schuhknecht, G.F.P., and Stratford, K.J. (2021). Structure and function of a neocortical synapse. *Nature* 591, 111–116.
- Holt, C.E., Martin, K.C., and Schuman, E.M. (2019). Local translation in neurons: visualization and function. *Nat. Struct. Mol. Biol.* 26, 557–566.
- Holtmaat, A., and Svoboda, K. (2009). Experience-dependent structural synaptic plasticity in the mammalian brain. *Nat. Rev. Neurosci.* 10, 647–658.
- Hotulainen, P., and Saarikangas, J. (2016). The initiation of post-synaptic protrusions. *Commun. Integr. Biol.* 9.
- Hruska, M., and Dalva, M.B. (2012). Ephrin regulation of synapse formation, function and plasticity. *Mol. Cell. Neurosci.* 50, 35–44.
- Huang, Z.J., and Paul, A. (2019). The diversity of GABAergic neurons and neural communication elements. *Nat. Rev. Neurosci.* 20, 563–572.

- Huntley, G.W., Elste, A.M., Patil, S.B., Bozdagi, O., Benson, D.L., and Steward, O. (2012). Synaptic loss and retention of different classic cadherins with LTP-associated synaptic structural remodeling in vivo. *Hippocampus* 22, 17–28.
- Hurles, M. (2004). Gene duplication: The genomic trade in spare parts. *PLoS Biol.* 2.
- Huttenlocher, P.R. (1979). Synaptic density in human frontal cortex - developmental changes and effects of aging. *Brain Res.* 163, 195–205.
- Ide, N., Hata, Y., Deguchi, M., Hirao, K., Yao, I., and Takai, Y. (1999). Interaction of S-SCAM with neural plakophilin-related armadillo-repeat protein/ δ -catenin. *Biochem. Biophys. Res. Commun.* 256, 456–461.
- Ishiyama, N., and Ikura, M. (2012). The three-dimensional structure of the cadherin-catenin complex. In *Sub-Cellular Biochemistry*, pp. 39–62.
- Ishiyama, N., Lee, S.-H., Liu, S., Li, G.-Y., Smith, M.J., Reichardt, L.F., and Ikura, M. (2010). Dynamic and Static Interactions between p120 Catenin and E-Cadherin Regulate the Stability of Cell-Cell Adhesion. *Cell* 141, 117–128.
- Israely, I., Costa, R.M., Xie, C.W., Silva, A.J., Kosik, K.S., and Liu, X. (2004). Deletion of the Neuron-Specific Protein Delta-Catenin Leads to Severe Cognitive and Synaptic Dysfunction. *Curr. Biol.* 14, 1657–1663.
- Iwata, R., and Vanderhaeghen, P. (2020). Tempus fugit: How time flies during development. *Science* (80-.). 369, 1431–1432.
- Jabaudon, D. (2017). Fate and freedom in developing neocortical circuits. *Nat. Commun.* 8.
- Jahn, R., and Fasshauer, D. (2012). Molecular machines governing exocytosis of synaptic vesicles. *Nature* 490, 201–207.
- Jang, S., Lee, H., and Kim, E. (2017). Synaptic adhesion molecules and excitatory synaptic transmission. *Curr. Opin. Neurobiol.* 45, 45–50.
- Janovjak, H., Sandoz, G., and Isacoff, E.Y. (2011). A modern ionotropic glutamate receptor with a K⁺ selectivity signature sequence. *Nat. Commun.* 2.
- Ji, Y., Pang, P.T., Feng, L., and Lu, B. (2005). Cyclic AMP controls BDNF-induced TrkB phosphorylation and dendritic spine formation in mature hippocampal neurons. *Nat. Neurosci.* 8, 164–172.
- Jones, S.B., Lanford, G.W., Chen, Y.H., Moribito, M., Kim, K., and Lu, Q. (2002). Glutamate-induced δ -catenin redistribution and dissociation from postsynaptic receptor complexes. *Neuroscience* 115, 1009–1021.
- Kaesler, P.S., and Regehr, W.G. (2017). The readily releasable pool of synaptic vesicles. *Curr. Opin. Neurobiol.* 43, 63–70.
- Kakegawa, W., Mitakidis, N., Miura, E., Abe, M., Matsuda, K., Takeo, Y.H., Kohda, K., Motohashi, J., Takahashi, A., Nagao, S., et al. (2015). Anterograde C1ql1 signaling is required in order to determine and maintain a single-winner climbing fiber in the mouse cerebellum. *Neuron* 85, 316–329.
- Kalmbach, B.E., Buchin, A., Long, B., Close, J., Nandi, A., Miller, J.A., Bakken, T.E., Hodge, R.D., Chong, P., de Frates, R., et al. (2018). h-Channels Contribute to Divergent Intrinsic Membrane Properties of Supragranular Pyramidal Neurons in Human versus Mouse Cerebral Cortex. *Neuron* 100, 1194–1208.e5.
- Kano, M., and Hashimoto, K. (2009). Synapse elimination in the central nervous system. *Curr. Opin. Neurobiol.* 19, 154–161.
- Kasai, H., Fukuda, M., Watanabe, S., Hayashi-Takagi, A., and Noguchi, J. (2010). Structural dynamics of dendritic spines in memory and cognition. *Trends Neurosci.* 33, 121–129.
- Kaszak, I., Witkowska-Piłaszewicz, O., Niewiadomska, Z., Dworecka-Kaszak, B., Toka, F.N., and Jurka, P. (2020). Role of cadherins in cancer—a review. *Int. J. Mol. Sci.* 21, 1–17.
- Kilinc, M., Creson, T., Rojas, C., Aceti, M., Ellegood, J., Vaissiere, T., Lerch, J.P., and Rumbaugh, G. (2018). Molecular and Cellular Neuroscience Species-conserved SYNGAP1 phenotypes associated with neurodevelopmental disorders. *Mol. Cell. Neurosci.* 91, 140–150.
- Kim, E., and Sheng, M. (2004). PDZ domain proteins of synapses. *Nat. Rev. Neurosci.* 5, 771–781.
- Kim, H.Y., Um, J.W., and Ko, J. (2021). Proper synaptic adhesion signaling in the control of neural circuit architecture and brain function. *Prog. Neurobiol.* 200, 101983.
- Kim, J.S., Bareiss, S., Kim, K.K., Tatum, R., Han, J.R., Jin, Y.H., Kim, H., Lu, Q., and Kim, K. (2006). Presenilin-1 inhibits δ -catenin-induced cellular branching and promotes δ -catenin processing and turnover. *Biochem. Biophys. Res. Commun.* 351, 903–908.
- Kins, S., Betz, H., and Kirsch, J. (2000). Collybistin, a newly identified brain-specific GEF, induces submembrane clustering of gephyrin. *Nat. Neurosci.* 3, 22–29.
- Klingler, E., Francis, F., Jabaudon, D., and Cappello, S. (2021). Mapping the molecular and cellular complexity of cortical malformations. *Science* (80-.). 371.
- Kneussel, M., and Betz, H. (2000). Receptors, gephyrin and gephyrin-associated proteins: Novel insights into the assembly of inhibitory postsynaptic membrane specializations. *J. Physiol.* 525, 1–9.

- Knott, G.W., Holtmaat, A., Wilbrecht, L., Welker, E., and Svoboda, K. (2006). Spine growth precedes synapse formation in the adult neocortex in vivo. *Nat. Neurosci.* 9, 1117–1124.
- Koopmans, F., van Nierop, P., Andres-Alonso, M., Byrnes, A., Cijssouw, T., Coba, M.P., Cornelisse, L.N., Farrell, R.J., Goldschmidt, H.L., Howrigan, D.P., et al. (2019). SynGO: An Evidence-Based, Expert-Curated Knowledge Base for the Synapse. *Neuron* 103, 217–234.e4.
- Kourtidis, A., Ngok, S.P., and Anastasiadis, P.Z. (2013). P120 catenin: An essential regulator of cadherin stability, adhesion-induced signaling, and cancer progression. *Prog. Mol. Biol. Transl. Sci.* 116, 409–432.
- Kourtidis, A., Lu, R., Pence, L.J., and Anastasiadis, P.Z. (2017). A central role for cadherin signaling in cancer. *Exp. Cell Res.* 358, 78–85.
- Kriegstein, A., and Alvarez-Buylla, A. (2009). The glial nature of embryonic and adult neural stem cells. *Annu. Rev. Neurosci.* 32, 149–184.
- Krol, A., and Feng, G. (2018). Windows of opportunity: timing in neurodevelopmental disorders. *Curr. Opin. Neurobiol.* 48, 59–63.
- Krueger-Burg, D., Papadopoulos, T., and Brose, N. (2017). Organizers of inhibitory synapses come of age. *Curr. Opin. Neurobiol.* 45, 66–77.
- Kubota, Y., Hatada, S., Kondo, S., Karube, F., and Kawaguchi, Y. (2007). Neocortical inhibitory terminals innervate dendritic spines targeted by thalamocortical afferents. *J. Neurosci.* 27, 1139–1150.
- Kumar, S.S., Bacci, A., Kharazia, V., and Huguenard, J.R. (2002). A developmental switch of AMPA receptor subunits in neocortical pyramidal neurons. *J. Neurosci.* 22, 3005–3015.
- Kwon, H.B., and Sabatini, B.L. (2011). Glutamate induces de novo growth of functional spines in developing cortex. *Nature* 474, 100–104.
- Lagache, T., Grassart, A., Dallongeville, S., Faklaris, O., Sauvonnet, N., Dufour, A., Danglot, L., and Olivo-Marin, J.-C. (2018). Mapping molecular assemblies with fluorescence microscopy and object-based spatial statistics. *Nat. Commun.* 9, 698.
- Lambert, J.T., Hill, T.C., Park, D.K., Culp, J.H., and Zito, K. (2017). Protracted and asynchronous accumulation of PSD95-family MAGUKs during maturation of nascent dendritic spines. *Dev. Neurobiol.* 77, 1161–1174.
- Laura, R.P., Witt, A.S., Held, H.A., Gerstner, R., Deshayes, K., Koehler, M.F.T., Kosik, K.S., Sidhu, S.S., and Lasky, L.A. (2002). The Erbin PDZ domain binds with high affinity and specificity to the carboxyl termini of δ -catenin and ARVCF. *J. Biol. Chem.* 277, 12906–12914.
- Laurie, D.J., Wisden, W., and Seeburg, P.H. (1992). The distribution of thirteen GABA(A) receptor subunit mRNAs in the rat brain. III. Embryonic and postnatal development. *J. Neurosci.* 12, 4151–4172.
- Lefebvre, J.L., Kostadinov, D., Chen, W. V., Maniatis, T., and Sanes, J.R. (2012). Protocadherins mediate dendritic self-avoidance in the mammalian nervous system. *Nature* 488, 517–521.
- Lewis, A.S., Schwartz, E., Chan, C.S., Noam, Y., Shin, M., Wadman, W.J., Surmeier, D.J., Baram, T.Z., Macdonald, R.L., and Chetkovich, D.M. (2009). Alternatively spliced isoforms of TRIP8b differentially control h channel trafficking and function. *J. Neurosci.* 29, 6250–6265.
- Li, J., Han, S., Li, H., Udeshi, N.D., Svinkina, T., Mani, D.R., Xu, C., Guajardo, R., Xie, Q., Li, T., et al. (2020). Cell-Surface Proteomic Profiling in the Fly Brain Uncovers Wiring Regulators. *Cell* 180, 373–386.e15.
- Li, M., Cui, Z., Niu, Y., Liu, B., Fan, W., Yu, D., and Deng, J. (2010). Synaptogenesis in the developing mouse visual cortex. *Brain Res. Bull.* 81, 107–113.
- Li, M.Y., Miao, W.Y., Wu, Q.Z., He, S.J., Yan, G., Yang, Y., Liu, J.J., Taketo, M.M., and Yu, X. (2017). A Critical Role of Presynaptic Cadherin/Catenin/p140Cap Complexes in Stabilizing Spines and Functional Synapses in the Neocortex. *Neuron* 94, 1155–1172.e8.
- Libé-Philippot, B., and Vanderhaeghen, P. (2021). Cellular and Molecular Mechanisms Linking Human Cortical Development and Evolution. *Annu. Rev. Genet.* 55, 1–27.
- Linaro, D., Vermaercke, B., Iwata, R., Ramaswamy, A., Libé-Philippot, B., Boubakar, L., Davis, B.A., Wierda, K., Davie, K., Poovathingal, S., et al. (2019). Xenotransplanted Human Cortical Neurons Reveal Species-Specific Development and Functional Integration into Mouse Visual Circuits. *Neuron* 104, 972–986.e6.
- Liu, X., Somel, M., Tang, L., Yan, Z., Jiang, X., Guo, S., Yuan, Y., He, L., Oleksiak, A., Zhang, Y., et al. (2012). Extension of cortical synaptic development distinguishes humans from chimpanzees and macaques. *Genome Res.* 22, 611–622.
- López-Bendito, G., and Molnár, Z. (2003). Thalamocortical development: How are we going to get there? *Nat. Rev. Neurosci.* 4, 276–289.
- Lourenço, J., and Bacci, A. (2017). Human-Specific Cortical Synaptic Connections and Their Plasticity: Is That What Makes Us Human? *PLoS Biol.* 15, 1–5.

- Lu, Q., Aguilar, B.J., Li, M., Jiang, Y., and Chen, Y.-H. (2016). Genetic alterations of δ -catenin/NPRAP/Neurojuncin (CTNND2): functional implications in complex human diseases. *Hum. Genet.* 135, 1107–1116.
- Lučić, V., Förster, F., and Baumeister, W. (2005). Structural studies by electron tomography: From cells to molecules. *Annu. Rev. Biochem.* 74, 833–865.
- Luo, F., Sclip, A., Jiang, M., and Südhof, T.C. (2020). Neurexins cluster Ca²⁺ channels within the presynaptic active zone. *EMBO J.* 39, 1–14.
- MacGillavry, H.D., Song, Y., Raghavachari, S., and Blanpied, T.A. (2013). Nanoscale scaffolding domains within the postsynaptic density concentrate synaptic ampa receptors. *Neuron* 78, 615–622.
- Mansvelder, H.D., Verhoog, M.B., and Goriounova, N.A. (2019). Synaptic plasticity in human cortical circuits: cellular mechanisms of learning and memory in the human brain? *Curr. Opin. Neurobiol.* 54, 186–193.
- Marín, O. (2016). Developmental timing and critical windows for the treatment of psychiatric disorders. *Nat. Med.* 22, 1229–1238.
- Martin, L.J., Furuta, A., and Blackstone, C.D. (1998). AMPA receptor protein in developing rat brain: Glutamate receptor-1 expression and localization change at regional, cellular, and subcellular levels with maturation. *Neuroscience* 83, 917–928.
- Matsuda, K., Miura, E., Miyazaki, T., Kakegawa, W., Emi, K., Narumi, S., Fukazawa, Y., Ito-Ishida, A., Kondo, T., Shigemoto, R., et al. (2010). Cbln1 is a ligand for an orphan glutamate receptor $\delta 2$, a bidirectional synapse organizer. *Science* (80-.). 328, 363–368.
- Matter, C., Pribadi, M., Liu, X., and Trachtenberg, J.T. (2009). δ -Catenin Is Required for the Maintenance of Neural Structure and Function in Mature Cortex In Vivo. *Neuron* 64, 320–327.
- Mattila, P.K., Pykäläinen, A., Saarikangas, J., Paavilainen, V.O., Vihinen, H., Jokitalo, E., and Lappalainen, P. (2007). Missing-in-metastasis and IRSp53 deform PI(4,5)P₂-rich membranes by an inverse BAR domain-like mechanism. *J. Cell Biol.* 176, 953–964.
- McCrea, P.D., and Gottardi, C.J. (2016). Beyond β -catenin: Prospects for a larger catenin network in the nucleus. *Nat. Rev. Mol. Cell Biol.* 17, 55–64.
- McCrea, P.D., and Park, J. il (2007). Developmental functions of the P120-catenin sub-family. *Biochim. Biophys. Acta - Mol. Cell Res.* 1773, 17–33.
- Medina, M., Marinescu, R.C., Overhauser, J., and Kosik, K.S. (2000). Hemizygoty of δ -catenin (CTNND2) is associated with severe mental retardation in cri-du-chat syndrome. *Genomics* 63, 157–164.
- Mendez, P., De Roo, M., Poglia, L., Klauser, P., and Muller, D. (2010). N-cadherin mediates plasticity-induced long-term spine stabilization. *J. Cell Biol.* 189, 589–600.
- Mendonsa, A.M., Na, T.Y., and Gumbiner, B.M. (2018). E-cadherin in contact inhibition and cancer. *Oncogene* 37, 4769–4780.
- Merrill, M.A., Chen, Y., Strack, S., and Hell, J.W. (2005). Activity-driven postsynaptic translocation of CaMKII. *Trends Pharmacol. Sci.* 26, 645–653.
- Meyer-Dilhet, G., and Courchet, J. (2020). In Utero Cortical Electroporation of Plasmids in the Mouse Embryo. *STAR Protoc.* 1, 100027.
- Michaelson, S.D., Ozkan, E.D., Aceti, M., Maity, S., Llamas, N., Weldon, M., Mizrahi, E., Vaissiere, T., Gaffield, M.A., Christie, J.M., et al. (2018). SYNGAP1 heterozygosity disrupts sensory processing by reducing touch-related activity within somatosensory cortex circuits. *Nat. Neurosci.* 21.
- Milovanovic, D., and De Camilli, P. (2017). Synaptic Vesicle Clusters at Synapses: A Distinct Liquid Phase? *Neuron* 93, 995–1002.
- Mohan, H., Verhoog, M.B., Doreswamy, K.K., Eyal, G., Aardse, R., Lodder, B.N., Goriounova, N.A., Asamoah, B., Brakspear, A.B.C., Groot, C., et al. (2015). Dendritic and axonal architecture of individual pyramidal neurons across layers of adult human neocortex. *Cereb. Cortex* 25, 4839–4853.
- Monea, S., Jordan, B.A., Srivastava, S., DeSouza, S., and Ziff, E.B. (2006). Membrane localization of membrane type 5 matrix metalloproteinase by AMPA receptor binding protein and cleavage of cadherins. *J. Neurosci.* 26, 2300–2312.
- Moon, I.S., Sakagami, H., Nakayama, J., and Suzuki, T. (2008). Differential distribution of synGAP α 1 and synGAP β isoforms in rat neurons. *Brain Res.* 1241, 62–75.
- Moss, S.J., and Smart, T.G. (2001). Constructing inhibitory synapses. *Nat. Rev. Neurosci.* 2, 240–250.
- Mossink, B., van Rhijn, J.R., Wang, S., Linda, K., Vitale, M.R., Zöller, J.E.M., van Hugte, E.J.H., Bak, J., Verboven, A.H.A., Selten, M., et al. (2021). Cadherin-13 is a critical regulator of GABAergic modulation in human stem-cell-derived neuronal networks. *Mol. Psychiatry*.
- Mullins, C., Fishell, G., and Tsien, R.W. (2016). Unifying Views of Autism Spectrum Disorders: A Consideration of Autoregulatory Feedback Loops. *Neuron* 89, 1131–1156.
- Murase, S., Mosser, E., and Schuman, E.M. (2002). Depolarization drives β -catenin into neuronal spines promoting changes in synaptic structure and function. *Neuron* 35, 91–105.

- Nelson, S.B., and Valakh, V. (2015). Excitatory/Inhibitory Balance and Circuit Homeostasis in Autism Spectrum Disorders. *Neuron* 87, 684–698.
- Nikitczuk, J.S., Patil, S.B., Matikainen-Ankney, B.A., Scarpa, J., Shapiro, M.L., Benson, D.L., and Huntley, G.W. (2014). N-cadherin regulates molecular organization of excitatory and inhibitory synaptic circuits in adult hippocampus in vivo. *Hippocampus* 24, 943–962.
- Nishimura, W., Yao, I., Iida, J., Tanaka, N., and Hata, Y. (2002). Interaction of Synaptic Scaffolding Molecule and β -Catenin. *Neuron* 22, 757–765.
- Nithianantharajah, J., Komiyama, N.H., McKechnie, A., Johnstone, M., Blackwood, D.H., Clair, D.S., Emes, R.D., Van De Lagemaat, L.N., Saksida, L.M., Bussey, T.J., et al. (2013). Synaptic scaffold evolution generated components of vertebrate cognitive complexity. *Nat. Neurosci.* 16, 16–24.
- Niwa, F., Patrizio, A., Triller, A., and Specht, C.G. (2019). cAMP-EPAC-Dependent Regulation of Gephyrin Phosphorylation and GABAAR Trapping at Inhibitory Synapses. *IScience* 22, 453–465.
- Noctor, S.C., Martínez-Cerdeño, V., and Kriegstein, A.R. (2008). Distinct behaviors of neural stem and progenitor cells underlie cortical neurogenesis. *J. Comp. Neurol.* 508, 28–44.
- Nusser, Z. (2018). Creating diverse synapses from the same molecules. *Curr. Opin. Neurobiol.* 51, 8–15.
- Nusser, Z., Cull-Candy, S., and Farrant, M. (1997). Differences in synaptic GABA(A) receptor number underlie variation in GABA mini amplitude. *Neuron* 19, 697–709.
- Oberlaender, M., De Kock, C.P.J., Bruno, R.M., Ramirez, A., Meyer, H.S., Dercksen, V.J., Helmstaedter, M., and Sakmann, B. (2012a). Cell type-specific three-dimensional structure of thalamocortical circuits in a column of rat vibrissa cortex. *Cereb. Cortex* 22, 2375–2391.
- Oberlaender, M., Ramirez, A., and Bruno, R.M. (2012b). Sensory Experience Restructures Thalamocortical Axons during Adulthood. *Neuron* 74, 648–655.
- Oh, W.C., Lutz, S., Castillo, P.E., and Kwon, H.B. (2016). De novo synaptogenesis induced by GABA in the developing mouse cortex. *Science* (80-.). 353, 1037–1040.
- Ohno, S. (1970). *Evolution by Gene Duplication* (Springer-Verlag Berlin Heidelberg GmbH).
- Okabe, S. (2007). Molecular anatomy of the postsynaptic density. *Mol. Cell. Neurosci.* 34, 503–518.
- Okabe, S. (2020). Regulation of actin dynamics in dendritic spines: Nanostructure, molecular mobility, and signaling mechanisms. *Mol. Cell. Neurosci.* 109, 103564.
- Okabe, S., Miwa, A., and Okado, H. (2001). Spine formation and correlated assembly of presynaptic and postsynaptic molecules. *J. Neurosci.* 21, 6105–6114.
- Okada, H., Uezu, A., Mason, F.M., Soderblom, E.J., Moseley, M.A., and Soderling, S.H. (2011). SH3 domain-based phototrapping in living cells reveals rho family GTP signaling complexes. *Sci. Signal.* 4, 1–18.
- Okuda, T., Yu, L.M.Y., Cingolani, L.A., Kemler, R., and Goda, Y. (2007). beta-Catenin regulates excitatory postsynaptic strength at hippocampal synapses. *Proc. Natl. Acad. Sci.* 104, 13479–13484.
- Olivo-Marin, J.C. (2002). Extraction of spots in biological images using multiscale products. *Pattern Recognit.* 35, 1989–1996.
- Opazo, P., Sainlos, M., and Choquet, D. (2012). Regulation of AMPA receptor surface diffusion by PSD-95 slots. *Curr. Opin. Neurobiol.* 22, 453–460.
- Osterhout, J.A., Josten, N., Yamada, J., Pan, F., Wu, S. wen, Nguyen, P.L., Panagiotakos, G., Inoue, Y.U., Egusa, S.F., Volgyi, B., et al. (2011). Cadherin-6 mediates axon-target matching in a non-image-forming visual circuit. *Neuron* 71, 632–639.
- Pagnamenta, A.T., Khan, H., Walker, S., Gerrelli, D., Wing, K., Bonaglia, M.C., Giorda, R., Berney, T., Mani, E., Molteni, M., et al. (2011). Rare familial 16q21 microdeletions under a linkage peak implicate cadherin 8 (CDH8) in susceptibility to autism and learning disability. *J. Med. Genet.* 48, 48–54.
- Palay, S.L. (1956). Synapses in the central nervous system. *J. Biophys. Biochem. Cytol.* 2, 193–201.
- Papadopoulos, T., Korte, M., Eulenburg, V., Kubota, H., Retiounskaja, M., Harvey, R.J., Harvey, K., O'Sullivan, G.A., Laube, B., Hülsmann, S., et al. (2007). Impaired GABAergic transmission and altered hippocampal synaptic plasticity in collybistin-deficient mice. *EMBO J.* 26, 3888–3899.
- Peça, J., Feliciano, C., Ting, J.T., Wang, W., Wells, M.F., Venkatraman, T.N., Lascola, C.D., Fu, Z., and Feng, G. (2011). Shank3 mutant mice display autistic-like behaviours and striatal dysfunction. *Nature* 472, 437–442.
- Van De Peer, Y., Maere, S., and Meyer, A. (2009). The evolutionary significance of ancient genome duplications. *Nat. Rev. Genet.* 10, 725–732.

- Peixoto, R.T., Kunz, P.A., Kwon, H., Mabb, A.M., Sabatini, B.L., Philpot, B.D., and Ehlers, M.D. (2012). Transsynaptic Signaling by Activity-Dependent Cleavage of Neuroligin-1. *Neuron* 76, 396–409.
- Peixoto, R.T., Wang, W., Croney, D.M., Kozorovitskiy, Y., and Sabatini, B.L. (2016). Early hyperactivity and precocious maturation of corticostriatal circuits in Shank3B ^{-/-} mice. *Nat. Neurosci.* 19, 716–724.
- Peixoto, R.T., Chantranupong, L., Hakim, R., Levasseur, J., Wang, W., Merchant, T., Gorman, K., Budnik, B., and Sabatini, B.L. (2019). Abnormal Striatal Development Underlies the Early Onset of Behavioral Deficits in Shank3B^{-/-} Mice. *Cell Rep.* 29, 2016–2027.e4.
- Pennacchietti, F., Vascon, S., Nieuws, T., Rosillo, C., Das, S., Tyagarajan, S.K., Diaspro, A., del Bue, A., Petrini, E.M., Barberis, A., et al. (2017). Nanoscale molecular reorganization of the inhibitory postsynaptic density is a determinant of gabaergic synaptic potentiation. *J. Neurosci.* 37, 1747–1756.
- Perez de Arce, K., Schrod, N., Metzbow, S.W.R., Allgeyer, E., Kong, G.K.W., Tang, A.H., Krupp, A.J., Stein, V., Liu, X., Bewersdorf, J., et al. (2015). Topographic Mapping of the Synaptic Cleft into Adhesive Nanodomains. *Neuron* 88, 1165–1172.
- Petanjek, Z., Judaš, M., Šimić, G., Rašin, M.R., Uylings, H.B.M., Rakic, P., and Kostović, I. (2011). Extraordinary neoteny of synaptic spines in the human prefrontal cortex. *Proc. Natl. Acad. Sci. U. S. A.* 108, 13281–13286.
- Petralia, R.S., Sans, N., Wang, Y.X., and Wenthold, R.J. (2005). Ontogeny of postsynaptic density proteins at glutamatergic synapses. *Mol. Cell. Neurosci.* 29, 436–452.
- Pfeiffer, T., Poll, S., Bancelin, S., Angibaud, J., Inavalli, V.V.G.K., Keppler, K., Mittag, M., Fuhrmann, M., and Nägerl, U.V. (2018). Chronic 2P-STED imaging reveals high turnover of dendritic spines in the hippocampus in vivo. *Elife* 7, 1–17.
- Pizzarelli, R., Griguoli, M., Zacchi, P., Petrini, E.M., Barberis, A., Cattaneo, A., and Cherubini, E. (2020). Tuning GABAergic Inhibition: Gephyrin Molecular Organization and Functions. *Neuroscience* 439, 125–136.
- Popovic, M.A., Carnevale, N., Rozsa, B., and Zecevic, D. (2015). Electrical behaviour of dendritic spines as revealed by voltage imaging. *Nat. Commun.* 6.
- Poullet, P., Carpentier, S., and Barillot, E. (2007). myProMS, a web server for management and validation of mass spectrometry-based proteomic data. *Proteomics* 7, 2553–2556.
- Poulopoulos, A., Aramuni, G., Meyer, G., Soykan, T., Hoon, M., Papadopoulos, T., Zhang, M., Paarmann, I., Fuchs, C., Harvey, K., et al. (2009). Neuroligin 2 Drives Postsynaptic Assembly at Perisomatic Inhibitory Synapses through Gephyrin and Collybistin. *Neuron* 63, 628–642.
- Reddy-Alla, S., Schmitt, B., Birkenfeld, J., Eulenburg, V., Dutertre, S., Böhringer, C., Götz, M., Betz, H., and Papadopoulos, T. (2010). PH-Domain-driven targeting of collybistin but not Cdc42 activation is required for synaptic gephyrin clustering. *Eur. J. Neurosci.* 31, 1173–1184.
- Redies, C. (2000). Cadherins in the central nervous system. *Prog. Neurobiol.* 61, 611–648.
- Redies, C., Hertel, N., and Hübner, C.A. (2012). Cadherins and neuropsychiatric disorders. *Brain Res.* 1470, 130–144.
- Reiner, A., and Levitz, J. (2018). Glutamatergic Signaling in the Central Nervous System: Ionotropic and Metabotropic Receptors in Concert. *Neuron* 98, 1080–1098.
- Restituito, S., Khatir, L., Ninan, I., Mathews, P.M., Liu, X., Weinberg, R.J., and Ziff, E.B. (2011). Synaptic autoregulation by metalloproteases and γ -secretase. *J. Neurosci.* 31, 12083–12093.
- Riccomagno, M.M., and Kolodkin, A.L. (2015). Sculpting Neural Circuits by Axon and Dendrite Pruning. *Annu. Rev. Cell Dev. Biol.* 31, 779–805.
- Van Rootselaar, A.F., Groffen, A.J., Vries, B. De, Callenbach, P.M.C., Santen, G.W.E., Koelewijn, S., Vijfhuizen, L.S., Buijink, A., Tijssen, M.A.J., and Van Den Maagdenberg, A.M.J.M. (2017). δ -Catenin (CTNND2) missense mutation in familial cortical myoclonic tremor and epilepsy. *Neurology* 89, 2341–2350.
- Roux, L., and Buzsáki, G. (2015). Tasks for inhibitory interneurons in intact brain circuits. *Neuropharmacology* 88, 10–23.
- Rudenko, G. (2017). Dynamic control of synaptic adhesion and organizing molecules in synaptic plasticity. *Neural Plast.* 2017.
- Rumbaugh, G., Adams, J.P., Kim, J.H., and Huganir, R.L. (2006). SynGAP regulates synaptic strength and mitogen-activated protein kinases in cultured neurons. *Proc. Natl. Acad. Sci. U. S. A.* 103, 4344–4351.
- Runge, K., Cardoso, C., and de Chevigny, A. (2020). Dendritic Spine Plasticity: Function and Mechanisms. *Front. Synaptic Neurosci.* 12.
- Ryan, T.J., and Grant, S.G.N. (2009). The origin and evolution of synapses. *Nat. Rev. Neurosci.* 10, 701–712.
- Saarikangas, J., Zhao, H., and Lappalainen, P. (2010). Regulation of the actin cytoskeleton-plasma membrane interplay by phosphoinositides. *Physiol. Rev.* 90, 259–289.

- Saarikangas, J., Kourdougli, N., Senju, Y., Chazal, G., Segerstråle, M., Minkeviciene, R., Kuurne, J., Mattila, P.K., Garrett, L., Höltér, S.M., et al. (2015). MIM-Induced Membrane Bending Promotes Dendritic Spine Initiation. *Dev. Cell* 33, 644–659.
- Saglietti, L., Dequidt, C., Kamieniarz, K., Rousset, M.C., Valnegri, P., Thoumine, O., Beretta, F., Fagni, L., Choquet, D., Sala, C., et al. (2007). Extracellular Interactions between GluR2 and N-Cadherin in Spine Regulation. *Neuron* 54, 461–477.
- Saiyed, T., Paarmann, I., Schmitt, B., Haeger, S., Sola, M., Schmalzing, G., Weissenhorn, W., and Betz, H. (2007). Molecular basis of gephyrin clustering at inhibitory synapses: Role of G- and E-domain interactions. *J. Biol. Chem.* 282, 5625–5632.
- Sakarya, O., Armstrong, K.A., Adamska, M., Adamski, M., Wang, I.F., Tidor, B., Degnan, B.M., Oakley, T.H., and Kosik, K.S. (2007). A Post-Synaptic Scaffold at the Origin of the Animal Kingdom. *PLoS One* 2.
- Sanchez-Vives, M. V., Mattia, M., Compte, A., Perez-Zabalza, M., Winograd, M., Descalzo, V.F., and Reig, R. (2010). Inhibitory modulation of cortical up states. *J. Neurophysiol.* 104, 1314–1324.
- Sando, R., and Südhof, T.C. (2021). Latrophilin gpcr signaling mediates synapse formation. *Elife* 10, 1–22.
- Sando, R., Bushong, E., Zhu, Y., Huang, M., Considine, C., Phan, S., Ju, S., Uytiepo, M., Ellisman, M., and Maximov, A. (2017). Assembly of Excitatory Synapses in the Absence of Glutamatergic Neurotransmission. *Neuron* 94, 312–321.e3.
- Sanes, J.R., and Lichtman, J.W. (1999). Development of the vertebrate neuromuscular junction. *Annu. Rev. Neurosci.* 22, 389–442.
- Sanes, J.R., and Lichtman, J.W. (2001). Induction, assembly, maturation and maintenance of a postsynaptic apparatus. *Nat. Rev. Neurosci.* 2, 791–805.
- Sanes, J.R., and Zipursky, S.L. (2020). Synaptic Specificity, Recognition Molecules, and Assembly of Neural Circuits. *Cell* 181, 536–556.
- Sans, N., Wang, P.Y., Du, Q., Petralia, R.S., Wang, Y.X., Nakka, S., Blumer, J.B., Macara, I.G., and Wenthold, R.J. (2005). mPins modulates PSD-95 and SAP102 trafficking and influences NMDA receptor surface expression. *Nat. Cell Biol.* 7, 1079–1090.
- Santoro, B., Wainger, B.J., and Siegelbaum, S.A. (2004). Regulation of HCN channel surface expression by a novel C-terminal protein-protein interaction. *J. Neurosci.* 24, 10750–10762.
- Schapitz, I.U., Behrend, B., Pechmann, Y., Lappe-Siefke, C., Kneussel, S.J., Wallace, K.E., Stempel, A.V., Buck, F., Grant, S.G.N., Schweizer, M., et al. (2010). Neuroligin 1 is dynamically exchanged at postsynaptic sites. *J. Neurosci.* 30, 12733–12744.
- Scheiffele, P., Fan, J., Choih, J., Fetter, R., and Serafini, T. (2000). Neuroligin expressed in nonneuronal cells triggers presynaptic development in contacting axons. *Cell* 101, 657–669.
- Schindelin, J., Arganda-Carreras, I., Frise, E., Kaynig, V., Longair, M., Pietzsch, T., Preibisch, S., Rueden, C., Saalfeld, S., Schmid, B., et al. (2012). Fiji: An open-source platform for biological-image analysis. *Nat. Methods* 9, 676–682.
- Schmidt, E.R.E., Kupferman, J. V., Stackmann, M., and Polleux, F. (2019). The human-specific paralogs SRGAP2B and SRGAP2C differentially modulate SRGAP2A-dependent synaptic development. *Sci. Rep.* 9, 1–8.
- Schmidt, E.R.E., Zhao, H.T., Park, J.M., Dipoppa, M., Monsalve-mercado, M.M., Dahan, J.B., Rodgers, C.C., Lejeune, A., Hillman, E.M.C., Miller, K.D., et al. (2021). A human-specific modifier of cortical connectivity and circuit function. *Nature*.
- Schoch, S., and Gundelfinger, E.D. (2006). Molecular organization of the presynaptic active zone. *Cell Tissue Res.* 326, 379–391.
- Schoch, S., Castillo, P.E., Jo, T., Mukherjee, K., Geppert, M., Wang, Y., Schmitz, F., Malenka, R.C., and Südhof, T.C. (2002). RIM1α forms a protein scaffold for regulating neurotransmitter release at the active zone. *Nature* 415, 321–326.
- Schreiner, D., Savas, J.N., Herzog, E., Brose, N., and de Wit, J. (2017). Synapse biology in the 'circuit-age'—paths toward molecular connectomics. *Curr. Opin. Neurobiol.* 42, 102–110.
- Sheng, M., and Hoogenraad, C.C. (2007). The postsynaptic architecture of excitatory synapses: A more quantitative view. *Annu. Rev. Biochem.* 76, 823–847.
- Sheng, M., and Kim, E. (2011). The postsynaptic organization of synapses. *Cold Spring Harb. Perspect. Biol.* 3.
- Sherwood, C.C., and Gomez-Robles, A. (2017). Brain plasticity and human evolution. *Annu. Rev. Anthropol.* 46, 399–419.
- Shinoe, T., and Goda, Y. (2015). Tuning synapses by proteolytic remodeling of the adhesive surface. *Curr. Opin. Neurobiol.* 35, 148–155.
- Sigler, A., Oh, W.C., Imig, C., Altas, B., Kawabe, H., Cooper, B.H., Kwon, H.B., Rhee, J.S., and Brose, N. (2017). Formation and Maintenance of Functional Spines in the Absence of Presynaptic Glutamate Release. *Neuron* 94, 304–311.e4.
- Sigoillot, S.M., Iyer, K., Binda, F., González-Calvo, I., Talleur, M., Vojdani, G., Isope, P., and Selimi, F. (2015). The secreted protein C1QL1 and its receptor BAI3 control the synaptic connectivity of excitatory inputs converging on cerebellar purkinje cells. *Cell Rep.* 10, 820–832.
- Silva, C.G., Peyre, E., and Nguyen, L. (2019). Cell migration promotes dynamic cellular interactions to control cerebral cortex morphogenesis. *Nat. Rev. Neurosci.* 20, 318–329.

- Smith, K.R., Jones, K.A., Kopeikina, K.J., Burette, A.C., Copits, B.A., Yoon, S., Forrest, M.P., Fawcett-Patel, J.M., Hanley, J.G., Weinberg, R.J., et al. (2017). Cadherin-10 maintains excitatory/inhibitory ratio through interactions with synaptic proteins. *J. Neurosci.* *37*, 11127–11139.
- Song, J.Y., Ichtchenko, K., Südhof, T.C., and Brose, N. (1999). Neuroligin 1 is a postsynaptic cell-adhesion molecule of excitatory synapses. *Proc. Natl. Acad. Sci. U. S. A.* *96*, 1100–1105.
- Sotelo, C. (2020). The History of the Synapse. *Anat. Rec.* *303*, 1252–1279.
- Sousa, A.M.M., Meyer, K.A., Santpere, G., Gulden, F.O., and Sestan, N. (2017). Evolution of the Human Nervous System Function, Structure, and Development. *Cell* *170*, 226–247.
- Soykan, T., Schneeberger, D., Tria, G., Buechner, C., Bader, N., Svergun, D., Tessmer, I., Pouloupoulos, A., Papadopoulos, T., Varoqueaux, F., et al. (2014). A conformational switch in collybistin determines the differentiation of inhibitory postsynapses. *EMBO J.* *33*, 2113–2133.
- Specht, C.G., Izeddin, I., Rodriguez, P.C., ElBeheiry, M., Rostaing, P., Darzacq, X., Dahan, M., and Triller, A. (2013). Quantitative nanoscopy of inhibitory synapses: Counting gephyrin molecules and receptor binding sites. *Neuron* *79*, 308–321.
- Spence, E.F., and Soderling, S.H. (2015). Actin out: Regulation of the synaptic cytoskeleton. *J. Biol. Chem.* *290*, 28613–28622.
- Spence, E.F., Dube, S., Uezu, A., Locke, M., Soderblom, E.J., and Soderling, S.H. (2019). In vivo proximity proteomics of nascent synapses reveals a novel regulator of cytoskeleton-mediated synaptic maturation. *Nat. Commun.* *10*, 1–16.
- Stan, A., Pielarski, K.N., Brigadski, T., Wittenmayer, N., Fedorchenko, O., Gohla, A., Lessmann, V., Dresbach, T., and Gottmann, K. (2010). Essential cooperation of N-cadherin and neuroligin-1 in the transsynaptic control of vesicle accumulation. *Proc. Natl. Acad. Sci. U. S. A.* *107*, 11116–11121.
- Stefen, H., Chaichim, C., Power, J., and Fath, T. (2016). Regulation of the Postsynaptic Compartment of Excitatory Synapses by the Actin Cytoskeleton in Health and Its Disruption in Disease. *Neural Plast.* *2016*.
- Strack, S., Choi, S., Lovinger, D.M., and Colbran, R.J. (1997). Translocation of autophosphorylated calcium/calmodulin-dependent protein kinase II to the postsynaptic density. *J. Biol. Chem.* *272*, 13467–13470.
- Südhof, T.C. (2012). The presynaptic active zone. *Neuron* *75*, 11–25.
- Südhof, T.C. (2017). Synaptic Neurexin Complexes: A Molecular Code for the Logic of Neural Circuits. *Cell* *171*, 745–769.
- Südhof, T.C. (2018). Towards an Understanding of Synapse Formation. *Neuron* *100*, 276–293.
- Südhof, T.C. (2021). The cell biology of synapse formation. *J. Cell Biol.* *220*, 1–18.
- Sudmant, P.H., Kitzman, J.O., Antonacci, F., Alkan, C., Malig, M., Tsalenko, A., Sampas, N., Bruhn, L., Shendure, J., Eichler, E.E., et al. (2010). Diversity of human copy number variation and multicopy genes. *Science (80-.)*. *330*, 641–646.
- Sumita, K., Sato, Y., Iida, J., Kawata, A., Hamano, M., Hirabayashi, S., Ohno, K., Peles, E., and Hata, Y. (2007). Synaptic scaffolding molecule (S-SCAM) membrane-associated guanylate kinase with inverted organization (MAGI)-2 is associated with cell adhesion molecules at inhibitory synapses in rat hippocampal neurons. *J. Neurochem.* *100*, 154–166.
- Sun, H., Takesian, A.E., Wang, T.T., Lippman-Bell, J.J., Hensch, T.K., and Jensen, F.E. (2018). Early Seizures Prematurely Unsilence Auditory Synapses to Disrupt Thalamocortical Critical Period Plasticity. *Cell Rep.* *23*, 2533–2540.
- Suzuki, K., Hayashi, Y., Nakahara, S., Kumazaki, H., Prox, J., Horiuchi, K., Zeng, M., Tanimura, S., Nishiyama, Y., Osawa, S., et al. (2012). Activity-Dependent Proteolytic Cleavage of Neuroligin-1. *Neuron* *76*, 410–422.
- Szegedi, V., Paizs, M., Csakvari, E., Molnar, G., Barzo, P., Tamas, G., and Lamsa, K. (2016). Plasticity in Single Axon Glutamatergic Connection to GABAergic Interneurons Regulates Complex Events in the Human Neocortex. *PLoS Biol.* *14*, 1–21.
- Tai, C.Y., Mysore, S.P., Chiu, C., and Schuman, E.M. (2007). Activity-Regulated N-Cadherin Endocytosis. *Neuron* *54*, 771–785.
- Tai, C.Y., Kim, S.A., and Schuman, E.M. (2008). Cadherins and synaptic plasticity. *Curr. Opin. Cell Biol.* *20*, 567–575.
- Takahashi, H., Katayama, K.I., Sohya, K., Miyamoto, H., Prasad, T., Matsumoto, Y., Ota, M., Yasuda, H., Tsumoto, T., Aruga, J., et al. (2012). Selective control of inhibitory synapse development by Slitrk3-PTPδ trans-synaptic interaction. *Nat. Neurosci.* *15*, 389–398.
- Takano, T., and Soderling, S.H. (2021). Tripartite synaptomics: Cell-surface proximity labeling in vivo. *Neurosci. Res.*
- Takasaki, K., and Sabatini, B.L. (2014). Super-resolution 2-photon microscopy reveals that the morphology of each dendritic spine correlates with diffusive but not synaptic properties. *Front. Neuroanat.* *8*, 1–7.
- Takeichi, M. (2007). The cadherin superfamily in neuronal connections and interactions. *Nat. Rev. Neurosci.* *8*, 11–20.
- Takeichi, M. (2018). Multiple functions of α-catenin beyond cell adhesion regulation. *Curr. Opin. Cell Biol.* *54*, 24–29.
- Takeichi M. (1988). The cadherins: cell-cell adhesion molecules controlling animal morphogenesis. *Development* *102*, 639–655.

- Taketo, M., and Yoshioka, T. (2000). Developmental change of GABA(A) receptor-mediated current in rat hippocampus. *Neuroscience* 96, 507–514.
- Tang, A.H., Chen, H., Li, T.P., Metzbower, S.R., MacGillavry, H.D., and Blanpied, T.A. (2016). A trans-synaptic nanocolumn aligns neurotransmitter release to receptors. *Nature* 536, 210–214.
- Tang, X., Jaenisch, R., and Sur, M. (2021). The role of GABAergic signalling in neurodevelopmental disorders. *Nat. Rev. Neurosci.* 22, 290–307.
- Taylor, S.C., Ferri, S.L., Grewal, M., Smernoff, Z., Bucan, M., Weiner, J.A., Abel, T., and Brodtkin, E.S. (2020). The Role of Synaptic Cell Adhesion Molecules and Associated Scaffolding Proteins in Social Affiliative Behaviors. *Biol. Psychiatry* 88, 442–451.
- Testa-Silva, G., Verhoog, M.B., Goriounova, N.A., Loebel, A., Hjorth, J.J.J., Baayen, J.C., de Kock, C.P.J., and Mansvelder, H.D. (2010). Human synapses show a wide temporal window for spike-timing-dependent plasticity. *Front. Synaptic Neurosci.* 2, 1–11.
- Testa-Silva, G., Verhoog, M.B., Linaro, D., de Kock, C.P.J., Baayen, J.C., Meredith, R.M., De Zeeuw, C.I., Giugliano, M., and Mansvelder, H.D. (2014). High Bandwidth Synaptic Communication and Frequency Tracking in Human Neocortex. *PLoS Biol.* 12.
- Togashi, H., Abe, K., Mizoguchi, A., Takaoka, K., Chisaka, O., and Takeichi, M. (2002). Cadherin regulates dendritic spine morphogenesis. *Neuron* 35, 77–89.
- Tønnesen, J., and Nägerl, U.V. (2016). Dendritic spines as tunable regulators of synaptic signals. *Front. Psychiatry* 7.
- Tønnesen, J., Katona, G., Rózsa, B., and Nägerl, U.V. (2014). Spine neck plasticity regulates compartmentalization of synapses. *Nat. Neurosci.* 17, 678–685.
- Trachtenberg, J.T., Chen, B.E., Knott, G.W., Feng, G., Sanes, J.R., Welker, E., and Svoboda, K. (2002). Long-term in vivo imaging of experience-dependent synaptic plasticity in adult cortex. *Nature* 420, 788–794.
- Tritsch, N.X., Granger, A.J., and Sabatini, B.L. (2016). Mechanisms and functions of GABA co-release. *Nat. Rev. Neurosci.* 17, 139–145.
- Turner, T.N., Sharma, K., Oh, E.C., Liu, Y.P., Collins, R.L., Sosa, M.X., Auer, D.R., Brand, H., Sanders, S.J., Moreno-De-Luca, D., et al. (2015). Loss of δ -catenin function in severe autism. *Nature* 520, 51–56.
- Tyagarajan, S.K., and Fritschy, J.M. (2014). Gephyrin: A master regulator of neuronal function? *Nat. Rev. Neurosci.* 15, 141–156.
- Tyagarajan, S.K., Ghosh, H., Yévenes, G.E., Nikonenko, I., Ebeling, C., Schwerdel, C., Sidler, C., Zeilhofer, H.U., Gerrits, B., Muller, D., et al. (2011a). Regulation of GABAergic synapse formation and plasticity by GSK3 β -dependent phosphorylation of gephyrin. *Proc. Natl. Acad. Sci. U. S. A.* 108, 379–384.
- Tyagarajan, S.K., Ghosh, H., Harvey, K., and Fritschy, J.M. (2011b). Collybistin splice variants differentially interact with gephyrin and Cdc42 to regulate gephyrin clustering at GABAergic synapses. *J. Cell Sci.* 124, 2786–2796.
- Uchida, N., Honjo, Y., Johnson, K.R., Wheelock, M.J., and Takeichi, M. (1996). The catenin/cadherin adhesion system is localized in synaptic junctions bordering transmitter release zones. *J. Cell Biol.* 135, 767–779.
- Uemura, K., Kihara, T., Kuzuya, A., Okawa, K., Nishimoto, T., Bito, H., Ninomiya, H., Sugimoto, H., Kinoshita, A., and Shimohama, S. (2006). Activity-dependent regulation of β -catenin via ϵ -cleavage of N-cadherin. *Biochem. Biophys. Res. Commun.* 345, 951–958.
- Uemura, T., Lee, S.J., Yasumura, M., Takeuchi, T., Yoshida, T., Ra, M., Taguchi, R., Sakimura, K., and Mishina, M. (2010). Trans-synaptic interaction of GluR δ 2 and neurexin through Cbln1 mediates synapse formation in the cerebellum. *Cell* 141, 1068–1079.
- Uesaka, N., and Kano, M. (2018). Presynaptic Mechanisms Mediating Retrograde Semaphorin Signals for Climbing Fiber Synapse Elimination During Postnatal Cerebellar Development. *Cerebellum* 17, 17–22.
- Uezu, A., Kanak, D.J., Bradshaw, T.W.A., Soderblom, E.J., Catavero, C.M., Burette, A.C., Weinberg, R.J., and Soderling, S.H. (2016). Identification of an elaborate complex mediating postsynaptic inhibition. *Science* (80-.). 353, 1123–1129.
- Uezu, A., Hisey, E., Kobayashi, Y., Gao, Y., Bradshaw, T.W.A., Devlin, P., Rodriguez, R., Tata, P.R., and Soderling, S.H. (2019). Essential role for insyn1 in dystroglycan complex integrity and cognitive behaviors in mice. *Elife* 8, 1–31.
- Valenta, T., Hausmann, G., and Basler, K. (2012). The many faces and functions of beta-catenin. *EMBO J.* 31, 2714–2736.
- Valot, B., Langella, O., Nano, E., and Zivy, M. (2011). MassChroQ: A versatile tool for mass spectrometry quantification. *Proteomics* 11, 3572–3577.
- Varoqueaux, F., Sigler, A., Rhee, J.S., Brose, N., Enk, C., Reim, K., and Rosenmund, C. (2002). Total arrest of spontaneous and evoked synaptic transmission but normal synaptogenesis in the absence of Munc13-mediated vesicle priming. *Proc. Natl. Acad. Sci. U. S. A.* 99, 9037–9042.
- Verhage, M., Maia, A.S., Plomp, J.J., Brussaard, A.B., Heeroma, J.H., Vermeer, H., Toonen, R.F., Hammer, R.E., Van Den Berg, T.K., Missler, M., et al. (2000). Synaptic assembly of the brain in the absence of neurotransmitter secretion. *Science* (80-.). 287, 864–869.

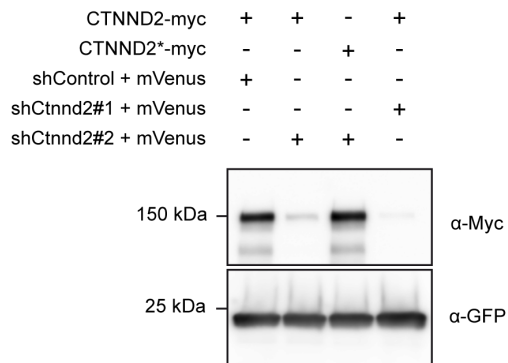
- van Versendaal, D., and Levelt, C.N. (2016). Inhibitory interneurons in visual cortical plasticity. *Cell. Mol. Life Sci.* **73**, 3677–3691.
- van Versendaal, D., Rajendran, R., Saiepour, H.M., Klooster, J., Smit-Rigter, L., Sommeijer, J.P., De Zeeuw, C.I., Hofer, S.B., Heimel, A.J., and Levelt, C.N. (2012). Elimination of Inhibitory Synapses Is a Major Component of Adult Ocular Dominance Plasticity. *Neuron* **74**, 374–383.
- Villa, K.L., Berry, K.P., Subramanian, J., Cha, J.W., Oh, W.C., Kwon, H.B., Kubota, Y., So, P.T.C., and Nedivi, E. (2016). Inhibitory Synapses Are Repeatedly Assembled and Removed at Persistent Sites In Vivo. *Neuron* **89**, 756–769.
- Vitureira, N., Letellier, M., White, I.J., and Goda, Y. (2012). Differential control of presynaptic efficacy by postsynaptic N-cadherin and β -catenin. *Nat. Neurosci.* **15**, 81–89.
- Vizcaíno, J.A., Csordas, A., Del-Toro, N., Dianes, J.A., Griss, J., Lavidas, I., Mayer, G., Perez-Riverol, Y., Reisinger, F., Ternent, T., et al. (2016). 2016 update of the PRIDE database and its related tools. *Nucleic Acids Res.* **44**, D447–D456.
- Walkup, W.G., Mastro, T.L., Schenker, L.T., Vielmetter, J., Hu, R., Iancu, A., Reghunathan, M., Bannion, B.D., and Kennedy, M.B. (2016). A model for regulation by SynGAP- α 1 of binding of synaptic proteins to PDZ-domain “Slots” in the postsynaptic density. *Elife* **5**, 1–31.
- Wamsley, B., and Fishell, G. (2017). Genetic and activity-dependent mechanisms underlying interneuron diversity. *Nat. Rev. Neurosci.* **18**, 299–309.
- Washbourne, P. (2015). Synapse assembly and neurodevelopmental disorders. *Neuropsychopharmacology* **40**, 4–15.
- Washbourne, P., Bennett, J.E., and McAllister, A.K. (2002). Rapid recruitment of NMDA receptor transport packets to nascent synapses. *Nat. Neurosci.* **5**, 751–759.
- Washbourne, P., Liu, X.B., Jones, E.G., and McAllister, A.K. (2004). Cycling of NMDA receptors during trafficking in neurons before synapse formation. *J. Neurosci.* **24**, 8253–8264.
- Wen, J.A., and Barth, A.L. (2011). Input-specific critical periods for experience-dependent plasticity in layer 2/3 pyramidal neurons. *J. Neurosci.* **31**, 4456–4465.
- Wierenga, C.J. (2017). Live imaging of inhibitory axons: Synapse formation as a dynamic trial-and-error process. *Brain Res. Bull.* **129**, 43–49.
- Wilton, D.K., Dissing-Olesen, L., and Stevens, B. (2019). Neuron-Glia Signaling in Synapse Elimination. *Annu. Rev. Neurosci.* **42**, 107–127.
- De Wit, J., and Ghosh, A. (2014). Control of neural circuit formation by leucine-rich repeat proteins. *Trends Neurosci.* **37**, 539–550.
- De Wit, J., and Ghosh, A. (2016). Specification of synaptic connectivity by cell surface interactions. *Nat. Rev. Neurosci.* **17**, 22–35.
- Won, S., Levy, J.M., Nicoll, R.A., and Roche, K.W. (2017). MAGUKs: multifaceted synaptic organizers. *Curr. Opin. Neurobiol.* **43**, 94–101.
- Woo, J., Kwon, S.K., Nam, J., Choi, S., Takahashi, H., Krueger, D., Park, J., Lee, Y., Bae, J.Y., Lee, D., et al. (2013). The adhesion protein IgSF9b is coupled to neuroligin 2 via S-SCAM to promote inhibitory synapse development. *J. Cell Biol.* **201**, 929–944.
- Woolfrey, K.M., and Dell'Acqua, M.L. (2015). Coordination of protein phosphorylation and dephosphorylation in synaptic plasticity. *J. Biol. Chem.* **290**, 28604–28612.
- Wu, K., Ge, L., Li, T., Castellano, D., Liu, C., and Wu, L. (2019). Shisa7 is a GABA_A receptor auxiliary subunit controlling benzodiazepine action. *Science (80-.)*. **366**, 246–250.
- Xiang, S., Kim, E.Y., Connelly, J.J., Nassar, N., Kirsch, J., Winking, J., Schwarz, G., and Schindelin, H. (2006). The Crystal Structure of Cdc42 in Complex with Cofilin II, a Gephyrin-interacting Guanine Nucleotide Exchange Factor. *J. Mol. Biol.* **359**, 35–46.
- Xu, C., Funahashi, Y., Namba, T., Takano, T., Nakamuta, S., Namba, T., and Kaibuchi, K. (2015). Radial glial cell–neuron interaction directs axon formation at the opposite side of the neuron from the contact site. *J. Neurosci.* **35**, 14517–14532.
- Xu, Y., Song, X., Wang, D., Wang, Y., Li, P., and Li, J. (2021). Proteomic insights into synaptic signaling in the brain: the past, present and future. *Mol. Brain* **14**, 1–18.
- Yam, P.T., Pincus, Z., Gupta, G.D., Bashkurov, M., Charron, F., Pelletier, L., and Colman, D.R. (2013). N-cadherin relocates from the periphery to the center of the synapse after transient synaptic stimulation in hippocampal neurons. *PLoS One* **8**, 1–12.
- Yamagata, M., Sanes, J.R., and Weiner, J.A. (2003). Synaptic adhesion molecules. *Curr. Opin. Cell Biol.* **15**, 621–632.
- Yamagata, M., Duan, X., and Sanes, J.R. (2018). Cadherins interact with synaptic organizers to promote synaptic differentiation. *Front. Mol. Neurosci.* **11**, 1–15.
- Yamasaki, T., Hoyos-Ramirez, E., Martenson, J.S., Morimoto-Tomita, M., and Tomita, S. (2017). GARLH Family Proteins Stabilize GABAA Receptors at Synapses. *Neuron* **93**, 1138–1152.e6.
- Yashiro, K., and Philpot, B.D. (2008). Regulation of NMDA receptor subunit expression and its implications for LTD, LTP, and metaplasticity. *Neuropharmacology* **55**, 1081–1094.

- Yasuda, R. (2017). Biophysics of Biochemical Signaling in Dendritic Spines: Implications in Synaptic Plasticity. *Biophys. J.* *113*, 2152–2159.
- Yizhar, O., Fenno, L.E., Prigge, M., Schneider, F., Davidson, T.J., Ogshea, D.J., Sohal, V.S., Goshen, I., Finkelstein, J., Paz, J.T., et al. (2011). Neocortical excitation/inhibition balance in information processing and social dysfunction. *Nature* *477*, 171–178.
- Yu, X., and Malenka, R.C. (2004). Multiple functions for the cadherin/catenin complex during neuronal development. *Neuropharmacology* *47*, 779–786.
- Yuan, L., and Arikath, J. (2017). Functional roles of p120ctn family of proteins in central neurons. *Semin. Cell Dev. Biol.* *69*, 70–82.
- Yuan, L., Seong, E., Beuscher, J.L., and Arikath, J. (2015). δ -catenin regulates spine architecture via cadherin and PDZ-dependent interactions. *J. Biol. Chem.* *290*, 10947–10957.
- Yuste, R. (2013). Electrical compartmentalization in dendritic spines. *Annu. Rev. Neurosci.* *36*, 429–449.
- Yuste, R., and Bonhoeffer, T. (2004). Genesis of dendritic spines: Insights from ultrastructural and imaging studies. *Nat. Rev. Neurosci.* *5*, 24–34.
- Yuzaki, M. (2018). Two Classes of Secreted Synaptic Organizers in the Central Nervous System. *Annu. Rev. Physiol.* *80*, 243–262.
- Zaslavsky, K., Zhang, W.B., McCready, F.P., Rodrigues, D.C., Deneault, E., Loo, C., Zhao, M., Ross, P.J., El Hajjar, J., Romm, A., et al. (2019). SHANK2 mutations associated with autism spectrum disorder cause hyperconnectivity of human neurons. *Nat. Neurosci.* *22*, 556–564.
- Zeng, M., Chen, X., Guan, D., Xu, J., Wu, H., Tong, P., and Zhang, M. (2018). Reconstituted Postsynaptic Density as a Molecular Platform for Understanding Synapse Formation and Plasticity. *Cell* *174*, 1172–1187.e16.
- Zheng, C.Y., Seabold, G.K., Horak, M., and Petralia, R.S. (2011). MAGUKs, synaptic development, and synaptic plasticity. *Neuroscientist* *17*, 493–512.
- Zhou, J., Liyanage, U., Medina, M., Ho, C., Simmons, A.D., Lovett, M., and Kosik, K.S. (1997). Presenilin 1 interaction in the brain with a novel member of the Armadillo family. *Neuroreport* *8*, 1489–1494.
- Zhu, F., Cizeron, M., Qiu, Z., Benavides-Piccione, R., Kopanitsa, M. V., Skene, N.G., Koniaris, B., DeFelipe, J., Fransén, E., Komiyama, N.H., et al. (2018a). Architecture of the Mouse Brain Synaptome. *Neuron* *99*, 781–799.e10.
- Zhu, Y., Sousa, A.M.M., Gao, T., Skarica, M., Li, M., Santpere, G., Esteller-Cucala, P., Juan, D., Ferrández-Peral, L., Gulden, F.O., et al. (2018b). Spatiotemporal transcriptomic divergence across human and macaque brain development. *Science* (80-.). 362.
- Zuber, B., Nikonenko, I., Klauser, P., Muller, D., and Dubochet, J. (2005). The mammalian central nervous synaptic cleft contains a high density of periodically organized complexes. *Proc. Natl. Acad. Sci. U. S. A.* *102*, 19192–19197.

Supplementary

Figure S1

A HEK cells



B Primary cortical neurons - endogenous CTNND2

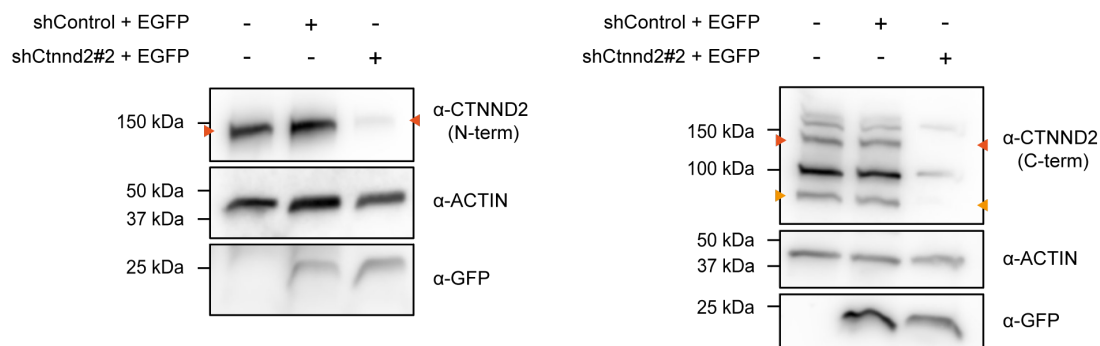


FIGURE S 1 Validation of the shRNA targeting CTNND2. Related to Figures 17-21.

(A) Validation of shRNAs against *ctnnd2* (shCtnnd2) and rescue construct (CTNND2*) in HEK cells. Cells harvested 48 hours after transfection with the indicated cDNAs. shControl: control shRNA. mVenus was expressed under a CAG promoter in the same vector as shRNAs. (B) Validation of shRNAs against endogenous *ctnnd2* in cortical neurons. Neurons were infected with lentiviral vectors driving the expression of shRNAs and EGFP after 4 days in vitro (DIV) and collected at DIV 21. The level of endogenous CTNND2 was assessed in western blot using an antibody directed against the N-terminus (left) or the C-terminus (right) of CTNND2 to ensure the depletion of CTNND2. Full length CTNND2 is indicated with dark orange arrowheads. Its molecular weight is 132 kDa. Shorter C-term isoforms (<https://gtexportal.org/home/gene/CTNND2>) were also detected (light orange) and sufficiently depleted with our shRNA. No other isoform was detected with the N-term antibody.

Figure S2

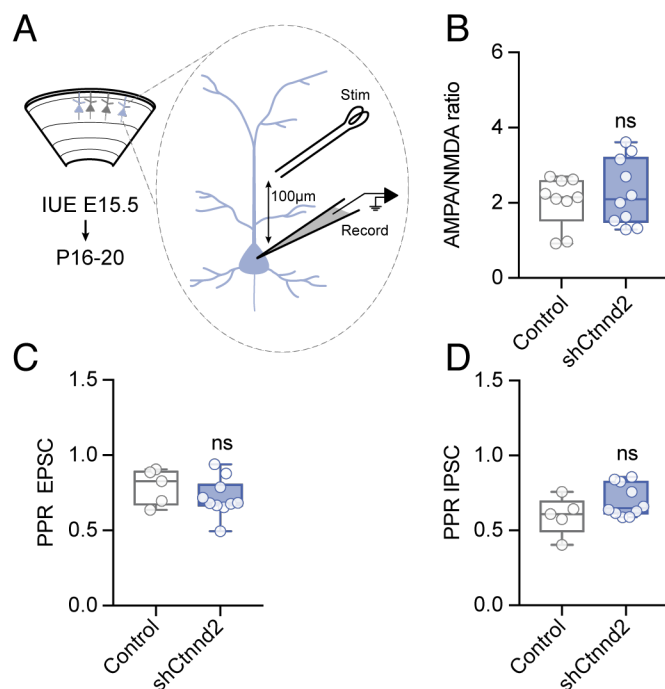


FIGURE S 2 Depletion of CTNND2 does not change the AMPA/NMDA or PPR ratio. Related to Figure 19

(A) Schematic: recording evoked postsynaptic currents in either electroporated layer 2/3 CPN expressing TdTomato and the shRNA against CTNND2 (blue) or neighboring non-electroporated control cells (gray) in acute brain slices from juvenile mice. (B) AMPA/NMDA ratio was measured in Control and shCtnnd2 neurons by recording evoked postsynaptic currents while clamping the cell subsequently at -70 mV and +40 mV. AMPA/NMDA ratio was calculated by taking the peak AMPA and the NMDAR components 50 ms post stimulation. ns: $p > 0.05$, Mann-Whitney test. (C+D) Paired Pulse Ratio (PPR) of excitatory and inhibitory postsynaptic currents in control vs shCtnnd2 condition respectively. EPSCs were recorded at -70mV and IPSCs at +10mV with a 50ms interval. Boxplots represent median and extend from the 25th to the 75th percentile, whiskers from smallest to largest value. For (B) non-parametric unpaired two-tailed t-tests with Welch correction. In (C+D) non-parametric unpaired two-tailed t-test with Mann-Whitney post-hoc. ns: $p > 0.05$.

Figure S3

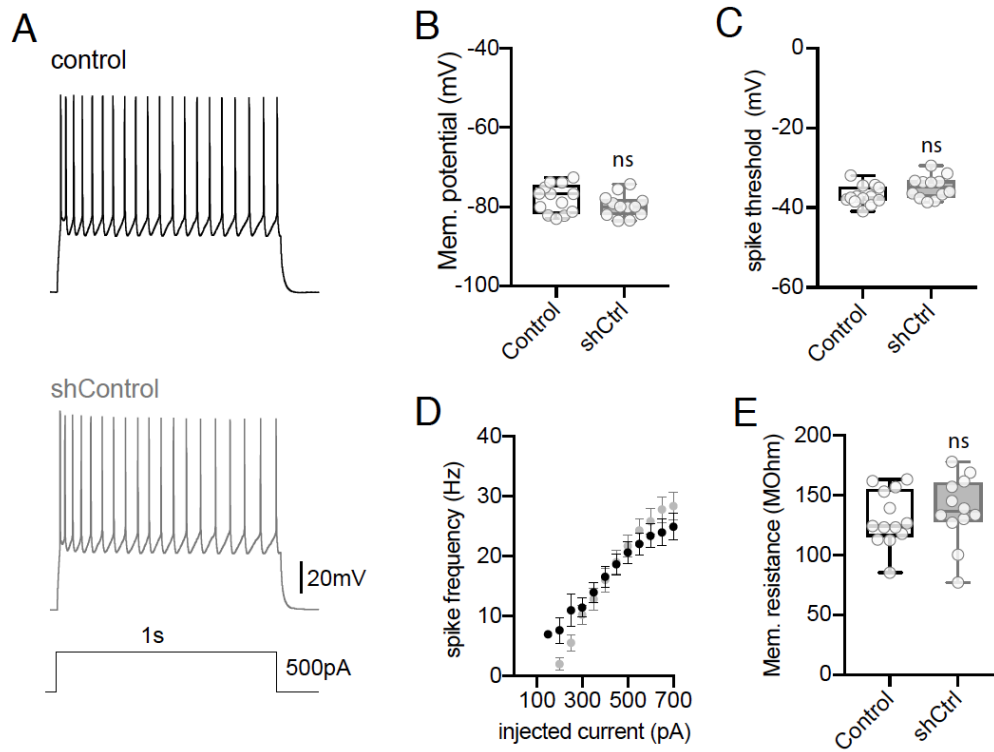


FIGURE S 3 Electroporation does not affect intrinsic excitability. Relevant to Figure 20

(A) Representative action potential traces from whole-cell current clamp recordings of non-electroporated control (black) and electroporated neurons expressing a scrambled control shRNA together with soluble TdTomato (shControl or shCtrl; gray) evoked by 1s depolarizing current steps. (B) Boxplot with individual values show the resting membrane potential of cells in both conditions. (C) Quantification of the spike threshold measured by injecting a current ramp (0-1000 pA over 1s). (D) Mean \pm SEM spike frequency depending on current injections for non-electroporated cells (black) and shControl electroporated cells (gray). (E) Membrane resistance measured at resting potential in voltage clamp through injection of 5 mV hyperpolarizing step for 100ms. Statistics: Ncontrol = 13 cells, NshControl = 12 cells. ns: $p > 0.05$, Mann-Whitney test.

TABLE S1

532/2507 proteins	Gene & Synonyms	anti-cateninDelta2 antibodyIgG						Total Pept.	MW (kDa)	Description
		Ratio	Log2	Adj. p-value	CV %	Dist. pept. used	Pept. used			
Q6ZPE2	Sbf1,Kiaa3020,Mtmr5	11.548871	3.5296799	4.09E-14	71.684234	66	264	312	208.7	Myotubularin-related protein 5
Q9QYX7	Pcdo,Acz	2.2532618	1.1720149	1.391E-05	126.48051	59	220	230	550.8	Protein piccolo
Q8BPN8	Dmx2,Kiaa0856	2.8358645	1.5037886	4.113E-05	126.68707	56	219	227	338.2	DmX-like protein 2
Q8CHG7	Rapgef2,Kiaa0313,Pdzgef1	12.000399	3.5850105	4.77E-15	61.486395	54	215	241	166.4	Rap guanine nucleotide exchange factor 2
O35927	Ctndd2,Catnd2,Nrap	6.9335672	2.7935978	7.953E-07	115.14404	45	208	262	135.0	Catenin delta-2
O88737	Bsn,Kiaa0434	3.1424284	1.6518799	2.215E-05	110.34374	62	206	220	418.8	Protein bassoon
Q9JLN9	Mtor,Frap,Frap1	3.0292955	1.5989823	6.74E-05	114.14817	52	198	204	288.8	Serine/threonine-protein kinase mTOR
Q77PH6	Mycbp2,Pam,Phr1	2.2553873	1.1733752	0.0002612	118.37427	46	172	172	517.7	E3 ubiquitin-protein ligase MYCBP2
Q5ND34	Wdr81	19.939307	4.3175434	6.319E-12	45.76109	49	169	203	211.9	WD repeat-containing protein 81
P16546	Sptan1,Spta2,Spta2	2.1459602	1.1016233	0.0086785	174.32929	38	149	173	284.6	Spectrin alpha chain, non-erythrocytic 1
Q811P8	Arhgap32,Grit,Kiaa0712,Rics	5.4958052	2.4583309	1.171E-14	53.178827	37	143	157	229.7	Rho GTPase-activating protein 32
F6SEU4	Syngap1	4.741666	2.245394	5.502E-07	79.277428	34	138	146	148.2	Ras/Rap GTPase-activating protein SynGAP
Q9QW6	Srcin1,Kiaa1684,P140	6.6289652	2.7287837	1.539E-09	68.332361	29	130	154	134.9	SRC kinase signaling inhibitor 1
Q6RHR9	Magi1,Baiap1,Bap1	6.3537432	2.6676068	2.016E-07	73.459695	30	129	129	162.0	Membrane-associated guanylate kinase, WW and PDZ domain-containing protein 1
Q61301	Ctnna2,Catna2	6.675257	3.1169065	6.082E-07	76.04038	30	121	141	105.3	Catenin alpha-2
A2A5R2	Arfgef2,Arfgef2,Big2	11.292232	3.4972587	6.038E-08	49.360454	34	119	123	202.2	Brefeldin A-inhibited guanine nucleotide-exchange protein 2
Q3UHD9	Agap2,Centg1,Kiaa0167	2.6202098	1.3896823	0.0013147	127.62994	22	119	123	124.5	Arf-GAP with GTPase, ANK repeat and PH domain-containing protein 2
Q68FH0	Pikp4,Armp	7.4093621	2.8893493	1.678E-12	50.617799	30	117	117	131.6	Plakophilin-4
Q61879	Myh10	2.2023757	1.1390606	0.0138608	163.75862	26	114	143	229.0	Myosin-10
Q6NSW3	Sphkap,Kiaa1678	9.8007018	3.2928851	1.091E-11	39.137452	29	106	113	185.1	A-kinase anchor protein SPHKAP
Q6BRT1	Clasp2,Kiaa0627	2.1347513	1.094068	0.0290022	176.26789	24	106	123	140.7	CLIP-associating protein 2
Q8CC35	Synpo,Kiaa1029	10.508144	3.393436	4.465E-07	63.644886	23	97	130	99.6	Synaptopodin
Q8VD65	Plk3r4	10.040236	3.3277213	3.563E-06	52.161422	28	94	96	152.6	Phosphoinositide 3-kinase regulatory subunit 4
P63017	Hspa8,Hsc70,Hsc73	5.5773196	2.4795719	0.0001536	101.46719	14	94	109	70.9	Heat shock cognate 71 kDa protein
A2AQ25	Skt,Elt4,Kiaa1217	10.110925	3.3378431	6.325E-08	45.787553	32	93	108	213.0	Sickle tail protein
P70398	Usp9x,Fall,Fam	3.2231906	1.6884895	0.0008086	85.512554	30	93	112	290.7	Probable ubiquitin carboxyl-terminal hydrolase FAF-X
Q58A65	Spag9,Jlp4,Jsap2,Kiaa0516,Mapk8ip4	14.767672	3.8843705	6.038E-08	44.661521	24	91	105	146.2	C-Jun-amino-terminal kinase-interacting protein 4
Q9QXL1	Kif21b,Kif6	6.8612306	2.7784673	5.718E-07	56.70364	27	91	101	186.2	Kinesin-like protein KIF21B
Q02248	Ctnnb1,Catnb	6.1195159	2.6134175	0.0027177	104.25234	25	91	110	85.5	Catenin beta-1
Q80X50	Ubap2l	8.7678421	3.1322218	0.000401	78.134345	25	88	117	116.8	Ubiquitin-associated protein 2-like
G5E8K5	Ank3	2.4606859	1.2990605	0.0003805	95.936256	25	88	102	214.1	Ankyrin-3
A2A690	Tanc2,Kiaa1148	2.090338	1.0637362	0.029735	119.19136	25	86	89	220.3	Protein TANC2
Q8BUV3	Gphn	18.837421	4.2355295	0.0002412	70.185707	23	85	105	83.3	Gephyrin
Q9JLM8	Dclk1,Dcamk1l,Dclk	2.7374783	1.4528475	0.0045497	121.70353	16	84	94	84.2	Serine/threonine-protein kinase DCLK1
Q77MQ7	Wdr91	17.377907	4.1191824	6.038E-08	49.537102	22	83	85	83.4	WD repeat-containing protein 91
Q03265	Atp5a1	3.3356603	1.7379724	0.0055245	131.08171	18	83	90	59.8	ATP synthase subunit alpha, mitochondrial
Q9D0E1	Hnnpnm,Hnnpnm	4.4086019	2.1403212	8.771E-05	87.870166	20	82	104	77.6	Heterogeneous nuclear ribonucleoprotein M
P11881	Itpr1,Insp3r,Pcd6,Pcp1	2.5019971	1.3230801	0.0139469	117.71941	22	80	90	313.2	Inositol 1,4,5-trisphosphate receptor type 1
Q80TE7	Lrrc7,Kiaa1365,Lap1	3.3970428	1.7642794	0.0006264	73.41021	23	79	88	166.9	Leucine-rich repeat-containing protein 7
Q8C3F2	Fam120c,ORF34	6.5190172	2.7046545	5.981E-06	59.951464	21	77	82	119.7	Constitutive coactivator of PPAR-gamma-like protein 2
P58871	Tnks1bp1,Kiaa1741,Tab182	4.2438446	2.0853718	2.387E-05	58.864	21	77	84	181.8	182 kDa tankyrase-1-binding protein
Q2M3X8	Phactr1	2.8096607	1.4903959	0.0037476	117.27707	14	77	85	66.3	Phosphatase and actin regulator 1
Q8K212	Pacs1	2.5499913	1.3504923	0.0277395	116.15267	22	76	86	104.8	Phosphofurin acidic cluster sorting protein 1
Q80U49	Cep170b,Kiaa0284	3.4328696	1.7794151	9.766E-06	64.643208	20	75	80	170.8	Centrosomal protein of 170 kDa protein B

Table S1 (continued 2/8)

532/2507 proteins	Gene & Synonyms	anti-cateninDelta2 antibody/IgG						Total Pept.	MW (kDa)	Description
		Ratio	Log2	Adj. p-value	CV %	Dist. pept. used	Pept. used			
Q9Z2C4	Mtmr1	14.756532	3.8832818	6.07E-10	48.80721	16	74	80	75.3	Myotubularin-related protein 1
Q8BYI9	Tnr	12.787635	3.6766776	1.44E-10	43.03556	21	73	78	149.6	Tenascin-R
Q920I9	Wdr7,Kiaa0541,Trag	8.061041	3.0109662	4.278E-07	53.224625	21	73	83	163.4	WD repeat-containing protein 7
Q3UJD6	Usp19,Kiaa0891	17.980593	4.1683687	8.76E-05	47.950401	24	72	78	150.5	Ubiquitin carboxyl-terminal hydrolase 19
Q6ZQ08	Cnot1,Kiaa1007	4.1589081	2.0562048	0.0006898	61.882098	23	72	72	266.8	CCR4-NOT transcription complex subunit 1
O89084	Pde4a	5.6124749	2.4886371	0.0198115	97.566162	19	68	68	93.6	cAMP-specific 3',5'-cyclic phosphodiesterase 4A
Q99NE5	Rims1,Kiaa0340,Rab3ip1,Rim1	2.2360362	1.1609435	0.0052663	105.4524	18	68	72	163.2	Regulating synaptic membrane exocytosis protein 1
P97291	Cdh8	8.206929	3.0368425	0.0010447	85.12289	16	67	78	88.2	Cadherin-8
P28660	Nckap1,Hem2,Kiaa0587,Nap1	4.3978665	2.1368038	0.0002847	83.93618	19	65	75	128.8	Nck-associated protein 1
P55288	Cdh11,Cad-11	11.557849	3.5308011	4.306E-05	58.859582	15	64	64	88.1	Cadherin-11
Q8BK12	Tnrc6b,Kiaa1093	4.5309575	2.179816	0.0006263	64.351043	21	64	72	192.0	Trinucleotide repeat-containing gene 6B protein
Q9EPJ0	Upf1,Rent1	4.0604354	2.0216345	0.0051065	84.208466	21	64	68	124.0	Regulator of nonsense transcripts 1
Q80YA9	Cnksr2,Kiaa0902	2.566125	1.3595914	0.0110517	107.10259	15	64	72	117.4	Connector enhancer of kinase suppressor of ras 2
Q6PCZ4	Magel1	8.9738875	3.1657331	0.0005764	59.896729	17	63	73	101.6	Melanoma-associated antigen E1
Q80TH2	Erbp2ip,Erbin,Kiaa1225,Lap2	5.4748489	2.4528191	2.437E-05	45.024264	21	62	64	157.2	Protein LAP2
Q80Y17	Llgl1,Llglh	6.0534505	2.5977577	9.766E-06	66.334546	17	59	59	112.6	Lethal(2) giant larvae protein homolog 1
Q6PAJ1	Bcr,Kiaa3017	6.436412	2.6862567	8.771E-05	49.404029	19	58	58	143.1	Breakpoint cluster region protein
Q6PF93	Plk3c3	3.5125502	1.8125188	0.0091158	92.843413	19	58	67	101.5	Phosphatidylinositol 3-kinase catalytic subunit type 3
O70507	Hcn4,Bcng3	7.4697914	2.9010679	0.0069218	66.756165	16	56	56	127.4	Potassium/sodium hyperpolarization-activated cyclic nucleotide-gated channel 4
Q9WVQ1	Magi2,Acvrip1,Aip1,Arip1	6.1853348	2.6288517	0.0001976	55.104118	18	56	60	140.9	Membrane-associated guanylate kinase, WW and PDZ domain-containing protein 2
Q7M6Y3	Picalm,Calm,Fit1	23.307802	4.5427411	3.957E-05	53.759457	16	53	61	71.5	Phosphatidylinositol-binding clathrin assembly protein
Q8K4Q0	Rptor,Raptor	8.435664	3.0765016	2.395E-05	53.311259	15	52	59	149.5	Regulatory-associated protein of mTOR
Q62318	Trim28,Krip1,Tif1b	4.8487125	2.2776017	0.0037476	72.341112	11	52	52	88.8	Transcription intermediary factor 1-beta
P12367	Prkar2a	4.4014351	2.137974	0.021089	121.10194	12	52	52	45.4	cAMP-dependent protein kinase type II-alpha regulatory subunit
P26231	Ctnna1,Catna1	8.2071324	3.0368782	0.013784	59.675852	16	51	55	100.1	Catenin alpha-1
Q9DAT5	Trmu,Mtu1,Tmt1	34.330402	5.1014149	1.698E-11	24.65298	12	50	54	47.2	Mitochondrial tRNA-specific 2-thiouridylase 1
Q80TQ2	Cyld,Cyld1,Kiaa0849	13.560403	3.7613282	0.00138	56.476165	15	50	57	106.6	Ubiquitin carboxyl-terminal hydrolase CYLD
P09405	Ncl,Nuc	5.0521671	2.3369023	1.72E-05	53.051111	10	50	59	76.7	Nucleolin
P29341	Pabpc1,Pabp1	5.5894146	2.4826972	0.0011777	71.982299	12	48	57	70.7	Polyadenylate-binding protein 1
Q64521	Gpd2,Gdm1	4.0191072	2.0068751	0.0043682	69.816216	14	48	54	81.0	Glycerol-3-phosphate dehydrogenase, mitochondrial
Q9DBR1	Xrn2,Dhm1	10.438785	3.3838819	0.000401	47.473779	17	47	54	108.7	5'-3' exonuclease 2
Q6DFV3	Arhgap21,Arhgap10,Kiaa1424	2.7248246	1.4461633	0.0135452	89.140372	13	47	47	215.7	Rho GTPase-activating protein 21
D3YZP9	Cdc6	15.616719	3.9650194	1.419E-06	44.076474	12	46	58	52.9	Coiled-coil domain-containing protein 6
Q8CFI0	Nedd4l,Kiaa0439,Nedd4b	3.7287098	1.8986765	0.0070352	82.634884	13	46	53	115.4	E3 ubiquitin-protein ligase NEDD4-like
Q9CZW4	Acs13,Acs3,Fad3	3.2403069	1.6961304	0.0054626	77.703189	14	46	51	80.5	Long-chain-fatty-acid-CoA ligase 3
Q9CZ62	Cep97,Lmq2	10.473981	3.388738	0.0001976	45.020108	14	45	51	94.6	Centrosomal protein of 97 kDa
Q8CBE3	Wdr37,Kiaa0982	7.3688852	2.8814464	0.0003805	61.547036	10	45	50	55.0	WD repeat-containing protein 37
Q8R0S2	Iqsec1,Kiaa0763	6.4977289	2.6999355	2.794E-09	30.308171	11	45	45	108.0	IQ motif and SEC7 domain-containing protein 1
P15116	Cdh2	6.0784957	2.6037143	0.022382	83.886496	13	45	45	99.8	Cadherin-2
Q7TMK9	Syncrip,Hnmpq,Nsap1,Nsap1l	4.5673719	2.1913643	0.0025985	71.319861	13	45	48	69.6	Heterogeneous nuclear ribonucleoprotein Q
O88845	Akap10	10.487118	3.3905464	2.719E-11	23.771659	13	44	48	73.6	A-kinase anchor protein 10, mitochondrial
B1AXH1	Nhs12	7.640199	2.9336102	0.0039297	58.083834	13	43	43	91.9	NHS-like protein 2
Q7TSH4	Ccp110,Cep110,Cp110,Kiaa0419	7.6430227	2.9341433	0.0016987	47.440382	12	42	50	111.1	Centriolar coiled-coil protein of 110 kDa
Q7TME0	Pippr4,Kiaa0455,Lppr4,Php1,Prg1	3.7862282	1.9207614	0.0052663	77.234462	12	42	54	83.3	Lipid phosphate phosphatase-related protein type 4
Q8C0C7	Farsa,Farsla	2.7732693	1.4715877	0.0193491	96.471199	11	42	47	57.6	Phenylalanine-tRNA ligase alpha subunit

Table S1 (continued 3/8)

532/2507 proteins	Gene & Synonyms	anti-cateninDelta2 antibody/IgG						Total Pept.	MW (kDa)	Description
		Ratio	Log2	Adj. p-value	CV %	Dist. pept. used	Pept. used			
Q8CHX7	Rftn2	17.676867	4.1437907	5.037E-05	25.625041	11	39	45	55.0	Raftlin-2
Q8BMS9	Rassf2,Kiaa0168	5.8402411	2.5460279	0.0211151	79.426651	10	39	39	38.0	Ras association domain-containing protein 2
P60469	Ppfla3	2.0235246	1.0168704	0.0316003	101.00941	11	39	44	133.4	Liprin-alpha-3
E9Q555	Rnf213	8.1227737	3.0219724	0.0060411	38.179564	16	38	38	584.5	E3 ubiquitin-protein ligase RNF213
Q6PFD9	Nup98	4.8166163	2.26802	0.0083913	59.225044	13	38	38	197.2	Nuclear pore complex protein Nup98-Nup96
Q3U0V1	Kharp,Fubp2	2.5765283	1.3654284	0.0132517	89.462034	8	37	60	76.8	Far upstream element-binding protein 2
Q8C437	Pex5l,Pex2,PexSr,Pxr2	8.7647725	3.1317167	3.111E-05	44.873279	10	36	39	63.1	PEX5-related protein
O88704	Hcn1,Bcng1,Hac2	5.2640152	2.3961637	0.0024865	48.701979	9	36	41	102.4	Potassium/sodium hyperpolarization-activated cyclic nucleotide-gated channel 1
Q6ZPQ6	Pitpnm2,Kiaa1457,Nir3	4.102612	2.0365427	0.0071789	57.885369	13	36	36	148.0	Membrane-associated phosphatidylinositol transfer protein 2
P17427	Ap2a2,Adtab	3.241698	1.6967497	0.024231	95.592966	7	36	36	104.0	AP-2 complex subunit alpha-2
Q8VDN2	Atp1a1	3.3777757	1.7560735	0.013784	85.327952	9	35	46	113.0	Sodium/potassium-transporting ATPase subunit alpha-1
Q3TLH4	Prrc2c,Bat2d,Bat2d1,Bat2l2,Kiaa1096	2.4032061	1.2649604	0.0049504	59.549452	9	35	39	310.9	Protein PRRC2C
P23819	Gria2,Glur2	2.9921414	1.5811783	0.0076652	57.751068	8	34	34	98.7	Glutamate receptor 2
Q5RJH3	Cdh12	20.33656	4.3460038	1.942E-05	29.991426	13	33	36	88.5	Cadherin-12
P14148	Rpl7	5.3551886	2.4209374	0.0027177	63.601	7	33	37	31.4	60S ribosomal protein L7
Q03137	Epha4,Sek,Sek1	4.8271062	2.2711586	0.0033799	62.454529	9	33	35	109.8	Ephrin type-A receptor 4
Q8BNN1	Spata2l,Kiaa4138	14.238987	3.8317746	0.0003421	40.504158	9	32	32	46.8	Spermatogenesis-associated protein 2-like protein
Q9ESN9	Mapk8ip3,Jip3,Jsap1,Syd2	13.052997	3.7063092	1.737E-05	34.042502	10	32	36	147.6	C-Jun-amino-terminal kinase-interacting protein 3
Q8BM92	Cdh7	13.773332	3.7838057	6.095E-05	28.204628	10	31	31	87.2	Cadherin-7
P84309	Adcy5	7.1646154	2.8408893	1.061E-05	32.515027	10	31	31	139.1	Adenylyate cyclase type 5
Q9D6F9	Tubb4a,Tubb4	4.9225078	2.2993935	0.0117951	74.286282	5	31	31	49.6	Tubulin beta-4A chain
Q9CZM2	Rpl15	15.323945	3.9377158	9.766E-06	38.319424	6	30	32	24.1	60S ribosomal protein L15
Q80TS7	Ddn,Gm748,Kiaa0749	4.6380924	2.2135316	0.0003388	37.473945	8	30	30	76.4	Dendrin
Q03173	Enah,Mena,Ndpp1	10.864765	3.4415851	0.0009937	40.751298	8	29	29	85.8	Protein enabled homolog
P54071	Idh2	4.7194536	2.2386198	0.0003105	46.625419	8	29	33	50.9	Isocitrate dehydrogenase [NADP], mitochondrial
Q6NZL0	Soga3	4.1120109	2.0398441	0.0033344	69.142612	8	29	29	103.5	Protein SOGA3
Q7TNM2	Trim46,Trific	3.5486663	1.8272769	0.0086785	43.737116	10	29	29	83.4	Tripartite motif-containing protein 46
Q6NZC7	Sec23ip	12.029668	3.5885249	0.0001903	28.274023	9	28	28	110.8	SEC23-interacting protein
Q8BH59	Slc25a12,Aralar1	4.8066405	2.2650289	0.0125565	49.956265	9	28	31	74.6	Calcium-binding mitochondrial carrier protein Aralar1
P14869	Rplp0,Arbp	7.15448	2.8388469	0.0043072	66.607799	7	27	44	34.2	60S acidic ribosomal protein P0
P61963	Dcaf7,Han11,Wdr68	3.2647119	1.7069557	0.0227915	69.443976	6	27	27	38.9	DDB1- and CUL4-associated factor 7
Q4KUS2	Unc13a	2.2770294	1.1871529	0.0149757	41.325425	9	27	27	193.8	Protein unc-13 homolog A
Q9Z0M3	Cdh20,Cdh7	16.891376	4.078215	0.0015556	36.042669	9	26	39	89.0	Cadherin-20
Q3TUH1	Tamm41	5.2690607	2.3975458	0.023232	73.291934	6	26	26	37.8	Phosphatidate cytidyltransferase, mitochondrial
Q8K1S4	Unc5a,Kiaa1976,Unc5h1	7.1613469	2.840231	0.0125186	38.55671	8	25	29	98.9	Netrin receptor UNC5A
Q99M87	Dnaja3,Tid1	3.1850635	1.6713221	0.000462	34.77903	8	25	25	52.4	DnaJ homolog subfamily A member 3, mitochondrial
Q6P5F6	Slc39a10,Kiaa1265,Zip10	1000	1000			8	24	24	94.4	Zinc transporter ZIP10
P70408	Cdh10	9.1971999	3.2011947	0.0008086	53.619794	6	24	31	88.3	Cadherin-10
P68181	Prkacb,Prkacb	8.2407368	3.0427733	0.0244886	77.973096	4	24	34	40.7	cAMP-dependent protein kinase catalytic subunit beta
Q8BTX9	Hsd1	4.3230777	2.1120588	0.0158544	64.145155	6	24	24	36.9	Inactive hydroxysteroid dehydrogenase-like protein 1
Q9EP89	Lactb,Lact1	23.037561	4.5259161	0.0043072		7	23	30	60.7	Serine beta-lactamase-like protein LACTB, mitochondrial
Q9CPY7	Lap3,Lapep	17.135714	4.0989344	0.0042669	29.547473	10	23	23	56.1	Cytosol aminopeptidase
O88703	Hcn2,Bcng2,Hac1	7.0932435	2.8264455	0.0075417	53.156463	7	23	23	94.7	Potassium/sodium hyperpolarization-activated cyclic nucleotide-gated channel 2
P62245	Rps15a	5.6185468	2.490197	0.0132438	56.121167	5	23	23	14.8	40S ribosomal protein S15a
Q9DC28	Csnk1d,Hckid	4.4754413	2.1620299	0.0022507	49.379215	5	23	23	47.3	Casein kinase I isoform delta
Q3UHB8	Ccdc177,Gm1568	3.1267198	1.64465	0.0085506	69.664547	5	23	23	79.9	Coiled-coil domain-containing protein 177

Table S1 (continued 4/8)

532/2507 proteins	Gene & Synonyms	anti-cateninDelta2 antibody/IgG						Total Pept.	MW (kDa)	Description
		Ratio	Log2	Adj. p-value	CV %	Dist. pept. used	Pept. used			
Q9WV34	Mpp2,Dlgh2	2.7219069	1.4446177	0.0232681	84.110457	6	23	28	61.6	MAGUK p55 subfamily member 2
Q61584	Fxr1,Fxr1h	7.8349624	2.9699264	0.0007099	28.395849	6	22	22	76.2	Fragile X mental retardation syndrome-related protein 1
Q9CR57	Rpl14	6.6389189	2.7309483	0.031589	73.938929	4	22	22	23.6	60S ribosomal protein L14
Q88705	Hcn3,Hac3	4.9954548	2.320616	0.0301718	47.970184	8	22	22	86.6	Potassium/sodium hyperpolarization-activated cyclic nucleotide-gated channel 3
Q9DBC7	Prkar1a	13.322596	3.7358033	0.0027716	35.870038	7	21	21	43.2	cAMP-dependent protein kinase type I-alpha regulatory subunit
Q7TSC1	Prcc2a,Bat2	5.338107	2.4163282	0.000129	30.90072	7	21	25	229.2	Protein PRRC2A
Q4U2R1	Herc2,Jdf2,Kiaa0393,Rjs	5.0707072	2.342187	0.0057498		8	21	21	527.5	E3 ubiquitin-protein ligase HERC2
Q61586	Gpam,Gpat1	4.5239735	2.1775905	0.0148108	59.028323	7	21	21	93.7	Glycerol-3-phosphate acyltransferase 1, mitochondrial
Q6PAK3	Prmt8,Hrmt114	3.007536	1.588582	0.0094796	56.989368	5	21	21	45.3	Protein arginine N-methyltransferase 8
Q88444	Adcy1	1000	1000			7	20	20	123.4	Adenylate cyclase type 1
Q8BX10	Pgam5	12.45918	3.6391372	0.0048613	44.279868	6	20	24	32.0	Serine/threonine-protein phosphatase PGAM5, mitochondrial
P50544	Acadvl,Vlcad	4.2749623	2.0959184	0.0003805	38.734761	7	20	22	70.9	Very long-chain specific acyl-CoA dehydrogenase, mitochondrial
Q8K406	Lgi3	3.5923619	1.8449327	0.0093389	57.391305	7	20	20	61.8	Leucine-rich repeat LGI family member 3
P56564	Slc1a3,Eaat1,Gmt1	13.744113	3.7807419	0.0224301	59.025111	3	19	19	59.6	Excitatory amino acid transporter 1
Q80W04	Tmcc2,Kiaa0481	3.7619624	1.9114854	0.0242568	54.89497	6	19	19	77.1	Transmembrane and coiled-coil domains protein 2
Q8VD37	Sgip1	3.6135772	1.8534277	0.0054511	32.168677	5	19	30	86.1	SH3-containing GRB2-like protein 3-interacting protein 1
Q6P1H6	Ankle2,D5Erd585e,Kiaa0692,Lem4	1000	1000			7	18	18	106.2	Ankyrin repeat and LEM domain-containing protein 2
Q9JIA1	Lgi1	17.854277	4.1581978	1.341E-06	25.300026	5	18	18	63.6	Leucine-rich glioma-inactivated protein 1
Q9WVR4	Fxr2,Fxr2h	13.429849	3.7473712	0.0011716	29.641853	5	18	18	73.7	Fragile X mental retardation syndrome-related protein 2
Q9ES63	Usp29	9.3650986	3.2272942	0.0004805	24.568177	6	18	21	97.8	Ubiquitin carboxyl-terminal hydrolase 29
Q3TDK6	Rogdi,Lzf	6.7115823	2.7466529	0.0302135	50.60922	6	18	22	32.1	Protein rogdi homolog
Q925N0	Sfxn5	6.5064736	2.7018758	2.313E-05	19.953414	6	18	18	37.3	Sideroflexin-5
Q99L04	Dhrs1,D14ertd484e	4.8547305	2.2793912	0.0207622	40.10748	5	18	18	34.0	Dehydrogenase/reductase SDR family member 1
Q8R366	Igsf8,Ew12,Kctd4,Pgri	4.5451679	2.1843336	0.0132438	31.553652	6	18	18	65.0	Immunoglobulin superfamily member 8
Q9DCD5	Tjap1,Pilt,Tjp4	23.719022	4.5679726	0.0007668		5	17	17	59.4	Tight junction-associated protein 1
Q69ZH9	Arhgap23,Kiaa1501,MNcb-1301	13.071542	3.7083574	0.0031679	25.509493	6	17	17	161.8	Rho GTPase-activating protein 23
Q8K2C9	ptlpld1,hacd3	6.3295995	2.6621142	0.0029884	31.486893	4	17	17	43.1	Very-long-chain (3R)-3-hydroxyacyl-CoA dehydratase 3
Q9JIF0	Prmt1,Hrmt112,Mmt1	3.2474471	1.699306	0.0290444	61.552943	3	17	17	42.4	Protein arginine N-methyltransferase 1
P61358	Rpl27	16.588911	4.0521473	0.0148596	56.567853	4	16	16	15.8	60S ribosomal protein L27
Q8BYM5	Nlgn3	11.873577	3.5696828	2.21E-05	20.238797	4	16	20	91.2	Neurologin-3
Q88986	Gcat,Kbl	11.028802	3.4632042	0.0029996	31.498793	4	16	22	44.9	2-amino-3-ketobutyrate coenzyme A ligase, mitochondrial
Q9Z321	Top3b,Top3b1	2.7699022	1.4698351	0.0192905	44.066427	5	16	16	96.9	DNA topoisomerase 3-beta-1
Q9DCX2	Atp5h	12.355164	3.6270423	0.0129462	42.190711	3	15	18	18.7	ATP synthase subunit d, mitochondrial
P70407	Cdh9	10.641445	3.4116221	0.0129212	26.436893	5	15	18	88.3	Cadherin-9
Q8K0V4	Cnot3,Not3	8.9305097	3.1587425	0.0076652	26.954005	6	15	15	81.9	CCR4-NOT transcription complex subunit 3
Q99JR1	Sfxn1,F	8.5150022	3.0900069	0.0076652	41.476319	4	15	19	35.6	Sideroflexin-1
Q9D3A9	Tlyh1	6.542795	2.7099071	0.0039899	33.87509	3	15	15	49.0	Protein tweety homolog 1
P63034	Cyth2,Pscd2,Sec7b	4.2190203	2.076908	0.0112522	48.5279	3	15	15	46.6	Cytohesin-2
A2AGT5	Ckap5	3.7370901	1.9019153	0.024231	50.951759	5	15	15	225.6	Cytoskeleton-associated protein 5
P23242	Gja1,Cxn-43	3.6162631	1.8544996	0.016739	18.330508	3	15	15	43.0	Gap junction alpha-1 protein
Q6A4J8	Usp7,Hausp	3.2580133	1.7039925	0.0025171		6	15	15	128.5	Ubiquitin carboxyl-terminal hydrolase 7
Q35127	Grcic10,C10	15.045205	3.9112318	6.825E-05	19.387757	3	14	19	13.2	Protein C10
Q3TZ77	Esyt2,D12Erd551e,Fam62b	12.07	3.5933538	0.0222579	37.508803	5	14	14	94.1	Extended synaptotagmin-2
Q6NVG1	Lpcat4,Agpat7,Aylt3	9.9267289	3.3113184	0.0088359	34.405774	5	14	18	57.1	Lysophospholipid acyltransferase LPCAT4
Q9WV55	Vapa,Vap33	5.6143681	2.4891237	0.0204993	46.26006	2	14	19	27.9	Vesicle-associated membrane protein-associated protein A
Q9CZT8	Rab3b	4.8541218	2.2792103	0.0132438	51.002088	3	14	14	24.8	Ras-related protein Rab-3B

Table S1 (continued 5/8)

532/2507 proteins	Gene & Synonyms	anti-cateninDelta2 antibody/IgG						Total Pept.	MW (kDa)	Description
		Ratio	Log2	Adj. p-value	CV %	Dist. pept. used	Pept. used			
Q61171	Prdx2,Tdpx1,Tpx	4.3985375	2.1370239	0.0050269	27.518196	3	14	18	21.8	Peroxiorexin-2
Q91VE0	Slc27a4,Acsvl4,Fatp4	3.2923711	1.7191269	0.0277395	36.346538	5	14	17	72.3	Long-chain fatty acid transport protein 4
Q60841	Reelin,RI	2.9321117	1.5519401	0.0016367	16.118572	5	14	14	387.5	Reelin
P70188	Kiflap3	1000	1000			4	13	13	91.3	Kinesin-associated protein 3
P83741	Wnk1,Hsn2,Prkwnk1	5.2088629	2.3809685	0.0139838	30.732996	5	13	13	250.9	Serine/threonine-protein kinase WNK1
Q8BHD7	Ptbp3,Rod1	1000	1000			4	12	12	56.7	Polypyrimidine tract-binding protein 3
Q8BU11	Tox4	1000	1000			5	12	12	66.0	TOX high mobility group box family member 4
Q8VHI6	Wasf3,Wave3	15.322805	3.9376085	0.0005509	19.012185	4	12	17	55.2	Wiskott-Aldrich syndrome protein family member 3
Q692S8	Kazn,Kaz,Kiaa1026	6.1865397	2.6291327	0.0148917	35.611411	4	12	12	86.7	Kazrin
Q3TRM4	Pnp1a6,Nle	3.4258303	1.7764537	0.0174129	32.251946	5	12	12	149.5	Neuropathy target esterase
P62141	Ppp1cb	2.4986758	1.3211637	0.0086785	15.956878	2	12	12	37.2	Serine/threonine-protein phosphatase PP1-beta catalytic subunit
A2AHG0	Lzts3,Prosapip1	1000	1000			4	11	11	75.0	Leucine zipper putative tumor suppressor 3
A2AJ15	Man1b1	1000	1000			4	11	11	75.2	Endoplasmic reticulum mannosyl-oligosaccharide 1,2-alpha-mannosidase
P48377	Rfx1	1000	1000			4	11	11	103.7	MHC class II regulatory factor RFX1
Q6NV72	Wdcp	1000	1000			5	11	11	72.3	WD repeat and coiled-coil-containing protein C2orf44 homolog
Q6ZQ03	Fnbp4,Fbp30,Kiaa1014	1000	1000			4	11	11	111.2	Formin-binding protein 4
Q8K077	Unc13c	1000	1000			5	11	11	249.8	Protein unc-13 homolog C
Q9Z280	Pld1	1000	1000			3	11	11	124.0	Phospholipase D1
Q9D6R2	ldh3a	28.792935	4.8476429	0.0134242	38.265337	3	11	14	39.6	Isocitrate dehydrogenase [NAD] subunit alpha, mitochondrial
P61982	Ywhag	23.43091	4.5503411	0.0086785		3	11	11	28.3	14-3-3 protein gamma
Q8C3Q5	Shisa7	12.884082	3.6875179	0.0024246	22.871297	4	11	17	58.3	Protein shisa-7
Q6PE13	Prt3	5.5879533	2.48232	0.0139838	35.823337	4	11	11	101.2	Proline-rich transmembrane protein 3
P57776	Eef1d	5.4785656	2.4537982	0.0088359	38.34527	3	11	11	31.3	Elongation factor 1-delta
Q9CY22	Tpd52l2	3.1153514	1.6393949	0.0295487	37.607502	3	11	11	24.0	Tumor protein D54
P06537	Nr3c1,Grl,Grl1	1000	1000			5	10	10	86.1	Glucocorticoid receptor
Q3U213	Serac1,D17Etd141e	1000	1000			4	10	10	74.0	Protein SERAC1
Q61151	Ppp2r5e,Kiaa4006	1000	1000			3	10	10	54.7	Serine/threonine-protein phosphatase 2A 56 kDa regulatory subunit epsilon isoform
Q9QYS2	Grm3,Gprc1c,Mglur3	1000	1000			5	10	10	99.1	Metabotropic glutamate receptor 3
Q9Z2A0	Pdpk1,Pdk1	1000	1000			4	10	10	63.8	3-phosphoinositide-dependent protein kinase 1
O55126	Gbas,Nipsnap2	13.246109	3.7274968	0.0129212	30.568154	3	10	10	32.9	Protein NipSnap homolog 2
O54967	Tnk2,Ack1	12.240429	3.6135823	0.0037476	24.308118	3	10	13	117.0	Activated CDC42 kinase 1
Q8BLF1	Nceh1,Aadac1,Kiaa1363	8.0487666	3.0087677	0.0132438	35.736897	3	10	10	45.7	Neutral cholesterol ester hydrolase 1
Q6WVG3	Kctd12,Pfet1	7.4148688	2.8904212	0.0029996	13.602641	3	10	10	35.9	BTB/POZ domain-containing protein KCTD12
Q8CGY8	Ogt	7.0843114	2.8246276	0.0013241	13.931004	3	10	13	117.0	UDP-N-acetylglucosamine--peptide N-acetylglucosaminyltransferase 110 kDa subunit
O35129	Phb2,Bap,Bcap37,Rea	6.9610949	2.7993143	0.013784	22.522178	4	10	10	33.3	Prohibitin-2
P68040	Gnb2l1,Gnb2-rs1	6.0715478	2.6020643	0.0116596	34.766722	3	10	10	35.1	Guanine nucleotide-binding protein subunit beta-2-like 1
Q7TN99	Cpeb3,Kiaa0940	4.5009436	2.1702275	0.0043426		3	10	10	78.3	Cytoplasmic polyadenylation element-binding protein 3
Q99K10	Aco2	4.3093781	2.1074797	0.022382	35.713518	3	10	10	85.5	Aconitate hydratase, mitochondrial
O55203	Ldb2,Clim1	1000	1000			3	9	9	42.7	LIM domain-binding protein 2
P05132	Prkaca,Pkaca	1000	1000			3	9	9	40.6	cAMP-dependent protein kinase catalytic subunit alpha
P20934	Evi2a,Evi-2,Evi-2a,Evi2	1000	1000			3	9	9	24.1	Protein EVI2A
Q6NXJ0	Wwc2,D8Etd594e,MNCb-4173	1000	1000			4	9	9	132.6	Protein WWC2
Q8C7X2	Emc1,Kiaa0090	1000	1000			4	9	9	111.6	ER membrane protein complex subunit 1
Q9R0M0	Celsr2	1000	1000			3	9	9	317.6	Cadherin EGF LAG seven-pass G-type receptor 2
Q8C132	Bag5	5.786608	2.5327179	0.0104342		3	9	9	50.9	BAG family molecular chaperone regulator 5
Q5SP85	Ccdc85a,Kiaa1912	3.9521616	1.982642	0.0195136	45.244887	2	9	9	54.5	Coiled-coil domain-containing protein 85A

Table S1 (continued 6/8)

532/2507 proteins	Gene & Synonyms	anti-cateninDelta2 antibody/IgG						Total Pept.	MW (kDa)	Description
		Ratio	Log2	Adj. p-value	CV %	Dist. pept. used	Pept. used			
Q2WF71	Lrnf1,Salm2,Semo1	2.9293195	1.5505656	0.0029996	11.139464	2	9	9	81.9	Leucine-rich repeat and fibronectin type III domain-containing protein 1
Q61324	Amt2,Kiaa0307	2.204634	1.1405391	0.0227915	29.383394	3	9	9	77.9	Aryl hydrocarbon receptor nuclear translocator 2
P03995	Gfap	1000	1000			3	8	8	49.9	Glial fibrillary acidic protein
P17225	Ptbp1,Ptbt	1000	1000			2	8	8	56.5	Polypyrimidine tract-binding protein 1
P27601	Gna13,Gna-13	1000	1000			4	8	8	44.1	Guanine nucleotide-binding protein subunit alpha-13
P30275	Ckmt1	1000	1000			3	8	8	47.0	Creatine kinase U-type, mitochondrial
P51175	Ppox	1000	1000			4	8	8	50.9	Protoporphyrinogen oxidase
Q5NCX5	Neur4,Kiaa1787	1000	1000			3	8	8	167.6	Neutralized-like protein 4
Q80TM9	Nisch,Kiaa0975	1000	1000			4	8	8	175.0	Nischarin
Q812E0	Cpeb2	1000	1000			3	8	8	58.4	Cytoplasmic polyadenylation element-binding protein 2
Q8BTS4	Nup54	1000	1000			4	8	8	55.7	Nuclear pore complex protein Nup54
Q9CY73	Mrip44	1000	1000			3	8	8	37.5	39S ribosomal protein L44, mitochondrial
Q9D287	Bcas2,Dam1	1000	1000			4	8	8	26.1	Pre-mRNA-splicing factor SPF27
Q9Z0R9	Fads2,Fadsd2	1000	1000			4	8	8	52.4	Fatty acid desaturase 2
Q9Z1R4	D17h6s53e	1000	1000			3	8	8	32.0	Uncharacterized protein C6orf47 homolog
Q9QZB0	Rgs17,Rgsz2	10.927664	3.4499131	0.0151284	22.099242	2	8	8	24.3	Regulator of G-protein signaling 17
Q8CBC4	Cnst	3.7375461	1.9020914	0.0129462	32.823551	2	8	8	76.9	Consortin
O86689	Pcdha4,Cnr1	1000	1000			3	7	7	103.1	Protocadherin alpha-4
P17710	Hk1	1000	1000			3	7	7	108.3	Hexokinase-1
Q01405	Sec23a,Sec23,Sec23r	1000	1000			3	7	7	86.2	Protein transport protein Sec23A
Q14BI2	Gmm2,Gprc1b,Mglur2	1000	1000			3	7	7	95.9	Metabotropic glutamate receptor 2
Q6PEM6	Gramd3	1000	1000			3	7	7	49.3	GRAM domain-containing protein 3
Q8C145	Slc39a6,Zip6	1000	1000			3	7	7	86.4	Zinc transporter ZIP6
Q91YD3	Dcp1a,Mitc1,Smif	1000	1000			3	7	7	65.2	mRNA-decapping enzyme 1A
Q91YX5	Lpgat1,Fam34a	1000	1000			3	7	7	43.1	Acyl-CoA:lysophosphatidylglycerol acyltransferase 1
Q9QZX7	Srr	1000	1000			3	7	7	36.4	Serine racemase
P35282	Rab21	11.898727	3.5727353	0.0046902	18.387183	1	7	7	24.1	Ras-related protein Rab-21
Q8BPM0	Daam1	8.4388833	3.0770521	0.0083913		2	7	7	123.4	Disheveled-associated activator of morphogenesis 1
Q60803	Traf3,Craf1,Trafamn	7.8771339	2.9776708	0.0119876	27.514587	2	7	13	64.3	TNF receptor-associated factor 3
Q62074	Prkci,Pkci	6.25636	2.6453235	0.0071479		2	7	7	68.2	Protein kinase C iota type
Q3TY86	Aifm3,Aifl	5.2780853	2.4000147	0.0076652		2	7	7	66.8	Apoptosis-inducing factor 3
P47740	Aldh3a2,Ahd-3,Ahd3,Aldh3,Aldh4	4.6504816	2.2173801	0.0022768		2	7	7	54.0	Fatty aldehyde dehydrogenase
O08644	Ephb6,Cekl	1000	1000			3	6	6	110.1	Ephrin type-B receptor 6
O08665	Sema3a,Semad,SemD	1000	1000			3	6	6	88.8	Semaphorin-3A
O35454	Clcn6,Clc6	1000	1000			2	6	6	97.0	Chloride transport protein 6
O35544	Slc1a6,Eaat4	1000	1000			3	6	6	60.8	Excitatory amino acid transporter 4
O88809	Dcx,Dcn	1000	1000			2	6	6	40.6	Neuronal migration protein doublecortin
P02089	Hbb-b2	1000	1000			2	6	6	15.9	Hemoglobin subunit beta-2
P15975	Usp53,Phx3	1000	1000			3	6	6	119.3	Inactive ubiquitin carboxyl-terminal hydrolase 53
P28028	Braf,B-raf	1000	1000			2	6	6	88.8	Serine/threonine-protein kinase B-raf
P35438	Grin1,Glurz1	1000	1000			2	6	6	105.5	Glutamate receptor ionotropic, NMDA 1
P35569	Irs1,Irs-1	1000	1000			2	6	6	130.7	Insulin receptor substrate 1
P97855	G3bp1,G3bp	1000	1000			3	6	6	51.8	Ras GTPase-activating protein-binding protein 1
P97950	Rab33a,Rabs10	1000	1000			2	6	6	26.5	Ras-related protein Rab-33A
Q5PR73	Diras2	1000	1000			2	6	6	22.5	GTP-binding protein Di-Ras2
Q68EF4	Gmm4,Gprc1d,Mglur4	1000	1000			3	6	6	101.8	Metabotropic glutamate receptor 4
Q6PGF3	Med16,Thrap5	1000	1000			2	6	6	91.8	Mediator of RNA polymerase II transcription subunit 16

Table S1 (continued 7/8)

532/2507 proteins	Gene & Synonyms	anti-cateninDelta2 antibody/IgG						Total Pept.	MW (kDa)	Description
		Ratio	Log2	Adj. p-value	CV %	Dist. pept. used	Pept. used			
Q78FY7	Snd1	1000	1000			3	6	6	102.1	Staphylococcal nuclease domain-containing protein 1
Q8BFZ2	Plpp1,Kiaa4247,Lppr1,Prg3	1000	1000			2	6	6	35.9	Lipid phosphate phosphatase-related protein type 1
Q8CGM1	Bai2	1000	1000			3	6	6	169.9	Adhesion G protein-coupled receptor B2
Q8K1E0	Stx5,Stx5a	1000	1000			2	6	6	39.7	Syntaxin-5
Q9CS84	Nrxn1,Kiaa0578	1000	1000			2	6	6	166.2	Neurexin-1
Q9D032	Ssbp3,Last,Ssdp1	1000	1000			2	6	6	40.4	Single-stranded DNA-binding protein 3
Q9D211	Cdkn2aipn1,D11Ert497e,MNCb-1520	1000	1000			3	6	6	13.2	CDKN2AIP N-terminal-like protein
Q9EQH3	Vps35,Mem3	1000	1000			4	6	6	91.7	Vacuolar protein sorting-associated protein 35
Q9WTX2	Prkra,Rax	1000	1000			3	6	6	34.4	Interferon-inducible double-stranded RNA-dependent protein kinase activator A
Q9WV66	March7,Axot	1000	1000			3	6	6	76.6	E3 ubiquitin-protein ligase MARCH7
Q9Z1Q2	Abhd16a,Bat5,Ng26	1000	1000			3	6	6	63.1	Abhydrolase domain-containing protein 16A
Q9DBR3	Armcb	9.6976033	3.2776282	0.0147718		2	6	6	75.4	Armadillo repeat-containing protein 8
P61750	Arf4	9.1196705	3.1889817	0.0244229		1	6	6	20.4	ADP-ribosylation factor 4
P43024	Cox6a1,Cox6al	8.1578871	3.0281955	0.0292853		1	6	6	12.4	Cytochrome c oxidase subunit 6A1, mitochondrial
B0F2B4	Nlgn4L,Nlgn4,Nlgn4x	1000	1000			2	5	5	97.3	Neurexin-4-like
O08756	Hsd17b10,Erab,Hadh2	1000	1000			2	5	5	27.4	3-hydroxyacyl-CoA dehydrogenase type-2
O35083	Agpat1	1000	1000			2	5	5	31.7	1-acyl-sn-glycerol-3-phosphate acyltransferase alpha
O89079	Cope,Cope1	1000	1000			2	5	5	34.6	Coatamer subunit epsilon
P51830	Adcy9	1000	1000			2	5	5	151.0	Adenylate cyclase type 9
P56135	Atp5j2	1000	1000			2	5	5	10.3	ATP synthase subunit f, mitochondrial
P57716	Ncstn	1000	1000			2	5	5	78.5	Nicastrin
P70302	Stim1,Sim	1000	1000			2	5	5	77.6	Stromal interaction molecule 1
Q0VGY8	Tanc1	1000	1000			2	5	5	200.8	Protein TANC1
Q3U6U5	Gtpbp6	1000	1000			2	5	5	56.5	Putative GTP-binding protein 6
Q3UHK1	Slc2a13	1000	1000			2	5	5	69.1	Proton myo-inositol cotransporter
Q3UQ84	Tars2,Tars1	1000	1000			2	5	5	81.7	Threonine--tRNA ligase, mitochondrial
Q5NCF2	Trappc1	1000	1000			2	5	5	16.9	Trafficking protein particle complex subunit 1
Q61418	Clcn4,Clc4,Clcn4-2	1000	1000			2	5	5	83.7	H(+)/Cl(-) exchange transporter 4
Q61474	Msi1,Msi1h	1000	1000			2	5	5	39.1	RNA-binding protein Musashi homolog 1
Q80U95	Ube3c,Kiaa0010,Kiaa10	1000	1000			3	5	5	124.0	Ubiquitin-protein ligase E3C
Q811U4	Mfn1	1000	1000			2	5	5	83.7	Mitofusin-1
Q8BGD5	Cpt1c	1000	1000			3	5	5	90.0	Carnitine O-palmitoyltransferase 1, brain isoform
Q8BU31	Rap2c	1000	1000			2	5	5	20.7	Ras-related protein Rap-2c
Q8K4Q7	Cerk	1000	1000			2	5	5	59.8	Ceramide kinase
Q91WD5	Ndufs2	1000	1000			2	5	5	52.6	NADH dehydrogenase [ubiquinone] iron-sulfur protein 2, mitochondrial
Q924T7	Rnf31,Paul	1000	1000			2	5	5	119.3	E3 ubiquitin-protein ligase RNF31
Q99KI3	Emc3,Tmem111	1000	1000			2	5	5	30.0	ER membrane protein complex subunit 3
Q9CQV8	Ywhab	1000	1000			2	5	5	28.1	14-3-3 protein beta/alpha
Q9D1D4	Tmed10,Tmp21	1000	1000			2	5	5	24.9	Transmembrane emp24 domain-containing protein 10
Q9D2E2	Toe1	1000	1000			2	5	5	56.9	Target of EGR1 protein 1
Q9D9V7	Dennd6b	1000	1000			2	5	5	66.6	Protein DENND6B
Q9EPF9	Atp13a1,Atp13a	1000	1000			2	5	5	132.4	Manganese-transporting ATPase 13A1
Q9WVJ0	Kcnh3,Elk2	1000	1000			2	5	5	117.7	Potassium voltage-gated channel subfamily H member 3
Q9Z0V2	Kcnd2,Kiaa1044,MNCb-7013	1000	1000			2	5	5	70.6	Potassium voltage-gated channel subfamily D member 2
Q9Z101	Pard6a,Par6a	1000	1000			2	5	5	37.3	Partitioning defective 6 homolog alpha
Q9Z2W9	Gria3,Glur3,Kiaa4184	1000	1000			2	5	5	100.5	Glutamate receptor 3
P63137	Gabbr2,Gabbr-2	8.7121442	3.1230278	0.0212902		1	5	5	59.2	Gamma-aminobutyric acid receptor subunit beta-2

Table S1 (continued 8/8)

532/2507 proteins	Gene & Synonyms	anti-cateninDelta2 antibody/IgG						Total Pept.	MW (kDa)	Description
		Ratio	Log2	Adj. p- value	CV %	Dist. pept. used	Pept. used			
Q91Y02	Pcdhb18	2.7630072	1.4662393	0.0296492		1	5	5	87.0	Protocadherin beta-18

ANNEX 1

***Trans*-Synaptic Signaling through the Glutamate Receptor Delta-1 Mediates Inhibitory Synapse Formation in Cortical Pyramidal Neurons**

Highlights

- GluD1 mediates the formation and specification of inhibitory synapses in the cortex
- GluD1 forms *trans*-synaptic interactions via Cbln4, a protein secreted by SST⁺ INs
- GluD1 elicits agonist-dependent postsynaptic signaling via ARHGEF12 and PPP1R12A
- GluD1 is a maverick iGluR operating through non-ionotropic mechanisms

Authors

Matteo Fossati, Nora Assendorp, Olivier Gemin, ..., Guillaume Arras, Damarys Loew, Cécile Charrier

Correspondence

cecile.charrier@ens.fr

In Brief

Fossati et al. show that, in stark contrast to other iGluRs, the glutamate receptor delta-1 (GluD1) operates at inhibitory, rather than excitatory, synapses in the cortex. GluD1 mediates *trans*-synaptic signaling governing the formation of synapses between specific interneurons and pyramidal neurons.

Trans-Synaptic Signaling through the Glutamate Receptor Delta-1 Mediates Inhibitory Synapse Formation in Cortical Pyramidal Neurons

Matteo Fossati,^{1,3,4} Nora Assendorp,¹ Olivier Gemin,¹ Sabrina Colasse,¹ Florent Dingli,² Guillaume Arras,² Damarys Loew,² and Cécile Charrier^{1,5,*}

¹Institut de Biologie de l'Ecole Normale Supérieure (IBENS), Ecole Normale Supérieure, CNRS, INSERM, PSL Research University, 75005 Paris, France

²Institut Curie, PSL Research University, Centre de Recherche, Laboratoire de Spectrométrie de Masse Protéomique, 75248 Paris Cedex 05, France

³Present address: CNR – Institute of Neuroscience, 20129 Milano, Italy

⁴Present address: Humanitas Clinical and Research Center, 20089 Rozzano MI, Italy

⁵Lead Contact

*Correspondence: cecile.charrier@ens.fr

<https://doi.org/10.1016/j.neuron.2019.09.027>

SUMMARY

Fine orchestration of excitatory and inhibitory synaptic development is required for normal brain function, and alterations may cause neurodevelopmental disorders. Using sparse molecular manipulations in intact brain circuits, we show that the glutamate receptor delta-1 (GluD1), a member of ionotropic glutamate receptors (iGluRs), is a postsynaptic organizer of inhibitory synapses in cortical pyramidal neurons. GluD1 is selectively required for the formation of inhibitory synapses and regulates GABAergic synaptic transmission accordingly. At inhibitory synapses, GluD1 interacts with cerebellin-4, an extracellular scaffolding protein secreted by somatostatin-expressing interneurons, which bridges postsynaptic GluD1 and presynaptic neurexins. When binding to its agonist glycine or D-serine, GluD1 elicits non-ionotropic postsynaptic signaling involving the guanine nucleotide exchange factor ARHGEF12 and the regulatory subunit of protein phosphatase 1 PPP1R12A. Thus, GluD1 defines a *trans*-synaptic interaction regulating postsynaptic signaling pathways for the proper establishment of cortical inhibitory connectivity and challenges the dichotomy between iGluRs and inhibitory synaptic molecules.

INTRODUCTION

Synapses constitute the elementary functional units of the brain. They convey excitatory or inhibitory signals that need to be coordinated in space and time for optimal brain function (Mullins et al., 2016; Nelson and Valakh, 2015). Excitatory and inhibitory synapses in the mammalian brain mainly use glutamate and gamma-aminobutyric acid (GABA) as a neurotransmitter, respectively. They are multi-molecular nanomachines

composed of almost exclusive sets of proteins (Krueger-Burg et al., 2017; Sheng and Kim, 2011; Tyagarajan and Fritschy, 2014). Yet they share the same basic organization, which ensures the efficacy and fine-tuning of synaptic transmission. The organization of synapses relies on transient, highly regulated interactions between various categories of proteins (neurotransmitter receptors, scaffolding proteins, adhesion proteins, signaling molecules, and cytoskeleton elements) and accommodates a great level of molecular diversity (Choquet and Triller, 2013; Emes and Grant, 2012; Sheng and Hoogenraad, 2007; Tyagarajan and Fritschy, 2014; Ziv and Fisher-Lavie, 2014). The molecular diversity of synapses enables the establishment of complex neuronal networks: it specifies their functional properties and shapes the transfer of information between neurons throughout the brain. Hence, synaptic dysfunctions cause a wide range of neurodevelopmental and psychiatric disorders, such as epilepsy, autisms, or schizophrenia (Bourgeron, 2015; Mullins et al., 2016; Nelson and Valakh, 2015; Ting et al., 2012; Zoghbi and Bear, 2012). *Trans*-synaptic molecular interactions critically contribute to both the development and diversification of synaptic connections. They instruct the formation of synapses following initial contact (McAllister, 2007; Missler et al., 2012), match pre- and post-synaptic neurons (Berns et al., 2018; de Wit and Ghosh, 2016), control the recruitment of neurotransmitter receptors and postsynaptic scaffolding proteins (Aoto et al., 2013; Bemben et al., 2015; Fukata et al., 2006; Lovero et al., 2015; Mondin et al., 2011; Nam and Chen, 2005; Pouloupoulos et al., 2009), and regulate synaptic plasticity (Bemben et al., 2015; Jang et al., 2017; Tai et al., 2008; Yuzaki and Aricescu, 2017). Nonetheless, frequent discrepancies between *in vitro* and *in vivo* studies have made the role of some *trans*-synaptic molecular interactions difficult to precisely delineate. Furthermore, the scarcity of information on how *trans*-synaptic signals are transduced in the post-synaptic neuron stymies our understanding of the molecular logic governing the assembly of synaptic connections.

Individual synaptic proteins may operate through a diversity of modalities. Recently, it has emerged that ionotropic glutamate receptors (iGluRs), which are the main excitatory

neurotransmitter receptors in the CNS, do not solely operate through ionotropic mechanisms (Dore et al., 2015; Rodríguez-Moreno and Sihra, 2007; Yuzaki and Aricescu, 2017). At least some iGluRs engage in *trans*-synaptic interactions along with conventional cell adhesion molecules (CAMs) (Matsuda et al., 2010, 2016; Uemura et al., 2010) or mediate non-ionotropic signaling critical for synaptic development and plasticity (Babiec et al., 2014; Carter and Jahr, 2016; Dore et al., 2015; Grabauskas et al., 2007; Hayashi et al., 1999; Kakegawa et al., 2011; Lerma and Marques, 2013; Nabavi et al., 2013; Saglietti et al., 2007; Stein et al., 2015). Alternative functions of iGluRs are best characterized for the glutamate receptor delta-2 (GluD2), an iGluR of the delta subfamily (comprising GluD1 and GluD2 receptor subunits, encoded by the genes *grid1* and *grid2*) predominantly expressed in the cerebellum (Araki et al., 1993). GluD2 is confined in the postsynaptic membrane of excitatory synapses between parallel fibers (PFs) and Purkinje cells (PCs). It contributes to synaptic adhesion by interacting with presynaptic neurexins containing an insert in the splice site 4 through the extracellular scaffolding proteins cerebellins (Cblns), presynaptically secreted molecules that belong to the C1q family of the classical complement pathway (Südhof, 2017; Uemura et al., 2010; Yuzaki, 2017, 2018). This *trans*-synaptic interaction controls the specification and maintenance of PF-PC synapses. In addition, activation of GluD2 by its agonist initiates signaling cascades regulating the local accumulation of α -amino-3-hydroxy-5-methyl-4-isoxazolepropionic acid (AMPA) receptors and long-term depression (Kakegawa et al., 2011; Yuzaki and Aricescu, 2017). GluD1 can also form triads with Cblns and neurexins (Yasumura et al., 2012; Yuzaki and Aricescu, 2017). It is widely expressed in the neocortex, hippocampus, striatum, and cerebellum, where its expression is strongly upregulated during the period of synaptogenesis and remains high in adults (Hepp et al., 2015; Konno et al., 2014). GluD1 has been implicated in the formation of excitatory synapses in the cerebellum (Konno et al., 2014) and hippocampus (Tao et al., 2018) and in pruning in the hippocampus and medial prefrontal cortex (Gupta et al., 2015). Other studies have suggested a role in the firing of dopaminergic neurons or at inhibitory synapses (Benamer et al., 2018; Ryu et al., 2012; Yasumura et al., 2012). Notwithstanding, GluD1 function remains poorly understood.

In the present study, we have investigated the role of GluD1 in the development of excitatory and inhibitory synapses in the somato-sensory cortex. By depleting GluD1 *in vivo* in a few layer 2/3 cortical pyramidal neurons (CPNs) using sparse *in utero* electroporation (IUE), we demonstrate that GluD1 regulates the formation of inhibitory synapses in dendrites as well as inhibitory synaptic transmission. In contrast, GluD1 is dispensable for the formation and maintenance of excitatory synapses in CNPs. Using an *in vivo* structure/function analysis, we demonstrate that the regulation of inhibitory synapses by GluD1 requires *trans*-synaptic interaction via Cbln4, an extracellular scaffolding protein secreted by somatostatin-expressing (SST⁺) interneurons (INs) (Favuzzi et al., 2019), activation of the receptor by its endogenous agonists glycine and D-Serine, and post-synaptic signaling via the intracellular C-terminal tail of the receptor. Using mass spectrometry, we characterize GluD1 interactome in developing synapses. We show that GluD1 serves as a hub for

molecules implicated in inhibitory synaptogenesis, and we identify two major partners of GluD1, the signaling molecules rho guanine nucleotide exchange factor 12 (ARHGEF12) and protein phosphatase 1 regulatory subunit 12A (PPP1R12A), as critical regulators of inhibitory synapse formation in CPNs. Together, our results define a *trans*-synaptic signaling pathway centered on an atypical iGluR for the formation and specification of cortical inhibitory circuits.

RESULTS

GluD1 Is Selectively Required for the Formation of Inhibitory Synapses

In order to assess the role of GluD1 in synaptic development, we used cortex-directed IUE at embryonic day (E)15.5. IUE at E15.5 allows the sparse and specific modification of layer 2/3 CPNs in their intact environment and the dissection of cell autonomous mechanisms operating at synapses *in vivo* (Figure 1A). We analyzed the consequences of GluD1 depletion or overexpression on excitatory and inhibitory synapses formed on oblique apical dendrites of layer 2/3 CPNs of the somato-sensory cortex using a morphometric approach (Figure 1A). We first used dendritic spines, the postsynaptic site of the majority of excitatory synaptic inputs in the brain (Bourne and Harris, 2008; Yuste, 2013), and clusters of PSD-95, a major scaffolding protein of excitatory synapses (Sheng and Hoogenraad, 2007), as a proxy for excitatory synapses (Figure 1B). We found that GluD1 depletion using short hairpin RNAs (shRNAs) (shGluD1; Figure S1A) did not affect the density of dendritic spines in juvenile (postnatal day [P]20–22) or adult (P > 69) mice (102% \pm 3% and 105% \pm 5% of control in juvenile and adult neurons respectively; Figures 1B–1D) or the density of endogenous PSD-95 clusters visualized using EGFP-tagged fibronectin intrabodies generated with mRNA display (FingR) (Gross et al., 2013) (94% \pm 5% of control; Figures 1E and 1F). GluD1 overexpression, however, decreased spine density to 75% \pm 4% of the control value (Figures 1B and 1C). These results suggest that GluD1 is not necessary for the formation or maintenance of excitatory synapses in layer 2/3 CPNs, though GluD1 may constrain their number if upregulated.

We then assessed the role of GluD1 at inhibitory synapses. To that aim, we expressed small amounts of fluorescent (EGFP-tagged) gephyrin (Figure 1A), the core component of inhibitory postsynaptic scaffolds (Krueger-Burg et al., 2017; Tyagarajan and Fritschy, 2014). This approach has been shown to reliably label inhibitory synaptic contacts without affecting synaptic development or inhibitory neurotransmission (Chen et al., 2012; Fossati et al., 2016; van Versendaal et al., 2012). In juvenile mice, GluD1 knockdown (KD) using shRNAs decreased the density of gephyrin clusters compared to control neurons (77% \pm 4% of control; Figures 1G and 1H; Figure S2). Normal gephyrin cluster density was rescued by co-electroporating shGluD1 with a KD-resistant GluD1 construct (GluD1⁺; Figures 1G and 1H; Figure S1A). Remarkably, the decrease in gephyrin cluster density induced by GluD1 KD was maintained in adults (79% \pm 4% of control; Figure 1I), indicating that the loss of inhibitory synapses was not compensated over time. To further substantiate the role of GluD1 at inhibitory synapses, we knocked out *grid1* in single cells using the CRISPR-Cas9 system. We expressed

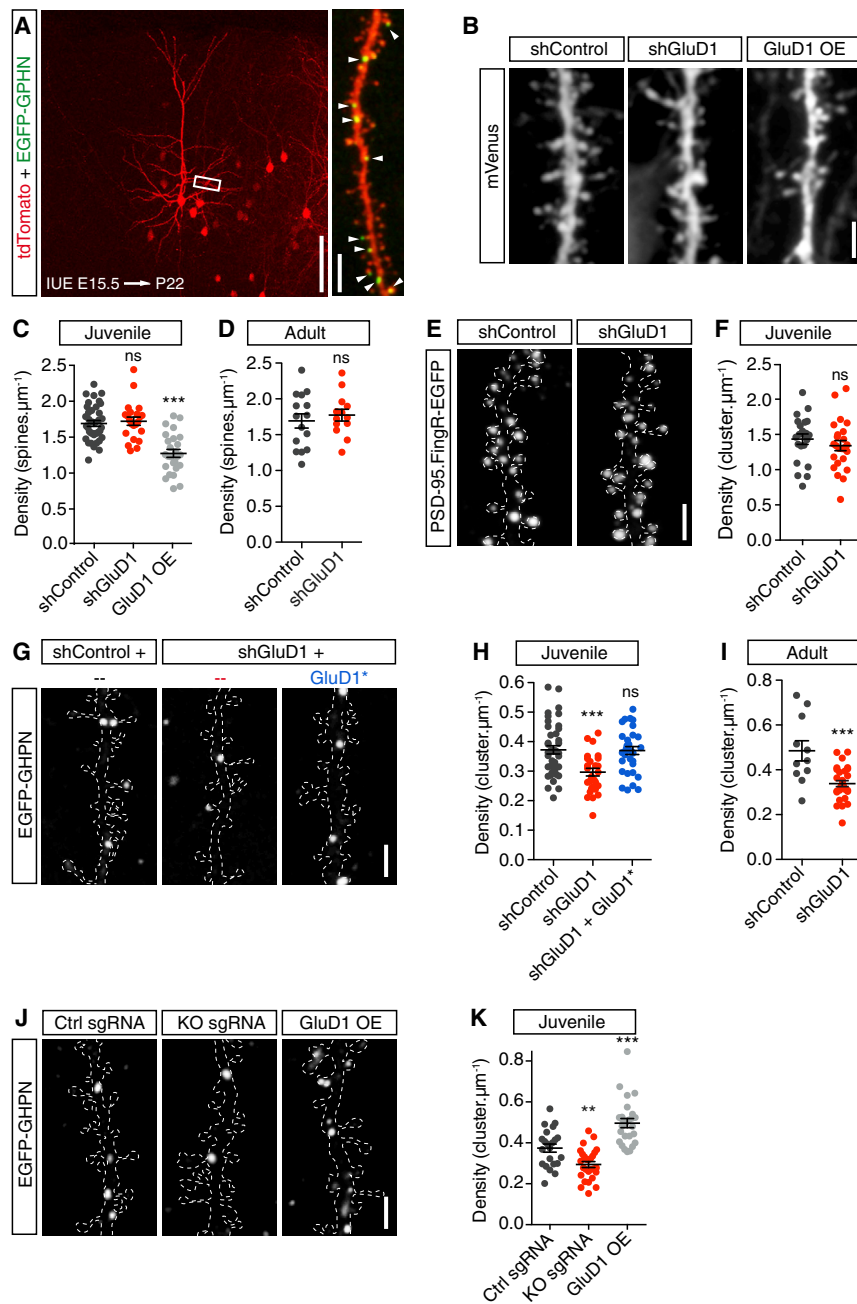


Figure 1. Selective Control of Inhibitory Synapse Density by GluD1 in CPNs

(A) Sparse labeling of layer 2/3 CPNs after *in utero* electroporation (IUE) with soluble tdTomato (red) and EGFP-gephyrin (EGFP-GPHN, green). Arrowheads in the enlarged area highlight inhibitory synapses in oblique apical dendrites. E15.5, embryonic day 15.5; P22: postnatal day 22. Scale bars: 100 μ m (left) and 5 μ m (right).

(B) Segments of dendrites expressing shControl or shGluD1 or overexpressing (OE) GluD1 along with mVenus to visualize dendritic spines in juvenile mice. Scale bar: 2 μ m.

(C and D) Quantification of dendritic spine density in juvenile (C) and adult mice (D). Juveniles: $n_{shControl} = 38$, $n_{shGluD1} = 22$, $n_{GluD1 OE} = 26$. Adults: $n_{shControl} = 15$, $n_{shGluD1} = 13$.

(E) Segments of dendrites expressing shControl or shGluD1 along with PSD95.FingR-EGFP in juvenile mice. Dashed lines define the contours of tdTomato fluorescence. Scale bar: 2 μ m.

(F) Quantification of PSD-95 cluster density. $n_{shControl} = 21$, $n_{shGluD1} = 24$.

(G) EGFP-gephyrin clusters in representative segments of dendrites expressing shControl, shGluD1, or shGluD1 together with shGluD1-resistant GluD1* in juvenile mice. Scale bar: 2 μ m. (H and I) Quantifications of gephyrin cluster density in juvenile (H) and adult mice (I). Juveniles: $n_{shControl} = 41$, $n_{shGluD1} = 30$, $n_{shGluD1 + GluD1*} = 32$. Adults: $n_{shControl} = 11$, $n_{shGluD1} = 30$.

(J) Segments of dendrites illustrating the effects of Crispr-mediated *Grid1* knockout (KO) and GluD1 OE on gephyrin cluster density. Ctrl sgRNA, control sgRNA; KO sgRNA, *Grid1*-targeting sgRNAs. Scale bar: 2 μ m.

(K) Quantification of gephyrin cluster density in the conditions described above. $n_{Ctrl sgRNA} = 22$, $n_{KO sgRNA} = 27$, and $n_{GluD1 OE} = 26$.

Statistics: bars indicate mean \pm SEM, ns: $p > 0.05$, ** $p < 0.01$, *** $p < 0.001$. One-way ANOVA test followed by Tukey's post test in (C) and (H); unpaired t test in (D), (F), and (K); and Mann-Whitney test for the comparison of GluD1 OE in K with corresponding control (shControl) in (H).

the enhanced specificity espCas9(1.1) (Slaymaker et al., 2016) and a combination of two guide RNAs (gRNAs) using IUE. In *grid1* knockout (KO) neurons, the density of gephyrin clusters was decreased by $22\% \pm 5\%$ compared to control neurons expressing espCas9(1.1) with mismatched gRNAs (Figures 1J and 1K), which is consistent with GluD1 KD experiments with shRNAs. In line with these results, GluD1 overexpression increased the density of gephyrin clusters along dendrites by $33\% \pm 4\%$ (Figures 1J and 1K).

To test the physiological consequences of GluD1 inactivation on synaptic transmission, we performed whole-

cell patch-clamp recording in electroporated GluD1-depleted neurons and in neighboring non-electroporated control neurons (Figure 2A). We compared miniature excitatory and inhibitory post-synaptic currents (mEPSCs and mIPSCs, respectively) in brain slices from juvenile mice (Figure 2B). In line with the morphological data, GluD1 KD did not affect the amplitude or the frequency of mEPSCs ($98\% \pm 8\%$ and $100\% \pm 4\%$ of control, respectively) (Figures 2B–2D). In contrast, GluD1 KD slightly increased the amplitude of mIPSCs and decreased their frequency by $\approx 35\%$ (Figures 2B, 2E, and 2F), which is consistent with the reduced gephyrin cluster density observed in the oblique dendrites of GluD1 KD and KO neurons. We conclude that GluD1 in CPNs is selectively required for the formation of inhibitory synapses. It regulates both the

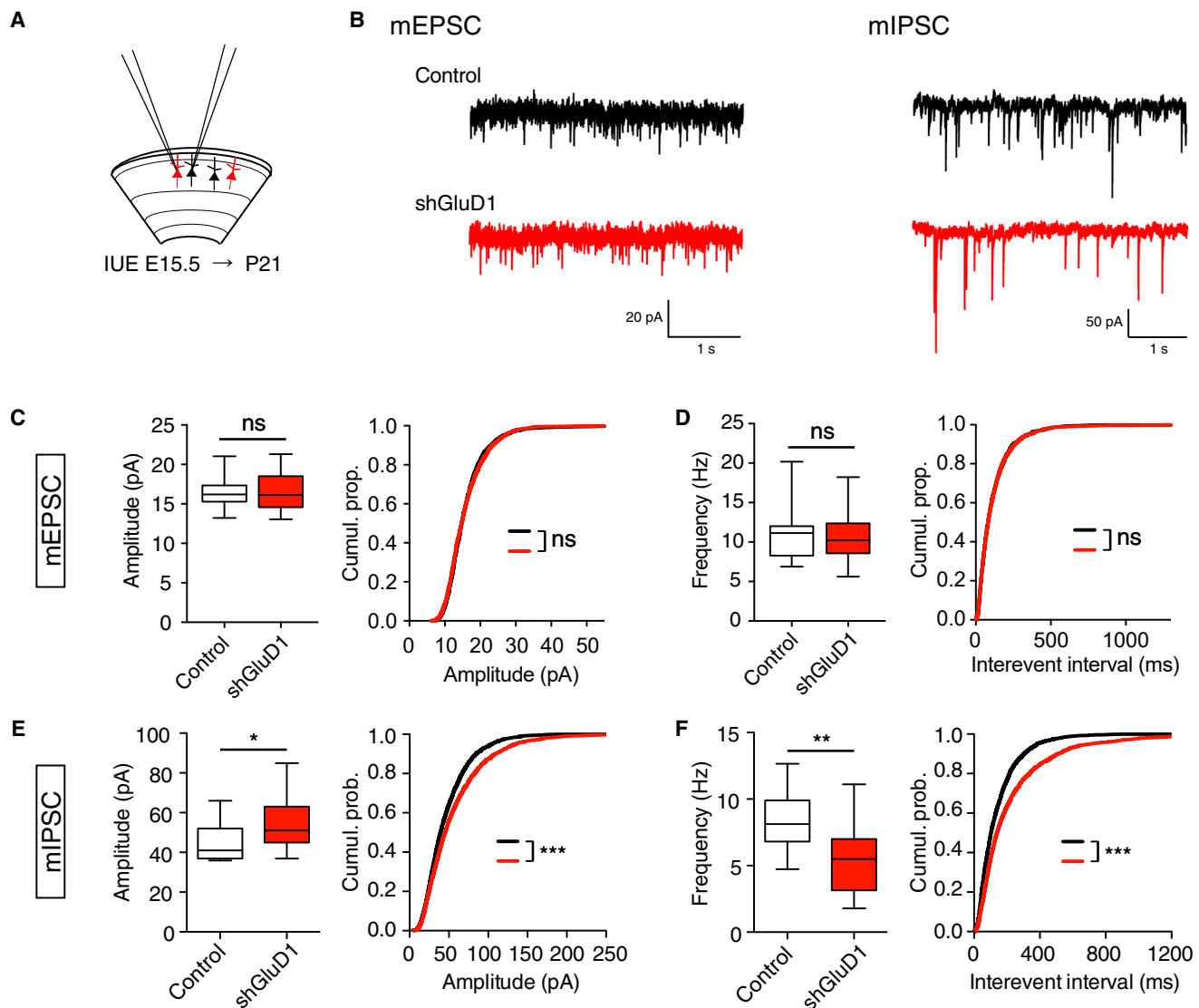


Figure 2. GluD1 Regulates Inhibitory Synaptic Transmission

(A) Schematic: recording of electroporated layer 2/3 CPN expressing shGluD1 with tdTomato (red) and neighboring control neuron (black) from juvenile mouse brain slice.

(B) Representative traces of mEPSCs and mIPSCs in control and shGluD1-electroporated neurons.

(C and D) Quantification of mEPSC amplitude (C) and frequency (D). Boxplots (left) show the distribution of the mean value per cell. $n = 14$ in both conditions. Cumulative distributions (right) of the amplitudes and interevent intervals of the first 200 events of each cell.

(E and F) Same as (C) and (D) for mIPSCs. $n = 15$ in both conditions.

Statistics: ns $p > 0.05$, * $p < 0.05$, ** $p < 0.01$, *** $p < 0.001$, Mann-Whitney test.

assembly of the gephyrin-based postsynaptic scaffold and inhibitory synaptic transmission.

GluD1 Localizes to Inhibitory Postsynaptic Sites

It is unexpected for a member of the iGluR family to control the formation of inhibitory synapses. Therefore, we asked whether GluD1 accumulates at inhibitory synapses. To answer this question, we performed immunohistochemistry in brain slices from juvenile mice. GluD1 fluorescent puncta were frequently associated with gephyrin clusters in the upper layers of the so-

mato-sensory cortex (Figure 3A). To determine the precise subcellular localization of GluD1, we employed immuno-electron microscopy (EM). In cortical layer 2/3, inhibitory synapses represent only 10% of the total number of synapses, and they are “symmetrical” when observed in EM, meaning that they do not show the electron-dense post-synaptic differentiation facilitating the detection of excitatory synapses. To unambiguously identify inhibitory synapses, we performed double immunostaining of the vesicular GABA transporter (VGAT) and GluD1 (Figure 3B). We used diaminobenzidine (DAB) to reveal

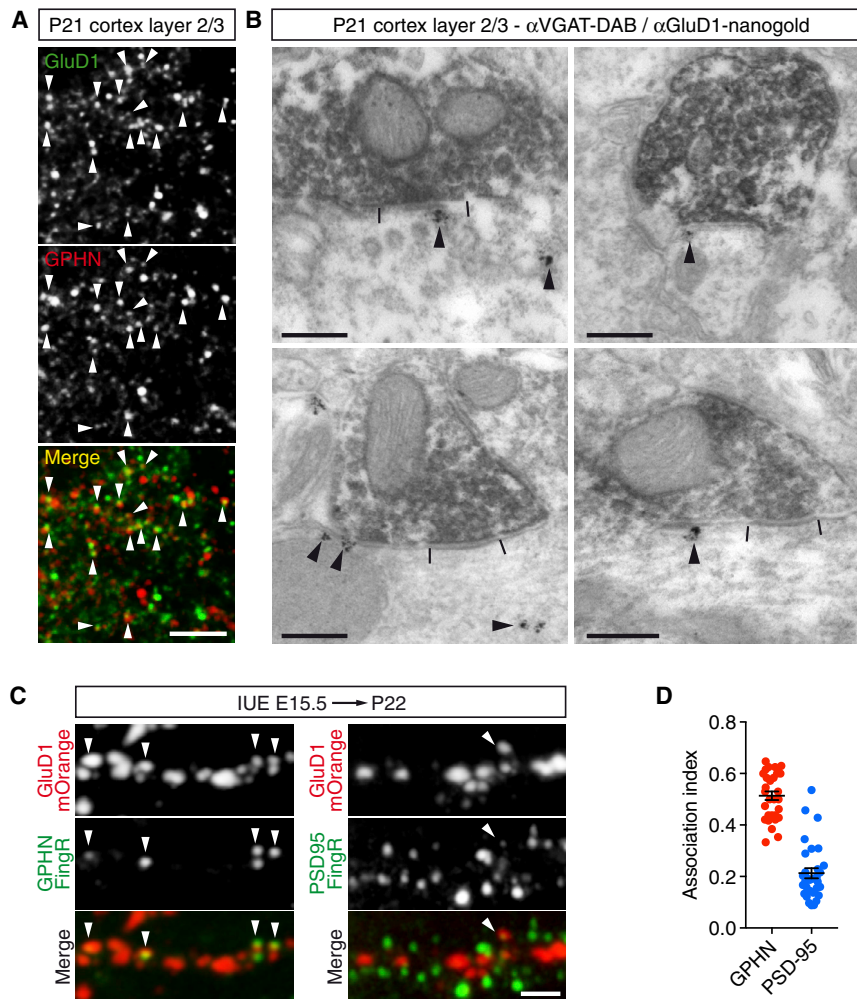


Figure 3. GluD1 Localizes to Inhibitory Synapses

(A) Representative immunofluorescence image of P21 cortical slices stained with anti-GluD1 (green) and anti-gephyrin (red) antibodies. Arrowheads indicate the association between GluD1- and GPHN-positive clusters. Scale bar: 5 μ m.

(B) Electron micrographs showing GluD1 (stained using nanogold particles and silver enhancement) and VGAT (revealed with diaminobenzidine-positive) immunoreactivity in P21 layer 2/3 cortices. As indicated by the arrowheads, GluD1 was detected in front of inhibitory presynaptic terminals (top left image), or lateral to the active zone (delimited by two bars, other images) and in intracellular compartments (left images). Scale bars: 250 nm.

(C) Segments of oblique apical dendrites from P22 neurons *in utero* electroporated with GluD1-mOrange and GPHN.FingR-EGFP or PSD95.FingR-EGFP. Arrowheads display the association between GluD1 and indicated synaptic markers. Scale bar: 2 μ m.

(D) Scatterplot showing the fraction of gephyrin and PSD-95 clusters associated with GluD1-mOrange puncta (association index). Gephyrin, $n = 31$; PSD-95, $n = 30$. Bars indicate mean \pm SEM.

Inhibitory Synapse Formation Requires GluD1 Binding to Cbln and Activation by Glycine or D-Serine

To determine the molecular basis for GluD1-mediated regulation of inhibitory synapses, we took advantage of the recent crystallographic analysis of the interactions between GluD, Cbln, and neuroligin and the abundant literature on the structure/function of GluD2

VGAT. DAB oxidation forms electron-dense precipitates that largely stained VGAT-positive inhibitory presynaptic terminals. To visualize and precisely localize GluD1 in cortical tissue, we used nanogold particles and silver enhancement. Nanogold particles corresponding to GluD1 were detected in front of VGAT-positive presynaptic terminals and in intracellular compartments in dendrites (Figure 3B). Within synapses, GluD1 was frequently observed in postsynaptic membrane domains located at the edge or in the periphery of the active zone, which is consistent with the distribution profile of other synaptic adhesion molecules (Triller and Choquet, 2003; Uchida et al., 1996). To quantify the proportion of synapses containing GluD1, we electroporated mOrange-tagged GluD1 together with EGFP-tagged GPHN or PSD95 FingRs and a soluble blue fluorescent protein to visualize neuronal morphology (Figure 3C, blue filler not shown). In oblique apical dendrites of layer 2/3 CPNs, $\approx 50\%$ of inhibitory synapses contained GluD1 (Figure 3D). In contrast, GluD1 was rarely associated with excitatory synapses ($21\% \pm 2\%$) (Figure 3D). Collectively, these results demonstrate the presence of GluD1 at inhibitory synapses and indicate that GluD1 directly operates at inhibitory synapses.

(Cheng et al., 2016; Elegheert et al., 2016; Kakegawa et al., 2007, 2009; Kuroyanagi and Hirano, 2010; Yuzaki and Aricescu, 2017). GluD1s, as all members of the iGluR family, are tetrameric receptors (Traynelis et al., 2010). Each subunit has a modular architecture. The extracellular region contains a distal N-terminal domain (NTD), followed by an agonist-binding domain (ABD). The NTD of the GluD receptor interacts with the extracellular scaffolding protein Cbln (Matsuda et al., 2010; Uemura et al., 2010), and their ABD binds to glycine and D-serine (but not glutamate) (Naur et al., 2007), as in some N-methyl-D-aspartate (NMDA) receptor subunits (Paoletti et al., 2013). The transmembrane domain (TMD) lines the pore of the ion channel. Finally, GluD1s contain a C-terminal cytoplasmic domain (CTD) regulating their trafficking and intracellular interactions (Kakegawa et al., 2008; Kohda et al., 2013). To assay the functional importance of known domains or molecular interactions, we generated key mutant forms of GluD1 (Figure 4B). We then used an *in utero* gene replacement strategy to inactivate endogenous *grid1* with shRNAs and replace it with individual mutant forms *in vivo* and throughout development (Fossati et al., 2016). This strategy prevents the formation of heteromers between wild-type and mutant subunits of GluD1, which could mask or attenuate

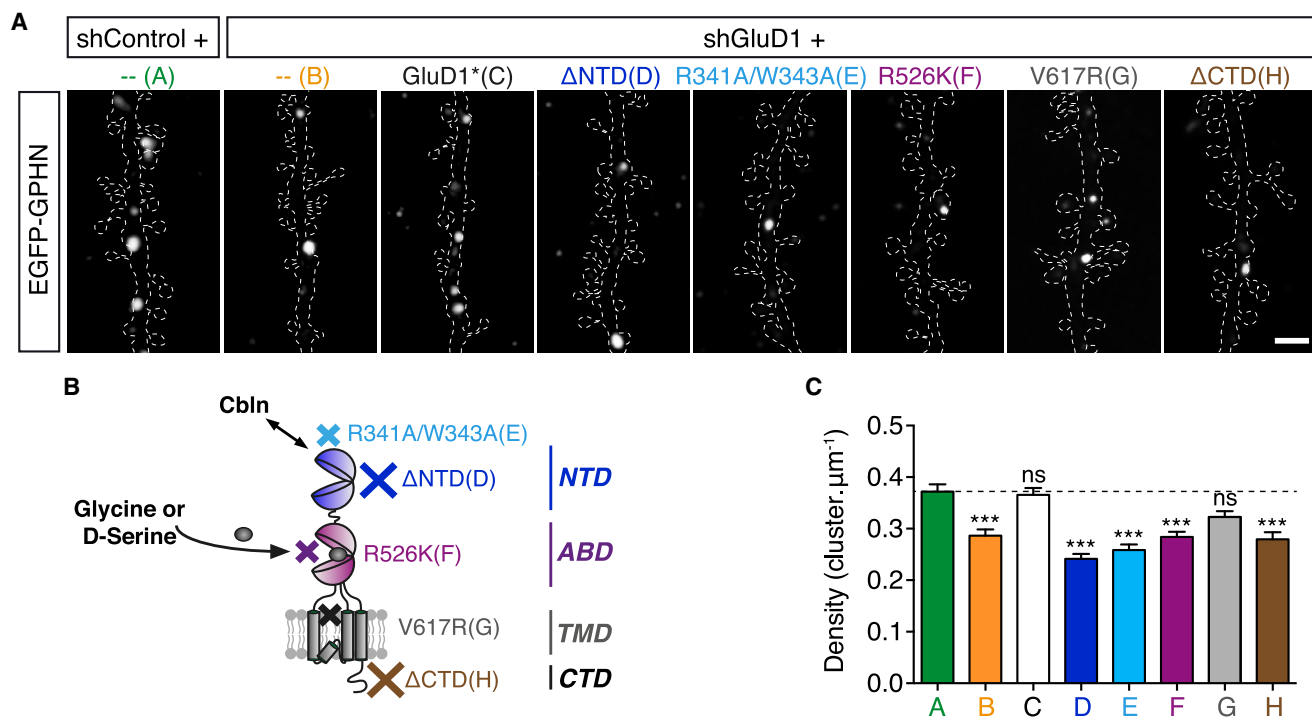


Figure 4. In Vivo Structure-Function Analysis of GluD1 Function at Inhibitory Synapses

(A) EGFP-gephyrin clusters in representative segments of oblique dendrites in control condition (shControl) or after *in utero* replacement of endogenous GluD1 with indicated mutants in P20–22 mice. Dashed lines, dendritic contours based on tdTomato fluorescence. Scale bar: 2 μ m.

(B) Schematic of a GluD1 subunit and localization of the indicated mutations. GluD1 receptors interact with Cbln bound to presynaptic neuroligin via their NTD and use glycine or D-serine as agonists. NTD, N-terminal domain; ABD, agonist-binding domain; TMD, transmembrane domain; CTD, C-terminal domain.

(C) Quantification of GPHN cluster density in conditions represented in (A).

Histogram represents means \pm SEM. Data corresponding to shControl, shGluD1, and shGluD1 + GluD1* are the same as in Figure 1G. $n_{shControl} = 41$, $n_{shGluD1} = 30$, $n_{shGluD1} + GluD1^* = 32$, $n_{shGluD1} + GluD1 \Delta NTD = 30$, $n_{shGluD1} + GluD1 R341A/W343A = 32$, $n_{shGluD1} + GluD1 R526K = 30$, $n_{shGluD1} + GluD1 V617R = 29$, $n_{shGluD1} + GluD1 \Delta CTD = 28$. ns $p > 0.05$, *** $p < 0.001$, determined by one-way ANOVA test followed by Tukey's post test.

some phenotypes. Importantly, all mutants were properly trafficked to the cell surface (Figure S3A).

We first examined whether GluD1 function involves *trans*-synaptic interaction via Cbln. To that aim, we replaced endogenous GluD1 with a Δ NTD mutant lacking the whole NTD. In juvenile mice, gephyrin cluster density in neurons expressing this mutant was lower than in control ($65\% \pm 4\%$ of control), suggesting that the NTD is critical for GluD1 function (Figures 4A and 4C). We then specifically disrupted GluD1 interaction with Cbln by introducing two point mutations in the NTD (R341A/W343A, Figure S3B; residues corresponding to R345 and W347 in GluD2; Elegheert et al., 2016). Replacement of GluD1 with the R341A/W343A mutant also led to a lower density of gephyrin clusters ($69\% \pm 4\%$ of control; Figures 4A and 4C), indicating that GluD1 interaction with the extracellular scaffolding protein Cbln is required for inhibitory synapse formation. Next, we tested whether the regulation of inhibitory synapses requires GluD1 gating by glycine/D-serine, ion-flux through GluD1 channel, and signaling via the CTD of the receptor. Replacement of GluD1 with a mutant containing an arginine to lysine substitution at position 526, which abolishes the affinity for glycine or D-serine (R526K mutant corresponding to position 530 in GluD2) (Kakegawa et al., 2009, 2011; Naur et al., 2007), decreased the

density of gephyrin clusters ($71\% \pm 4\%$ of control; Figures 4A and 4C), as observed after GluD1 KD. A similar effect was found with a mutant lacking the intracellular CTD ($75\% \pm 5\%$ of control; Figures 4A and 4C). In contrast, preventing ion flux through the pore with a single point mutation (V617R) (Ady et al., 2014; Kakegawa et al., 2007; Robert et al., 2002) did not interfere with the formation of inhibitory synapses (Figures 4A and 4C). Collectively, these results demonstrate that the control of inhibitory synapse formation by GluD1 in CPNs requires *trans*-synaptic interactions via Cbln and glycine/D-serine-dependent non-ionic postsynaptic mechanisms involving intracellular interactions via the C-terminal tail of the receptor.

GluD1 Specifies Synapses between SST⁺ INs and Layer 2/3 CPNs

We wondered if GluD1 mediates the formation of inhibitory synapses between layer 2/3 CPNs and specific classes of INs. In the cortex, distinct subtypes of INs express distinct isoforms of Cblns, with SST⁺ INs in upper cortical layers expressing Cbln4 and vasoactive intestinal peptide-positive (VIP⁺) INs expressing Cbln2 (Paul et al., 2017; Tasic et al., 2016). Therefore, we tested if Cbln2 and Cbln4 regulate the density of inhibitory synapses. To that end, adeno-associated viral vectors (AAVs) carrying an

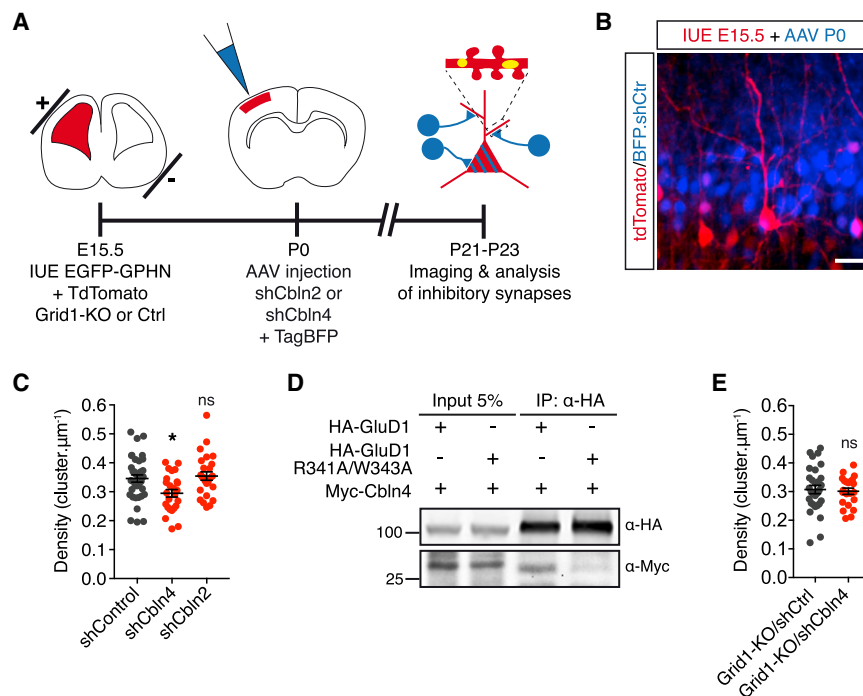


Figure 5. GluD1 Regulates Inhibitory Synaptogenesis via Cerebellin-4

(A) Schematic of the experimental workflow: neurons and inhibitory synapses were labeled using IUE at E15.5, which also allowed *grid1* knockout with Crispr. The lateral ventricle corresponding to the electroporated hemisphere was then injected with AAVs at P0 to knock down Cbln2 or Cbln4 with shRNAs. Inhibitory synapses were analyzed in juvenile mice.

(B) Representative image of a cortical slice derived from a juvenile mouse. Electroporated layer 2/3 CPNs are labeled with tdTomato. Infected neurons are labeled with TagBFP. Scale bar: 20 μm.

(C and E) Quantification of GPHN cluster density in neurons in the indicated conditions. $n_{\text{shControl}} = 37$, $n_{\text{shCbln4}} = 25$, $n_{\text{shCbln2}} = 26$, $n_{\text{GluD1-KO/shCtrl}} = 30$, $n_{\text{GluD1-KO/shCbln4}} = 22$. Bars indicate mean \pm SEM. ns $p > 0.05$, * $p < 0.05$, determined by one-way ANOVA test followed by Tukey's post test (C) or unpaired t test (E).

(D) Coimmunoprecipitation (coIP) in HEK cells of Myc-Cbln4 with wild-type HA-GluD1 or HA-GluD1 containing R341A/W343A mutation in the Cbln binding site.

shRNA directed against Cbln4, Cbln2, or a control shRNA (Figure S1D) were injected *in vivo* in the lateral ventricles of newborn pups previously electroporated *in utero* with EGFP-GPHN and tdTomato (Figures 5A and 5B). We then quantified the density of gephyrin clusters in sparse electroporated neurons surrounded by numerous infected cells (Figure 5B). In juvenile mice, Cbln4, but not Cbln2, inactivation significantly decreased the density of inhibitory synapses ($85\% \pm 4\%$ of control for shCbln4 and $102\% \pm 4\%$ for shCbln2; Figure 5C). GluD1 interacted with Cbln4 (Figure 5D), and Cbln4 KD did not further decrease the density of gephyrin clusters in *grid1* KO neurons ($98\% \pm 5\%$ of Grid1-KO/shCtrl neurons; Figure 5E), indicating that Cbln4 operates via GluD1. The role of Cbln4 at inhibitory synapses between SST⁺ INs and CPNs has recently been characterized in more detail by Favuzzi et al. (2019). Taken together, these results indicate that GluD1 specifies inhibitory cortical connectivity by mediating synaptogenesis between Cbln4-expressing SST⁺ INs and CPNs. This is compatible with the partial colocalization of GluD1 and gephyrin (Figures 3C and 3D) in oblique apical dendrites, which are also contacted by other classes of interneurons (Fishell and Kepecs, 2019).

Postsynaptic Signaling Controlling Inhibitory Synapse Formation

To determine the postsynaptic mechanisms through which GluD1 regulates the formation of inhibitory synaptic machineries, we performed an unbiased proteomic screen aimed at identifying GluD1 interacting partners at synapses. We employed subcellular fractionations from P15 mouse brains to enrich our samples in proteins associated with synaptic membranes and efficiently immunoprecipitate GluD1 (Figure 6A). The proteins co-immunoprecipitated with GluD1 (gene name *Grid1*) were separated by liquid chromatography and identified using tandem

mass spectrometry (LC-MS/MS) (Figures 6A and 6B; Table S1). We focused on the proteins that were the most represented in terms of the number of detections in LC-MS/MS biological triplicates relative to their molecular weight. GluD1 was strongly associated with regulators of GTPases (e.g., ARHGEF12 and SRGAP3) and regulators of protein phosphorylation (e.g., the serine/threonine phosphatase 1 regulatory subunit PPP1R12A and the serine/threonine protein kinase MRCK α , encoded *cdc42bpa*), pointing out the involvement of signaling pathways.

To determine the contribution of these proteins to the development of inhibitory synapses, we manipulated their expression *in vivo* using IUE. We first investigated the role of ARHGEF12 (also referred to as LARG), a guanine nucleotide exchange factor for RhoA (Chen et al., 1999). We generated a shRNA against *arhgef12* (shArhgef12) and an shRNA-resistant construct (ARHGEF12*; Figure S1B). In juvenile mice, sparse *arhgef12* KD decreased the density of gephyrin clusters to $79\% \pm 3\%$ of the control value (Figure 6C). Normal gephyrin cluster density was rescued by ARHGEF12* ($94\% \pm 3\%$). These data identify ARHGEF12 as a new determinant of inhibitory synapse formation in the dendrites of CPNs. We next considered the role of Slit-Robo Rho GTPase-activating proteins (SRGAPs). In LC-MS/MS, GluD1 was associated not only with SRGAP3, but also with SRGAP1 and SRGAP2 (Table S1). SRGAP3 and SRGAP2 have previously been shown to interact with gephyrin and regulate the development of inhibitory synapses in the hippocampus and the cortex, respectively (Fossati et al., 2016; Okada et al., 2011). We found that SRGAP2 inactivation decreases the cell surface expression of GluD1 in young (15 days *in vitro*), but not older (22–23 days *in vitro*), neurons (Figure S4), suggesting a developmental regulation of GluD1 trafficking.

We then assayed the role of MRCK α and PPP1R12A, two proteins likely to modulate the phosphorylation state of proteins

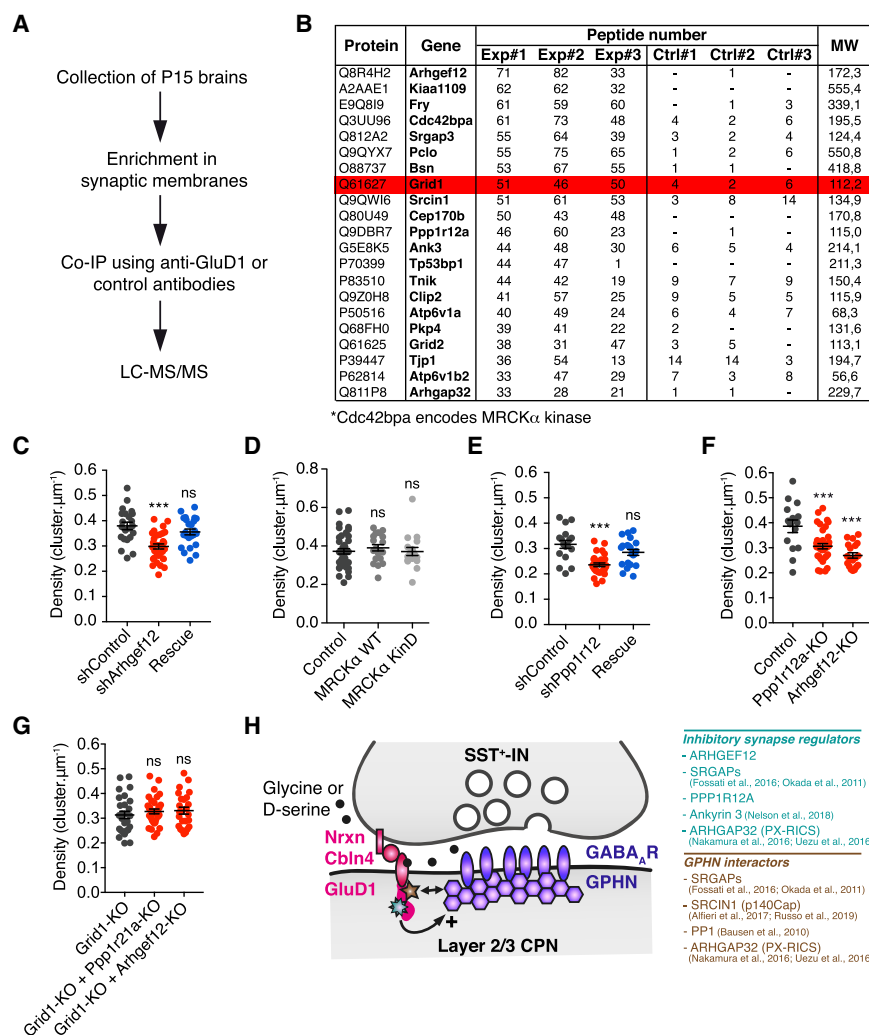


Figure 6. Signaling Pathways Regulated by GluD1 at Inhibitory Synapses

(A) Schematic of the experimental workflow used for mass spectrometry analysis. CoIP, co-immunoprecipitation; LC-MS/MS, liquid chromatography followed by tandem mass spectrometry.

(B) Table displaying the 20 most abundant GluD1-interacting proteins. Exp#1–#3 represent independent coIP replicates with anti-GluD1 antibody; Ctrl#1–#3 corresponds to the control coIPs with total rabbit IgG. Only proteins enriched at least three times in GluD1 coIPs are indicated. GluD1 (encoded by the gene *grid1*) is highlighted in red.

(C–G) Quantification of GPHN cluster density in oblique dendrites of layer 2/3 CPNs *in utero* electroporated in the indicated conditions (juvenile stage). MRCK α KinD, MRCK α kinase-dead mutant; MRCK α WT, wild-type MRCK α . $n_{\text{shControl}}$ (C) = 22, $n_{\text{shArhgef12}}$ = 32, n_{Rescue} (C) = 24, n_{Control} (D) = 41, $n_{\text{MRCK}\alpha \text{ WT}}$ = 20, $n_{\text{MRCK}\alpha \text{ KinD}}$ = 18, $n_{\text{shControl}}$ (E) = 17, $n_{\text{shPpp1r12a}}$ = 30, n_{Rescue} (E) = 21, n_{Control} (F) = 15, $n_{\text{Ppp1r12a-KO}}$ = 38, $n_{\text{Arhgef12-KO}}$ = 19, $n_{\text{Grid1-KO}}$ (G) = 27, $n_{\text{Grid1-KO} + \text{Ppp1r12a-KO}}$ = 34, $n_{\text{Grid1-KO} + \text{Arhgef12-KO}}$ = 25.

Statistics: bars indicate mean \pm SEM, ns $p > 0.05$, *** $p < 0.001$ determined by one-way ANOVA test followed by Tukey's post test in (D–G) and Kruskal-Wallis test followed by Dunn's post test in (C).

(H) Schematic illustrating GluD1 *trans*-synaptic signaling regulating inhibitory synapse development. See text for details.

(Figure 6F), we found that neither *grid1/arhgef12* double KO nor *grid1/ppp1r12a* double KO further reduced the density of inhibitory synapses compared to single *grid1* KO (104% \pm 3% of Grid1-KO for Grid1-KO + Ppp1r12a-KO and 105% \pm 4% of Grid1-KO for Grid1-KO + Arhgef12-KO; Figure 6G), indicating that GluD1 requires ARHGEF12 and PPP1R12A to operate at inhibitory synapses. Interestingly, other major partners of GluD1 (Figure 6B), such as the Rho GTPase-activating protein 32 (ARHGAP32/PX-RICS) (Nakamura et al., 2016; Uezu et al., 2016), SRCIN1 (p140cap) (Alfieri et al., 2017; Russo et al., 2019), and Ankyrin 3 (Ankyrin G) (Nelson et al., 2018), have been shown to interact with gephyrin and/or regulate inhibitory synaptogenesis. This supports the notion that GluD1 serves as a signaling hub for the formation and specification of inhibitory synapses (Figure 6H), and that the regulation of inhibitory synaptogenesis is a major function of GluD1 in the neocortex.

DISCUSSION

In the present study, we employed sparse *in vivo* molecular manipulations and proteomic approaches to characterize the role of GluD1 in synaptic development in layer 2/3 pyramidal neurons of the somato-sensory cortex. We demonstrate that GluD1 is a maverick among iGluRs, operating at inhibitory synapses rather than excitatory synapses. GluD1 is necessary for

implicated in building up inhibitory synapses. Neither the overexpression of a kinase-dead dominant-negative mutant of MRCK α (MRCK α KinD, with K106A substitution) (Leung et al., 1998) nor that of wild-type MRCK α (MRCK α WT) affected the density of gephyrin clusters (Figure 6D) in juvenile mice, indicating that MRCK α is not critical for the formation of inhibitory synapses. In contrast, depletion of PPP1R12A (also referred to as MYPT1), a targeting subunit of PP1, with shRNAs decreased the density of gephyrin clusters (74% \pm 3% of the control), and normal gephyrin cluster density was rescued with the shRNA-resistant mutant PPP1R12A* (Figure 6E; Figure S1C), demonstrating that PPP1R12A is required for the formation of inhibitory synapses in dendrites. These data are in line with a previous study indicating that PP1 physically interacts with gephyrin and regulates the density of gephyrin clusters (Bausen et al., 2010).

Since both ARHGEF12 and PPP1R12A inactivation mimic GluD1 loss of function, our data suggest that GluD1 might signal through these two proteins to mediate the formation of inhibitory synapses. Using the CRISPR-Cas9 system combined with IUE to inactivate *grid1* (Figures 1J and 1K), *ppp1r12a*, and *arhgef12*

the formation of specific inhibitory synapses along dendrites and regulates GABAergic synaptic transmission accordingly. In the upper layers of the cortex, GluD1 is enriched in the postsynaptic membrane of inhibitory synapses, lateral to the active zone, where it establishes *trans*-synaptic interactions via Cbln4, an extracellular scaffolding protein secreted by SST⁺ INs (Favuzzi et al., 2019), which, in turn, binds to presynaptic neurexins (Yuzaki, 2017; Zhong et al., 2017). When interacting with Cbln4 and binding to glycine or D-serine, GluD1 activates postsynaptic signaling pathways that do not depend on ion flux through its channel, but it involves intracellular interactions via its C-terminal tail, organizing the assembly of inhibitory postsynaptic machineries at contact sites with SST⁺ INs. These interactions involve ARHGEF12 and PPP1R12A, two molecules required for GluD1 function at inhibitory synapses and probably other molecules implicated at GABAergic synapses.

Region-Specific Function of GluD1 at Inhibitory Synapses

Although the repertoire of inhibitory synaptic proteins has recently expanded (Krueger-Burg et al., 2017), the molecular diversity of inhibitory synapses and the difficulty of investigating their biochemistry and their cell biology *in vivo* has obscured the mechanistic understanding of inhibitory synaptogenesis. Hence, few CAMs and signaling molecules have been shown to selectively control inhibitory synapse assembly (Krueger-Burg et al., 2017; Tyagarajan and Fritschy, 2014). These molecules show domain-specific functions at perisomatic (Früh et al., 2016; Pouloupoulos et al., 2009), dendritic (Li et al., 2017), or axo-axonic synapses (Panzanelli et al., 2011). Their function also varies depending on brain areas. In particular, extensive studies of neuroligin 2 and collybistin (ARHGEF9), two proteins present in virtually all inhibitory synapses in the CNS, have highlighted fundamental differences between the cell biology of hippocampal and cortical inhibitory synapses (Gibson et al., 2009; Pouloupoulos et al., 2009; Papadopoulos et al., 2007). Since the mechanisms of synaptogenesis in the forebrain are predominantly studied in hippocampal neurons, the molecular underpinning of inhibitory synapse formation in the cortex has remained enigmatic.

Previous *in vitro* hemi-synapse formation assays suggested a synaptogenic activity of GluD1 in cortical neurons (Ryu et al., 2012; Yasumura et al., 2012). However, it was unclear whether the synaptogenic activity was selective for inhibitory synapses (Yasumura et al., 2012) or common to excitatory and inhibitory synapses (Ryu et al., 2012), and the role of endogenous GluD1 in cortical neurons *in vivo* remained unclear (Gupta et al., 2015). Here, we used *in vivo* single cell approaches based on sparse IUE to manipulate GluD1 expression and function in isolated layer 2/3 CPNs in the intact brain. Targeting a specific cell type allowed us to investigate a relatively homogeneous population of neurons and dissect cell-autonomous mechanisms with a subcellular resolution in spatially identified synapses along the dendritic tree. Moreover, sparse *in vivo* manipulations help avoid compensatory and adaptive changes at the network level, which might occur in KO mouse models. Our results provide direct evidence that GluD1 is necessary for the formation of specific cortical inhibitory synapses *in vivo*. While we do not exclude

that GluD1 could regulate some properties of excitatory synapses in the cortex, we clearly show that GluD1 is not required for their formation, which is consistent with a previous study (Gupta et al., 2015). Therefore, GluD1 function in CPNs starkly contrasts with GluD1 function in cerebellar INs (Konno et al., 2014) and hippocampal pyramidal neurons (Tao et al., 2018), where GluD1 is required for the formation of excitatory synapses. This raises fundamental questions on the molecular basis underlying the region-specific function of GluD1 at excitatory or inhibitory synapses and the synaptic dysfunction associated with GluD1 mutations in brain disorders (Cooper et al., 2011; Fallin et al., 2005; Gleessner et al., 2009; Guo et al., 2007; Treutlein et al., 2009).

An iGluR-Dependent Signaling Pathway at Inhibitory Synapses

It is unconventional for a member of the iGluR family to locate and operate at inhibitory synapses. We show that *trans*-synaptically engaged GluD1 binding to glycine or D-serine initiates postsynaptic signaling via non-ionotropic mechanisms, probably through conformational changes that are transmitted through the TMD, and controls intracellular interactions (Elegheert et al., 2016). Whether GluD1 binds to glycine or D-serine in CPNs is unknown, but both glycine and D-serine may contribute to the regulation of inhibitory synapse formation. Glycine is present in the extracellular space, where it activates extrasynaptic NMDA receptors (Papouin et al., 2012) and mediates tonic inhibition in layer 2/3 CPNs (McCracken et al., 2017; Salling and Harrison, 2014). In the brainstem and spinal cord, where glycine is a major inhibitory neurotransmitter and GluD1 is highly expressed (<https://www.gtportal.org/home/gene/GRID1>), presynaptic release of glycine may directly regulate the formation and maintenance of inhibitory synapses. D-serine is also present in the extracellular environment. It is synthesized through conversion of L-serine by serine racemase and released at least by the neuronal alanine-serine-cysteine transporter 1 (Asc-1) (Rosenberg et al., 2013). Ambient D-serine level is regulated by excitatory glutamatergic activity (Van Horn et al., 2017; Ma et al., 2014), and low D-serine levels are associated with epilepsy (Klatte et al., 2013) and schizophrenia-like behaviors (Ma et al., 2013), consistent with defects in synaptic inhibition and GluD1 function. So far, in the forebrain, the role of D-serine and, to some extent, glycine has been envisioned through the activation of NMDA receptors (Oliet and Mothet, 2009). The role of GluD1 in establishing the equilibrium between excitation and inhibition and the requirement of GluD1 activation by glycine/D-serine suggests that some functions initially attributed to NMDA receptors might instead depend on GluD1 signaling.

Proteomic and functional analyses of GluD1 interactome allowed us to identify signaling pathways controlling the postsynaptic organization of inhibitory machineries. We found that two major partners of GluD1, ARHGEF12 and PPP1R12A, are necessary for inhibitory synapse formation in layer 2/3 CPNs. Double inactivation experiments showed that ARHGEF12 and PPP1R12A operate in the same pathway as GluD1 and therefore also contribute to the specification of inhibitory connectivity between SST⁺ INs and layer 2/3 CPNs. ARHGEF12 contains a Dbl-homology (DH) domain mediating guanosine diphosphate

(GDP)/guanosine triphosphate (GTP) exchange activity and a pleckstrin-homology (PH) domain, which binds phosphoinositides and regulates its membrane targeting (Hyvönen et al., 1995). ARHGEF12 also contains an N-terminal PDZ domain, which may interact with the C-terminal PDZ-binding motif of GluD1, and a regulator of G-protein signaling-like (RGSL) domain. Although further experiments are needed to determine how ARHGEF12 contributes to inhibitory synaptic development, one possibility is that ARHGEF12 links *trans*-synaptic interaction with phosphoinositide and G-protein signaling to mediate inhibitory synaptogenesis. Furthermore, our data on PPP1R12A suggest that targeting PP1 to GluD1-mediated contact sites between INs and pyramidal neurons and locally regulating the post-translational state of inhibitory synaptic components is critical to initiate or promote postsynaptic assembly. This is congruent with previous studies showing that PP1 associates with gephyrin and the beta-3 subunit of GABA_A receptors (GABA_ARs) (Bausen et al., 2010; Pribram and Stellwagen, 2013) and that pharmacological inhibition of PP1 induces a loss of gephyrin clusters (Bausen et al., 2010). Among the most represented interactors of GluD1 we identify here, Ankyrin 3, ARHGAP32/PX-RICS, SRCIN1/p140Cap, and SRGAPs were previously implicated at inhibitory synapses. Ankyrin 3 interacts with GABA_AR-associated protein (GABARAP) and contributes to stabilization of GABA_ARs in the postsynaptic membrane (Nelson et al., 2018). ARHGAP32 interacts with gephyrin, and its inactivation impairs GABA_AR trafficking at synapses (Nakamura et al., 2016; Uezu et al., 2016). SRCIN1, SRGAP3, and SRGAP2 also associate with gephyrin and regulate GABAergic synaptogenesis (Alfieri et al., 2017; Fossati et al., 2016; Okada et al., 2011; Russo et al., 2019). Therefore, GluD1 *trans*-synaptic signaling provides local regulation of protein phosphorylation and GTPase activity and allows the recruitment of synaptic molecules for the assembly of inhibitory postsynaptic machineries in an input-specific and agonist-dependent manner. Interestingly, in young neurons, GluD1 expression at the cell surface was decreased by SRGAP2 inactivation. SRGAP2, and by homology SRGAP3, is inhibited by the human-specific protein SRGAP2C (Charrier et al., 2012; Coutinho-Budd et al., 2012). This regulation could contribute to the delay of the development of inhibitory synapses in human neurons (Fossati et al., 2016) and modify inhibitory circuitry to accommodate a greater diversity of IN subtypes (Defelipe, 2011). Understanding the diversity of *trans*-synaptic interactions and signaling pathways coordinating the establishment of neocortical inhibitory circuitry, their interplay, their evolution in human, and their dysregulations in brain disorders will be a fertile area for future research.

STAR★METHODS

Detailed methods are provided in the online version of this paper and include the following:

- KEY RESOURCES TABLE
- LEAD CONTACT AND MATERIALS AVAILABILITY
- EXPERIMENTAL MODEL AND SUBJECT DETAILS
 - Animals
 - Primary cultures of mouse cortical neurons
 - HEK293T cells

● METHOD DETAILS

- Plasmids for protein expression
- shRNA and Crispr constructs and shRNA validation
- Lentivirus production and infection
- In utero electroporation, AAV injection and slice preparation
- Immunohistochemistry for confocal microscopy
- Confocal image acquisition
- Electron microscopy
- Electrophysiology
- Transfection and western blotting
- Cell surface biotinylation
- Subcellular fractionation
- Immunoprecipitation
- Proteomics

● QUANTIFICATION AND STATISTICAL ANALYSIS

- Confocal image analysis
- mEPSC and mIPSC analysis
- Proteomic analysis
- Statistics

● DATA AND CODE AVAILABILITY

SUPPLEMENTAL INFORMATION

Supplemental Information can be found online at <https://doi.org/10.1016/j.neuron.2019.09.027>.

ACKNOWLEDGMENTS

We thank members of A. Triller's laboratory (IBENS, Paris, France), D. Stroebel, P. Paoletti, M. Casado, F. Selimi, and F. Polleux, for helpful discussions and comments on the manuscript; P. Rostaing for his help with electron microscopy; L. Tricoire for kindly providing anti-GluD1 antibody and HA-GluD1 plasmid; M. Bünnemann for *ARHGEF12* plasmid; and B. Roska, D.B. Arnold, and F. Zhang for plasmids available through Addgene. This work was supported by INSERM, the Agence Nationale de la Recherche (ANR-13-PDOC-0003 and ANR-17-ERC3-0009 to C.C.), the European Research Council (ERC starting grant 803704 to C.C.), the Fyssen Foundation (to C.C.), the Région Ile-de-France (to D.L.), and the Fondation pour la Recherche Médicale (to D.L.). We are grateful to the IBENS Imaging Facility (France Biomed, supported by ANR-10-INBS-04, ANR-10-LABX-54 MEMO LIFE, and ANR-11-IDEX-000-02 PSL* Research University, "Investments for the future"; NERF 2011-45; FRM DGE 20111123023; and FRC Rotary International France), the IBENS acute transgenesis facility, and the imaging unit of the Humanitas Clinical and Research Center.

AUTHOR CONTRIBUTIONS

M.F., C.C., N.A., O.G., and S.C. performed experiments and analyzed data. F.D. carried out the MS experimental work, G.A. analyzed MS data, and D. L. supervised MS and data analysis. M.F. and C.C. designed the study, interpreted the results, prepared the figures, and wrote the manuscript.

DECLARATION OF INTEREST

The authors declare no competing interests.

Received: July 30, 2018
 Revised: August 11, 2019
 Accepted: September 17, 2019
 Published: November 5, 2019

REFERENCES

- Ady, V., Perroy, J., Tricoire, L., Piochon, C., Dadak, S., Chen, X., Dusart, I., Fagni, L., Lambolez, B., and Levenes, C. (2014). Type 1 metabotropic glutamate receptors (mGlu1) trigger the gating of GluR2 delta glutamate receptors. *EMBO Rep.* 15, 103–109.
- Alfieri, A., Sorokina, O., Adrait, A., Angelini, C., Russo, I., Morellato, A., Matteoli, M., Menna, E., Boeri Erba, E., McLean, C., et al. (2017). Synaptic Interactome Mining Reveals p140Cap as a New Hub for PSD Proteins Involved in Psychiatric and Neurological Disorders. *Front. Mol. Neurosci.* 10, 212.
- Aoto, J., Martinelli, D.C., Malenka, R.C., Tabuchi, K., and Südhof, T.C. (2013). Presynaptic neurexin-3 alternative splicing trans-synaptically controls postsynaptic AMPA receptor trafficking. *Cell* 154, 75–88.
- Araki, K., Meguro, H., Kushiya, E., Takayama, C., Inoue, Y., and Mishina, M. (1993). Selective expression of the glutamate receptor channel δ 2 subunit in cerebellar Purkinje cells. *Biochem. Biophys. Res. Commun.* 197, 1267–1276.
- Babiec, W.E., Guglietta, R., Jami, S.A., Morishita, W., Malenka, R.C., and O'Dell, T.J. (2014). Ionotropic NMDA receptor signaling is required for the induction of long-term depression in the mouse hippocampal CA1 region. *J. Neurosci.* 34, 5285–5290.
- Bausen, M., Weltzien, F., Betz, H., and O'Sullivan, G.A. (2010). Regulation of postsynaptic gephyrin cluster size by protein phosphatase 1. *Mol. Cell. Neurosci.* 44, 201–209.
- Bemben, M.A., Shipman, S.L., Nicoll, R.A., and Roche, K.W. (2015). The cellular and molecular landscape of neuroligins. *Trends Neurosci.* 38, 496–505.
- Benamer, N., Marti, F., Lujan, R., Hepp, R., Aubier, T.G., Dupin, A.A.M., Frébourg, G., Pons, S., Maskos, U., Faure, P., et al. (2018). GluR1, linked to schizophrenia, controls the burst firing of dopamine neurons. *Mol. Psychiatry* 23, 691–700.
- Berns, D.S., DeNardo, L.A., Pederick, D.T., and Luo, L. (2018). Teneurin-3 controls topographic circuit assembly in the hippocampus. *Nature* 554, 328–333.
- Bodmann, E.L., Krett, A.L., and Bünemann, M. (2017). Potentiation of receptor responses induced by prolonged binding of $G\alpha_{13}$ and leukemia-associated RhoGEF. *FASEB J.* 31, 3663–3676.
- Bourgeron, T. (2015). From the genetic architecture to synaptic plasticity in autism spectrum disorder. *Nat. Rev. Neurosci.* 16, 551–563.
- Bourne, J.N., and Harris, K.M. (2008). Balancing structure and function at hippocampal dendritic spines. *Annu. Rev. Neurosci.* 31, 47–67.
- Carter, B.C., and Jahr, C.E. (2016). Postsynaptic, not presynaptic NMDA receptors are required for spike-timing-dependent LTD induction. *Nat. Neurosci.* 19, 1218–1224.
- Charrier, C., Joshi, K., Coutinho-Budd, J., Kim, J.-E., Lambert, N., de Marchena, J., Jin, W.-L., Vanderhaeghen, P., Ghosh, A., Sassa, T., and Polleux, F. (2012). Inhibition of SRGAP2 function by its human-specific paralogs induces neoteny during spine maturation. *Cell* 149, 923–935.
- Chen, X.-Q., Tan, I., Leung, T., and Lim, L. (1999). The myotonic dystrophy kinase-related Cdc42-binding kinase is involved in the regulation of neurite outgrowth in PC12 cells. *J. Biol. Chem.* 274, 19901–19905.
- Chen, J.L., Villa, K.L., Cha, J.W., So, P.T.C., Kubota, Y., and Nedivi, E. (2012). Clustered dynamics of inhibitory synapses and dendritic spines in the adult neocortex. *Neuron* 74, 361–373.
- Cheng, S., Seven, A.B., Wang, J., Skiniotis, G., and Özkan, E. (2016). Conformational Plasticity in the Transsynaptic Neurexin-Cerebellin-Glutamate Receptor Adhesion Complex. *Structure* 24, 2163–2173.
- Choquet, D., and Triller, A. (2013). The dynamic synapse. *Neuron* 80, 691–703.
- Cooper, G.M., Coe, B.P., Girirajan, S., Rosenfeld, J.A., Vu, T.H., Baker, C., Williams, C., Stalker, H., Hamid, R., Hannig, V., et al. (2011). A copy number variation morbidity map of developmental delay. *Nat. Genet.* 43, 838–846.
- Coutinho-Budd, J., Ghukasyan, V., Zylka, M.J., and Polleux, F. (2012). The F-BAR domains from srGAP1, srGAP2 and srGAP3 regulate membrane deformation differently. *J. Cell Sci.* 125, 3390–3401.
- de Wit, J., and Ghosh, A. (2016). Specification of synaptic connectivity by cell surface interactions. *Nat. Rev. Neurosci.* 17, 22–35.
- Defelipe, J. (2011). The evolution of the brain, the human nature of cortical circuits, and intellectual creativity. *Front. Neuroanat.* 5, 29.
- Dore, K., Aow, J., and Malinow, R. (2015). Agonist binding to the NMDA receptor drives movement of its cytoplasmic domain without ion flow. *Proc. Natl. Acad. Sci. USA* 112, 14705–14710.
- Elegheert, J., Kakegawa, W., Clay, J.E., Shanks, N.F., Behiels, E., Matsuda, K., Kohda, K., Miura, E., Rossmann, M., Mitakidis, N., et al. (2016). Structural basis for integration of GluR receptors within synaptic organizer complexes. *Science* 353, 295–299.
- Emes, R.D., and Grant, S.G.N. (2012). Evolution of synapse complexity and diversity. *Annu. Rev. Neurosci.* 35, 111–131.
- Fallin, M.D., Lasseter, V.K., Avramopoulos, D., Nicodemus, K.K., Wolyniec, P.S., McGrath, J.A., Steel, G., Nestadt, G., Liang, K.Y., Haganir, R.L., et al. (2005). Bipolar I disorder and schizophrenia: a 440-single-nucleotide polymorphism screen of 64 candidate genes among Ashkenazi Jewish case-parent trios. *Am. J. Hum. Genet.* 77, 918–936.
- Favuzzi, E., Deogracias, R., Marques-Smith, A., Maeso, P., Jezequel, J., Exposito-Alonso, D., Balia, M., Kroon, T., Hinojosa, A.J., Maraver, E.F., and Rico, B. (2019). Distinct molecular programs regulate synapse specificity in cortical inhibitory circuits. *Science* 363, 413–417.
- Fishell, G., and Kepecs, A. (2019). Interneuron Types as Attractors and Controllers. *Annu. Rev. Neurosci.* Published online July 12, 2019. 10.1146/annurev-neuro-070918-050421.
- Fossati, M., Pizzarelli, R., Schmidt, E.R., Kupferman, J.V., Stroebel, D., Polleux, F., and Charrier, C. (2016). SRGAP2 and Its Human-Specific Paralog Co-Regulate the Development of Excitatory and Inhibitory Synapses. *Neuron* 91, 356–369.
- Früh, S., Romanos, J., Panzanelli, P., Bürgisser, D., Tyagarajan, S.K., Campbell, K.P., Santello, M., and Fritschy, J.-M. (2016). Neuronal Dystroglycan Is Necessary for Formation and Maintenance of Functional CCK-Positive Basket Cell Terminals on Pyramidal Cells. *J. Neurosci.* 36, 10296–10313.
- Fukata, Y., Adesnik, H., Iwanaga, T., Bredt, D.S., Nicoll, R.A., and Fukata, M. (2006). Epilepsy-related ligand/receptor complex LGI1 and ADAM22 regulate synaptic transmission. *Science* 313, 1792–1795.
- Gibson, J.R., Huber, K.M., and Südhof, T.C. (2009). Neuroligin-2 deletion selectively decreases inhibitory synaptic transmission originating from fast-spiking but not from somatostatin-positive interneurons. *J. Neurosci.* 29, 13883–13897.
- Glessner, J.T., Wang, K., Cai, G., Korvatska, O., Kim, C.E., Wood, S., Zhang, H., Estes, A., Brune, C.W., Bradfield, J.P., et al. (2009). Autism genome-wide copy number variation reveals ubiquitin and neuronal genes. *Nature* 459, 569–573.
- Grabaukas, G., Lancaster, B., O'Connor, V., and Wheal, H.V. (2007). Protein kinase signalling requirements for metabotropic action of kainate receptors in rat CA1 pyramidal neurones. *J. Physiol.* 579, 363–373.
- Gross, G.G., Junge, J.A., Mora, R.J., Kwon, H.-B., Olson, C.A., Takahashi, T.T., Liman, E.R., Ellis-Davies, G.C.R., McGee, A.W., Sabatini, B.L., et al. (2013). Recombinant probes for visualizing endogenous synaptic proteins in living neurons. *Neuron* 78, 971–985.
- Guo, S.Z., Huang, K., Shi, Y.Y., Tang, W., Zhou, J., Feng, G.Y., Zhu, S.M., Liu, H.J., Chen, Y., Sun, X.D., and He, L. (2007). A case-control association study between the GRID1 gene and schizophrenia in the Chinese Northern Han population. *Schizophr. Res.* 93, 385–390.
- Gupta, S.C., Yadav, R., Pavuluri, R., Morley, B.J., Stairs, D.J., and Dravid, S.M. (2015). Essential role of GluR1 in dendritic spine development and GluN2B to GluN2A NMDAR subunit switch in the cortex and hippocampus reveals ability of GluN2B inhibition in correcting hyperconnectivity. *Neuropharmacology* 93, 274–284.

- Hayashi, T., Umemori, H., Mishina, M., and Yamamoto, T. (1999). The AMPA receptor interacts with and signals through the protein tyrosine kinase Lyn. *Nature* 397, 72–76.
- Hepp, R., Hay, Y.A., Aguado, C., Lujan, R., Dauphinot, L., Potier, M.C., Nomura, S., Poirel, O., El Mestikawy, S., Lambolez, B., and Tricoire, L. (2015). Glutamate receptors of the delta family are widely expressed in the adult brain. *Brain Struct. Funct.* 220, 2797–2815.
- Hyvönen, M., Macias, M.J., Nilges, M., Oschkinat, H., Saraste, M., and Wilmanns, M. (1995). Structure of the binding site for inositol phosphates in a PH domain. *EMBO J.* 14, 4676–4685.
- Jang, S., Lee, H., and Kim, E. (2017). Synaptic adhesion molecules and excitatory synaptic transmission. *Curr. Opin. Neurobiol.* 45, 45–50.
- Kakegawa, W., Kohda, K., and Yuzaki, M. (2007). The $\delta 2$ 'ionotropic' glutamate receptor functions as a non-ionotropic receptor to control cerebellar synaptic plasticity. *J. Physiol.* 584, 89–96.
- Kakegawa, W., Miyazaki, T., Emi, K., Matsuda, K., Kohda, K., Motohashi, J., Mishina, M., Kawahara, S., Watanabe, M., and Yuzaki, M. (2008). Differential regulation of synaptic plasticity and cerebellar motor learning by the C-terminal PDZ-binding motif of GluRdelta2. *J. Neurosci.* 28, 1460–1468.
- Kakegawa, W., Miyazaki, T., Kohda, K., Matsuda, K., Emi, K., Motohashi, J., Watanabe, M., and Yuzaki, M. (2009). The N-terminal domain of GluRdelta2 (GluRdelta2) recruits presynaptic terminals and regulates synaptogenesis in the cerebellum in vivo. *J. Neurosci.* 29, 5738–5748.
- Kakegawa, W., Miyoshi, Y., Hamase, K., Matsuda, S., Matsuda, K., Kohda, K., Emi, K., Motohashi, J., Konno, R., Zaitzu, K., and Yuzaki, M. (2011). D-serine regulates cerebellar LTD and motor coordination through the $\delta 2$ glutamate receptor. *Nat. Neurosci.* 14, 603–611.
- Klatte, K., Kirschstein, T., Otte, D., Pothmann, L., Müller, L., Tokay, T., Kober, M., Uebachs, M., Zimmer, A., and Beck, H. (2013). Impaired D-serine-mediated cotransmission mediates cognitive dysfunction in epilepsy. *J. Neurosci.* 33, 13066–13080.
- Kohda, K., Kakegawa, W., Matsuda, S., Yamamoto, T., Hirano, H., and Yuzaki, M. (2013). The $\delta 2$ glutamate receptor gates long-term depression by coordinating interactions between two AMPA receptor phosphorylation sites. *Proc. Natl. Acad. Sci. USA* 110, E948–E957.
- Konno, K., Matsuda, K., Nakamoto, C., Uchigashima, M., Miyazaki, T., Yamasaki, M., Sakimura, K., Yuzaki, M., and Watanabe, M. (2014). Enriched expression of GluR1 in higher brain regions and its involvement in parallel fiber-interneuron synapse formation in the cerebellum. *J. Neurosci.* 34, 7412–7424.
- Krueger-Burg, D., Papadopoulos, T., and Brose, N. (2017). Organizers of inhibitory synapses come of age. *Curr. Opin. Neurobiol.* 45, 66–77.
- Kuroyanagi, T., and Hirano, T. (2010). Flap loop of GluR2 binds to Cbln1 and induces presynaptic differentiation. *Biochem. Biophys. Res. Commun.* 398, 537–541.
- Lerma, J., and Marques, J.M. (2013). Kainate receptors in health and disease. *Neuron* 80, 292–311.
- Leung, T., Chen, X.Q., Tan, I., Manser, E., and Lim, L. (1998). Myotonic dystrophy kinase-related Cdc42-binding kinase acts as a Cdc42 effector in promoting cytoskeletal reorganization. *Mol. Cell. Biol.* 18, 130–140.
- Li, J., Han, W., Pelkey, K.A., Duan, J., Mao, X., Wang, Y.-X., Craig, M.T., Dong, L., Petralia, R.S., McBain, C.J., and Lu, W. (2017). Molecular Dissection of Neurologin 2 and Slitrk3 Reveals an Essential Framework for GABAergic Synapse Development. *Neuron* 96, 808–826.e8.
- Lovero, K.L., Fukata, Y., Granger, A.J., Fukata, M., and Nicoll, R.A. (2015). The LGI1-ADAM22 protein complex directs synapse maturation through regulation of PSD-95 function. *Proc. Natl. Acad. Sci. USA* 112, E4129–E4137.
- Ma, T.M., Abazyan, S., Abazyan, B., Nomura, J., Yang, C., Seshadri, S., Sawa, A., Snyder, S.H., and Pletnikov, M.V. (2013). Pathogenic disruption of DISC1-serine racemase binding elicits schizophrenia-like behavior via D-serine depletion. *Mol. Psychiatry* 18, 557–567.
- Ma, T.M., Paul, B.D., Fu, C., Hu, S., Zhu, H., Blackshaw, S., Wolosker, H., and Snyder, S.H. (2014). Serine racemase regulated by binding to stargazin and PSD-95: potential N-methyl-D-aspartate- α -amino-3-hydroxy-5-methyl-4-isoxazolepropionic acid (NMDA-AMPA) glutamate neurotransmission cross-talk. *J. Biol. Chem.* 289, 29631–29641.
- Matsuda, K., Miura, E., Miyazaki, T., Kakegawa, W., Emi, K., Narumi, S., Fukazawa, Y., Ito-Ishida, A., Kondo, T., Shigemoto, R., et al. (2010). Cbln1 Is a Ligand for an Orphan Glutamate Receptor 2, a Bidirectional Synapse Organizer. *Science* 328, 363–368.
- Matsuda, K., Budisantoso, T., Mitakidis, N., Sugaya, Y., Miura, E., Kakegawa, W., Yamasaki, M., Konno, K., Uchigashima, M., Abe, M., et al. (2016). Transsynaptic Modulation of Kainate Receptor Functions by C1q-like Proteins. *Neuron* 90, 752–767.
- McAllister, A.K. (2007). Dynamic aspects of CNS synapse formation. *Annu. Rev. Neurosci.* 30, 425–450.
- McCracken, L.M., Lowes, D.C., Salling, M.C., Carreau-Vollmer, C., Odean, N.N., Blednov, Y.A., Betz, H., Harris, R.A., and Harrison, N.L. (2017). Glycine receptor $\alpha 3$ and $\alpha 2$ subunits mediate tonic and exogenous agonist-induced currents in forebrain. *Proc. Natl. Acad. Sci. USA* 114, E7179–E7186.
- Missler, M., Südhof, T.C., and Biederer, T. (2012). Synaptic cell adhesion. *Cold Spring Harb. Perspect. Biol.* 4, a005694–a005694.
- Mondin, M., Labrousse, V., Hosy, E., Heine, M., Tessier, B., Levet, F., Poujol, C., Blanchet, C., Choquet, D., and Thoumine, O. (2011). Neuroligin-neurologin adhesions capture surface-diffusing AMPA receptors through PSD-95 scaffolds. *J. Neurosci.* 31, 13500–13515.
- Mullins, C., Fishell, G., and Tsien, R.W. (2016). Unifying Views of Autism Spectrum Disorders: A Consideration of Autoregulatory Feedback Loops. *Neuron* 89, 1131–1156.
- Nabavi, S., Kessels, H.W., Alfonso, S., Aow, J., Fox, R., and Malinow, R. (2013). Metabotropic NMDA receptor function is required for NMDA receptor-dependent long-term depression. *Proc. Natl. Acad. Sci. USA* 110, 4027–4032.
- Nakamura, T., Arima-Yoshida, F., Sakaue, F., Nasu-Nishimura, Y., Takeda, Y., Matsuura, K., Akshoomoff, N., Mattson, S.N., Grossfeld, P.D., Manabe, T., and Akiyama, T. (2016). PX-RICS-deficient mice mimic autism spectrum disorder in Jacobsen syndrome through impaired GABAA receptor trafficking. *Nat. Commun.* 7, 10861.
- Nam, C.I., and Chen, L. (2005). Postsynaptic assembly induced by neuroligin-neurologin interaction and neurotransmitter. *Proc. Natl. Acad. Sci. USA* 102, 6137–6142.
- Naur, P., Hansen, K.B., Kristensen, A.S., Dravid, S.M., Pickering, D.S., Olsen, L., Vestergaard, B., Egebjerg, J., Gajhede, M., Traynelis, S.F., and Kastrup, J.S. (2007). Ionotropic glutamate-like receptor delta2 binds D-serine and glycine. *Proc. Natl. Acad. Sci. USA* 104, 14116–14121.
- Nelson, S.B., and Valakh, V. (2015). Excitatory/Inhibitory Balance and Circuit Homeostasis in Autism Spectrum Disorders. *Neuron* 87, 684–698.
- Nelson, A.D., Caballero-Florán, R.N., Rodríguez Díaz, J.C., Hull, J.M., Yuan, Y., Li, J., Chen, K., Walder, K.K., Lopez-Santiago, L.F., Bennett, V., et al. (2018). Ankyrin-G regulates forebrain connectivity and network synchronization via interaction with GABARAP. *Mol. Psychiatry*. Published online November 30, 2018. <https://doi.org/10.1038/s41380-018-0308-x>.
- Okada, H., Uezu, A., Mason, F.M., Soderblom, E.J., Moseley, M.A., 3rd, and Soderling, S.H. (2011). SH3 domain-based phototrapping in living cells reveals Rho family GAP signaling complexes. *Sci. Signal.* 4, rs13–rs13.
- Oliet, S.H.R., and Mothet, J.-P. (2009). Regulation of N-methyl-D-aspartate receptors by astrocytic D-serine. *Neuroscience* 158, 275–283.
- Panzanelli, P., Gunn, B.G., Schlatter, M.C., Benke, D., Tyagarajan, S.K., Scheiffele, P., Belelli, D., Lambert, J.J., Rudolph, U., and Fritschy, J.-M. (2011). Distinct mechanisms regulate GABAA receptor and gephyrin clustering at perisomatic and axo-axonic synapses on CA1 pyramidal cells. *J. Physiol.* 589, 4959–4980.

- Paoletti, P., Bellone, C., and Zhou, Q. (2013). NMDA receptor subunit diversity: impact on receptor properties, synaptic plasticity and disease. *Nat. Rev. Neurosci.* **14**, 383–400.
- Papadopoulos, T., Korte, M., Eulenburg, V., Kubota, H., Retiounskaia, M., Harvey, R.J., Harvey, K., O'Sullivan, G.A., Laube, B., Hülsmann, S., et al. (2007). Impaired GABAergic transmission and altered hippocampal synaptic plasticity in collybistin-deficient mice. *EMBO J.* **26**, 3888–3899.
- Papouin, T., Ladépêche, L., Ruel, J., Sacchi, S., Labasque, M., Hanini, M., Groc, L., Pollegioni, L., Mothet, J.P., and Oliet, S.H.R. (2012). Synaptic and extrasynaptic NMDA receptors are gated by different endogenous coagonists. *Cell* **150**, 633–646.
- Paul, A., Crow, M., Raudales, R., He, M., Gillis, J., and Huang, Z.J. (2017). Transcriptional Architecture of Synaptic Communication Delineates GABAergic Neuron Identity. *Cell* **171**, 522–539.e20.
- Poulet, P., Carpentier, S., and Barillot, E. (2007). myProMS, a web server for management and validation of mass spectrometry-based proteomic data. *Proteomics* **7**, 2553–2556.
- Pouloupoulos, A., Aramuni, G., Meyer, G., Soykan, T., Hoon, M., Papadopoulos, T., Zhang, M., Paarmann, I., Fuchs, C., Harvey, K., et al. (2009). Neuroligin 2 drives postsynaptic assembly at perisomatic inhibitory synapses through gephyrin and collybistin. *Neuron* **63**, 628–642.
- Pribragi, H., and Stellwagen, D. (2013). TNF- α downregulates inhibitory neurotransmission through protein phosphatase 1-dependent trafficking of GABA(A) receptors. *J. Neurosci.* **33**, 15879–15893.
- Robert, A., Hyde, R., Hughes, T.E., and Howe, J.R. (2002). The expression of dominant-negative subunits selectively suppresses neuronal AMPA and kainate receptors. *Neuroscience* **115**, 1199–1210.
- Rodríguez-Moreno, A., and Sihra, T.S. (2007). Kainate receptors with a metabotropic modus operandi. *Trends Neurosci.* **30**, 630–637.
- Rosenberg, D., Artoul, S., Segal, A.C., Kolodney, G., Radziszewsky, I., Dikopoltsev, E., Foltyn, V.N., Inoue, R., Mori, H., Billard, J.-M., and Wolosker, H. (2013). Neuronal D-serine and glycine release via the Asc-1 transporter regulates NMDA receptor-dependent synaptic activity. *J. Neurosci.* **33**, 3533–3544.
- Russo, I., Gavello, D., Menna, E., Vandaal, D., Veglia, C., Morello, N., Corradini, I., Focchi, E., Alfieri, A., Angelini, C., et al. (2019). P140CAP regulates GABAergic synaptogenesis and development of hippocampal inhibitory circuits. *Cereb. Cortex* **29**, 91–105.
- Ryu, K., Yokoyama, M., Yamashita, M., and Hirano, T. (2012). Induction of excitatory and inhibitory presynaptic differentiation by GluD1. *Biochem. Biophys. Res. Commun.* **417**, 157–161.
- Saglietti, L., Dequidt, C., Kamieniarz, K., Rousset, M.-C., Valnegri, P., Thoumine, O., Beretta, F., Fagni, L., Choquet, D., Sala, C., et al. (2007). Extracellular interactions between GluR2 and N-cadherin in spine regulation. *Neuron* **54**, 461–477.
- Salling, M.C., and Harrison, N.L. (2014). Strychnine-sensitive glycine receptors on pyramidal neurons in layers II/III of the mouse prefrontal cortex are tonically activated. *J. Neurophysiol.* **112**, 1169–1178.
- Schindelin, J., Arganda-Carreras, I., Frise, E., Kaynig, V., Longair, M., Pietzsch, T., Preibisch, S., Rueden, C., Saalfeld, S., Schmid, B., et al. (2012). Fiji: An open-source platform for biological-image analysis. *Nat. Methods.* **9**, 676–682.
- Sheng, M., and Hoogenraad, C.C. (2007). The postsynaptic architecture of excitatory synapses: a more quantitative view. *Annu. Rev. Biochem.* **76**, 823–847.
- Sheng, M., and Kim, E. (2011). The postsynaptic organization of synapses. *Cold Spring Harb. Perspect. Biol.* **3**, a005678–a005678.
- Slaymaker, I.M., Gao, L., Zetsche, B., Scott, D.A., Yan, W.X., and Zhang, F. (2016). Rationally engineered Cas9 nucleases with improved specificity. *Science* **351**, 84–88.
- Stein, I.S., Gray, J.A., and Zito, K. (2015). Non-Ionotropic NMDA Receptor Signaling Drives Activity-Induced Dendritic Spine Shrinkage. *J. Neurosci.* **35**, 12303–12308.
- Südhof, T.C. (2017). Synaptic Neurexin Complexes: A Molecular Code for the Logic of Neural Circuits. *Cell* **171**, 745–769.
- Tai, C.-Y., Kim, S.A., and Schuman, E.M. (2008). Cadherins and synaptic plasticity. *Curr. Opin. Cell Biol.* **20**, 567–575.
- Tao, W., Díaz-Alonso, J., Sheng, N., and Nicoll, R.A. (2018). Postsynaptic $\delta 1$ glutamate receptor assembles and maintains hippocampal synapses via Cbln2 and neurexin. *Proc. Natl. Acad. Sci. USA* **115**, E5373–E5381.
- Tasic, B., Menon, V., Nguyen, T.N., Kim, T.K., Jarsky, T., Yao, Z., Levi, B., Gray, L.T., Sorensen, S.A., Dolbeare, T., et al. (2016). Adult mouse cortical cell taxonomy revealed by single cell transcriptomics. *Nat. Neurosci.* **19**, 335–346.
- Ting, J.T., Peça, J., and Feng, G. (2012). Functional consequences of mutations in postsynaptic scaffolding proteins and relevance to psychiatric disorders. *Annu. Rev. Neurosci.* **35**, 49–71.
- Traynelis, S.F., Wollmuth, L.P., McBain, C.J., Menniti, F.S., Vance, K.M., Ogden, K.K., Sorensen, K.B., Yuan, H., Myers, S.J., and Dingledine, R. (2010). Glutamate receptor ion channels: structure, regulation, and function. *Pharmacol. Rev.* **62**, 405–496.
- Trembleau, A., Morales, M., and Bloom, F.E. (1994). Aggregation of vasopressin mRNA in a subset of axonal swellings of the median eminence and posterior pituitary: light and electron microscopic evidence. *J. Neurosci.* **14**, 39–53.
- Treutlein, J., Mühleisen, T.W., Frank, J., Mattheisen, M., Herms, S., Ludwig, K.U., Treutlein, T., Schmael, C., Strohmaier, J., Bösschen, K.V., et al. (2009). Dissection of phenotype reveals possible association between schizophrenia and Glutamate Receptor Delta 1 (GRID1) gene promoter. *Schizophr. Res.* **111**, 123–130.
- Triller, A., and Choquet, D. (2003). Synaptic structure and diffusion dynamics of synaptic receptors. *Biol. Cell* **95**, 465–476.
- Tyagarajan, S.K., and Fritschy, J.-M. (2014). Gephyrin: a master regulator of neuronal function? *Nat. Rev. Neurosci.* **15**, 141–156.
- Uchida, N., Honjo, Y., Johnson, K.R., Wheelock, M.J., and Takeichi, M. (1996). The catenin/cadherin adhesion system is localized in synaptic junctions bordering transmitter release zones. *J. Cell Biol.* **135**, 767–779.
- Uemura, T., Lee, S.-J., Yasumura, M., Takeuchi, T., Yoshida, T., Ra, M., Taguchi, R., Sakimura, K., and Mishina, M. (2010). Trans-synaptic interaction of GluRdelta2 and Neurexin through Cbln1 mediates synapse formation in the cerebellum. *Cell* **141**, 1068–1079.
- Uezu, A., Kanak, D.J., Bradshaw, T.W.A., Soderblom, E.J., Catavero, C.M., Burette, A.C., Weinberg, R.J., and Soderling, S.H. (2016). Identification of an elaborate complex mediating postsynaptic inhibition. *Science* **353**, 1123–1129.
- Van Horn, M.R., Strasser, A., Miraucourt, L.S., Pollegioni, L., and Ruthazer, E.S. (2017). The Gliotransmitter d-Serine Promotes Synapse Maturation and Axonal Stabilization *In Vivo*. *J. Neurosci.* **37**, 6277–6288.
- van Versendaal, D., Rajendran, R., Saiepour, M.H., Klooster, J., Smit-Rigter, L., Sommeijer, J.P., De Zeeuw, C.I., Hofer, S.B., Heimel, J.A., and Levelt, C.N. (2012). Elimination of inhibitory synapses is a major component of adult ocular dominance plasticity. *Neuron* **74**, 374–383.
- Vizcaino, J.A., Csordas, A., Del-Toro, N., Dienes, J.A., Griss, J., Lavidas, I., Mayer, G., Perez-Riverol, Y., Reisinger, F., Ternent, T., et al. (2016). 2016 update of the PRIDE database and its related tools. *Nucleic Acids Res.* **44**, D447–D456.
- Wertz, A., Trenholm, S., Yonehara, K., Hillier, D., Raics, Z., Leinweber, M., Szalay, G., Ghanem, A., Keller, G., Rozsa, B., Conzelmann, K.K., and Roska, B. (2015). Single-cell-initiated monosynaptic tracing reveals layer-specific cortical network modules. *Science* **349**, 70–74.
- Yasumura, M., Yoshida, T., Lee, S.-J., Uemura, T., Joo, J.-Y., and Mishina, M. (2012). Glutamate receptor $\delta 1$ induces preferentially inhibitory presynaptic differentiation of cortical neurons by interacting with neurexins through cerebellin precursor protein subtypes. *J. Neurochem.* **121**, 705–716.

- Yuste, R. (2013). Electrical compartmentalization in dendritic spines. *Annu. Rev. Neurosci.* 36, 429–449.
- Yuzaki, M. (2017). The C1q complement family of synaptic organizers: not just complementary. *Curr. Opin. Neurobiol.* 45, 9–15.
- Yuzaki, M. (2018). Two Classes of Secreted Synaptic Organizers in the Central Nervous System. *Annu. Rev. Physiol.* 80, 243–262.
- Yuzaki, M., and Aricescu, A.R. (2017). A GluD Coming-Of-Age Story. *Trends Neurosci.* 40, 138–150.
- Zhong, C., Shen, J., Zhang, H., Li, G., Shen, S., Wang, F., Hu, K., Cao, L., He, Y., and Ding, J. (2017). Cbln1 and Cbln4 Are Structurally Similar but Differ in GluD2 Binding Interactions. *Cell Rep.* 20, 2328–2340.
- Ziv, N.E., and Fisher-Lavie, A. (2014). Presynaptic and postsynaptic scaffolds: dynamics fast and slow. *Neuroscientist* 20, 439–452.
- Zoghbi, H.Y., and Bear, M.F. (2012). Synaptic dysfunction in neurodevelopmental disorders associated with autism and intellectual disabilities. *Cold Spring Harb. Perspect. Biol.* 4, a009886–a009886.

STAR★METHODS

KEY RESOURCES TABLE

REAGENT or RESOURCE	SOURCE	IDENTIFIER
Antibodies		
Mouse anti-HA	Covance	Cat# MMS-101P; RRID:AB_2314672
Rabbit anti-GFP	Thermo Fisher Scientific	Cat# A-6455; RRID:AB_221570
Rabbit anti-Myc	Cell Signaling Technology	Cat# 2272; RRID:AB_10692100
Mouse anti-Myc	Cell Signaling Technology	Cat# 2276; RRID:AB_331783
Rabbit anti-GluD1	Hepp et al., 2015	N/A
Mouse anti-gephyrin	Synaptic Systems	Cat# 147 011; RRID:AB_887717
Rabbit anti-Arhgef12	Thermo Fisher Scientific	Cat# PA5-39418; RRID:AB_2556008
Rabbit anti-Ppp1r12a	Thermo Fisher Scientific	Cat# PA5-17164; RRID:AB_10978517
Rabbit anti-RFP	Rockland	Cat# 600-401-379; RRID:AB_2209751
Rabbit anti-Srgap2	Charrier et al., 2012	N/A
Rabbit anti-GAPDH	Synaptic Systems	Cat# 247 002; RRID:AB_10804053
Mouse anti-VGAT	Synaptic Systems	Cat# 131 011; RRID:AB_887872
Goat anti-mouse HRP	Jackson ImmunoResearch Labs	Cat# 115-035-003; RRID:AB_10015289
Goat anti-rabbit HRP	Jackson ImmunoResearch Labs	Cat# 111-035-144; RRID:AB_2307391
Goat anti-rabbit Alexa 488	Thermo Fisher Scientific	Cat# A27034; RRID:AB_2536097
Goat anti-mouse Cy3	Jackson ImmunoResearch Labs	Cat# 115-165-003; RRID:AB_2338680
Goat biotinylated anti-mouse	Vector Laboratories	Cat# BA-9200; RRID:AB_2336171
Nanogold goat anti-rabbit	Nanoprobes	Cat# 2003; RRID:AB_2687591
Bacterial and Virus Strains		
AAV2/1 H1-shControl.Syn-TagBFP	This paper	N/A
AAV2/1 H1-shCbln2.Syn-TagBFP	This paper	N/A
AAV2/1 H1-shCbln4.Syn-TagBFP	This paper	N/A
Lentivirus H1-shControl.Syn-EGFP	This paper	N/A
Lentivirus H1-shGluD1.Syn-EGFP	This paper	N/A
Lentivirus H1-shPpp1r12a.Syn-EGFP	This paper	N/A
Lentivirus H1-shPpp1r12a.Syn-EGFP	This paper	N/A
Lentivirus H1-shSrgap2.Syn-EGFP	This paper	N/A
Chemicals, Peptides, and Recombinant Proteins		
Tetrodotoxin	Abcam	Cat# ab120055
NBQX	Abcam	Cat# ab120046
D-AP5	Abcam	Cat# ab120003
Gabazine	Abcam	Cat# ab120042
Experimental Models: Cell Lines		
HEK293T	ATCC	Cat# CRL-1573; RRID:CVCL_0045
Experimental Models: Organisms/Strains		
Mouse: Swiss/CD-1	Janvier Labs	N/A
Mouse: C57BL/6J	Janvier Labs	N/A
Oligonucleotides		
shRNA oligos, see methods detail	This paper	N/A
gRNA oligos, see methods detail	This paper	N/A
Recombinant DNA		
pCAG HA-GluD1	This paper	N/A
pCAG HA-GluD1-mOrange	This paper	N/A

(Continued on next page)

Continued

REAGENT or RESOURCE	SOURCE	IDENTIFIER
pCAG_PSD95.FingR-EGFP-CCR5TC	Gross et al., 2013	RRID:Addgene_46295
pCAG_GPHN.FingR-EGFPCCR5TC	Gross et al., 2013	RRID:Addgene_46296
Mouse Ppp1r12a cDNA	Dharmacon	Cat# MMM1013-211691718
Human MRCK α cDNA	Dharmacon	Cat# MHS6278-213663984
pCDNA3 mRFP-ARHGEF12	Bodmann et al., 2017	N/A
Mouse Cbln2 cDNA	Dharmacon	Cat# MMM1013-202798518
Mouse Cbln4 cDNA	Dharmacon	Cat# MMM1013-202798044
pCAG 3xMyc-MRCK α	This paper	N/A
pCAG 3xMyc-Ppp1r12a	This paper	N/A
pCAG ARHGEF12	This paper	N/A
pCAG Myc-Cbln2	This paper	N/A
pCAG Myc-Cbln4	This paper	N/A
pH1SCV2 vectors	Charrier et al., 2012	N/A
pH1SCTd2 vectors	Fossati et al., 2016	N/A
Lenti H1-shRNA.Syn-EGFP vectors	This paper	N/A
pAAV H1-shRNA.Syn-TagBFP vectors	This paper	N/A
eSpCas9(1.1) vectors	Slaymaker et al., 2016	RRID:Addgene_71814
Software and Algorithms		
GPP sgRNA Designer	Broad Institute	https://portals.broadinstitute.org/gpp/public/analysis-tools/sgna-design
myProMS v3.6	Pouillet et al., 2007	http://bioinfo-out.curie.fr/myproms/proms.html
Fiji	Schindelin et al., 2012	https://fiji.sc/ ; RRID:SCR_002285
pCLAMP10	Molecular Devices	RRID:SCR_011323
Prism 7	GraphPad	RRID:SCR_002798

LEAD CONTACT AND MATERIALS AVAILABILITY

Further information and requests for resources and reagents should be directed to and will be fulfilled by the Lead Contact, Cécile Charrier (cecile.charrier@ens.fr).

EXPERIMENTAL MODEL AND SUBJECT DETAILS

Animals

All animals were handled according to French and EU regulations (APAFIS#1530-2015082611508691v3). In utero electroporations were performed on pregnant Swiss females at E14.5-15.5 (Janvier labs). For viral injections in the lateral ventricles, newborn pups (P0) of undetermined sex were used. Primary cultures were prepared from timed pregnant C57BL/6J mice at E18.5 (Janvier labs). Juveniles correspond to mice between P20 and P22. Adults correspond to mice between P69 and P75. Mice were maintained in a 12 hr light/dark cycle with unlimited access to food and water.

Primary cultures of mouse cortical neurons

Primary cultures were performed as described previously ([Charrier et al., 2012](#)) with few modifications. After dissection and dissociation of mouse cortices from E18.5 embryos, neurons were plated on glass coverslips coated with poly-D-ornytine (80 μ g/ml, Sigma) in MEM supplemented with sodium pyruvate, L-glutamine and 10% horse serum. Medium was changed 2-3 h after plating with Neurobasal supplemented with L-glutamine (2 mM), B27 (1X) and penicillin (2.5 units/ml) - streptomycin (2.5 μ g/ml). Then, one third of the medium was changed every 5 days. Unless otherwise indicated, all products were from Life Technologies. Cells were maintained at 37°C in 5% CO₂ until use.

HEK293T cells

HEK293T (CRL-1573 from ATCC) cells were cultured according to suggested protocols. Briefly, cells were maintained in DMEM (GIBCO) supplemented with 10% fetal bovine serum (GIBCO) and 1% Penicillin- Streptomycin (GIBCO) at 37°C, 5% CO₂, and passaged by trypsin/EDTA digestion (GIBCO) upon reaching confluency.

METHOD DETAILS

Plasmids for protein expression

EGFP-GPHN was previously described (Fossati et al., 2016) and it was used to visualize inhibitory synapses. HA-tagged mouse *grid1* (gift from Ludovic Tricoire, IBPS, Paris, France) was inserted into pCAG vector by PCR between XhoI and BsrGI to obtain pCAHA GluD1 or between XhoI and KpnI to obtain pCAHA GluD1-EGFP. EGFP was then replaced by mOrange between KpnI and NotI to generate pCAHA GluD1-mOrange. pCAG_PSD95.FingR-EGFP-CCR5TC and pCAG_GPHN.FingR-EGFP-CCR5TC were purchased from Addgene (plasmids #46295 and #46296, respectively). Mouse *ppp1r12a* (GenBank: BC125381, cDNA clone MGC:159084 IMAGE:40129896) and human *CDC42BPA* (encoding MRCK α , GenBank: BC136333, cDNA clone MGC:167943 IMAGE:9020320) cDNAs were obtained from Dharmacon and subcloned by PCR into pCAG vector between AgeI and BsrGI or AgeI and NotI, respectively. Both constructs were Myc-tagged by inserting a DNA cassette containing a start codon and 3x-Myc between AgeI and KpnI. Human *ARHGEF12* (gift from Moritz Bünemann, Marburg University, Germany) was inserted into pCAG vector by PCR between AgeI and BsrGI. Indicated mutations were introduced in *grid1*, *CDC42BPA*, *ppp1r12a*, and *ARHGEF12* using the QuickChange mutagenesis kit (Agilent). Mouse *cbln2* (GenBank: BC055682, cDNA clone MGC:66500 IMAGE:6412317) and *cbln4* (GenBank: BC094540, cDNA clone MGC:106619 IMAGE:5708067) cDNAs were obtained from Dharmacon and subcloned by PCR into pCAG vector between AgeI and NotI. The three constructs were Myc-tagged at the N terminus by inserting a DNA cassette containing a start codon, the signal sequence of Cbln1 (for Cbln2) or of Cbln4 (for Cbln4) and one Myc tag between EcoRI and AgeI.

shRNA and Crispr constructs and shRNA validation

For in utero knockdown experiments with shRNAs, we used the previously described pH1SCV2 and pH1SCTdT2 vectors (Charrier et al., 2012; Fossati et al., 2016). An H1 promoter drives the expression of the shRNA and a CAG promoter that of myristoylated Venus (mVenus) or TdTomato, respectively. The vector pH1SCV2 was used for dendritic spine analysis, pH1SCTdT2 was co-expressed with EGFP-GPHN to analyze inhibitory synapses. For shRNA validation on endogenous mouse *grid1*, *arhgef12* and *ppp1r12a*, we used a lentiviral vector carrying the H1 promoter to drive shRNA expression and the synapsin promoter to drive EGFP expression (Fossati et al., 2016). For AAV-mediated *in vivo* knockdown of *cbln2* and *cbln4* the plasmid pAAV-eIF1 α -tdTomato-WPRE-pGHPA (Addgene, plasmid #67527; Wertz et al., 2015) was modified as follows: a DNA cassette containing the shRNA with the H1 promoter and EGFP with the synapsin promoter was amplified by PCR from the lentiviral vector described above and inserted into pAAV-eIF1 α -tdTomato-WPRE-pGHPA between MluI and EcoRI. EGFP was then replaced by TagBFP between EcoRI and NheI. AAVs (serotype 2/1) were produced by the Centre of vector production of INSERM (CPV, UMR1089, Nantes, France). Control shRNA (shControl) was described previously (Charrier et al., 2012). The following shRNAs targeted the corresponding seed sequences: shGluD1: 5'-GAAGATAGCTCAAATCCTTAT-3'; shARHGEF12: 5'-GCAGCTGTTCCAGAGCATTG-3'; shPpp1r12a: 5'-GCTGAAATCAGTGCCTCTAAA-3'; shCbln2: 5'-GCTTAATGCAGAATGGCTACC-3'; shCbln4: 5'-GCCGTTCTGCTGATTCTAGTG-3'. ShRNAs were validated as previously described (Charrier et al., 2012). Briefly, HEK293T cells were co-transfected with mouse HA-GluD1, Myc-Ppp1r12a, Myc-Cbln2, Myc-Cbln4 or human RFP-ARHGEF12 together with the corresponding shRNA at 1:2 ratio. Two days after transfection, cells were collected and lysed in RIPA buffer (150 mM NaCl, 1.0% NP-40, 0.5% sodium deoxycholate, 0.1% SDS, 50 mM Tris, pH 8.0, Sigma-Aldrich) and further processed for western blot analysis of the relative protein expression levels. The knockdown of endogenous *grid1*, *arhgef12* and *ppp1r12a* was further validated in primary cultures of cortical neurons infected with lentiviral vectors. Neurons infected at DIV (days *in vitro*) 4 were harvested at DIV21 and lysed in RIPA buffer under agitation for 1 h at 4°C. 20 μ g of total proteins for neurons infected with shGluD1 and shArhgef12 or 40 μ g of total proteins for neurons infected with shPpp1r12a were separated by SDS-PAGE and further processed for western blot analysis. For rescue experiments, four point silent mutations were introduced in *grid1* (c1193t_t1194a_c1195_g_a1196c), *ppp1r12a* (c1355t_a1356t_g1357c_t1358a) and *ARHGEF12* (g1119a_a1120t_g1121c_c1122a) to resist to shRNA-mediated knockdown (mutants named GluD1*, Ppp1r12a* and ARHGEF12*, respectively). To knock out *grid1*, *arhgef12* and *ppp1r12a* with Crispr, we used an engineered spCas9 with enhanced specificity (espCas9(1.1), Addgene plasmid #71814) (Slaymaker et al., 2016). gRNAs were designed using the prediction software: <https://portals.broadinstitute.org/gpp/public/analysis-tools/sgRNA-design>. Each gene was knocked-out using two gRNAs that were encoded by the same plasmid together with the espCas(1.1). A DNA cassette containing the U6 promoter and one gRNA was inserted between XbaI and KpnI into espCas9(1.1) plasmid carrying a second gRNA. *grid1*: 5'-GGCCAATAATCCGTTCCAGG-3' (targets exon 2) and 5'-GAAACTCCATAACCCCTGTG-3' (targets exon 8); *arhgef12*: 5'-GTCTACTATCACGGACAGGT-3' (targets exon 1) and 5'-GGCATCACCTAATGGCCTGG-3' (targets exon 11); *ppp1r12a*: 5'-GGTGAAGCGCCAGAAGACCA-3' (targets exon 1) and 5'-GTGTTGATATAGAAGCGGCT-3' (targets exon 4).

Lentivirus production and infection

48 h after transfection of HEK293T cells, the viral supernatant was collected, centrifuged at 3,000 g for 5 min at 4°C to remove cell debris, and ultracentrifuged at 25,000 g for 2 h on a 20% sucrose cushion. Viral pellets were resuspended in sterile PBS, aliquoted and stored at -80°C. When indicated, cortical neurons were infected 4 days after plating with concentrated lentiviruses driving the expression of shRNA and EGFP.

In utero electroporation, AAV injection and slice preparation

In utero electroporation was performed as previously described (Fossati et al., 2016). Pregnant Swiss females at E14.5–15.5 (Janvier labs) were anesthetized with isoflurane (3.5% for induction and 2% during the surgery) and subcutaneously injected with 0.1 mg/kg of buprenorphine for analgesia. The uterine horns were exposed after laparotomy. Electroporation was performed using a square wave electroporator (ECM 830, BTX) and tweezer-type platinum disc electrodes (5mm-diameter, Sonidel). The electroporation settings were: 4 pulses of 40 V for 50 ms with 500 ms interval. Endotoxin-free DNA was injected using a glass pipette into one ventricle of the mouse embryos. The volume of injected DNA was adjusted depending on the experiments. Plasmids were used at the following concentrations: shRNA vectors: 0.5 $\mu\text{g}/\mu\text{l}$ (adults) or 1 $\mu\text{g}/\mu\text{l}$ (juveniles); GluD1, ARHGEF12, MRCK α and Ppp1r12a constructs: 1 $\mu\text{g}/\mu\text{l}$, except the shRNA-resistant Ppp1r12a mutant (Ppp1r12a*) and GluD1-mOrange which were used 0.5 $\mu\text{g}/\mu\text{l}$; EGFP-GPHN: 0.3 $\mu\text{g}/\mu\text{l}$; Crispr knock out plasmids: 0.5 $\mu\text{g}/\mu\text{l}$. pCAG dsRed: 0.5 $\mu\text{g}/\mu\text{l}$, pCAG TagBFP: 1 $\mu\text{g}/\mu\text{l}$, GPHN.FingR-EGFP and PSD95.FingR-EGFP: 0.7 $\mu\text{g}/\mu\text{l}$. AAV injection was performed at P0 on newborn pups previously in utero electroporated at E14.5–15.5. Upon hypothermia-induced anesthesia (avoiding direct contact of the animal with the ice), pups were injected in the lateral ventricle corresponding to the electroporated side using a graduated glass pipette. The volume corresponding to 3×10^{10} vg (viral genome) was used. Injected pups were then rapidly warmed up and kept on a heating pad set at 37°C until complete recovery. Animals were sacrificed at the indicated age by terminal perfusion of 4% paraformaldehyde (Electron Microscopy Sciences) in PBS. Unless otherwise indicated, 100 μm coronal brain sections were obtained using a vibrating microtome (Leica VT1200S, Leica Microsystems). Sections were mounted on slides in Vectashield.

Immunohistochemistry for confocal microscopy

Animals at postnatal day 21 were intracardially perfused with PBS and 4% paraformaldehyde (see above). After post-fixation, dissected brains were cryoprotected in 20% sucrose at 4°C for at least 16 h and then frozen at -80°C . 20 μm coronal sections were obtained using a cryostat and further processed for immunohistochemistry. Briefly, slices were incubated in 0.1% Triton X-100 and 0.25% fish gelatin (Sigma-Aldrich) in PBS to permeabilize and block unspecific staining. Primary antibodies were incubated overnight at 4°C and secondary antibodies for 3 h at room temperature under gentle agitation. Both primary and secondary antibodies were diluted in 0.1% Triton X-100 and 0.125% fish gelatin in PBS. Coverslips were mounted on slides in Vectashield (Vector Laboratories). Mouse anti-Gephyrin (Synaptic Systems Clone 7a, 1:400) and rabbit anti-GluD1 (kind gift from L. Tricoire, IBPS, Paris, France) (Benamer et al., 2018; Hepp et al., 2015) were used as primary antibodies. All secondary antibodies Alexa- (Invitrogen) or Cyanin-conjugated (Jackson ImmunoResearch) were diluted 1:500.

Confocal image acquisition

Confocal images were acquired in 1024x1024 mode using Leica TCS SP8 confocal laser scanning platforms controlled by the LAF AS software and equipped with a tunable white laser and hybrid detectors (Leica Microsystems) or, for slices infected with AAVs expressing TagBFP, in 512x512 mode using an inverted microscope (Nikon Ti PSF) equipped with a CSUX1-A1 Yokogawa spinning disc and an EMCCD camera and controlled by the Metamorph software (Molecular Devices). We used the following objective lenses: 10X PlanApo, NA 0.45 (identification of electroporated neurons and low magnification images) and 100X HC-PL APO, NA 1.44 CORR CS (Leica) or 100 X HC-PlanApo, NA 1.4 (Nikon) (images of spines, gephyrin and PSD-95 clusters and association between GluD1, immunostained gephyrin and PS-D95 or Gephyrin.FingRs). Images were blindly acquired and analyzed. Z stacks of images were acquired with spacing of 150 nm.

Electron microscopy

Anesthetized P21 mice were intracardially perfused with 2% paraformaldehyde (PFA) and 0.1% glutaraldehyde in phosphate-buffered saline (PBS) and post-fixed overnight at 4°C in 2% PFA. Coronal sections (200 μm) were obtained using a vibratome (see above) and cryoprotected overnight in 20% glycerol and 20% sucrose under gentle agitation at 4°C. They were permeabilized with 3 freeze-thawing cycles performed by floating them on liquid nitrogen in an aluminum cup. They were then extensively rinsed in PBS, and immersed for 20 min in 50 mM ammonium chloride and for 30 min in PBS with 0.1% gelatin (PBSg). For double detection of VGAT and GluD1, GluD1 labeling was performed first. Coronal sections were incubated for 60 h at 4°C with a rabbit anti-GluD1 antibody (1:1,000 dilution, see immunohistochemistry). Sections were rinsed extensively in PBSg and then incubated 6h at room temperature with a goat anti-rabbit secondary antibody coupled with nanogold particles (Nanoprobe, 1:100). Gold particles were intensified for 5 min at 20°C with HQ silver kit (Nanoprobe) in a dark room. Gold toning (Trembleau et al., 1994) was performed on the sections. They were then rinsed extensively in PBS and PBSg. For the detection of VGAT, sections were incubated for 48 h at 4°C with anti-VGAT mouse monoclonal antibody (Synaptic Systems, 1:100), rinsed extensively in PBSg and then incubated 4 h at room temperature with a biotinylated goat anti-mouse antibody (Vector Laboratories, 1:100). Detection of the biotinylated antibody was carried by the avidin–biotin complex method (Elite Vectastain kit, Vector; and Sigma fast DAB, Sigma-Aldrich). Antigen-antibody complexes were stabilized by dipping the sections for 5 min in 1% glutaraldehyde in PBS. Sections were then post-fixed for 1 h in 2% OsO₄ in PBS at 4°C in the dark, dehydrated in graded ethanol and flat-embedded in epoxy resin (Araldite, Polysciences). Embedded sections were mounted orthogonally on a resin block and cut tangentially to the pial surface. To reach cortical layers 2/3, 200 sections

of 1 μm thickness of tissue were removed from the onset of layer 1 using an UC6 ultramicrotome (Leica Microsystems). Ultrathin sections (70 nm, pale yellow) were contrasted with uranyl acetate and Reynolds lead citrate. Observations were performed with a TECNAI 12 electron microscope (Philips).

Electrophysiology

Acute coronal brain slices (300 μm thick) were obtained from juvenile (postnatal day 16–19) Swiss mice electroporated in utero with shGluD1 in pH1SCTdT2. Whole-cell patch-clamp recordings were performed in layer 2/3 cortical pyramidal neurons of the somatosensory cortex. Briefly, after decapitation the brain was quickly removed from the skull and placed in ice-cold (4°C) ‘cutting solution’ containing (in mM): 85 NaCl, 64 sucrose, 25 glucose, 2.5 KCl, 1.2 NaH₂PO₄, 24 NaHCO₃, 0.5 CaCl₂, and 7 MgCl₂, saturated with 95% O₂ and 5% CO₂ (pH 7.3–7.4). Slices were cut using the 7000 smz-2 tissue slicer (Campden Instrument). Slices recovered in oxygenated artificial cerebrospinal fluid (ACSF) containing (in mM): 125 NaCl, 2.5 KCl, 2 CaCl₂, 1 MgCl₂, 1.2 NaH₂PO₄, 24 NaHCO₃, and 25 glucose (pH 7.4), at 35°C for 10 min and then at room temperature for at least 45 min. For electrophysiological recordings, slices were transferred to a submerged recording chamber and continuously perfused at 33–34°C with oxygenated ACSF at a rate of 4–5 ml/min. Inhibitory and excitatory miniature post-synaptic miniature currents (mIPSCs and mEPSCs, respectively) were recorded at a holding potential of –60 mV in the presence of 0.5 μM TTX. mIPSCs were isolated by adding NBQX (10 μM) and D-AP5 (50 μM) to the ACSF. mEPSCs were isolated using gabazine (10 μM). mIPSCs were recorded using an intracellular solution containing (in mM): 150 KCl, 1.5 MgCl₂, 10 HEPES 10, 1 EGTA, 2 NaATP, 0.5 NaGTP (pH adjusted to \sim 7.3 with KOH). mEPSCs were recorded using an intracellular solution containing (in mM): 144 K-gluconate, 7 KCl, 10 HEPES, 1 EGTA, 1.5 MgCl₂, 2 NaATP, 0.5 NaGTP, (pH adjusted to \sim 7.3 with KOH). Access and input resistance were monitored by applying 5 mV hyperpolarizing steps of current. All drugs were obtained from Abcam.

Transfection and western blotting

Transfection was performed using Jet-Prime (Polyplus Transfection) according to the manufacturer protocol. Western blotting was performed using the following primary antibodies: mouse anti-HA (HA.11 Clone 16B12 Monoclonal Antibody, Covance, 1:1,000), rabbit anti-GFP (Life Technologies, 1:2,000), rabbit anti-Myc (Cell Signaling Technology, 1:1,000), rabbit anti-GluD1 (gift from L. Tricoire, 1:1000), rabbit anti-Arhgef12 (ThermoFisher Scientific, 1:1,000), rabbit anti-Ppp1r12a (ThermoFisher Scientific, 1:1,000), rabbit anti-RFP (Rockland Immunochemicals, 1:1,000), rabbit anti-SRGAP2 (1:2,000; (Charrier et al., 2012; Fossati et al., 2016), rabbit anti-GAPDH (Synaptic Systems, 1:1,000). All HRP-conjugated secondary antibodies were used at 1:30,000 dilution (Jackson ImmunoResearch). Protein visualization was performed by chemiluminescence using LumiLight western blotting (Roche) or Clarity Western ECL (Biorad) substrates and ImageQuant LAS 4000 (GE Healthcare) or Chemidoc (Biorad) imagers.

Cell surface biotinylation

Transfected HEK cells or primary cultures of cortical neurons at 15 or 22–23 days *in vitro* (DIV) were washed 3 times in ice-cold PBS supplemented with 0.8 mM CaCl₂ and 0.5 mM MgCl₂ (PBS²⁺) and then incubated for 12 min at room temperature followed by further 12 min at 4°C with 1 mg/ml Sulfo-NHS-SS-Biotin (ThermoFisher Scientific) in PBS²⁺. After rinsing in ice-cold PBS²⁺, biotin was quenched in 50 mM glycine in PBS²⁺ for 10 min. Cells were scraped in NaCl-Tris buffer supplemented with protease inhibitory cocktail (Roche) and then lysed (150 mM NaCl, 50 mM TrisHCl, 2% Triton X-100, 2 mM EDTA, 1 mM PMSF, protease inhibitor cocktail) for 1 h at 4°C. Biotinylated proteins were pulled down by incubating cell lysates with neutravidin agarose beads (ThermoFisher Scientific) for 2 h at 4°C. After extensive washes, beads were resuspended in gel loading buffer (Sigma-Aldrich) and bound proteins were eluted with boiling. Relative cell surface expression levels were analyzed by western blotting. Inputs correspond to 20% of the cell surface fraction.

Subcellular fractionation

Subcellular fractionation was performed from Swiss P15 mouse brains. All steps were performed at 4°C. Briefly, brains were homogenized in ice-cold HEPES-buffered sucrose (0.32 M sucrose, 4 mM HEPES pH 7.4, 5 mM EDTA, 5 mM EGTA, protease inhibitor cocktail, from Sigma) using a motor driven glass-teflon homogenizer. The homogenate was centrifuged at 3,000 g for 15 min. The resulting supernatant was centrifuged at 38,400 g for 15 min, yielding the crude synaptosomal pellet. The pellet was then subjected to hypo-osmotic shock and centrifuged at 38,400 g for 20 min. The resulting pellet was lysed for 1 h using HEPES-buffered NaCl (100 mM NaCl, 4 mM HEPES pH 7.4, 5 mM EDTA, 5 mM EGTA, protease inhibitor cocktail) supplemented with 1% CHAPS (Sigma) and centrifuged at 100,000 g for 1 h. The corresponding supernatant is referred to as synaptic fraction or synaptic membranes. Protein concentration was measured and protein samples were subjected to immunoprecipitation.

Immunoprecipitation

For HEK cells, 1 mg of total protein from each sample was diluted in NP-40 buffer (1% Igepal, 50mM Tris pH 7.4, 150mM NaCl, 2mM EDTA, protease inhibitor cocktail) and incubated overnight at 4°C, with either 5 μg of mouse anti-HA antibody (HA.11 Clone 16B12 Monoclonal Antibody, Covance) or 5 μg of mouse anti-Myc antibody (clone 9B11 Monoclonal Antibody, Cell Signaling Technology) and 5 μg of mouse IgG as negative control. Protein G-agarose beads (Thermo Fisher Scientific) were then added for 2 h at 4°C. After extensive washes (1% Igepal, 50mM Tris pH 7.4, 200mM NaCl, 2mM EDTA, protease inhibitor cocktail), the beads were resuspended

in gel-loading buffer and bound proteins were released with boiling. Inputs correspond to 50 μ g of proteins. Samples were subjected to western blot analysis. For brain samples and mass spectrometry analysis, the immunoprecipitations were performed using antibodies covalently cross-linked to protein G magnetic beads (Pierce). 36 μ g of rabbit anti-GluD1 antibody, or total rabbit IgG in control condition, were incubated 1 h at room temperature and cross-linked with 20 mM DMP (dimethylpimelimidate, Pierce) in 0.2 M Sodium Borate pH 9. After 30 min, the reaction was blocked for 1 h with 0.2 M Ethanolamine pH 8. Eventual unbound antibody molecules were washed out by incubating beads for 5 min in 0.1 M glycine pH 3. The efficiency of cross-linking was checked by running samples on polyacrylamide 4%–15% gradient gels (Biorad) followed by Coomassie Blue staining. 1 mg of total proteins from purified synaptic membranes were diluted in a HEPES-NaCl buffer (20 mM HEPES pH 7.4, 150 mM NaCl, 5 mM EDTA, 5 mM EGTA, protease inhibitor cocktail) supplemented with 1% CHAPS and incubated overnight at 4°C with 36 μ g of rabbit anti-GluD1 antibody, or total rabbit IgG in control condition, covalently cross-linked to protein G magnetic beads. The beads were rinsed 3 times using HEPES-NaCl buffer supplemented with 0.1% CHAPS and further washed 3 times in a buffer containing 20 mM HEPES pH 7.4 and 150 mM NaCl. The samples were then subjected to mass spectrometry analysis (see below). GluD1-immunoprecipitation from brain extracts was repeated three times.

Proteomics

Proteins on magnetic beads were washed twice with 100 μ L of 25 mM NH_4HCO_3 and we performed on-beads digestion with 0.2 μ g of trypsin/LysC (Promega) for 1 h in 100 μ L of 25 mM NH_4HCO_3 . Samples were then loaded onto a homemade C18 StageTips for desalting (principle by stacking one 3M Empore SPE Extraction Disk Octadecyl (C18) and beads from SepPak C18 Cartridge Waters into a 200 μ L micropipette tip). Peptides were eluted using 40/60 MeCN/ H_2O + 0.1% formic acid and vacuum concentrated to dryness.

Online chromatography was performed with an RSLCnano system (Ultimate 3000, Thermo Scientific) coupled online to an Orbitrap Fusion Tribrid mass spectrometer (Thermo Scientific). Peptides were trapped on a C18 column (75 μ m inner diameter \times 2 cm; nanoViper Acclaim PepMap 100, Thermo Scientific) with buffer A (2/98 MeCN/ H_2O in 0.1% formic acid) at a flow rate of 4.0 μ L/min over 4 min. Separation was performed on a 50 cm \times 75 μ m C18 column (nanoViper Acclaim PepMap RSLC, 2 μ m, 100Å, Thermo Scientific) regulated to a temperature of 55°C with a linear gradient of 5% to 25% buffer B (100% MeCN in 0.1% formic acid) at a flow rate of 300 nL/min over 100 min. Full-scan MS was acquired in the Orbitrap analyzer with a resolution set to 120,000 and ions from each full scan were HCD fragmented and analyzed in the linear ion trap.

QUANTIFICATION AND STATISTICAL ANALYSIS

Confocal image analysis

Gephyrin and PSD-95 clusters, dendritic spines and the association of GluD1 with Gephyrin and PSD95 were quantified in the proximal part of oblique dendrites directly originating from the apical trunk using Fiji (Schindelin et al., 2012; <https://fiji.sc/>). Only dendrites that were largely parallel to the plane of the slice and acquired from sections of comparable rostro-caudal position were analyzed (usually no more than 1 dendrite per neuron). The density of dendritic spines and gephyrin clusters along dendrites was calculated as described (Charrier et al., 2012; Fossati et al., 2016). Gephyrin and PSD-95 clusters were quantified over a dendrite of a minimal length of 60 μ m. The length of the dendritic segment was measured on the z projection. The fraction of gephyrin and PSD-95 clusters associated with GluD1 (association index) was manually determined on individual dendrites. A gephyrin or PSD-95 cluster labeled with EGFP-tagged FingRs was considered associated with GluD1 if it overlapped with a GluD1-mOrange puncta.

mEPSC and mIPSC analysis

Data were sampled at 10 kHz and filtered at 2 kHz. Miniature currents were analyzed over 1 min periods using pClamp 10.0 (Molecular Devices). Cells showing > 20% change in access and input resistance upon application of 5 mV hyperpolarizing steps of current were excluded from the analysis. Overlapping events were excluded from amplitude analysis. Cumulative probability graphs were obtained by taking the first 200 events within the analyzed time window of each recorded cell.

Proteomic analysis

For protein identification, data were searched against the *Mus musculus* (Mouse) UniProt database using Sequest HF through proteome discoverer (version 2.1). Enzyme specificity was set to trypsin and a maximum of two missed cleavage site were allowed. Oxidized methionine, N-terminal acetylation, and carbamidomethyl cysteine were set as variable modifications. Maximum allowed mass deviation was set to 10 ppm for monoisotopic precursor ions and 0.6 Da for MS/MS peaks. The resulting files were further processed using myProMS (Poulet et al., 2007) v3.6 (work in progress). FDR calculation used Percolator and was set to 1% at the peptide level for the whole study.

Statistics

Data are a minimum of three independent experiments. For in utero electroporations and AAV injections, data were obtained from at least three experiments or three animals from two independent litters.

For statistical analysis, we first checked the normality of the distributions using the D'Agostino-Pearson normality test. In case of normal distributions, we used unpaired Student's t test or one-way analysis of variance followed by Tukey's post test. Non-normal

distributions were assessed using the non-parametric Mann-Whitney test or the Kruskal-Wallis test followed by the Dunn's multiple comparison test. A test was considered significant when $p < 0.05$. Data represent the distribution (or the mean) of the mean value per cell in the main figures. The whiskers of the boxplots in [Figure 2](#) are the minimal and maximal values. Statistical analyses were performed with Prism (GraphPad Software).

DATA AND CODE AVAILABILITY

The mass spectrometry dataset generated in this study has been deposited to the ProteomeXchange Consortium via the PRIDE ([Vizcaino et al., 2016](#)) partner repository with the dataset identifier PXD010373.

Neuron, Volume 104

Supplemental Information

***Trans*-Synaptic Signaling through the Glutamate Receptor Delta-1 Mediates Inhibitory Synapse Formation in Cortical Pyramidal Neurons**

Matteo Fossati, Nora Assendorp, Olivier Gemin, Sabrina Colasse, Florent Dingli, Guillaume Arras, Damarys Loew, and Cécile Charrier

SUPPLEMENTAL INFORMATION

SUPPLEMENTAL DATA

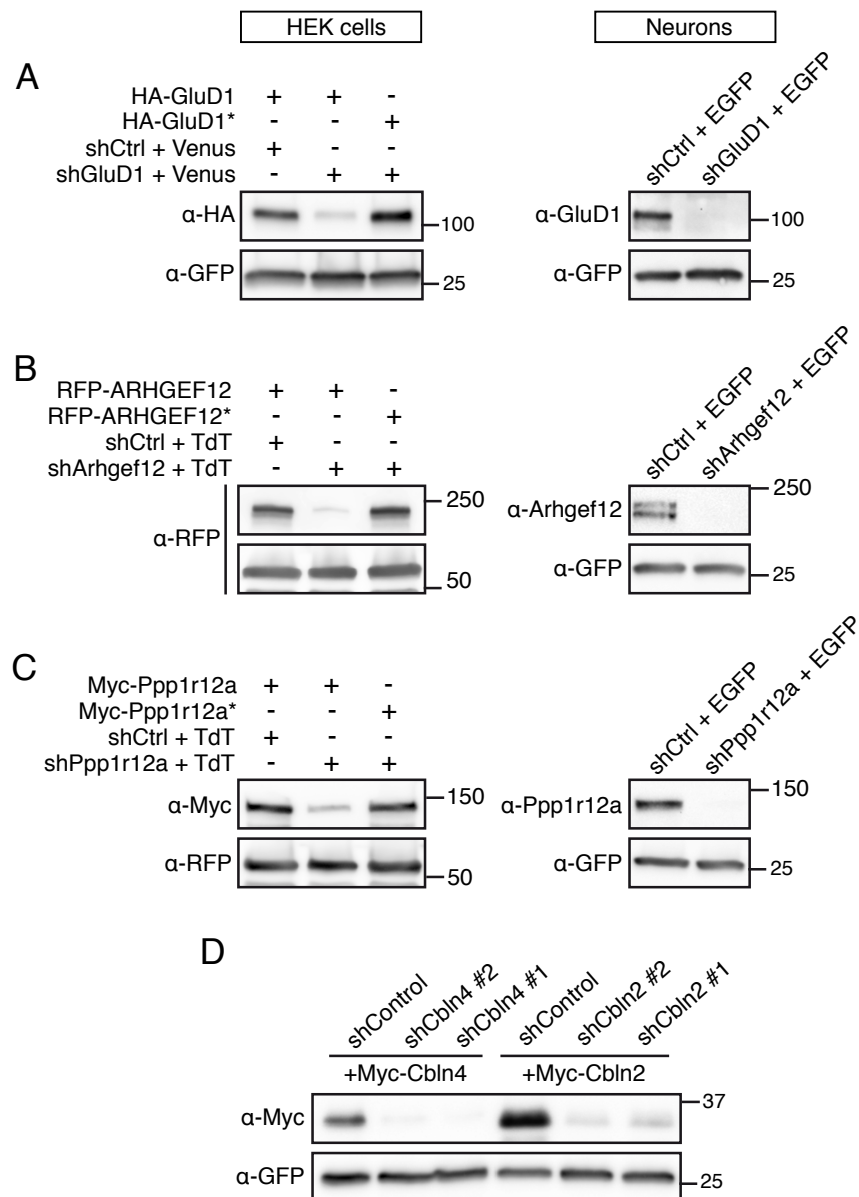


Figure S1. Validation of the shRNAs targeting *grid1*, *arhgef12*, *ppp1r12a*, *cbln2* and *cbln4* (related to Figures 1, 5 and 6).

(A-C) Validation of shRNAs targeting *grid1* (encoding GluD1) (A), *arhgef12* (B) and *ppp1r12a* (C) in HEK cells transfected with the indicated cDNAs (left panels) and in cortical neurons infected with lentiviral vectors driving the expression of shRNAs along with EGFP (right panels). HEK cells were transfected and harvested after 48 hours. Cortical neurons were infected at DIV 4 and collected at DIV 21. Cells were then lysed and subjected to western blot analysis as described in the method section. shCtrl: control shRNA; TdT: tdTomato. Constructs labeled with asterisks correspond to shRNA-resistant mutants for rescue experiments.

(D) Validation of shRNAs targeting *cbln2* and *cbln4* in HEK cells (see methods for details). shCbln4 #1 and shCbln2 #2 were selected and inserted into AAV vectors to knockdown the expression of *cbln4* and *cbln2* in mouse cortices in vivo (Figure 5).

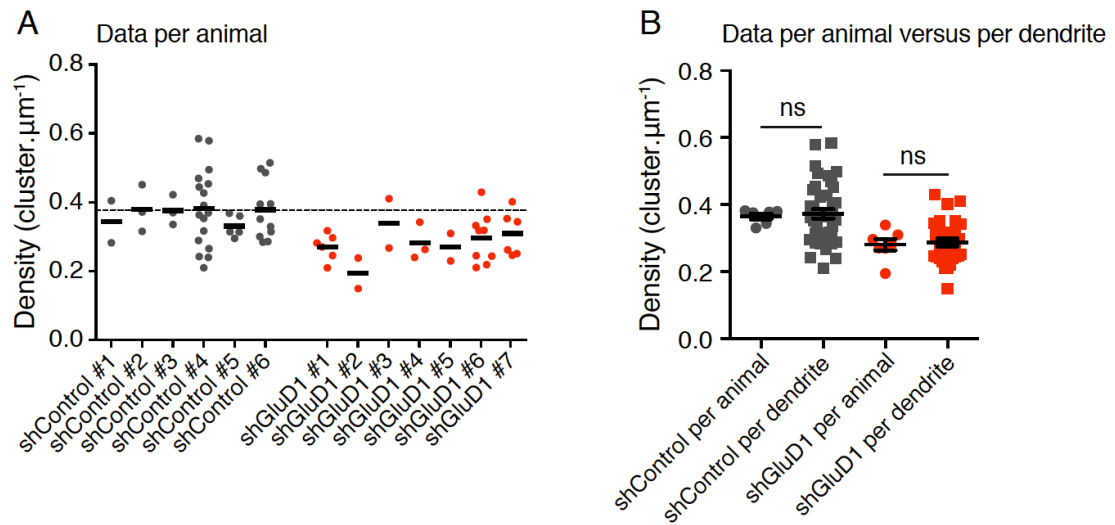


Figure S2. EGFP-gephyrin cluster analysis per animal (related to Figure 1).

(A) Plot showing the distribution of gephyrin cluster density per animal in layer 2/3 pyramidal neurons expressing a scramble shRNA (shControl) and against mouse *grid1* (shGluD1) at juvenile stage (P20-22). Each dot represents one dendrite and the bars indicate the mean value. The dotted line is the average density of gephyrin clusters in control neurons (same data as in Figure 1). #: mouse identification.

(B) Comparison of EGFP-gephyrin cluster density when the dendrites are averaged per animal or analyzed individually. Per animal analysis: $n_{\text{shControl}} = 6$, $n_{\text{shGluD1}} = 7$. Per dendrite analysis: $n_{\text{shControl}} = 41$, $n_{\text{shGluD1}} = 30$. Bars represent mean \pm SEM, ns: $p > 0.05$ determined by Mann-Whitney test.

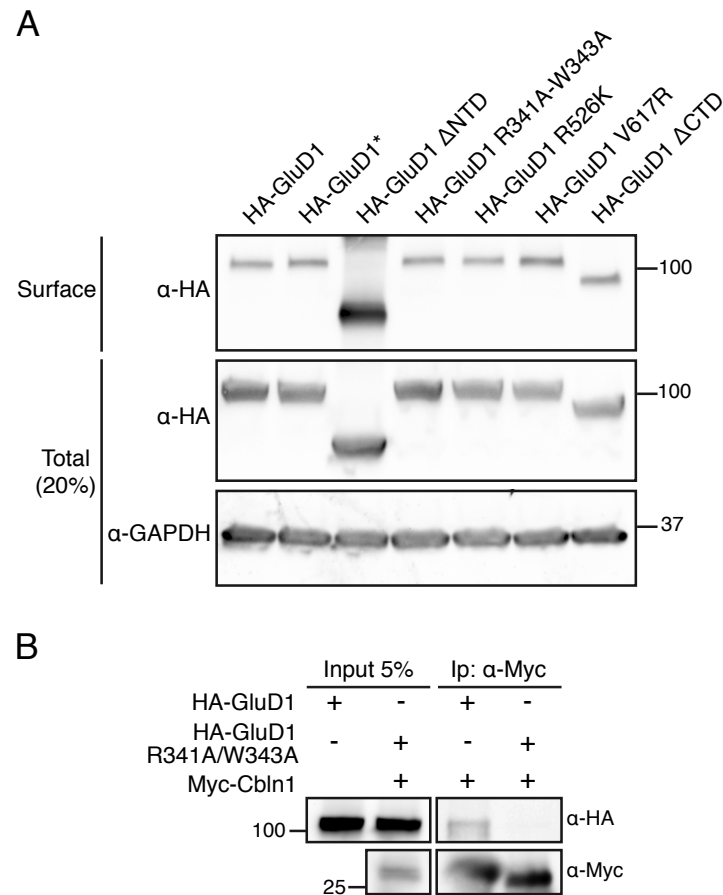


Figure S3. Characterization of GluD1 mutants (related to Figure 4).

(A) HEK cells were transfected for 24 hours with GluD1 mutants and their cell surface expression was probed with cell surface biotinylation followed by western blot. GAPDH expression level was used as a loading control. All GluD1 mutants were trafficked to the plasma membrane and their relative expression levels at the cell surface were quantified as surface/total ratio and normalized to HA-GluD1* mutant (HA-GluD1: 0.78; HA-GluD1 ΔNTD: 5.3; HA-GluD1 R341A/W343A: 1.4; HA-GluD1 R526K: 0.8; HA-GluD1 V617R: 1.7; HA-GluD1 ΔCTD: 1.6). Note that all mutants are delivered to the cell surface at least as efficiently as HA-GluD1, demonstrating that the phenotypes observed in Figure 4 cannot be ascribed to a defect in protein transport. Also, note that the overexpression of GluD1 increased the density of gephyrin clusters (Figure 1), further highlighting the importance of the NTD of GluD1 in the regulation of inhibitory synapse formation.

(B) Coimmunoprecipitation (coIP) of HA-GluD1 or HA-GluD1 R341A/W343A mutant with Myc-Cbln1 in HEK cells. Lysates of cells transfected with HA-GluD1 or HA-GluD1 R341A/W343A and lysates derived from cells overexpressing Myc-Cbln1 were mixed together and subjected to immunoprecipitation and western blot analysis (see methods for details). Note the absence of interaction between Cbln1 and the HA-GluD1 R341A/W343A mutant.

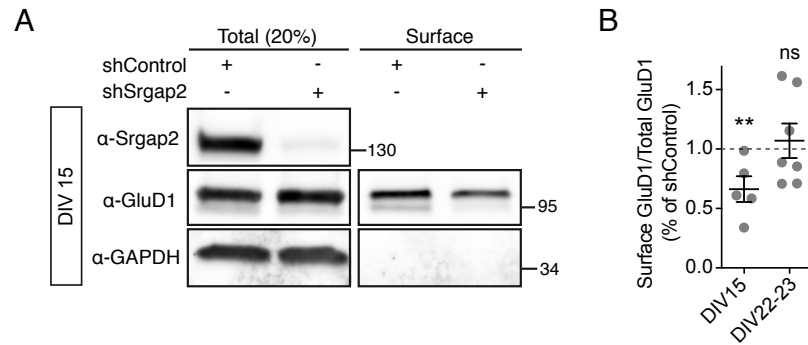


Figure S4. SRGAP2 controls the trafficking of GluD1 in cortical neurons (related to Figure 6).

(A) Cell surface expression of GluD1 using cell surface biotinylation followed by western blot in dissociated cortical neurons at 15 days in vitro (DIV). Neurons were infected at DIV4 with lentiviruses carrying either a control shRNA (shControl) or an shRNA against *Srgap2* (shSrgap2). GAPDH expression level was used as a loading control and to check the specificity of cell surface labeling.





(B) Quantification of cell surface expression levels of GluD1 in neurons expressing shSrgap2 at DIV15 and DIV22-23. Data are normalized to control neurons (dotted line). $n_{\text{DIV15}} = 5$ cultures, $n_{\text{DIV22-23}} = 7$ cultures. Bars represent mean \pm SEM, **: $p < 0.01$ and ns: $p > 0.05$ determined by Mann-Whitney test.

Lentiviral constructs were previously described in (Fossati et al., 2016).


ANNEX 2

RESEARCH ARTICLE

Unique properties of dually innervated dendritic spines in pyramidal neurons of the somatosensory cortex uncovered by 3D correlative light and electron microscopy

Olivier Gemin¹, Pablo Serna^{1,2}, Joseph Zamith¹, Nora Assendorp¹, Matteo Fossati¹, Philippe Rostaing¹, Antoine Triller^{1*}, Cécile Charrier^{1*}

1 Institut de Biologie de l'Ecole Normale Supérieure (IBENS), CNRS, INSERM, PSL Research University, Paris, France, **2** Laboratoire de Physique de l'Ecole Normale Supérieure, ENS, PSL Research University, CNRS, Sorbonne Université, Université Paris-Diderot, Sorbonne Paris Cité, Paris, France

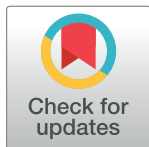
 These authors contributed equally to this work.

^{¶a} Current address: Structural and Computational Biology Unit, European Molecular Biology Laboratory, Heidelberg, Germany

^{¶b} Current address: CNR—Institute of Neuroscience, URT-Humanitas, Rozzano, Italy

^{¶c} Current address: Humanitas Clinical and Research Center—IRCCS, Rozzano, Italy

* antoine.triller@ens.psl.eu (AT); cecile.charrier@ens.psl.eu (CC)



OPEN ACCESS

Citation: Gemin O, Serna P, Zamith J, Assendorp N, Fossati M, Rostaing P, et al. (2021) Unique properties of dually innervated dendritic spines in pyramidal neurons of the somatosensory cortex uncovered by 3D correlative light and electron microscopy. PLoS Biol 19(8): e3001375. <https://doi.org/10.1371/journal.pbio.3001375>

Academic Editor: Eunjoon Kim, Institute for Basic Science, REPUBLIC OF KOREA

Received: October 16, 2020

Accepted: July 29, 2021

Published: August 24, 2021

Copyright: © 2021 Gemin et al. This is an open access article distributed under the terms of the [Creative Commons Attribution License](https://creativecommons.org/licenses/by/4.0/), which permits unrestricted use, distribution, and reproduction in any medium, provided the original author and source are credited.

Data Availability Statement: All light and electron microscopy files are available from our institute's database at the following address: <https://www.opendata.bio.ens.psl.eu/3DCLEM-Spines> (login: guest; password: EnsData0811). All scripts and files defining the computational model are available at the following address: <https://github.com/pabloserna/SpineModel>. The numerical data presented in the figures are available here (login: guest; password: EnsData0811): <https://www.opendata.bio.ens.psl.eu/3DCLEM-Spines/data/>. All

Abstract

Pyramidal neurons (PNs) are covered by thousands of dendritic spines receiving excitatory synaptic inputs. The ultrastructure of dendritic spines shapes signal compartmentalization, but ultrastructural diversity is rarely taken into account in computational models of synaptic integration. Here, we developed a 3D correlative light–electron microscopy (3D-CLEM) approach allowing the analysis of specific populations of synapses in genetically defined neuronal types in intact brain circuits. We used it to reconstruct segments of basal dendrites of layer 2/3 PNs of adult mouse somatosensory cortex and quantify spine ultrastructural diversity. We found that 10% of spines were dually innervated and 38% of inhibitory synapses localized to spines. Using our morphometric data to constrain a model of synaptic signal compartmentalization, we assessed the impact of spinous versus dendritic shaft inhibition. Our results indicate that spinous inhibition is locally more efficient than shaft inhibition and that it can decouple voltage and calcium signaling, potentially impacting synaptic plasticity.

Introduction

In the mammalian cortex, the vast majority of excitatory synapses are formed on dendritic spines, small membrane protrusions that decorate the dendrites of pyramidal neurons (PNs) [1–3]. Dendritic spines are composed of a bulbous head connected to the dendritic shaft by a narrow neck [4,5]. They exist in a large variety of shapes and sizes along individual dendrites. Spine head volume can vary between 3 orders of magnitude (0.01 to 1.5 μm^3), neck length between 0.2 μm and 3 μm , and minimal neck diameter between 20 and 500 nm [6]. Spine

other relevant data are within the paper and its [Supporting Information](#) files.

Funding: This work was supported by INSERM, the Agence Nationale de la Recherche (<https://anr.fr/>) (ANR-13-PDOC-0003 and ANR-17-ERC3-0009 to C.C.), the European Research Council (<https://erc.europa.eu/>) (ERC starting grant 803704 to C.C.), the Labex Memolife (<https://www.memolife.biologie.ens.fr/?lang=fr>) (901/IBENS/LD09 to O.G.), the company NIKON France via the CIFRE program (convention n° 2015/1049 to O.G.) and the European Union's Horizon 2020 Framework Programme for Research and Innovation under the Specific Grant Agreement No. 785907 (Human Brain Project SGA2 to P.S.). We are grateful to the IBENS Imaging Facility (France BioImaging, supported by ANR-10-INBS-04, ANR-10-LABX-54 MEMO LIFE, and ANR-11-IDEX-000-02 PSL* Research University, "Investments for the future"; NERF 2011-45; FRM DGE 20111123023; and FRC Rotary International France). The funders had no role in study design, data collection and analysis, decision to publish, or preparation of the manuscript.

Competing interests: The authors have declared that no competing interests exist.

Abbreviations: AMPA, α -amino-3-hydroxy-5-methyl-4-isoxazolepropionic acid; DAB, 3,3'-diaminobenzidine; DiSSs, dually innervated spines; EM, electron microscopy; ePSD, excitatory postsynaptic density; EPSP, excitatory postsynaptic potential; GFP-GPHN, GFP-tagged gephyrin; GLM, generalized linear model; HPF, high-pressure freezing; iPSD, inhibitory postsynaptic density; IPSP, inhibitory postsynaptic potential; IUE, *in utero* electroporation; KS test, Kolmogorov-Smirnov test; LM, light microscopy; LTD, long-term depression; LTP, long-term potentiation; L2/3, layer 2/3; MIB, Microscopy Image Browser; NIRB, near-infrared branding; NMDA, N-Methyl-D-aspartate; PBS, phosphate-buffered saline; PFA, paraformaldehyde; PN, pyramidal neuron; RC, resistor-capacitor; ROI, region of interest; SA, spine apparatus; SBEM, serial block-face scanning EM; SER, smooth endoplasmic reticulum; SiSSs, singly innervated spines; SRGAP2C, Slit-Robo Rho GTPase-activating protein 2C; SSC, somatosensory cortex; STED, stimulated emission depletion; TCH, thiocarbonylhydrazide; VDCC, voltage-dependent calcium channel; 3D-CLEM, 3D correlative light-electron microscopy.

heads are typically contacted by an excitatory synaptic input and harbor an excitatory postsynaptic density (ePSD) that contains glutamatergic α -amino-3-hydroxy-5-methyl-4-isoxazole-propionic acid (AMPA) and N-Methyl-D-aspartate (NMDA) neurotransmitter receptors, scaffolding proteins, adhesion molecules, and a complex machinery of proteins undertaking the transduction of synaptic signals. The size of the spine head correlates with the size of the ePSD and the strength of synaptic transmission [7–11]. In addition to the ePSD, spines contain ribosomes, which mediate local protein synthesis, and endosomes, which play a critical role in membrane and receptor trafficking [12,13]. The largest spines often contain a spine apparatus (SA), which contributes to calcium signaling and synaptic plasticity [12,14], and some spines, especially in the upper layers of the cortex, also house an inhibitory postsynaptic specialization [15]. Spine necks are diffusional barriers that biochemically isolate spine heads from their parent dendrite [16–19]. In addition, they can filter the electrical component of synaptic signals and amplify spine head depolarization [20–22] (but see [23–25]). Both spine heads and spine necks are remodeled depending on neuronal activity [9,26,27] and in pathology [28,29]. While the relationship between spine morphology and function is widely acknowledged, and although dendritic spines are known to participate in different neural circuits depending on their location in the dendritic tree [30], the extent of synaptic ultrastructural diversity along individual identified dendrites has not been quantified, and the consequences of this variability on signal compartmentalization and dendritic integration remain to be investigated.

Dendritic signaling can be modeled based on anatomical and biophysical parameters [31] using “realistic” multicompartment models [32]. These models were pioneered by Wilfrid Rall following the seminal works of Hodgkin and Huxley [33,34]. They have provided a powerful theoretical framework for understanding dendritic integration [35], spine function [36], inhibitory signaling [37,38], and electrical compartmentalization in spines [22,39,40]. However, spines and synapses are usually modeled with *ad hoc* or averaged biophysical parameters, which limit the accuracy of the prediction [41]. Modeling the actual behavior of dendritic spines requires an accurate description of their ultrastructural heterogeneity with a cell-type- and dendritic-type-resolution. To acquire such data, it is necessary to combine the nanometer resolution of electron microscopy (EM) with an approach that allows the identification of the origin of dendritic spines (i.e., location on the dendrite, type of dendrite, and type of neuron) without obscuring the intracellular content. This task is arduous: 1 mm³ of mouse cortex contains over 50,000 of neurons, each of which establishes approximately 8,000 synaptic connections with neighboring neurons, and these synapses are highly specific, connecting multiple neuronal subtypes from various brain regions [42–45]. Reconstructing selected dendritic spines and synaptic contacts along dendritic trees requires either enormous volumes of 3D-EM acquisitions using resource-consuming approaches adapted from connectomics [46–49] or combining EM with a lower-scale imaging modality such as confocal or 2-photon light microscopy (LM) to guide 3D-EM image acquisitions to the region of interest (ROI) [50–52]. While very powerful *in vitro* [50,53,54], correlative light-electron microscopy (CLEM) is difficult to implement in brain tissues [55–57]. New protocols are required to facilitate the *in situ* identification of targeted dendrites and synapses in different imaging modalities and to make 3D-CLEM more accessible to the neuroscientific community.

Here, we have developed a CLEM workflow combining confocal light microscopy with serial block-face scanning EM (SBEM) and targeted photoprecipitation of 3,3'-diaminobenzidine (DAB) to facilitate ROI recovery. We applied this workflow to reconstruct dendritic spines located exclusively on the basal dendrites of genetically labelled PNs in layer 2/3 (L2/3) of the somatosensory cortex (SSC) of adult mice. We analyzed the variability of their ultrastructure and estimated the electrical resistance of their neck. We also examined the distribution and the morphology of inhibitory synapses. We specifically examined dendritic spines

receiving both excitatory and inhibitory inputs, which represented 10% of all spines along basal dendrites. These dually innervated spines (DiSs) exhibited wider heads and larger ePSDs than singly innervated spines (SiSs), and they were more electrically isolated from the dendritic shaft than SiSs of comparable head size. We then used our measurements to constrain a multi-compartment model of synaptic signaling and compartmentalization in dendrites. We assessed the effects of individual excitatory and inhibitory signals on membrane voltage and calcium concentration depending on inhibitory synapse placement (i.e., on a spine head or on the dendritic shaft) and input timing. Our results challenge the view that spinous inhibition strictly vetoes single excitatory inputs and rather suggest that it fine-tunes calcium levels in DiSs. Our simulations indicate that a single inhibitory postsynaptic potential (IPSP) evoked in a DiS within 10 ms after an excitatory postsynaptic potential (EPSP) can curtail the local increase of calcium concentration without affecting the amplitude of membrane depolarization. This decoupling effect could impact long-term synaptic plasticity in cortical circuits.

Results

Combining light and electron microscopy to access the ultrastructure of targeted populations of dendritic spines in brain slices

In the cortex, the morphology and distribution of dendritic spines vary depending on cortical area and layer in which the cell body is located [5,35,58,59], and dendritic spines are differently regulated depending on their location within dendritic trees—e.g., basal or apical dendrites [30,49,60–62]. Therefore, it is critical to take into account both the cellular and dendritic context to characterize the diversity of spine ultrastructure. To that aim, we developed a 3D-CLEM workflow allowing the ultrastructural characterization of dendritic spines on genetically defined neuronal cell types and along identified types of dendrites in intact cortical circuits. In order to sparsely label specific subtypes of neurons, we used cortex-directed *in utero* electroporation (IUE) in mice. We electroporated neuronal progenitors generating L2/3 cortical PNs at embryonic day (E)15.5 with a plasmid expressing the fluorescent cytosolic filler tdTomato, granting access to the morphology of electroporated neurons, their dendrites, and their dendritic spines in LM. We perfused adult mice with aldehyde fixatives and collected vibratome sections of the electroporated area. To facilitate sample handling, we designed custom-made chambers allowing sample immersion in different solutions during confocal imaging and subsequent retrieval of the sample before EM preparation steps (S1 Fig). We enclosed 10 to 20 mm² fragments of brain sections in these chambers and acquired images of optically isolated basal dendrites of bright electroporated neurons with confocal microscopy (Fig 1A).

A major challenge of CLEM in brain tissue is to recover the ROI in EM after imaging in LM. Several methods have been proposed to facilitate ROI recovery [50–52], but they come with the following caveats: (1) using only intrinsic landmarks has a low throughput [57,63]; (2) filling target neurons with DAB masks intracellular ultrastructure [64]; and (3) scarring the tissue with an infrared laser to generate extrinsic landmarks, a.k.a. “NIRB” for “near-infrared branding” [56,65–68], produces landmarks with low pixel intensity in EM and can damage ultrastructure [63,69]. To facilitate ultrastructural measurements in non-obscured identified dendrites, we took advantage of the photo-oxidability of DAB [70,71]. We immersed the samples in DAB solution and applied focalized UV light at user-defined positions (Fig 1A) to imprint osmiophilic DAB landmarks around targeted dendrites (see S1B–S1E Fig) and pattern the tissue with localized electron-dense DAB precipitates (Fig 1B). After sample retrieval (see panel F in S1 Fig), tissue sections were processed for SBEM and embedded in minimal amounts of epoxy resin in order to maximize sample conductivity and SBEM image quality (see Materials and methods). In 3D-EM stacks, ROIs were recovered within the complex

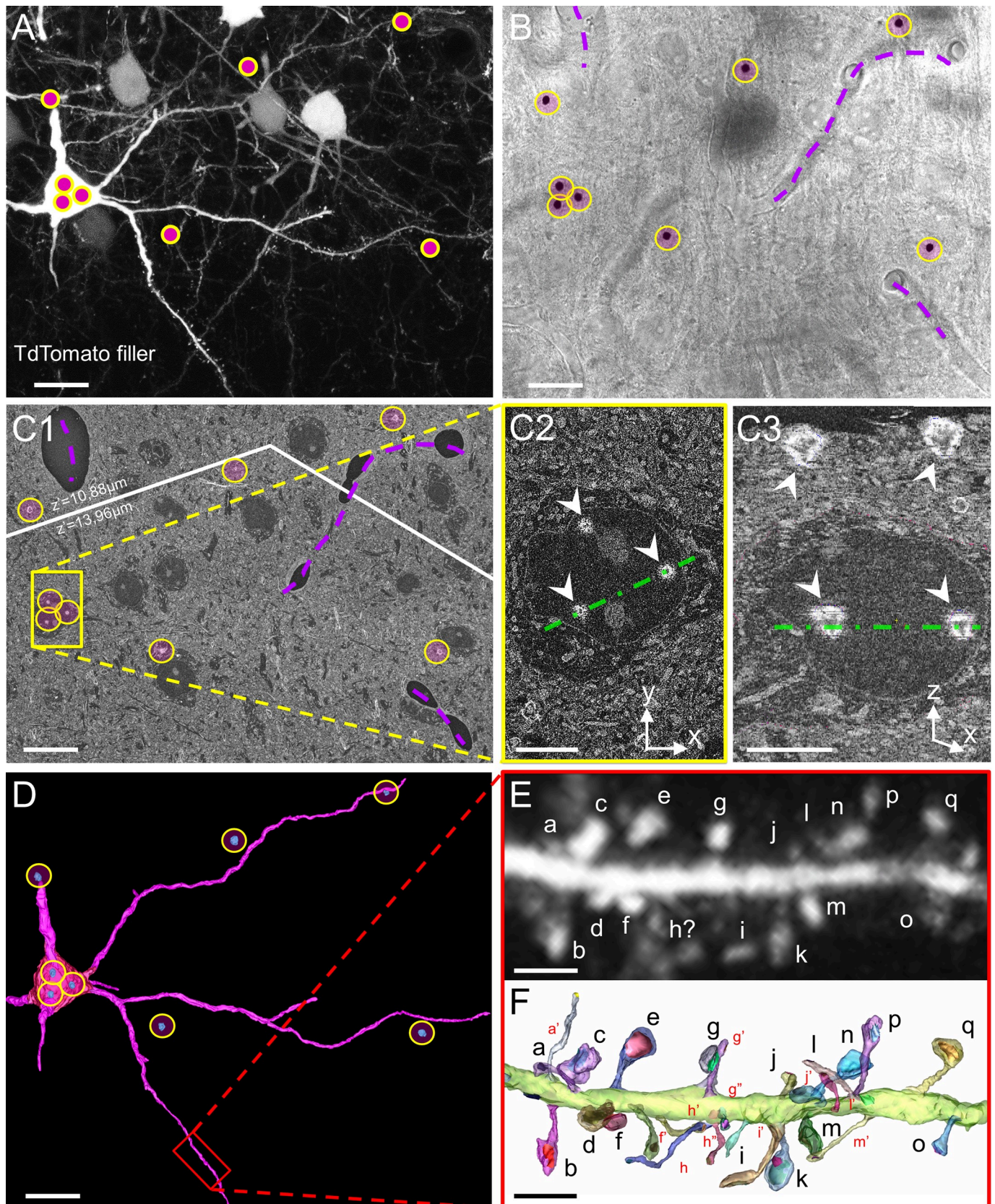


Fig 1. CLEM imaging of identified spines within intact cortical circuits. (A) Visualization of basal dendrites of a PN expressing cytosolic TdTomato in L2/3 of adult mouse SSC. DAB was photoprecipitated using focused UV light to insert correlative landmarks (pink dots in yellow circles). (B) Transmitted light image of the same field of view after DAB photoprecipitation. DAB precipitates are highlighted with yellow circles. Blood vessels are outlined with purple dashed lines. (C) Composite SEM image displaying DAB patterning at the depth of the neuron of interest (yellow circles). Slight mismatch between LM and SEM observation planes resulted in DAB landmarks appearing in different z-planes during block facing; the white line represents stitching between z-shifted images. In C1, landmarks are arranged as in B. C2 is a close-up on the soma of the electroporated neuron, labelled with 3 DAB landmarks (arrowheads). C3 is an orthogonal (x, z) view of the SEM stack along the axis represented as a green dashed line in C2 and C3. The superficial DAB layer enabled ROI targeting, and the deeper layer enabled retrospective identification of the target neuron. (D) 3D reconstruction of dendrites of interest from the overview SEM stack. DAB landmarks are reconstructed in blue (in yellow circles). The red rectangle outlines the portion of dendrite represented in E and F. (E) Z-projection of the confocal stack corresponding to the portion of dendrite reconstructed in D. Letters identify individual spines. (F) 3D-EM reconstruction. Individual dendritic spines were manually segmented and randomly colored. Spines that were detected in CLEM but not in LM alone are labelled in red. Scale bars: A, B, C1, D: 10 μm ; C2, C3: 5 μm ; E, F: 2 μm . CLEM, correlative light–electron microscopy; DAB, 3,3-diaminobenzidine; LM, light microscopy; L2/3, layer 2/3; PN, pyramidal neuron; ROI, region of interest; SEM, scanning EM; SSC, somatosensory cortex; 3D-EM, three-dimensional electron microscopy.

<https://doi.org/10.1371/journal.pbio.3001375.g001>

environment of brain tissues using both intrinsic landmarks such as blood vessels (Fig 1B) and high-contrast DAB precipitates (Fig 1C; see also panel G in S1 Fig). We then segmented and reconstructed targeted dendrites in 3D (Fig 1D) and registered whole portions of dendrites in both LM and EM to identify each dendritic spine unequivocally using neighboring spines as dependable topographic landmarks (Fig 1E and 1F). CLEM-based 3D reconstruction enabled the identification of dendritic spines that were not visible in LM or EM alone. In LM, the limited axial resolution prevents the identification of axially oriented spines, which are easily detected in 3D-EM [49] (Fig 1E and 1F; see also corresponding movie at https://www.opendata.bio.ens.psl.eu/3DCLEM-Spines/S1_Movie.zip; login: guest, password: EnsData0811). On the other hand, laterally oriented spines with the longest and thinnest necks are conspicuous in LM stacks but can be difficult to find in 3D-EM datasets without the cues provided by LM. The proportion of spines recovered with CLEM versus LM alone could amount to up to 30% per ROI, and 5% per ROI versus EM alone, highlighting the advantage of CLEM over unimodal microscopy approaches.

Spine ultrastructure along the basal dendrites of L2/3 cortical pyramidal neurons

We used our CLEM workflow to quantify the full extent of the ultrastructural diversity of dendritic spines along the basal dendrites of L2/3 PNs of the SSC of 3 adult mice. We exhaustively segmented 254 μm of the basal dendritic arborization of 4 neurons, and we reconstructed a total of 390 individual spines (S1 Data). As spine distance to the soma spanned from 20 to 140 μm , with basal dendrites extending up to 150 μm [72–75], our dataset can be considered representative of the whole spine population on these dendrites. The average linear density of dendritic spines was 1.5 ± 0.3 spine. μm^{-1} . We then quantified the following parameters for each spine: neck length, neck diameter, head volume, head longitudinal diameter (referred to as “head length”), head orthogonal diameter (referred to as “head diameter”), number of PSDs, and PSD area (Fig 2A, S1 Data). In agreement with previous reports in both basal and apical dendrites of mouse cortical and hippocampal neurons [4,6,76,77], we found that ePSD area correlates linearly with the volume of the spine head (Fig 2B). We also observed a nonlinear correlation between the length of the spine neck and its diameter (Fig 2C): Long spines (neck length > 2 μm) always had thin necks (neck diameter < 0.2 μm), although short necks could also be thin. By contrast, there was no correlation between the position of the spine or the interspine distance and any of the morphological parameters we measured (S2 Fig). There was also no correlation between the length or the diameter of the neck and the morphometry of the spine head or ePSD (S1 Data), which is consistent with previous EM studies of L2/3 PNs of mouse neocortex [4,72] (but see [40,78] for different conclusions in other brain areas).

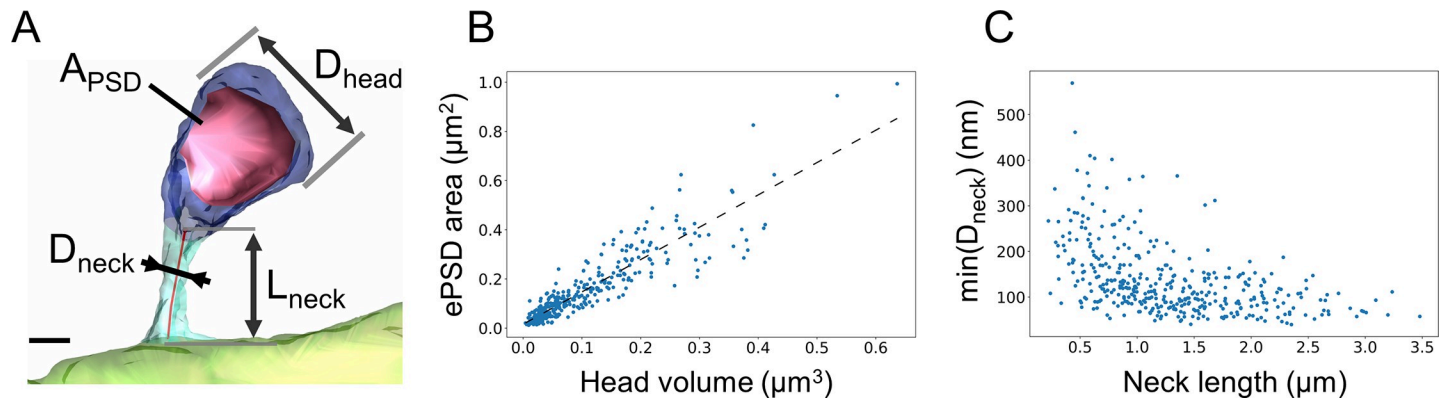


Fig 2. Spine morphometry along basal dendrites of L2/3 cortical PNs. (A) 3D reconstruction of a dendritic spine from an SBEM stack. Dendritic shaft is in light green, spine neck in turquoise, spine head in blue, and PSD surface in red. The following parameters were measured: PSD area, head diameter, neck diameter, and neck length. Scale bar: 300 nm. (B) Linear correlation of PSD area and spine head volume. $R^2 = 0.82$. (C) Plot of the minimal spine neck diameter as a function of spine neck length. Spearman correlation coefficient is -0.58 . $N = 390$. The data underlying this figure can be found in https://www.opendata.bio.ens.psl.eu/3DCLEM-Spines/data/Data_related_to_Fig_2.xlsx (login: guest; password: EnsData0811). ePSD, excitatory postsynaptic density; L2/3, layer 2/3; PN, pyramidal neuron; PSD, postsynaptic density; SBEM, serial block-face scanning EM.

<https://doi.org/10.1371/journal.pbio.3001375.g002>

Since our CLEM approach grants access to the cytosolic content of spines (Fig 3A), we quantified the occurrence of SA, a complex stacked membrane specialization of smooth endoplasmic reticulum (SER), which contributes to calcium signaling, integral membrane protein trafficking, local protein synthesis, and synaptic plasticity [12–14,79,80]. In basal dendrites, about 54% of spines contained an SA (Fig 3B), which is substantially higher than previous reports in the mature hippocampus [12,81]. These spines were randomly distributed along the dendrites. They had larger heads (Fig 3C), larger ePSDs (Fig 3D), and wider necks than spines devoid of SA (Fig 3E), consistent with previous morphological studies of CA1 PNs [12,81,82]. The probability that a spine contained an SA depending on spine head volume followed a sigmoid model (Fig 3F), predicting that all spines with a head diameter larger than $1.1 \mu\text{m}$ (21% spines in our reconstructions) contain an SA.

Next, we used our ultrastructural data to estimate the electrical resistance of spine necks using $R_{\text{neck}} = \rho W_{\text{neck}}$, where ρ is the cytosolic resistivity (set to $300 \Omega\cdot\text{cm}$ [83,84]) and W_{neck} is the diffusional neck resistance that restricts the diffusion of molecules and charges between spine heads and dendritic shafts [23]. To quantify W_{neck} , for each spine, we measured a series of orthogonal cross-sections of the neck along its principal axis and integrated $W_{\text{neck}} = \int d\ell / A(\ell)$, where $A(\ell)$ is the neck cross-section area at the abscissa ℓ along the neck axis. W_{neck} ranged from $2 \mu\text{m}^{-1}$ to $480 \mu\text{m}^{-1}$ and R_{neck} from $8 \text{ M}\Omega$ to $1450 \text{ M}\Omega$, with a median value of $188 \text{ M}\Omega$. These values are consistent with previous estimations based on EM reconstructions and stimulated emission depletion (STED) super-resolutive light microscopy [17,85] and with direct electrophysiological recordings [86]. It has been proposed that the SA, which may occupy some of the spine neck volume, could increase W_{neck} [13,79,87]. Therefore, we subtracted SA cross-section from $A(\ell)$ when computing W_{neck} in SA+ spines (see Materials and methods). This correction increased W_{neck} by $13\% \pm 2\%$ in SA+ spines (S3 Fig). However, because of their wider necks, W_{neck} of SA+ spines was still lower (59% in average) than W_{neck} of spines devoid of SA (Fig 3G). These results suggest that, in addition to supplying large dendritic spines with essential resources, the SA may adjust W_{neck} and influence spine compartmentalization [12,13,81].

Excitatory and inhibitory synapses in dually innervated spines

We noticed that a small proportion of dendritic spines were contacted by 2 distinct presynaptic boutons (DiSs). DiSs have long been described in the literature as receiving both an excitatory

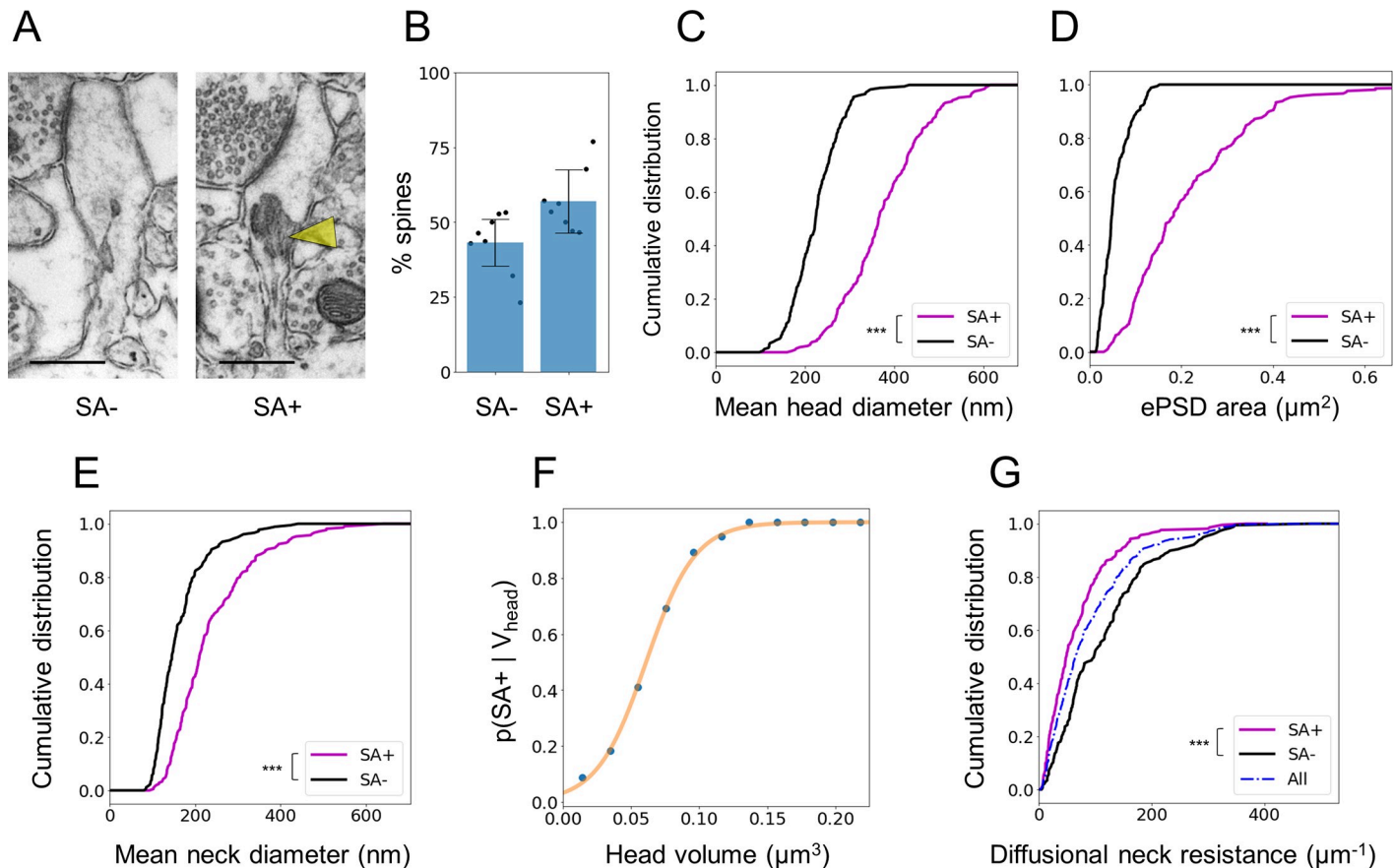


Fig 3. Spines containing an SA have larger head and wider neck. (A) TEM images of spines either devoid of SA (left) or containing an SA (SA+) (right, yellow arrowhead). Scale bars: 500 nm. (B) Proportion of SA- and SA+ spines. Histogram represents mean \pm SD, from 390 spines in $N = 8$ dendrites. (C) Distribution of mean head diameter for SA- and SA+ spines. $N = 179$ and 221 , respectively ($p < 10^{-38}$). (D) Distribution of ePSD area. ($p < 10^{-40}$). (E) Distribution of mean neck diameter. ($p < 10^{-12}$). (F) Probability of harboring an SA as a function of spine head volume. Blue: experimental data. Orange: sigmoid fit. (G) Distribution of the diffusional resistance of the spine neck (W_{neck}) calculated based on neck morphology ($p < 10^{-5}$). ***: $p < 0.001$ calculated using Mann-Whitney test. The data underlying this figure can be found in https://www.opendata.bio.ens.psl.eu/3DCLEM-Spines/data/Data_related_to_Fig_3.xlsx (login: guest; password: EnsData0811). ePSD, excitatory postsynaptic density; SA, spine apparatus; TEM, transmission electron microscopy.

<https://doi.org/10.1371/journal.pbio.3001375.g003>

and an inhibitory synaptic contact [88–91]. In the SSC, DiSs are contacted by VGLUT2-positive thalamocortical inputs [15], and they are sensitive to sensory experiences. The number of DiSs increases in response to sensory stimulation and decreases in response to sensory deprivation [73,92–94], suggesting their importance in synaptic integration and sensory processing. However, their scarcity in the cortex has been an obstacle to their ultrastructural and functional characterization. We took advantage of our CLEM approach and the molecular signature of this population of spines (i.e., the presence of a cluster of gephyrin, the core protein of inhibitory postsynaptic scaffolds [95,96]) to examine their morphological properties. To label inhibitory synapses in cortical PNs (Fig 4A), we co-expressed tdTomato with small amounts of GFP-tagged gephyrin (GFP-GPHN) [73,94,97,98]. We identified in LM spines containing a gephyrin cluster (Fig 4B), and we ascertained their dual innervation in EM after back-correlating spine identity between LM and SBEM acquisitions. To do so, we aligned reconstructed dendrites on LM images (Fig 4C) and matched individual spines in both modalities (lettered in Fig 4B and 4C). While ePSDs look asymmetrical and more electron dense than inhibitory PSDs (iPSDs) in transmission EM [99,100], the anisotropic resolution of SBEM does not allow the distinction of ePSDs and iPSDs in most DiSs [49]. Therefore, we identified iPSDs on DiSs

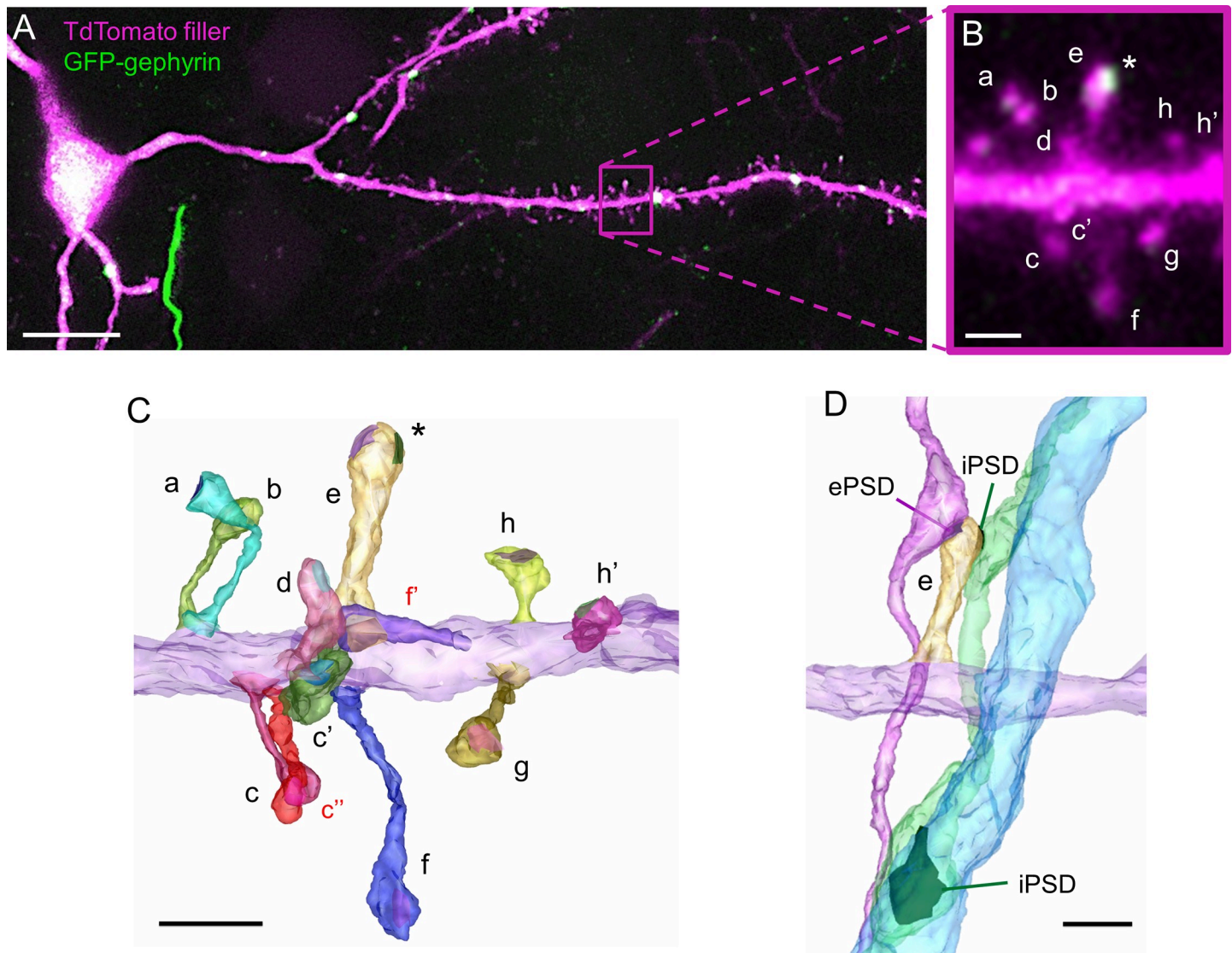


Fig 4. Identification of excitatory and inhibitory synapse on DiSs using CLEM. (A) Confocal image of basal dendrites of a cortical L2/3 PN that was electroporated with cytosolic TdTomato and GFP-GPHN to label inhibitory synapses. The magenta rectangle outlines the region enlarged in B. (B) Enlargement of a portion of the dendrite in A harboring several dendritic spine (lettered). Spine “e” contains a cluster of GFP-GPHN (asterisk) and corresponds to a putative DiS. (C) 3D-EM reconstruction of the same dendritic fragment as in B. Dendritic shaft is colored in purple; individual spines and PSDs are colored randomly. Spines visible in EM but not in LM are labelled in red. The iPSD (colored in green) on spine “e” is identified based on the position of the GFP-GPHN cluster (asterisk in B and C). GFP-GPHN-negative PSDs are defined as excitatory. (D) 3D-EM reconstruction of spine “e” (yellow) with its presynaptic partners (magenta and green). As the “green” axon also targets a neighboring dendritic shaft (blue), it is defined as inhibitory. Scale bars: A: 10 μ m; B, C, D: 1 μ m. CLEM, correlative light–electron microscopy; DiS, dually innervated spine; EM, electron microscopy; ePSD, excitatory postsynaptic density; GFP-GPHN, GFP-tagged gephyrin; iPSD, inhibitory PSD; LM, light microscopy; L2/3, layer 2/3; PN, pyramidal neuron; PSD, postsynaptic density; 3D-EM, three-dimensional electron microscopy.

<https://doi.org/10.1371/journal.pbio.3001375.g004>

based on GFP-GPHN cluster position in LM images. In 89% of DiSs (33/37), the excitatory (GFP-GPHN-negative) PSD and the inhibitory (GFP-GPHN-positive) PSD could be clearly discriminated. However, in 11% of DiSs (4/37 DiSs), distinguishing ePSD from iPSD was not obvious due to the coarse axial resolution of LM imaging. To resolve ambiguities, we reconstructed the axons innervating the DiSs and determined their identity based on their other targets in the neuropil, either soma and dendritic shaft for inhibitory axons [2,101,102], or other dendritic spines for excitatory axons [49] (Fig 4D). As a result, we could unequivocally

determine the excitatory or inhibitory nature of each synaptic contact on electroporated neurons, within approximately $10^5 \mu\text{m}^3$ 3D-EM acquisition volume.

In CLEM, we measured an average density of 1.4 ± 0.5 iPSDs per $10 \mu\text{m}$ of dendrite on DiSs and 2.1 ± 1.2 iPSDs per $10 \mu\text{m}$ of dendrite on the dendritic shaft—amounting to 3.5 ± 1.1 iPSDs per $10 \mu\text{m}$ of dendrite. iPSDs were homogeneously distributed either on spines or shaft from $24 \mu\text{m}$ away from the soma to the dendritic tip, which contrasts with apical dendrites where spinous inhibitory synapses are distally enriched [73]. Along the basal dendrites of L2/3 cortical PNs, 38% of inhibitory contacts occurred on dendritic spines, which is higher than previously estimated [73,98]. This percentage was stable from P21 but lower in young (P10) neurons and in layer 5 PNs (S4 Fig). DiSs represented $10\% \pm 3\%$ of all spines (Fig 5A). They had larger heads than SiSs (Fig 5B), in line with previous reports [15,103], and $86\% \pm 13\%$ of them contained an SA (Fig 5C). DiSs also differed in terms of neck morphology. They had longer necks than SiSs of comparable head volume ($V_{\text{head}} > 0.05 \mu\text{m}^3$), although neck length distribution was similar in the whole populations of SiSs and DiSs (Fig 5D). DiSs also had lower $D_{\text{neck}}/V_{\text{head}}$ ratio than SiSs (Fig 5E), although D_{neck} distribution was similar between SiSs and DiSs (S5 Fig), suggesting that excitatory signals generated in DiSs are more compartmentalized than signals of similar amplitude generated in SiSs. Accordingly, DiSs had a higher W_{neck} than SiSs of comparable head size (52% larger in average) (Fig 5F). In spine heads, ePSDs on DiSs were larger than ePSDs on SiSs ($174\% \pm 113\%$ of ePSD area) (Fig 5G), consistent with the larger head size of DiSs. By contrast, iPSDs on DiSs were smaller than shaft iPSDs ($53\% \pm 15\%$ of shaft iPSD area) (Fig 5H). The area of iPSDs on DiSs did not correlate with spine head volume (S6 Fig). In 95% of DiSs, iPSDs were smaller than ePSDs (half the area, in average) (Fig 5I). Together, these results indicate that DiSs represent a specific population of dendritic spines with distinctive ultrastructural features that could impact their functional properties.

Morphologically constrained modeling of synaptic signaling

Next, we wanted to assess the impact of spine diversity on synaptic signals. We used a computational approach based on a multicompartment “ball-and-stick” model of the neuronal membrane [40,104]. This model comprises an isopotential soma and 2 dendritic compartments structured as cables featuring passive resistor–capacitor (RC) circuits and conductance-based synapses. The 2 dendritic compartments correspond to the dendrite receiving the synaptic inputs and to the remainder of the dendritic tree (Fig 6A1) [105,106]. We constrained this model with morphological parameters measured in CLEM (i.e., for 390 spines and 37 DiSs: spine head volume and membrane area, ePSD and iPSD area, neck resistance, distance between spine and soma, dendritic diameter), taking into account the structural shrinkage resulting from chemical fixation (see S7 Fig). Individual synaptic AMPA, NMDA, and GABA_A conductances (Fig 6A2) were scaled proportionally to PSD areas [77,107–110]. Voltage-dependent calcium channels (VDCCs) were modeled in spine heads using Goldman–Hodgkin–Katz equations [111], and their conductance was scaled proportionally to spine head areas. Conductances were adjusted to fit published electrophysiological values (see Materials and methods) [37,38,112–122].

We first examined the propagation of simulated EPSPs. The amplitude of the depolarization evoked in spine heads followed a log-normal distribution reflecting the morphological variability of spines (Fig 6B). The maximal amplitude of the depolarization (ΔV_{max}) was sharply attenuated between the head of the spine and the dendritic shaft (51% attenuation in average), and about 5% of ΔV_{max} reached the soma (Fig 6B and 6C), which is in the range of measurements performed in basal dendrites of L5 cortical PNs using voltage dyes, electrophysiology, and glutamate uncaging [25,123]. To determine the contribution of individual

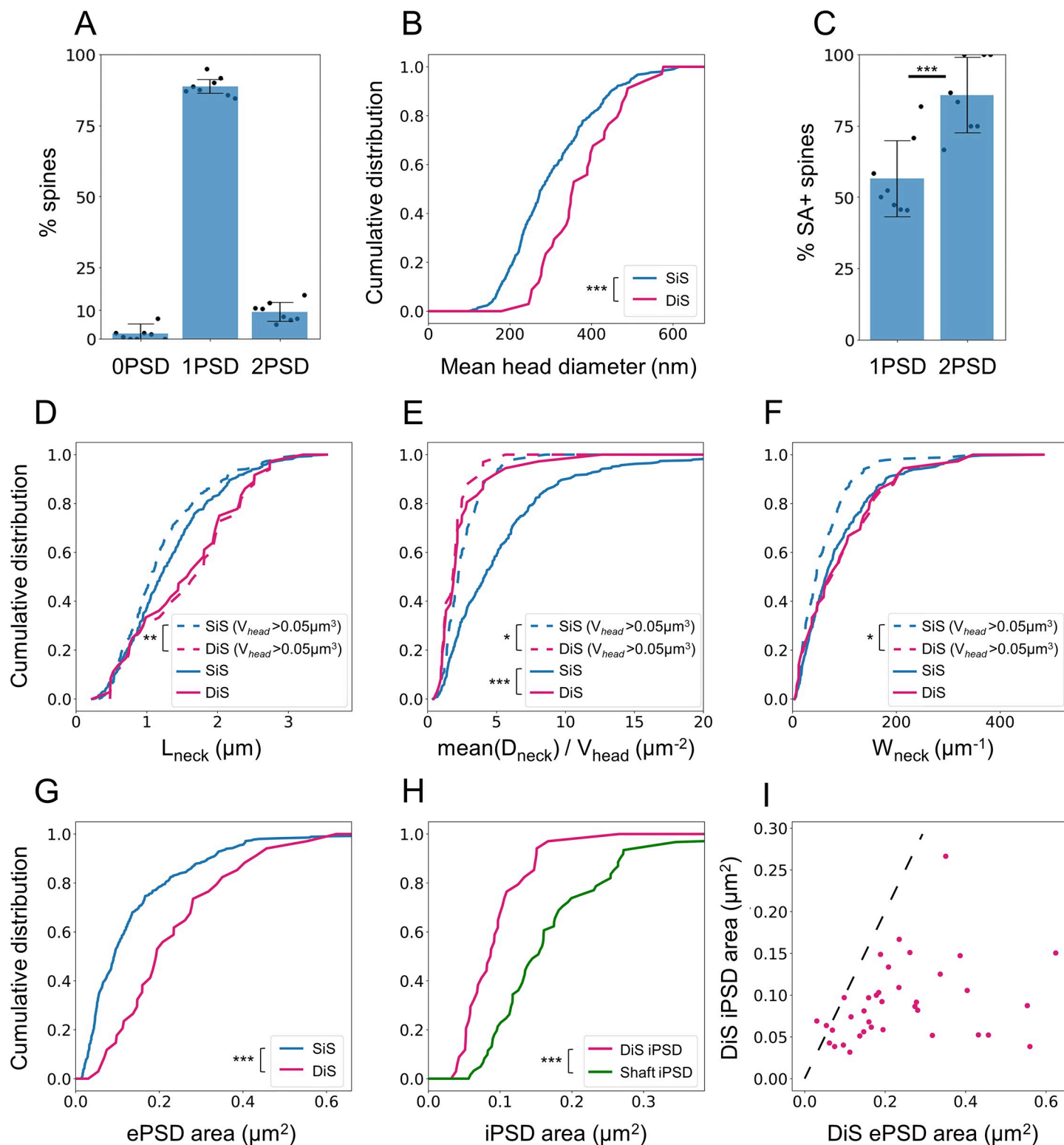


Fig 5. DiSSs have unique anatomical properties. (A) Proportion of spines harboring 0, 1, or 2 synaptic contacts, quantified with CLEM. Histograms represent mean \pm SD, from 390 spines in $N = 8$ dendrites. (B) Quantification of mean spine head diameter for SiSs (blue) and DiSs (red) ($p < 10^{-4}$). (C) Proportion of SiSs and DiSs harboring an SA ($p < 10^{-10}$ using Pearson χ^2 test). (D–F) Quantification of neck length (D), the ratio between mean neck diameter and head volume (E), and the diffusional neck resistance (W_{neck}) (F) between SiSs and DiSs (solid lines, $N = 349$ and 37 , respectively) and between DiSs with SiSs of similar head volume (spines with $V_{\text{head}} > 0.05 \mu\text{m}^3$, dashed lines, $N = 186$ and 34 , respectively). (G) Quantification of ePSD area in SiSs or DiSs ($p < 10^{-5}$). (H) Quantification of iPSD area in DiSs and

dendritic shafts. $N = 37$ and 62 , respectively ($p < 10^{-6}$). (I) Plot of iPSD area as a function of ePSD area in individual DiSs. The dashed line ($y = x$) highlights that the ePSD is larger than the iPSD in most of DiSs. $N = 37$. p -values were computed using Mann–Whitney test (B, D–H) or Pearson χ^2 test (C). Only significant ($p < 0.05$) p -values are shown (* $p < 0.05$; ** $p < 0.01$; *** $p < 0.001$). The data underlying this figure can be found in https://www.opendata.bio.ens.psl.eu/3DCLEM-Spines/data/Data_related_to_Fig_5.xlsx (login: guest; password: EnsData0811). CLEM, correlative light–electron microscopy; DiSs, dually innervated spines; ePSD, excitatory postsynaptic density; iPSD, inhibitory PSD; PSD, postsynaptic density; SA, spine apparatus; SiSs, singly innervated spines.

<https://doi.org/10.1371/journal.pbio.3001375.g005>

morphological parameters to the variance of ΔV_{\max} in spine heads, we used a generalized linear model (GLM) [124]. In SiSs, A_{ePSD} and R_{neck} accounted for 60% and 19% of the variance of ΔV_{\max} , respectively (also see S8 Fig for the dependence of ΔV_{\max} on R_{neck}). In DiSs, the contribution of R_{neck} to ΔV_{\max} was much higher, reaching 38% of the variance, while A_{ePSD} contribution dropped to 47% (S1 Table). In 56% of dendritic spines, R_{neck} was large enough ($> 145 \text{ M}\Omega$) to attenuate EPSP amplitude by $> 50\%$ across the spine neck, and more than 90% of spine necks attenuated the signal by at least 10% (Fig 6D), suggesting that most spine necks constitutively compartmentalize electrical signals in the head of spines.

We next estimated the elevation of calcium ion concentration induced in spine heads by an EPSP. The amplitude of calcium transients ($\Delta[\text{Ca}^{2+}]$) was similar in SiSs and DiSs and varied nonlinearly with A_{ePSD} (Fig 6E). A_{ePSD} accounted for 30% of $\Delta[\text{Ca}^{2+}]$ in SiSs and 45% in DiSs, followed by R_{neck} (9%; S1 Table). NMDA receptors (NMDARs) had the largest contribution to $\Delta[\text{Ca}^{2+}]$, consistent with numerous experimental observations reviewed in [125,126] (S9 Fig). Overall, our model provides quantitative insights into the variability of EPSP amplitude originating from spine diversity and highlights differences in the contribution of morphological parameters to membrane depolarization and calcium signals in SiSs and DiSs.

Temporal interplay of excitatory and inhibitory signals in dually innervated spines

We used our model to compare the effects of dendritic shaft inhibition and spinous inhibition, whose functional relevance is still unclear. To understand how spine ultrastructure and iPSD location influence synaptic integration, we modeled the interaction between one IPSP and one EPSP under the constraint of our morphological measurements. Assessing the extent of signal variability originating from spine morphological heterogeneity required a large number of simulations ($N \geq 1,000$). To expand our distribution of DiSs and shaft iPSDs (S1 Data), we used a bootstrapping method [127], which provided unbiased estimations of the mean and variance of the signals (see Materials and methods). We first simulated the interaction of one EPSP and one IPSP generated with a time difference of Δt (Fig 7A). For $\Delta t < 0$ (IPSP before EPSP), IPSPs decreased the amplitude of the EPSPs (Fig 7B1). For $\Delta t > 0$ (IPSP after EPSP), IPSPs had no effect on the amplitude but abruptly decreased the tail of the EPSPs [128] (Fig 7B2).

Next, we modeled $N = 3,700$ DiSs located between $20 \mu\text{m}$ and $140 \mu\text{m}$ from the soma, and we compared 2 configurations: (1) activation of the ePSD of the DiS and a shaft iPSD placed next to it ($\Delta x = 0.7 \mu\text{m}$) (Fig 7C1); and (2) activation of the ePSD and iPSD of the DiS (Fig 7C2). To quantify how the timing of inhibition affects EPSP amplitude, we compared the amplitude of individual EPSPs in the absence ($\Delta V_{\max, \text{E}}$) or presence ($\Delta V_{\max, \text{E+I}}$) of inhibition and computed the drop in depolarization amplitude $\text{inh}_V(\Delta t) = 1 - \Delta V_{\max, \text{E+I}} / \Delta V_{\max, \text{E}}$. $\text{inh}_V = 0$ indicates no inhibition of the EPSP, while $\text{inh}_V = 1$ indicates complete inhibition of the EPSP. inh_V was an asymmetrical function of Δt (Fig 7D) [36,128]. It was maximal at $\Delta t = -4 \text{ ms}$ for spinous inhibition and at $\Delta t = -6 \text{ ms}$ for dendritic shaft inhibition, and it decreased ΔV_{\max} by 26% and 16%, respectively (median values at the peaks in Fig 7D). Therefore, despite the smaller size of spinous iPSDs compared to shaft iPSDs and the favorable placement of the

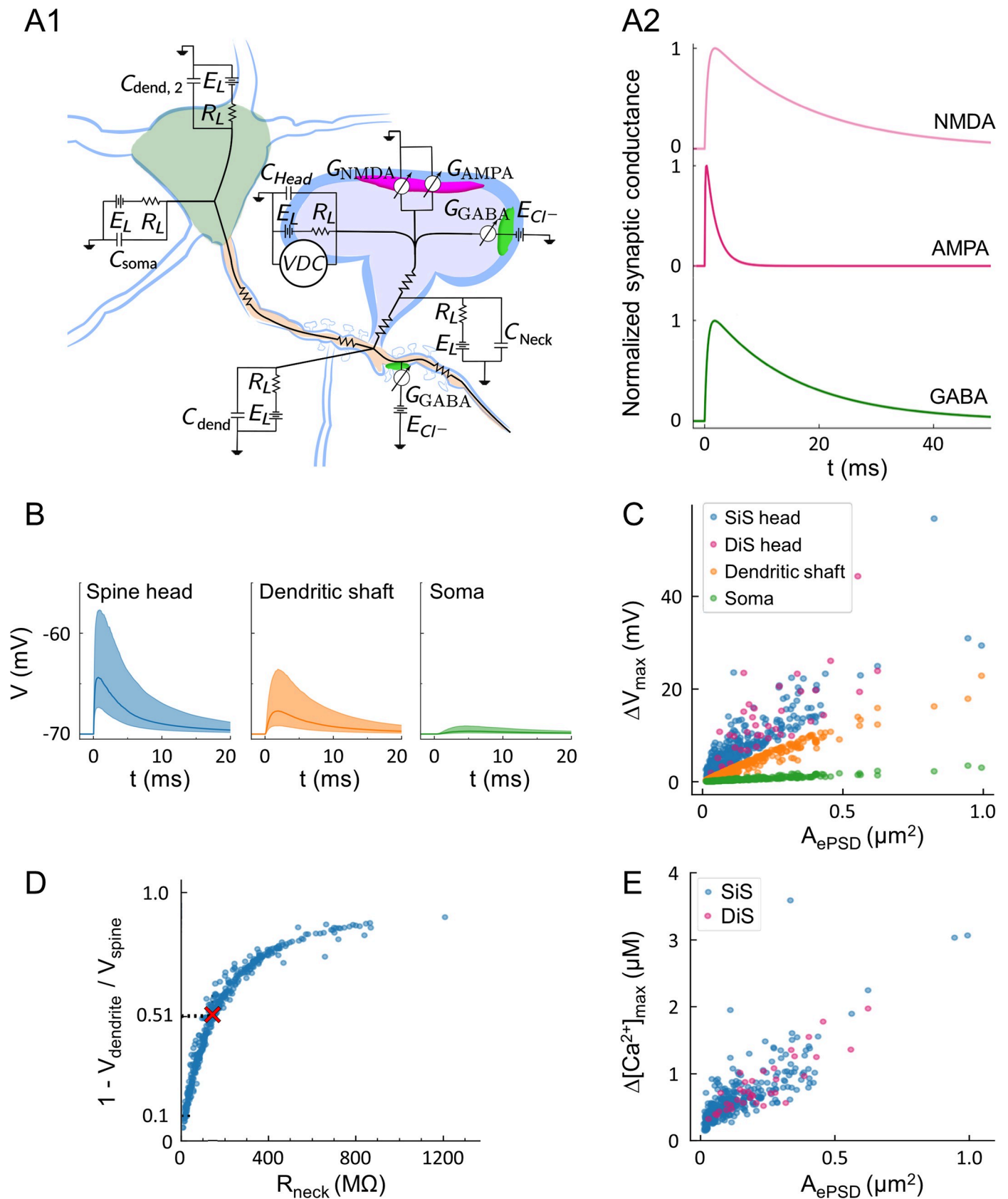


Fig 6. Morphologically constrained modeling of synaptic signaling. (A) Schematic of the circuit model (A1) and representative time course of excitatory (magenta) and inhibitory (green) conductance based on the kinetics of AMPA, NMDA, and GABA_A receptors (A2). All compartments include passive RC circuits to model cell membrane properties and optionally include an active conductance that models VDC. All modeled spines feature an excitatory synapse with glutamatergic AMPA and NMDA currents. Spines and dendritic compartments can also feature an inhibitory synapse with GABAergic currents. All conductances were scaled to PSD area (see [Materials and methods](#)). (B) Simulation of the time courses of membrane depolarization following an EPSP, taking into account spine diversity (i.e., R_{neck} , ePSD area, and distance to soma, as measured in CLEM) in the spine head (blue), in the dendritic shaft in front of the spine (orange), and in the soma (green). (C) Amplitude of evoked depolarization (ΔV_{max}) as a function of ePSD area at 3 distinct locations: head of SiSs (blue) or DiSs (magenta) where the EPSP was elicited, dendritic shaft 1 μ m from the spine (orange) or soma (green). (D) Attenuation of the amplitude of depolarization between the spine head and the dendrite as a function of the resistance of the neck (R_{neck}). The attenuation was calculated as: $\alpha = 1 - \Delta V_{max, shaft} / \Delta V_{max, spine}$. Red cross: mean value of α . (E) Estimated amplitude of intracellular calcium concentration transients $\Delta[Ca^{2+}]_{max}$ following activation of NMDA receptors and VDCCs as a function of ePSD area. Three spiking outliers are not represented. The data underlying this figure can be found in https://www.opendata.bio.ens.psl.eu/3DCLEM-Spines/data/Data_related_to_Fig_6.xlsx (login: guest; password: EnsData0811). AMPA, α -amino-3-hydroxy-5-methyl-4-isoxazolepropionic acid; CLEM, correlative light-electron microscopy; DiSs, dually innervated spines; ePSD, excitatory postsynaptic density; EPSP, excitatory postsynaptic potential; NMDA, N-Methyl-D-aspartate; PSD, postsynaptic density; RC, resistor-capacitor; SiSs, singly innervated spines; VDC, voltage-dependent current; VDCC, voltage-dependent calcium channel.

<https://doi.org/10.1371/journal.pbio.3001375.g006>

shaft iPSD in these simulations, our results indicate that local spinous inhibition is stronger than shaft inhibition.

To determine how the timing of inhibition impacts calcium signals in DiSs, we then calculated $inh_{[Ca^{2+}]}(\Delta t) = 1 - [Ca^{2+}]_{max,E+I} / [Ca^{2+}]_{max,E}$. $inh_{[Ca^{2+}]}$ peaked at $\Delta t = 0$ ms for both

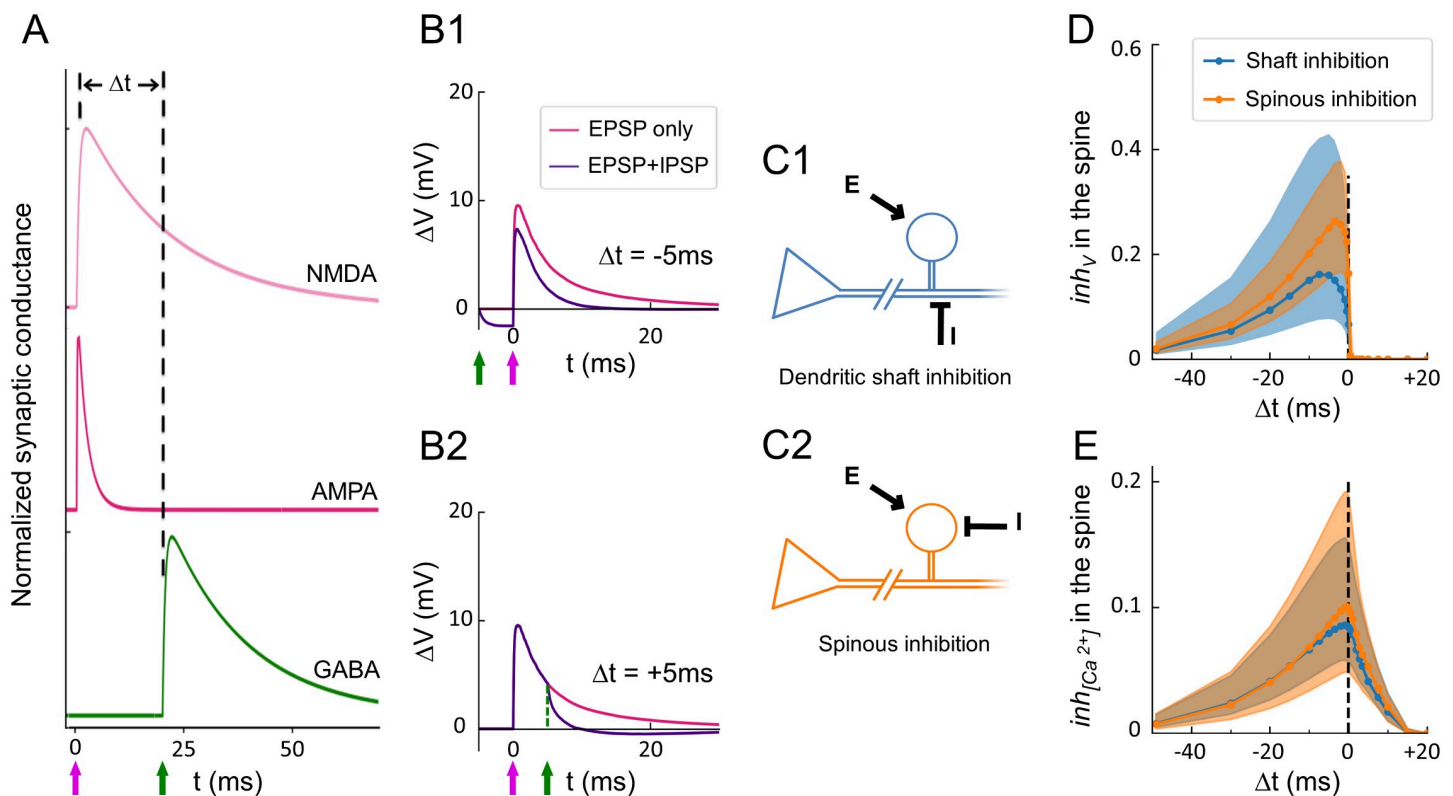


Fig 7. Input timing determines EPSP and IPSP integration and decoupling of voltage and calcium signals in DiSs. (A) Schematic: excitatory AMPA and NMDA conductances were activated at $t = 0$. The inhibitory GABAergic conductance was activated at an interval Δt before or after the onset of excitation. (B) Examples of the time course of depolarization in the spine head for $\Delta t = +5$ ms (B1) and $\Delta t = -5$ ms (B2) (purple curves) compared to no inhibition (magenta curves). Arrows represent the onset of excitatory and inhibitory inputs (magenta and green arrows, respectively). (C) Schematics: inhibition (τ symbol) of an EPSP (arrow) by an IPSP elicited either in the shaft next to the spine (C1, blue) or directly in the spine head (C2, orange). (D) Voltage inhibition in the spine head, inh_v , induced by dendritic (blue) or spinous (orange) IPSPs as a function of Δt . (E) Inhibition of the calcium influx in the spine head, $inh_{[Ca^{2+}]_j}$, induced by dendritic (blue) or spinous (orange) IPSPs as a function of Δt . The data underlying this figure can be found in https://www.opendata.bio.ens.psl.eu/3DCLEM-Spines/data/Data_related_to_Fig_7.xlsx (login: guest; password: EnsData0811). AMPA, α -amino-3-hydroxy-5-methyl-4-isoxazolepropionic acid; DiSs, dually innervated spines; EPSP, excitatory postsynaptic potential; IPSP, inhibitory postsynaptic potential; NMDA, N-Methyl-D-aspartate.

<https://doi.org/10.1371/journal.pbio.3001375.g007>

spinous and shaft inhibition. More precisely, spinous inhibition reduced calcium transient amplitude by 10% in average, reaching >36% in the top 10% simulations, while shaft inhibition reduced it by 8.6% in average and >28% in the top 10% simulations (Fig 7E), consistent with double uncaging experiments [129]. Importantly, IPSPs could decrease the amplitude of calcium transients within a short time window (Δt between 0 and +10 ms) in which depolarization amplitude was not affected (Fig 7D and 7E), thereby decoupling calcium signals from electrical activity in DiSs.

To further assess the importance of spine morphological features in the model outputs, we examined the case of adult L2/3 cortical PNs expressing the human-specific gene *Slit-Robo Rho GTPase-activating protein 2C* (*SRGAP2C*). We have previously shown that *SRGAP2C* regulates synapse density, spine neck length, and DiS proportion in oblique apical dendrites [97,130]. CLEM reconstructions showed that *SRGAP2C* expression did not affect the density of synapses or DiSs in basal dendrites. However, dendritic spines in the basal dendrites of *SRGAP2C*-expressing neurons had smaller ePSDs and smaller necks than in control neurons (see panels A–C in S10 Fig). Remarkably, *SRGAP2C* expression slightly increased the impact of inhibition on ΔV_{\max} in spine heads, while it strongly reduced the inhibition of $\Delta[Ca^{2+}]$ (see panel D in S10 Fig), suggesting distinct voltage/calcium dynamics imposed by spine ultrastructure. These results highlight the critical need of morphologically constrained models to understand synaptic integration.

Discussion

In the present study, we developed a novel 3D-CLEM workflow allowing the ultrastructural and quantitative characterization of specific populations of dendritic spines in genetically defined types of neurons. We used this workflow to exhaustively reconstruct spines and synaptic contacts along the basal dendrites of fluorescently labelled L2/3 cortical PNs of the SSC and to provide a quantitative description of their diversity. We input our measurements in a computational model to analyze the variability of electrical and calcium synaptic signals originating from spine ultrastructural diversity and to characterize the local integration of excitatory and inhibitory inputs in dendritic spines. Our results shed light on unique properties of DiSs, which represent 10% of all spines and 38% of all inhibitory synapses along the basal dendrites of L2/3 cortical PNs. While individual inhibitory synapses distributed along dendritic shafts can be powerful enough to block several EPSPs [102], we show that spinous inhibition affects excitatory signals more efficiently than shaft inhibition in DiSs. Furthermore, the activation of a spinous inhibitory synapse within a few milliseconds after an EPSP can decouple voltage and calcium signals in DiSs, which could impact calcium-dependent signaling cascades that drive spine plasticity.

The molecular composition and biophysical properties of spines and synapses are heterogeneous along dendritic segments and across dendritic trees. However, most computational models usually overlook this diversity and consider that inhibition only occurs on the soma or in dendrites (e.g., [131–133]). The 3D-CLEM approach we propose provides an accessible solution for detailed quantification of synaptic diversity beyond the micrometer scale in intact brain circuits. Although there can be variation in synaptic transmission at a given synapse due to the stochasticity of the molecular processes involved, EM measurements of synapse size are predictive of the average strength of individual synapses in L2/3 cortical PNs [110]. Therefore, our approach will help implement morphologically constrained computational models to improve modeling accuracy and assess the functional outcomes of ultrastructural changes induced by experience, mutations, or diseases. Our workflow is applicable to any type of tissue and allows anatomical measurements of any kind of genetically labelled cells and organelles.

One technical limitation is the need for chemical fixation, which may distort tissue morphology [134,135] and require correction based on a morphological comparison with physically fixed tissues (see panel B3 in S7 Fig) in order to reliably depict *in vivo* situations. Future development of aldehyde-free cryo-CLEM methods for tissue analysis will be important to grant access to cellular and synaptic ultrastructure in close-to-native environments.

Applying 3D-CLEM to the basal dendrites of L2/3 cortical PNs allowed us to quantitatively describe the landscape of synaptic diversity and to characterize the ultrastructural features of a scarce population of dendritic spines receiving both excitatory and inhibitory synaptic inputs (DiSs). In the cortex, DiSs are mostly contacted by VGluT2-positive excitatory thalamocortical inputs [15], and they receive inhibition from somatostatin-expressing and parvalbumin-expressing interneurons [129,136], which are the 2 main sources of inhibitory inputs to the basal dendrites of L2/3 cortical PNs [137,138]. *In vivo* 2-photon imaging experiments have shown that DiSs are among the most stable spines along the dendrites of L2/3 PNs [103]. The inhibitory synapse in DiSs is smaller and more labile than inhibitory synapses along dendritic shafts, and it is very sensitive to sensory experience [73,93,94,103]. Whisker stimulation induces a lasting increase in the occurrence of iPSDs in spines of the barrel cortex [93], and monocular deprivation destabilizes iPSDs housed in spines of the visual cortex [73,94,103], suggesting their role in experience-dependent plasticity. Our morphological and computational analysis provides new insights into the biophysical properties of DiSs. We show that DiSs have larger heads and larger ePSDs than SiSs, and most often contain an SA. However, the ratio between mean spine neck diameter and spine head volume (or ePSD area) was smaller in DiSs than in SiSs, and DiSs had longer necks than SiSs of comparable head volume, so that EPSPs of similar amplitudes encounter a higher neck resistance in DiSs than in SiSs. Thus, DiSs are uniquely compartmentalized by their ultrastructural features and the presence of an inhibitory synapse.

Our model predicts that IPSPs occurring in DiSs within milliseconds after an EPSP can curtail calcium transients without affecting depolarization, thereby locally decoupling voltage and calcium signaling. This is expected to impact the induction of long-term forms of synaptic plasticity, such as long-term potentiation (LTP) or long-term depression (LTD), which underlie learning and memory [79,139–141]. The induction of LTP versus LTD is determined by the magnitude and time course of calcium flux, with brief, high calcium elevation generating LTP, sustained moderate calcium elevation generating LTD, and low calcium level inducing no plasticity [142–144]. Therefore, a small reduction in the amplitude of calcium transients may limit spine potentiation or even cause depression [145–147]. In the cortex, thalamocortical inputs may contact DiSs on the basal dendrites of L2/3 PNs both directly (excitatory connection) and indirectly through feed-forward inhibition via parvalbumin-expressing fast-spiking interneurons [148,149]. The delay between thalamocortical excitatory and feed-forward inhibitory signals is typically +1 ms to +3 ms [148], within the 10 ms time window for voltage–calcium decoupling in DiSs. Therefore, the presence of inhibitory synapses in DiSs could prevent synaptic potentiation and thereby increase the temporal precision of cortical response to sensory stimulation [93,148,150]. On the contrary, the removal of spine inhibitory synapses during experience-dependent plasticity such as monocular deprivation could favor synaptic potentiation to strengthen inputs from the nondeprived eye [73,94,151]. Likewise, the partial alleviation of calcium transient reduction by the human-specific gene *SRGAP2C* might facilitate long-term plasticity in DiSs. In the future, these hypotheses will have to be tested experimentally and using more elaborate morphologically constrained models allowing the computation of complex events at the basis of long-term plasticity.

Our understanding of synaptic and dendritic computations is intimately linked to the quantitative description of synaptic distribution, ultrastructure, nano-organization, activity,

and diversity in neural circuits. The CLEM workflow we propose opens new avenues for the ultrastructural characterization of synapses with distinct molecular signatures defining their identity or activation profile. Another milestone to better model the biophysics of synaptic integration will be to combine EM with quantitative super-resolution LM to measure the density and nano-organization of molecular species (e.g., AMPARs, NMDARs, and VDCCs) in specific populations of synapses in intact brain circuits. Combining circuit and super-resolution approaches through CLEM will be critical to refine large-scale circuit models [74,152,153] (but see [32]) and bridge the gap between molecular, system, and computational neurosciences.

Materials and methods

Ethics statement

All animals were handled according to European and French regulations (directive 2010/63, decree 2013–118). The reference of our authorization was APAFIS#1530-2015082611508691v3. It was delivered by the French Ministry of Research after evaluation by the Comité d’Ethique en Experimentation Animale n°005.

Animals and *in utero* cortical electroporation

In utero cortical electroporation was performed as described previously [154]. Briefly, pregnant Swiss female mice at E15.5 (Janvier Labs, France) were anesthetized with isoflurane (3.5% for induction, 2% during the surgery) and subcutaneously injected with 0.1 mg/kg of buprenorphine for analgesia. The uterine horns were exposed after laparotomy. Electroporation was performed using a square wave electroporator (ECM 830, BTX, Holliston, MA) and tweezer-type platinum disc electrodes (5-mm-diameter, Sonidel, Dublin, Ireland). The electroporation settings were 4 pulses of 40 V for 50 ms with 500 ms interval. Endotoxin-free DNA was injected using a glass pipette into one ventricle of the mouse embryos at the following concentrations: pH1SCV2 TdTomato: 0.5 µg/µL; pCAG EGFP-GPHN: 0.3 µg/µL; and pCAHA SRGAP2C: 0.7 µg/µL. All constructs have been described before [97].

Cortical slice preparation

Electroporated animals aged between postnatal day P78 and P129 were anesthetized with ketamin 100 mg/kg and xylazin 10 mg/kg and intracardiacally perfused with first 0.1 mL of heparin (5000 U.I./mL, Sanofi, Paris, France), then an aqueous solution of 4% w/v paraformaldehyde (PFA) (CliniSciences) and 0.5% glutaraldehyde (GA) (Clinisciences, Nanterre, France) in 0.1 M phosphate-buffered saline (PBS). The fixative solution was made extemporaneously and kept at ice-cold temperature throughout the perfusion. The perfusion was gravity-driven at a flow rate of about 0.2 ml/s, and the total perfused volume was about 100 ml per animal. Brains were collected and postfixed overnight at 4°C in a 4% PFA solution. Coronal brain sections with 30-µm thickness were obtained using a vibrating microtome (Leica VT1200S).

Fluorescence microscopy of fixed tissue

Slices containing electroporated neurons were trimmed to small (5 to 10 mm²) pieces centered on a relatively isolated fluorescent neuron, then mounted in a custom-made chamber on #1.5 glass coverslips. The mounting procedure consisted in enclosing the slices between the glass coverslip and the bottom of a cell culture insert (Falcon, ref. 353095) adapted to the flat surface with a silicon O-ring gasket (Leica, Wetzlar, Germany) and fixed with fast-curing silicon glue (see panel A in S1 Fig). Volumes of GFP and tdTomato signals were acquired in 12 bits mode

(1024 × 1024 pixels) with z-steps of 400 nm using an inverted Leica TCS SP8 confocal laser scanning microscope equipped with a tunable white laser and hybrid detectors and controlled by the LAF AS software. The objective lenses were a 10X PlanApo, NA 0.45 lens for identifying electroporated neurons, and a 100X HC-PL APO, NA 1.44 CORR CS lens (Leica) for higher magnification images. GFP-GPHN puncta with a peak signal intensity at least 4 times above shot noise background levels were considered for CLEM.

Placement of DAB fiducial landmarks

Following confocal imaging, slices were immersed in a solution of 1 mg/mL 3,3'-diaminobenzidine tetrahydrochloride (DAB, Sigma Aldrich, Darmstadt, Germany) in Tris buffer (0.05 M, pH 7.4). The plugin "LAS X FRAP" (Leica) was used to focus the pulsed laser in the tissue in custom patterns of 10-to-20 points using 100% power in 4 wavelengths (470 to 494 nm) for 30 seconds to 60 seconds per point at 3 different depths: the top of the slice, the depth of the targeted soma, then the bottom of the slice (surface closest to the objective). DAB precipitates were imaged in transmitted light mode. Slices were subsequently rinsed twice in Tris buffer and prepared for EM.

Tissue preparation for serial block-face scanning electron microscopy (SBEM)

Using a scalpel blade under a M165FC stereomicroscope (Leica), imaged tissue slices were cut to approximately 1 mm² asymmetrical pieces of tissue centered on the ROI, and then kept in plastic baskets (Leica) through the osmification and dehydration steps. Samples were treated using an osmium bridging technique adapted from the NCMIR protocol (OTO) [155]. The samples were washed 3 times in ddH₂O and immersed for 1 hour in a reduced osmium solution containing 2% osmium tetroxide and 1.5% potassium ferrocyanide in ddH₂O. Samples were then immersed for 20 minutes in a 1% thiocarbohydrazide (TCH) solution (EMS, Hatfield, PA) prepared in ddH₂O at room temperature. The samples were then postfixed with 2% OsO₄ in ddH₂O for 30 minutes at room temperature and colored *en bloc* with 1% aqueous uranyl acetate at 4°C during 12 hours. Postfixed samples were subjected to Walton's *en bloc* lead aspartate staining at 60°C for 30 minutes (Walton, 1979). After dehydration in graded concentrations of ice-cold ethanol solutions (20%, 50%, 70%, 90%, and twice 100%, 5 minutes per step), the samples were rinsed twice for 10 minutes in ice-cold anhydrous acetone. Samples were then infiltrated at room temperature with graded concentrations of Durcupan (EMS) prepared without plastifier (components A, B, and C only). In detail, blocks were infiltrated with 25% Durcupan for 30 minutes, 50% Durcupan for 30 minutes, 75% Durcupan for 2 hours, 100% Durcupan overnight, and 100% fresh Durcupan for 2 hours before being polymerized in a minimal amount of resin in a flat orientation in a sandwich of ACLAR 33C Films (EMS) at 60°C for 48 hours. Samples were mounted on aluminum pins using conductive colloidal silver glue (EMS). Before curing, tissue blocks were pressed parallel to the pin surface using a modified glass knife with 0° clearance angle on an ultramicrotome (Ultracut UC7, Leica) in order to minimize the angular mismatch between LM and SEM imaging planes. Pins then cured overnight at 60°C. Samples were then trimmed around the ROI with the help of fluorescent overviews of the ROI within their asymmetrical shape. Minimal surfacing ensured that superficial DAB landmarks were detected at the SBEM before block-facing.

SBEM acquisition

SBEM imaging was performed with a Teneo VS microscope (FEI, Eindhoven, The Netherlands) on the ImagoSeine imaging platform at Institut Jacques Monod, Paris. The software

MAPS (Thermo Fisher Scientific, Waltham, MA) was used to acquire SEM images of targeted volumes at various magnifications. Acquisition parameters were 1,7830 kV, 500 ns/px, 100 pA, 40-nm-thick sectioning, and 8200 × 8200 pixels resolution with either 2.5 nm or 25 nm pixel size for high- and low-magnification images, respectively. Placing an electromagnetic trap above the diamond knife to catch discarded tissue sections during days-long imaging sessions was instrumental to achieve continuous 3D-EM acquisitions.

Image segmentation

Dendrites were segmented from SBEM stacks using the software Microscopy Image Browser (MIB) [156]. 3D reconstruction was performed with the software IMOD [157] (<http://bio3d.colorado.edu/imod/>). Individual PSDs were manually outlined based on the apposition with a presynaptic terminal and differences in membrane contrast and thickness between postsynaptic and nonsynaptic membranes on individual SBEM images (see example movie at https://www.opendata.bio.ens.psl.eu/3DCLEM-Spines/S1_Movie.zip; login: guest, password: EnsData0811). 3D spine models were imported in the software Blender (www.blender.org) for subsampling, and the quantification of spine section areas along their main axis was done with in-house python scripts. Other measurements were performed using IMOD and in-house python scripts. Models and raw data are accessible at <https://www.opendata.bio.ens.psl.eu/3DCLEM-Spines> (login: guest; password: EnsData0811).

Tissue preparation for tissue shrinkage estimation

Two female mice (21 days postnatal) were used for the analysis of tissue shrinkage induced by chemical fixation. Mice were decapitated, and their brains were rapidly removed. The brains were transferred to an ice-cold dissection medium, containing (in mM) KCl, 2.5; NaHCO₃, 25; NaH₂PO₄, 1; MgSO₄, 8; glucose, 10 (pH 7.4). A mix of 95% O₂ and 5% CO₂ was bubbled through the medium for 30 minutes before use. Coronal brain sections with 300-μm thickness were obtained using a vibrating microtome (Leica VT1200S). Small fragments of the SSC were cut from those slices and fixed either by immersion in an ice-cold PBS solution containing 4% PFA and 0.5% GA or in frozen with liquid nitrogen under a pressure of 2,100 bars using a high-pressure freezing (HPF) system (HPM100, Leica). For HPF-frozen samples, the interval between removal of the brain and vitrification was about 7 minutes. Cryo-substitution and tissue embedding were performed in a Reichert AFS apparatus (Leica). Cryo-substitution was performed in acetone containing 0.1% tannic acid at −90°C for 4 days with one change of solution, then in acetone containing 2% osmium during the last 7 hours at −90°C. Samples were thawed slowly (5°C/h) to −20°C and maintained at −20°C for 16 additional hours, then thawed to 4°C (10°C/h). At 4°C, the slices were immediately washed in pure acetone. Samples were rinsed several times in acetone, then warmed to room temperature and incubated in 50% acetone–50% araldite epoxy resin for 1 hour, followed by 10% acetone–90% araldite for 2 hours. Samples were then incubated twice in araldite for 2 hours before hardening at 60°C for 48 hours. As for chemically fixed sections, they were postfixed for 30 minutes in ice-cold 2% osmium solution, rinsed in PBS buffer, dehydrated in graded ice-cold ethanol solutions, and rinsed twice in ice-cold acetone, before undergoing the same resin infiltration and embedding steps as HPF-frozen samples. After embedding, ultrathin sections were cut in L2/3 of the SSC, orthogonally to the apical dendrites of PNs, 200 to 300 μm from the pial surface using an ultramicrotome (Ultracut UC7, Leica). Ultrathin (pale yellow) sections were collected on formwar-coated nickel slot grids, then counterstained with 5% uranyl acetate in 70% methanol for 10 minutes, washed in distilled water, and air dried before observation on a Philips TECNAI 12 electron microscope (Thermo Fisher Scientific).

Measurement of shrinkage correction factors

Ultrathin sections of both HPF-frozen tissues and chemically fixed tissues were observed using a Philips TECNAI 12 electron microscope (Thermo Fisher Scientific). Cellular compartments contacted by a presynaptic bouton containing synaptic vesicles and exhibiting a visible electron-dense PSD at the contact site, but no mitochondrion within their cytosol, were identified as dendritic spine heads. Cross-section areas of random spine heads and the curvilinear lengths of their PSD were quantified in both conditions using the softwares MIB and IMOD. $N = 277$ spine head sections were segmented in HPF-frozen cortical slices from 2 female mice, and $N = 371$ spine head sections were segmented in chemically fixed cortical slices originating from the same 2 mice. χ^2 minimization was used between spine head cross-section area distributions in HPF or OTO conditions to compute average volume shrinkage and correction factors. PSD areas were not corrected as they exhibited no shrinkage.

Computation of the diffusional neck resistance

The diffusional resistance of spine necks W_{neck} was measured as follows. Using IMOD, we first modeled in 3D the principal axis of each spine neck as an open contour of total length L_{axis} connecting the base of the neck to the base of the spine head. Using Blender, we interpolated each spine neck path linearly with 100 points. We named $P(\ell)$ the plane that bisected the spine neck model orthogonally to the path at the abscissa ℓ , and $A(\ell)$ the spine neck cross-section within $P(\ell)$. In spines containing an SA, we corrected $A(\ell)$ by a scaling factor $\beta(\ell) = 1 - (D_{\text{SA}}/D_{\text{spine}})^2(\ell)$, where $D_{\text{SA}}/D_{\text{spine}}(\ell)$ is the local ratio of SA and neck diameter. We measured $D_{\text{SA}}/D_{\text{spine}}$ orthogonally to the neck path in 10 SA+ spines and in 3 different locations per spine on SBEM images: at the spine stem ($\ell/L_{\text{axis}} = 0.1$), at the center of the spine neck ($\ell/L_{\text{axis}} = 0.5$), and at the stem of the head ($\ell/L_{\text{axis}} = 0.9$). $D_{\text{SA}}/D_{\text{spine}}$ was $44\% \pm 11\%$, $31\% \pm 8\%$, and $37\% \pm 8\%$ respectively, and fluctuations were not statistically significant. We then divided each SA+ spine neck in thirds and scaled their neck cross-section areas along neck axis $A_{\text{SA}+}(\ell) = \beta(\ell)A(\ell)$ before computing $W_{\text{neck}} = \int d\ell / A(\ell)$ for all spines, using Simpson's integration rule.

Multicompartment electrical model

All simulations were implemented in Python using NEURON libraries [158] and in-house scripts. Ordinary differential equations were solved with NEURON-default backward Euler method, with $\Delta t = 0.05$ ms. Scripts and model definition files are available in a GitHub repository: <https://github.com/p-sera/SpineModel>. Biophysical constants were taken from the literature as follows: membrane capacitance $C_m = 1 \mu\text{F}/\text{cm}^2$ [38]; cytosolic resistivity $\rho = 300 \Omega\cdot\text{cm}$ [84,159]; synaptic conductivities were modeled as biexponential functions $g(t) = A g_{\text{max}} (e^{-t/t_2} - e^{-t/t_1})$ where A is a normalizing constant and (t_1, t_2) define the kinetics of the synapses: GABAergic conductance $(t_1, t_2) = (0.5, 15)$ ms, AMPAR-dependent conductance $(t_1, t_2) = (0.1, 1.8)$ ms, NMDAR-dependent conductance $(t_1, t_2) = (0.5, 17.0)$ ms (ModelDB: <https://senselab.med.yale.edu/ModelDB/>). The magnesium block of NMDA receptors was modeled by a voltage-dependent factor [160]. Remaining free parameters comprised the following: the leaking conductivity g_m (or, equivalently, the membrane time constant T_m); the peak synaptic conductance per area: g_{AMPA} , g_{NMDA} , g_{GABA} ; and the total membrane area of the modeled neuron. These parameters were adjusted so that signal distributions fitted published electrophysiological recordings [114,115,118,119,121]. In more detail, we first set up one “ball-and-stick” model per segmented spine ($N = 390$). The dendrite hosting the modeled spine was generated as a tube of diameter $d_{\text{dendrite}} = 0.87 \mu\text{m}$, and length $L_{\text{dendrite}} = 140 \mu\text{m}$. This dendrite was split in 3 segments, and the modeled spine was placed on the 2- μm -long middle segment. To

account for the passive electrical effects of neighboring spines, the membrane surfaces of both the proximal and distal sections of the studied dendrite were scaled by a correction factor $\gamma = 1 + \langle A_{\text{spine}} \rangle d_{\text{spine}} / \pi d_{\text{dendrite}} = 3.34$, with the density $d_{\text{spine}} = 1.63 \text{ spine} \cdot \mu\text{m}^{-1}$ and the average spine membrane area $\langle A_{\text{spine}} \rangle = 3.89 \mu\text{m}^2$. Spine head shrinkage was corrected by scaling the length and diameter of all spine heads by a factor $S = 1.22$ and spine head volume by $S^3 = 1.81$. PSD areas were not scaled (see panel C3 in [S7 Fig](#)). The leakage resistance was fitted to $65 \text{ M}\Omega$ [120], yielding a total membrane surface of the modeled neurons: $A_{\text{mb, total}} = 18,550 \mu\text{m}^2$. We calibrated synaptic conductances type by type, by fitting the signals generated in the whole distribution of 390 constrained models to published electrophysiological recordings. AMPA conductances of all excitatory synapses were set proportional to ePSD area and scaled by the free parameter g_A . In each model, we activated the AMPAR component of excitatory synapses and monitored the amplitude of resulting EPSCs in the soma. The average EPSC amplitude was adjusted to 58 pA [115,119], yielding a scaling factor $g_A = 3.15 \text{ nS}/\mu\text{m}^2$, which takes into account the average number of excitatory contacts per axon per PN in L2/3 of mouse SSC: $N_{\text{ePSD/axon}} = 2.8$ [115]. After this calibration, the maximal AMPA synaptic conductance g_{AMPA} ranged from 0.04 nS to 3.13 nS ($0.456 \pm 0.434 \text{ nS}$). NMDA conductances of all excitatory synapses were set proportional to ePSD area and scaled by the free parameter g_N . In each model, we activated both NMDA and AMPA components of excitatory synapses and fitted the amplitude ratio between the average AMPA+NMDA and AMPA-only responses to 1.05 [119], yielding $g_N = 3.4 \text{ nS}/\mu\text{m}^2$. As a result, g_{NMDA} ranged from 0.04 nS to 3.42 nS ($0.498 \pm 0.474 \text{ nS}$), in line with the literature [120]. Voltage-dependent sodium and potassium conductances were not included in our model because the amplitude of single EPSPs remained subthreshold ($<1\%$ of synapses generate EPSPs large enough to activate these conductances [74,161]; see [Fig 6B and 6C](#)). Therefore, this model is not fit to compute the integration of multiples EPSPs or spikes. Considering inhibition, the GABA conductances of all inhibitory synapses were set proportional to iPSD area and scaled by the free parameter $g_G = 5.9 \text{ nS}/\mu\text{m}^2$ to adjust the mean conductance of dendritic inhibitory synapses to 1 nS [37,121,122]. Following this calibration, g_{GABA} ranged from 0.33 nS to 3.36 nS ($1.00 \pm 0.577 \text{ nS}$) for synapses located on the shaft and from 0.19 nS to 1.56 nS ($0.528 \pm 0.277 \text{ nS}$) for inhibitory synapses located on spines. The reversal potential of chloride ions (E_{Cl^-}) was set to -80 mV [162] and considered constant, as it is regulated on timescales exceeding 100 ms [163], and we modeled signals in the 10 ms timescale. Calcium influxes were modeled in spine heads as output of the opening of NMDARs and VDCCs. The dynamics of L-, N-, and Q-type VDCCs were obtained from ModelDB (accession n°: 151458), and their conductivities were scaled to the head membrane area of each spine, A_{head} , excluding synaptic area (s). VDCC-type ratios and calcium conductivities were adjusted by fitting the average amplitude of calcium concentration transients to 20% of the NMDA conductance [112]. Calcium uptake from cytosolic buffers was set to 95% to yield an average amplitude of Ca^{2+} concentration transients of $0.7 \mu\text{M}$ [113].

Bootstrapping

To simulate a large number of spine–spine interactions with limited redundancy, we expanded our distribution of spines using a “smooth” bootstrapping method [127]. Specifically, the dataset (i.e., a matrix of dimensions $N \times N_f$) was resampled to generate a new matrix of dimension $M \times N_f$, where N is the number of spines, N_f is the number of selected features, and M is the final number of synthetic spines. M rows were randomly selected in the original dataset, and zero-centered, feature-dependent Gaussian noise was added to each element of the matrix (excluding absolute quantities, e.g., number of PSDs or presence of SA). To determine appropriate noise amplitude for each parameter, we generated a synthetic set of $M = 500$ spines from

the original dataset, including Gaussian noise with an arbitrary amplitude σ on 1 parameter at a time. This new feature distribution was compared to the original distribution using a 2-sample Kolmogorov–Smirnov test (KS test), and this procedure was repeated 1,000 times for each set value of σ . A conservative noise level ($\sigma = 10\%$) was sufficient to smear parameter distributions while the fraction of synthetic sets that were statistically different from the original set ($p < 0.05$, KS test) remained 0 over 1,000 iterations. $\sigma = 10\%$ was valid for all relevant features, and we assumed that such a small noise amplitude would minimally interfere with nonlinear correlations in our dataset. Synthetically generated spines were then used to simulate elementary synaptic signaling using in-house python scripts. We also used bootstrapping to estimate standard deviations in our simulations.

Statistics

No statistical methods were used to predetermine sample size. We used a one-way ANOVA on our 4 datasets to test that interneuron and intermic variability were small enough to pool all datasets together (S1 Data). We used KS test to determine that all measured morphological parameters followed a log-normal distribution (S1 Data). We used Mann–Whitney U test for statistical analyses of morphological parameters, except when comparing the probability for SiSs and DiSs to harbor SA, for which we used Pearson χ^2 test. All results in the text are mean \pm SD. In Figs 6 and 7, we plot medians as solid lines, as they better describe where log-normal distributions peak. Shaded areas represent 68% confidence intervals, which span approximately 1 SD on each side of the mean.

Supporting information

S1 Fig. ROI landmarking strategy for 3D-CLEM using DAB and a detachable chamber. (A) Schematic of ROI landmarking using DAB photo-oxidation. The tissue slice is held against a glass coverslip in a solution of DAB using a detachable chamber. Confocal imaging and ROI landmarking are performed using the same microscopy setup. (B) Transmitted light image of a cortical slice labelled with DAB precipitates. Varying the duration of UV illumination (T_{ill}) allows adjusting DAB spot size. (C) Example of labeling pattern around an optically isolated fluorescent neuron. DAB was photoprecipitated by focusing UV light for 40 seconds at each highlighted location (pink dots in yellow circles). (D) Transmitted light image of the same field of view after DAB photoprecipitation. (E) Overlay showing DAB precipitates in D (dark spots) arranged similarly to the UV focusing pattern in C. (F) Schematic of slice retrieval after ROI landmarking. Detaching the chamber (wide arrow) allows taking the sample to EM preparation steps, i.e., Osmium–TCH–Osmium postfixation [155], dehydration, resin infiltration, and plastic embedding. (G) ROI recovery in SBEM. DAB precipitates (circles) generated at the surface of the sample mark the (x,y) coordinates of the ROI. They are detected with an electron beam (e^-) before block facing the sample and acquiring SBEM images in targeted volumes. The DAB pattern generated at the depth of the targeted cell (in red) allows its retrospective identification. DAB, 3,3-diaminobenzidine; EM, electron microscopy; ROI, region of interest; SBEM, serial block–face scanning EM; TCH, thiocarbohydrazide; 3D-CLEM, 3D correlative light–electron microscopy. (TIF)

S2 Fig. Distance between spine and soma does not correlate with other measured parameters. Distance between spine and soma as a function of all measured morphological parameters of the spines that were segmented. No parameter exhibited a linear correlation with the distance between spine and soma. The data underlying this figure can be found in

https://www.opendata.bio.ens.psl.eu/3DCLEM-Spines/data/Data_related_to_FigS2.xlsx (login: guest; password: EnsData0811). ePSD, excitatory postsynaptic density; iPSD, inhibitory PSD. (TIF)

S3 Fig. Effect of the SA on diffusional neck resistance. Distribution of the diffusional neck resistance (W_{neck}) calculated using neck morphology for spines devoid of apparatus (SA−) or containing an SA (SA+). “SA+ uncorr.”: W_{neck} without SA correction for SA+ spines ($p = 0.1$ compared to corrected W_{neck}). *** $p < 0.001$ calculated using Mann–Whitney test. The data underlying this figure can be found in https://www.opendata.bio.ens.psl.eu/3DCLEM-Spines/data/Data_related_to_FigS3.xlsx (login: guest; password: EnsData0811). n.s., not significant; SA, spine apparatus. (TIF)

S4 Fig. Distribution of inhibitory synapses along basal dendrites of L2/3 and L5 cortical PNs. (A) Representative segments of dendrites of L2/3 and L5 PNs expressing GFP-GPHN (green) and TdTomato (red) in juvenile (postnatal days P21–P27) or young (P10) mice. Neuronal progenitors of L2/3 and L5 PNs were electroporated *in utero* at E15.5 and E12.5, respectively. Scale bar: 4 μm . (B, C) Quantification of gephyrin cluster density (B) and proportion of gephyrin clusters in spines (C). Data were acquired and analyzed as in our previous work [97]. Gephyrin cluster distribution was similar in adult (data in main text) and juvenile mice (density: 3.5 ± 1.1 clusters per 10 μm of dendrite in adults and 4.5 ± 1.0 clusters per 10 μm of dendrite in juveniles; proportion of gephyrin clusters in spines: 38% and 36% in adults and juveniles, respectively). However, both the density of gephyrin clusters and their proportion in spines was lower in younger (P10) mice, suggesting that DiSs represent mature spines (see also [103]). The proportion of gephyrin clusters in spines was also lower in L5 PNs than in L2/3 neurons. $N_{\text{L2/3 Juvenile}} = 18$, $N_{\text{L2/3 Young}} = 28$, $N_{\text{L5 Juvenile}} = 19$. N represents the number of cells. Cells come from at least 3 animals per conditions. *** $p < 0.001$, * $p < 0.05$, ANOVA test followed by Tukey multiple comparisons test. The data underlying this figure can be found in https://www.opendata.bio.ens.psl.eu/3DCLEM-Spines/data/Data_related_to_FigS4.xlsx (login: guest; password: EnsData0811). DiSs, dually innervated spines; GFP-GPHN, GFP-tagged gephyrin; L2/3, layer 2/3; L5, layer 5; PN, pyramidal neuron. (TIF)

S5 Fig. Comparison of SiS and DiS neck diameter. Quantification of minimal neck diameter (A) and mean neck diameter (B) for all spines ($N = 349$ SiSs and 37 DiSs; solid lines) and for spines with $V_{\text{head}} > 0.05 \mu\text{m}^3$ ($N = 186$ SiSs and 34 DiSs; dashed lines). $p > 0.05$ calculated using Mann–Whitney tests. The data underlying this figure can be found in https://www.opendata.bio.ens.psl.eu/3DCLEM-Spines/data/Data_related_to_FigS5.xlsx (login: guest; password: EnsData0811). DiSs, dually innervated spines; SiSs, singly innervated spines. (TIF)

S6 Fig. iPSD area as a function of DiS head volume. iPSD area as a function of spine head volume for $N = 37$ DiSs. Linear regression: $R^2 < 0.1$. The data underlying this figure can be found in https://www.opendata.bio.ens.psl.eu/3DCLEM-Spines/data/Data_related_to_FigS6.xlsx (login: guest; password: EnsData0811). DiS, dually innervated spine; iPSD, inhibitory PSD. (TIF)

S7 Fig. Fixation-induced shrinkage of spine heads but not PSD area. (A) TEM images of L2/3 SSC acute slices from the same mouse (postnatal day P21) upon either chemical fixation with aldehydes (A1) or physical fixation with HPF (A2). Spine head section areas (indicated in

red in A1 and in light blue in A2) and lengths of PSDs were segmented for quantification. Scale bars: 1 μm . (B) Normalized histograms of spine head cross-section areas for chemically fixed (Chem) samples ($N = 194$ for mouse “s1” and 178 for mouse “s2”; $p = 0.13$) or HPF samples ($N = 128$ for s1 and 150 for s2; $p = 0.052$) in B1 and B2, respectively. Data from mice s1 and s2 displayed no statistical difference and were pooled together in B3 to compare area distribution between HPF (blue) and chemically fixed tissue (orange). Head cross-section areas were $34\% \pm 5\%$ smaller in chemically fixed samples (orange) than in HPF samples (blue), implying approximately 45% head volume shrinkage ($p < 10^{-8}$). (C) Normalized histograms of PSD section lengths for chemically fixed ($p = 0.44$) and HPF samples ($p = 0.17$) in C1 and C2, respectively. PSDs were not significantly deformed by chemical fixation (C3; $p = 0.10$). Only significant ($p < 0.05$) p -values are shown. *** $p < 0.001$ calculated using Mann–Whitney test. The data underlying this figure can be found in https://www.opendata.bio.ens.psl.eu/3DCLEM-Spines/data/Data_related_to_FigS7.xlsx (login: guest; password: EnsData0811). HPF, high-pressure freezing; L2/3, layer 2/3; PSD, postsynaptic density; SSC, somatosensory cortex; TEM, transmission electron microscopy. (TIF)

S8 Fig. Influence of R_{neck} on ΔV_{max} in the spine head and dendritic shaft. Plot of the EPSP amplitude ΔV_{max} elicited in a dendritic spine while varying its neck resistance (R_{neck}) and keeping all other parameters constant. Increasing R_{neck} causes ΔV_{max} to increase in the spine head (blue) and to decrease in the dendritic shaft (orange). The data underlying this figure can be found in https://www.opendata.bio.ens.psl.eu/3DCLEM-Spines/data/Data_related_to_FigS8.xlsx (login: guest; password: EnsData0811). EPSP, excitatory postsynaptic potential. (TIF)

S9 Fig. Contribution of VDCCs and NMDAR to calcium transients. (A) Typical time course of a calcium transient elicited in spine head. The calcium signal was induced by an EPSP at $t = 120$ ms. The contributions of VDCCs and NMDARs to the total elevation of calcium concentration (blue curve) are plotted in orange and green, respectively. (B) Contribution of VDCCs to the total elevation of calcium concentration as a function of the estimated amplitude of the calcium transient in all spines ($N = 390$). The data underlying this figure can be found in https://www.opendata.bio.ens.psl.eu/3DCLEM-Spines/data/Data_related_to_FigS9.xlsx (login: guest; password: EnsData0811). EPSP, excitatory postsynaptic potential; NMDAR, NMDA receptor; VDCC, voltage-dependent calcium channel. (TIF)

S10 Fig. Morphofunctional properties of spines in basal dendrites of L2/3 neurons expressing the human-specific gene *SRGAP2C*. (A) Z-projection of the confocal stack showing a segment of basal dendrite of an L2/3 PN expressing cytosolic TdTomato (in magenta), GFP-GPHN (in green), and *SRGAP2C* in the adult mouse SSC. Neurons were electroporated *in utero* at E15.5. Numbers identify individual spines. Scale bar: 1 μm . (B) 3D-EM reconstruction. Individual dendritic spines are manually segmented and randomly colored. Spines that were detected in CLEM but not in LM alone are labelled in red. Scale bar: 1 μm . (C) Quantification of spine head volume (C1), ePSD area (C2), DiS–iPSD area (C3), neck length (L_{neck}) (C4), mean neck diameter (C5), and the diffusional neck resistance (W_{neck}) (C6) for WT spines (blue) and spines expressing *SRGAP2C* (red). $N = 73$ spines expressing *SRGAP2C* and 390 WT spines in panels C1–C2 and C4–C6. $N = 6$ DiSs expressing *SRGAP2C* and 37 WT DiSs in panel C3. *** $p < 10^{-3}$ for all quantities except for iPSD area, Mann–Whitney test. Comparison with our previous work on oblique apical dendrites [97,127] suggests that *SRGAP2C* expression has dendrite-type specific consequences on spine density and

morphology. (D) Similar panels as in Fig 7 but for spines along the basal dendrites of neurons expressing *SRGAP2C*. (D1) Voltage inhibition in the spine head, inh_V , induced by dendritic (blue) or spinous (orange) IPSPs as a function of Δt . (D2) Inhibition of the calcium influx in the spine head, $inh_{[Ca^{2+}]}$, induced by dendritic (blue) or spinous (orange) IPSPs as a function of Δt . The inhibition of calcium signals was approximately 40% lower in neurons expressing *SRGAP2C* than in control neurons (Fig 7). The data underlying this figure can be found in https://www.opendata.bio.ens.psl.eu/3DCLEM-Spines/data/Data_related_to_FigS10.xlsx (login: guest; password: EnsData0811). CLEM, correlative light–electron microscopy; DiS, dually innervated spine; ePSD, excitatory postsynaptic density; GFP-GPHN, GFP-tagged gephyrin; iPSD, inhibitory PSD; IPSP, inhibitory postsynaptic potential; LM, light microscopy; L2/3, layer 2/3; PN, pyramidal neuron; *SRGAP2C*, Slit-Robo Rho GTPase-activating protein 2C; SSC, somato-sensory cortex; WT, wild-type; 3D-EM, three-dimensional electron microscopy. (TIF)

S1 Table. Contribution of morphological parameters to the variance of ΔV_{max} and $\Delta[Ca^{2+}]_{max}$. Highest-ranking input parameters (A_{ePSD} , R_{neck} , and L_{dend}) are sorted by decreasing contribution to the variance of the simulation outputs, as estimated with a GLM. Numbers indicate to which proportion input variables accounted for the variance of considered output. (XLSX)

S1 Data. Quantification of the morphology of spines and synapses. The first sheet of the .xlsx file describes the samples used in our experiments. The second sheet reports scores for log-normality and intersample variability tests for each morphological variable. The 2 last sheets report spine and PSD anatomy in all segmented dendrites. Legends are included in the rightmost column. (XLSX)

Acknowledgments

We thank members of the Charrier and Triller laboratories (IBENS, Paris, France), Vincent Hakim and Boris Barbour for insightful discussions. We acknowledge the ImagoSeine imaging facility (Jean-Marc Verbavatz and Rémi Leborgne, Jacques Monod Institute, Paris, France) for SBEM availability, service, and support, Liesbeth Hekkings (Thermo Fisher Scientific) for technical support, the IBENS Imaging Facility, and the IBENS acute transgenesis facility (Caroline Mailhes-Hamon).

Author Contributions

Conceptualization: Olivier Gemin, Pablo Serna, Antoine Triller, Cécile Charrier.

Data curation: Olivier Gemin, Pablo Serna, Joseph Zamith.

Formal analysis: Olivier Gemin, Pablo Serna, Joseph Zamith.

Funding acquisition: Antoine Triller, Cécile Charrier.

Investigation: Olivier Gemin, Pablo Serna, Joseph Zamith.

Methodology: Olivier Gemin, Pablo Serna, Antoine Triller, Cécile Charrier.

Project administration: Antoine Triller, Cécile Charrier.

Resources: Olivier Gemin, Pablo Serna, Joseph Zamith, Nora Assendorp, Matteo Fossati, Cécile Charrier.

Software: Olivier Gemin, Pablo Serna.

Supervision: Philippe Rostaing, Antoine Triller, Cécile Charrier.

Validation: Olivier Gemin, Pablo Serna, Cécile Charrier.

Visualization: Olivier Gemin, Pablo Serna, Cécile Charrier.

Writing – original draft: Olivier Gemin, Pablo Serna, Cécile Charrier.

Writing – review & editing: Cécile Charrier.

References

1. Ramón y Cajal S. Reglas y consejos sobre investigación biológica (los tónicos de la voluntad). Impr de Fontanet Madrid. 1916.
2. Hersch SM, White EL. Quantification of synapses formed with apical dendrites of golgi-impregnated pyramidal cells: Variability in thalamocortical inputs, but consistency in the ratios of asymmetrical to symmetrical synapses. *Neuroscience*. 1981; 6. [https://doi.org/10.1016/0306-4522\(81\)90069-5](https://doi.org/10.1016/0306-4522(81)90069-5) PMID: 7279213
3. Yuste R, Bonhoeffer T. Genesis of dendritic spines: Insights from ultrastructural and imaging studies. *Nat Rev Neurosci*. 2004; 5:24–34. <https://doi.org/10.1038/nrn1300> PMID: 14708001
4. Arellano JL. Ultrastructure of dendritic spines: correlation between synaptic and spine morphologies. *Front Neurosci*. 2007; 1:131–43. <https://doi.org/10.3389/neuro.01.1.1.010.2007> PMID: 18982124
5. Harris KM, Weinberg RJ. Ultrastructure of Synapses in the Mammalian Brain. *Cold Spring Harb Perspect Biol*. 2012. <https://doi.org/10.1101/cshperspect.a005587> PMID: 22357909
6. Harris KM, Spacek J, Bell ME, Parker PH, Lindsey LF, Baden AD, et al. A resource from 3D electron microscopy of hippocampal neuropil for user training and tool development. *Sci Data*. 2015; 2:1–19. <https://doi.org/10.1038/sdata.2015.46> PMID: 26347348
7. Fifková E, Anderson CL. Stimulation-induced changes in dimensions of stalks of dendritic spines in the dentate molecular layer. *Exp Neurol*. 1981; 74:621–7. [https://doi.org/10.1016/0014-4886\(81\)90197-7](https://doi.org/10.1016/0014-4886(81)90197-7) PMID: 7297640
8. Nusser Z, Cull-Candy S, Farrant M. Differences in Synaptic GABAA Receptor Number Underlie Variation in GABA Mini Amplitude. *Neuron*. 1997; 19:697–709. [https://doi.org/10.1016/S0896-6273\(00\)80382-7](https://doi.org/10.1016/S0896-6273(00)80382-7) PMID: 9331359
9. Matsuzaki M, Honkura N, Ellis-Davies GCR, Kasai H. Structural basis of long-term potentiation in single dendritic spines. *Nature*. 2004; 429:761–6. <https://doi.org/10.1038/nature02617> PMID: 15190253
10. Bourne JN, Harris KM. Coordination of size and number of excitatory and inhibitory synapses results in a balanced. *Hippocampus*. 2011; 21:354–73. <https://doi.org/10.1002/hipo.20768> PMID: 20101601
11. Holderith N, Lorincz A, Katona G, Rózsa B, Kulik A, Watanabe M, et al. Release probability of hippocampal glutamatergic terminals scales with the size of the active zone. *Nat Neurosci*. 2012; 15:988–97. <https://doi.org/10.1038/nn.3137> PMID: 22683683
12. Bailey CH, Kandel ER, Harris KM. Structural components of synaptic plasticity and memory consolidation. *Cold Spring Harb Perspect Biol*. 2015; 7:1–29. <https://doi.org/10.1101/cshperspect.a021758> PMID: 26134321
13. Kennedy MJ, Hanus C. Architecture and Dynamics of the Neuronal Secretory Network. *Annu Rev Cell Dev Biol*. 2019; 35:1–24. <https://doi.org/10.1146/annurev-cellbio-100818-125427> PMID: 31394047
14. Korkotian E, Frotscher M, Segal M. Synaptopodin regulates spine plasticity: Mediation by calcium stores. *J Neurosci*. 2014; 34:11641–51. <https://doi.org/10.1523/JNEUROSCI.0381-14.2014> PMID: 25164660
15. Kubota Y, van C, Kondo S, Karube F, Kawaguchi Y. Neocortical Inhibitory Terminals Innervate Dendritic Spines Targeted by Thalamocortical Afferents. *J Neurosci*. 2007; 27:1139–50. <https://doi.org/10.1523/JNEUROSCI.3846-06.2007> PMID: 17267569
16. Alvarez VA, Sabatini BL. Anatomical and Physiological Plasticity of Dendritic Spines. *Annu Rev Neurosci*. 2007; 30:79–97. <https://doi.org/10.1146/annurev.neuro.30.051606.094222> PMID: 17280523
17. Tønnesen J, Katona G, Rózsa B, Nägerl UV. Spine neck plasticity regulates compartmentalization of synapses. *Nat Neurosci*. 2014; 17:678–85. <https://doi.org/10.1038/nn.3682> PMID: 24657968
18. Adrian M, Kusters R, Storm C, Hoogenraad CC, Kapitein LC. Probing the Interplay between Dendritic Spine Morphology and Membrane-Bound Diffusion. *Biophys J*. 2017; 113:2261–70. <https://doi.org/10.1016/j.bpj.2017.06.048> PMID: 28750887

19. Yasuda R. Biophysics of Biochemical Signaling in Dendritic Spines: Implications in Synaptic Plasticity. *Biophys J*. 2017; 113:2152–9. <https://doi.org/10.1016/j.bpj.2017.07.029> PMID: 28866426
20. Harnett MT, Makara JK, Spruston N, Kath WL, Magee JC. Synaptic amplification by dendritic spines enhances input cooperativity. *Nature*. 2012; 491:599–602. <https://doi.org/10.1038/nature11554> PMID: 23103868
21. Yuste R. Electrical Compartmentalization in Dendritic Spines. *Annu Rev Neurosci*. 2013; 36:429–49. <https://doi.org/10.1146/annurev-neuro-062111-150455> PMID: 23724997
22. Tønnesen J, Nägerl UV. Dendritic spines as tunable regulators of synaptic signals. *Front Psych*. 2016; 7. <https://doi.org/10.3389/fpsy.2016.00101> PMID: 27340393
23. Svoboda K, Tank DW, Denk W. Direct measurement of coupling between dendritic spines and shafts. *Science*. 1996; 271:716–9. <https://doi.org/10.1126/science.272.5262.716> PMID: 8614831
24. Takasaki K, Sabatini BL. Super-resolution 2-photon microscopy reveals that the morphology of each dendritic spine correlates with diffusive but not synaptic properties. *Front Neuroanat*. 2014; 8:1–7. <https://doi.org/10.3389/fnana.2014.00001> PMID: 24523676
25. Popovic MA, Carnevale N, Rozsa B, Zecevic D. Electrical behaviour of dendritic spines as revealed by voltage imaging. *Nat Commun*. 2015. <https://doi.org/10.1038/ncomms9436> PMID: 26436431
26. Honkura N, Matsuzaki M, Noguchi J, Ellis-Davies GCR, Kasai H. The Subspine Organization of Actin Fibers Regulates the Structure and Plasticity of Dendritic Spines. *Neuron*. 2008; 57:719–29. <https://doi.org/10.1016/j.neuron.2008.01.013> PMID: 18341992
27. Araya R, Vogels TP, Yuste R. Activity-dependent dendritic spine neck changes are correlated with synaptic strength. *PNAS*. 2014; 111. <https://doi.org/10.1073/pnas.1321869111> PMID: 24982196
28. Androuin A, Potier B, Nägerl UV, Cattaert D, Danglot L, Thierry M, et al. Evidence for altered dendritic spine compartmentalization in Alzheimer's disease and functional effects in a mouse model. *Acta Neuropathol*. 2018; 135:839–54. <https://doi.org/10.1007/s00401-018-1847-6> PMID: 29696365
29. Forrest MP, Parnell E, Penzes P. Dendritic structural plasticity and neuropsychiatric disease. *Nat Rev Neurosci*. 2018; 19:215–34. <https://doi.org/10.1038/nrn.2018.16> PMID: 29545546
30. Rajkovich KE, Loerwald KW, Hale CF, Hess CT, Gibson JR, Huber KM. Experience-Dependent and Differential Regulation of Local and Long-Range Excitatory Neocortical Circuits by Postsynaptic Mef2c. *Neuron*. 2017; 93:48–56. <https://doi.org/10.1016/j.neuron.2016.11.022> PMID: 27989458
31. Poirazi P, Papoutsis A. Illuminating dendritic function with computational models. *Nat Rev Neurosci*. 2020. <https://doi.org/10.1038/s41583-020-0301-7> PMID: 32393820
32. Almog M, Korngreen A. Is realistic neuronal modeling realistic? *J Neurophysiol*. 2016; 116:2180–209. <https://doi.org/10.1152/jn.00360.2016> PMID: 27535372
33. Rall W. Cable properties of dendrites and effects of synaptic location. In: Anderson P, Jansen JKS, editors. *Excitatory Synaptic Mechanisms*. Oslo: Universitetsforlag; 1970. p. 175–187.
34. Hodgkin AL, Huxley AF. A quantitative description of membrane current and its application to conduction and excitation in nerve. *J Physiol*. 1952; 117:500–44. <https://doi.org/10.1113/jphysiol.1952.sp004764> PMID: 12991237
35. Stuart GJ, Spruston N. Dendritic integration: 60 years of progress. *Nat Neurosci*. 2015; 18:1713–21. <https://doi.org/10.1038/nn.4157> PMID: 26605882
36. Segev I, Rall W. Computational study of an excitable dendritic spine. *J Neurophysiol*. 1988; 60:499–523. <https://doi.org/10.1152/jn.1988.60.2.499> PMID: 2459320
37. Gidon A, Segev I. Principles Governing the Operation of Synaptic Inhibition in Dendrites. *Neuron*. 2012; 75:330–41. <https://doi.org/10.1016/j.neuron.2012.05.015> PMID: 22841317
38. Doron M, Chindemi G, Muller E, Markram H, Segev I. Timed Synaptic Inhibition Shapes NMDA Spikes, Influencing Local Dendritic Processing and Global I/O Properties of Cortical Neurons. *Cell Rep*. 2017; 21:1550–61. <https://doi.org/10.1016/j.celrep.2017.10.035> PMID: 29117560
39. Yuste R, Majewska A, Holthoff K. From form to function: Calcium compartmentalization in dendritic spines. *Nat Neurosci*. 2000; 3:653–9. <https://doi.org/10.1038/76609> PMID: 10862697
40. Gullledge AT, Carnevale NT, Stuart GJ. Electrical advantages of dendritic spines. *PLoS ONE*. 2012; 7. <https://doi.org/10.1371/journal.pone.0036007> PMID: 22532875
41. Jadi MP, Behabadi BF, Poleg-Polsky A, Schiller J, Mel BW. An augmented two-layer model captures nonlinear analog spatial integration effects in pyramidal neuron dendrites. *Proc IEEE*. 2014; 102:782–98. <https://doi.org/10.1109/JPROC.2014.2312671> PMID: 25554708
42. Schüz A, Palm G. Density of neurons and synapses in the cerebral cortex of the mouse. *J Comp Neurol*. 1989; 286:442–55. <https://doi.org/10.1002/cne.902860404> PMID: 2778101

43. Herculano-Houzel S, Watson C, Paxinos G. Distribution of neurons in functional areas of the mouse cerebral cortex reveals quantitatively different cortical zones. *Front Neuroanat*. 2013; 7:1–14. <https://doi.org/10.3389/fnana.2013.00001> PMID: 23423949
44. Motta A, Berning M, Boergens KM, Staffler B, Beining M, Loomba S, et al. Dense connectomic reconstruction in layer 4 of the somatosensory cortex. *Science*. 2019;366. <https://doi.org/10.1126/science.aay3134> PMID: 31649140
45. Sanes JR, Zipursky SL. Synaptic Specificity, Recognition Molecules, and Assembly of Neural Circuits. *Cell*. 2020; 181:536–56. <https://doi.org/10.1016/j.cell.2020.04.008> PMID: 32359437
46. Briggman KL, Denk W. Towards neural circuit reconstruction with volume electron microscopy techniques. *Curr Opin Neurobiol*. 2006; 16:562–70. <https://doi.org/10.1016/j.conb.2006.08.010> PMID: 16962767
47. Helmstaedter M. Cellular-resolution connectomics: Challenges of dense neural circuit reconstruction. *Nat Methods*. 2013; 10:501–7. <https://doi.org/10.1038/nmeth.2476> PMID: 23722209
48. Kasthuri N, Hayworth KJ, Berger DR, Schalek RL, Conchello JA, Knowles-Barley S, et al. Saturated Reconstruction of a Volume of Neocortex. *Cell*. 2015; 162:648–61. <https://doi.org/10.1016/j.cell.2015.06.054> PMID: 26232230
49. Karimi A, Odenthal J, Drawitsch F, Boergens KM, Helmstaedter M. Cell-type specific innervation of cortical pyramidal cells at their apical dendrites. *elife*. 2020; 9:1–23. <https://doi.org/10.7554/eLife.46876> PMID: 32108571
50. De P, Hoogenboom JP, Giepmans BNG. Correlated light and electron microscopy: Ultrastructure lights up! *Nat Methods*. 2015; 12:503–13. <https://doi.org/10.1038/nmeth.3400> PMID: 26020503
51. Begemann I, Galic M. Correlative light electron microscopy: Connecting synaptic structure and function. *Front Synaptic Neurosci*. 2016; 8:1–12. <https://doi.org/10.3389/fnsyn.2016.00001> PMID: 26903854
52. Müller-Reichert T, Verkade P. Correlative Light and Electron Microscopy III. *Methods in Cell Biology*. Academic Press; 2017.
53. Watanabe S, Punge A, Hollopeter G, Willig KI, Hobson RJ, Davis MW, et al. Protein localization in electron micrographs using fluorescence nanoscopy. *Nat Methods*. 2011; 8:80–4. <https://doi.org/10.1038/nmeth.1537> PMID: 21102453
54. Russell MRG, Lerner TR, Burden JJ, Nkwe DO, Pelchen-Matthews A, Domart M-C, et al. 3D correlative light and electron microscopy of cultured cells using serial blockface scanning electron microscopy. *J Cell Sci*. 2017; 130:278–91. <https://doi.org/10.1242/jcs.188433> PMID: 27445312
55. Collman F, Buchanan J, Phend KD, Micheva KD, Weinberg RJ, Smith SJ. Mapping Synapses by Conjugate Light-Electron Array Tomography. *J Neurosci*. 2015; 35:5792–807. <https://doi.org/10.1523/JNEUROSCI.4274-14.2015> PMID: 25855189
56. Lees RM, Peddie CJ, Collinson LM, Ashby MC, Verkade P. Correlative two-photon and serial block face scanning electron microscopy in neuronal tissue using 3D near-infrared branding maps. *Methods in Cell Biology*. Elsevier Ltd; 2017. <https://doi.org/10.1016/bs.mcb.2017.03.007> PMID: 28528636
57. Maclachlan C, Sahlender DA, Hayashi S, Molnár Z, Knott G. Block Face Scanning Electron Microscopy of Fluorescently Labeled Axons Without Using Near Infra-Red Branding. *Front Neuroanat*. 2018; 12:1–8. <https://doi.org/10.3389/fnana.2018.00001> PMID: 29440997
58. Katz Y, Menon V, Nicholson DA, Geinisman Y, Kath WL, Spruston N. Synapse Distribution Suggests a Two-Stage Model of Dendritic Integration in CA1 Pyramidal Neurons. *Neuron*. 2009; 63:171–7. <https://doi.org/10.1016/j.neuron.2009.06.023> PMID: 19640476
59. Bosch C, Martínez A, Masachs N, Teixeira CM, Feraud I, Ulloa F, et al. FIB/SEM technology and high-throughput 3D reconstruction of dendritic spines and synapses in GFP-labeled adult-generated neurons. *Front Neuroanat*. 2015; 9. <https://doi.org/10.3389/fnana.2015.00060> PMID: 26052271
60. Globus A, Rosenzweig M, Bennett E, Diamond M. Effects of differential experience on dendritic spine counts in rat cerebral cortex. *Comp Physiol Psychol*. 1973; 82(2):175–81. <https://doi.org/10.1037/h0033910> PMID: 4571892
61. Feldmeyer D. Excitatory neuronal connectivity in the barrel cortex. *Front Neuroanat*. 2012; 6:1–22. <https://doi.org/10.3389/fnana.2012.00001> PMID: 22291620
62. Bian WJ, Miao WY, He SJ, Qiu Z, Yu X. Coordinated Spine Pruning and Maturation Mediated by Inter-Spine Competition for Cadherin/Catenin Complexes. *Cell*. 2015; 162:808–22. <https://doi.org/10.1016/j.cell.2015.07.018> PMID: 26255771
63. Luckner M, Burgold S, Filser S, Scheungrab M, Niyaz Y, Hummel E, et al. Label-free 3D-CLEM Using Endogenous Tissue Landmarks. *iScience*. 2018; 6:92–101. <https://doi.org/10.1016/j.isci.2018.07.012> PMID: 30240628

64. Meißlitz-Ruppitsch C, Röhl C, Neumüller J, Pavelka M, Ellinger A. Photooxidation technology for correlated light and electron microscopy. *J Microsc.* 2009; 235:322–35. <https://doi.org/10.1111/j.1365-2818.2009.03220.x> PMID: 19754726
65. Bishop D, Nikić I, Brinkoetter M, Knecht S, Potz S, Kerschensteiner M, et al. Near-infrared branding efficiently correlates light and electron microscopy. *Nat Methods.* 2011; 8:568–72. <https://doi.org/10.1038/nmeth.1622> PMID: 21642966
66. Maco B, Holtmaat A, Cantoni M, Kreshuk A, Straehle CN, Hamprecht FA, et al. Correlative In Vivo 2 Photon and Focused Ion Beam Scanning Electron Microscopy of Cortical Neurons. *PLoS ONE.* 2013; 8:1–7. <https://doi.org/10.1371/journal.pone.0057405> PMID: 23468982
67. Cane M, Maco B, Knott G, Holtmaat A. The relationship between PSD-95 clustering and spine stability In Vivo. *J Neurosci.* 2014; 34:2075–86. <https://doi.org/10.1523/JNEUROSCI.3353-13.2014> PMID: 24501349
68. Blazquez-Llorca L, Hummel E, Zimmerman H, Zou C, Burgold S, Rietdorf J, et al. Correlation of two-photon in vivo imaging and FIB/SEM microscopy. *J Microsc.* 2015; 259:129–36. <https://doi.org/10.1111/jmi.12231> PMID: 25786682
69. Karreman MA, Hyenne V, Schwab Y, Goetz JG. Intravital Correlative Microscopy: Imaging Life at the Nanoscale. *Trends Cell Biol.* 2016; 26:848–63. <https://doi.org/10.1016/j.tcb.2016.07.003> PMID: 27515435
70. Lübke J. Photoconversion of diaminobenzidine with different fluorescent neuronal markers into a light and electron microscopic dense reaction product. *Microsc Res Tech.* 1993; 24:2–14. <https://doi.org/10.1002/jemt.1070240103> PMID: 7679591
71. Grabenbauer M, Geerts WJC, Fernandez-Rodriguez J, Hoenger A, Koster AJ, Nilsson T. Correlative microscopy and electron tomography of GFP through photooxidation. *Nat Methods.* 2005; 2:857–62. <https://doi.org/10.1038/nmeth806> PMID: 16278657
72. Ballesteros-Yáñez I, Benavides-Piccione R, Elston GN, Yuste R, DeFelipe J. Density and morphology of dendritic spines in mouse neocortex. *Neuroscience.* 2006; 138:403–9. <https://doi.org/10.1016/j.neuroscience.2005.11.038> PMID: 16457955
73. Chen JL, Villa KL, Cha JW, So PTC, Kubota Y, Nedivi E. Clustered Dynamics of Inhibitory Synapses and Dendritic Spines in the Adult Neocortex. *Neuron.* 2012; 74:361–73. <https://doi.org/10.1016/j.neuron.2012.02.030> PMID: 22542188
74. Sarid L, Feldmeyer D, Gidon A, Sakmann B, Segev I. Contribution of intracolumnar layer 2/3-to-Layer 2/3 excitatory connections in shaping the response to whisker deflection in rat barrel cortex. *Cereb Cortex.* 2015; 25:849–58. <https://doi.org/10.1093/cercor/bht268> PMID: 24165834
75. Kubota Y, Kondo S, Nomura M, Hatada S, Yamaguchi N, Mohamed AA, et al. Functional effects of distinct innervation styles of pyramidal cells by fast spiking cortical interneurons. *Elife.* 2015; 4:1–27. <https://doi.org/10.7554/eLife.07919> PMID: 26142457
76. Knott GW, Holtmaat A, Wilbrecht L, Welker E, Svoboda K. Spine growth precedes synapse formation in the adult neocortex in vivo. *Nat Neurosci.* 2006; 9:1117–24. <https://doi.org/10.1038/nn1747> PMID: 16892056
77. Noguchi J, Nagaoka A, Watanabe S, Ellis-Davies GCR, Kitamura K, Kano M, et al. In vivo two-photon uncaging of glutamate revealing the structure-function relationships of dendritic spines in the neocortex of adult mice. *J Physiol.* 2011; 589:2447–57. <https://doi.org/10.1113/jphysiol.2011.207100> PMID: 21486811
78. Noguchi J, Matsuzaki M, Ellis-Davies GCR, Kasai H. Spine-neck geometry determines NMDA receptor-dependent Ca²⁺ signaling in dendrites. *Neuron.* 2005; 46:609–22. <https://doi.org/10.1016/j.neuron.2005.03.015> PMID: 15944129
79. Bourne JN, Harris KM. Balancing Structure and Function at Hippocampal Dendritic Spines. *Annu Rev Neurosci.* 2008; 31:47–67. <https://doi.org/10.1146/annurev.neuro.31.060407.125646> PMID: 18284372
80. Segal M, Korkotian E. Endoplasmic reticulum calcium stores in dendritic spines. *Front Neuroanat.* 2014; 8:1–7. <https://doi.org/10.3389/fnana.2014.00001> PMID: 24523676
81. Chirillo MA, Waters MS, Lindsey LF, Bourne JN, Harris KM. Local resources of polyribosomes and SER promote synapse enlargement and spine clustering after long-term potentiation in adult rat hippocampus. *Sci Rep.* 2019; 9:1–14. <https://doi.org/10.1038/s41598-018-37186-2> PMID: 30626917
82. Spacek J, Harris KM. Three-dimensional organization of smooth endoplasmic reticulum in hippocampal CA1 dendrites and dendritic spines of the immature and mature rat. *J Neurosci.* 1997; 17:190–203. <https://doi.org/10.1523/JNEUROSCI.17-01-00190.1997> PMID: 8987748

83. Elbohouty M, Wilson MT, Voss LJ, Steyn-Ross DA, Hunt LA. In vitro electrical conductivity of seizing and non-seizing mouse brain slices at 10 kHz. *Phys Med Biol*. 2013;58. <https://doi.org/10.1088/0031-9155/58/11/3599> PMID: 23640172
84. Miceli S, Ness T V., Einevoll GT, Schubert D. Impedance Spectrum in Cortical Tissue: Implications for Propagation of LFP Signals on the Microscopic Level. *Eneuro*. 2017; 4: ENEURO.0291-16.2016. <https://doi.org/10.1523/ENEURO.0291-16.2016> PMID: 28197543
85. Harris KM, Stevens JK. Dendritic spines of CA1 pyramidal cells in the rat hippocampus: Serial electron microscopy with reference to their biophysical characteristics. *J Neurosci*. 1989; 9:2982–97. <https://doi.org/10.1523/JNEUROSCI.09-08-02982.1989> PMID: 2769375
86. Jayant K, Hirtz JJ, La PIJ, Tsai DM, De Boer WDAM, Semonche A, et al. Targeted intracellular voltage recordings from dendritic spines using quantum-dot-coated nanopipettes. *Nat Nanotechnol*. 2017. <https://doi.org/10.1038/nnano.2016.268> PMID: 27941898
87. Lagache T, Jayant K, Yuste R. Electrodifusion models of synaptic potentials in dendritic spines. *J Comput Neurosci*. 2019; 47:77–89. <https://doi.org/10.1007/s10827-019-00725-5> PMID: 31410632
88. Jones EG, Powell TP. Morphological variations in the dendritic spines of the neocortex. *J Cell Sci*. 1969; 5(2): 509–29. Available from: <http://www.ncbi.nlm.nih.gov/pubmed/5362339> PMID: 5362339
89. Beaulieu C, Colonnier M. A Laminar Analysis of the Number of Round-Asymmetrical and Flat-Symmetrical Synapses on Spines, Dendritic Trunks, and Cell Bodies in Area 17 of the Cat. *J Comp Neurol*. 1985; 189:180–9. <https://doi.org/10.1002/cne.902310206> PMID: 3968234
90. Dehay C, Douglas RJ, Martin KAC, Nelson C. Excitation by geniculocortical synapses is not “vetoed” at the level of dendritic spines in cat visual cortex. *J Physiol*. 1991; 440:723–34. <https://doi.org/10.1113/jphysiol.1991.sp018732> PMID: 1804984
91. Fifková E, Eason H, Schaner P. Inhibitory contacts on dendritic spines of the dentate fascia. *Brain Res*. 1992; 577:331–6. [https://doi.org/10.1016/0006-8993\(92\)90293-i](https://doi.org/10.1016/0006-8993(92)90293-i) PMID: 1606504
92. Micheva KD, Beaulieu C. An anatomical substrate for experience-dependent plasticity of the rat barrel field cortex. *PNAS* 1995; 92: 11834–11838. Available: <https://pubmed.ncbi.nlm.nih.gov/8524859/> <https://doi.org/10.1073/pnas.92.25.11834> PMID: 8524859
93. Knott GW, Quairiaux C, Genoud C, Welker E. Formation of Dendritic Spines with GABAergic Synapses Induced by Whisker Stimulation in Adult Mice. *Neuron*. 2002; 34:265–73. [https://doi.org/10.1016/s0896-6273\(02\)00663-3](https://doi.org/10.1016/s0896-6273(02)00663-3) PMID: 11970868
94. van Versendaal D, Rajendran R, Saiepour HM, Klooster J, Smit-Rigter L, Sommeijer JP, et al. Elimination of Inhibitory Synapses Is a Major Component of Adult Ocular Dominance Plasticity. *Neuron*. 2012; 74:374–83. <https://doi.org/10.1016/j.neuron.2012.03.015> PMID: 22542189
95. Tyagarajan SK, Fritschy JM. Gephyrin: A master regulator of neuronal function? *Nat Rev Neurosci*. 2014; 15:141–56. <https://doi.org/10.1038/nrn3670> PMID: 24552784
96. Krueger-Burg D, Papadopoulos T, Brose N. Organizers of inhibitory synapses come of age. *Curr Opin Neurobiol*. 2017; 45:66–77. <https://doi.org/10.1016/j.conb.2017.04.003> PMID: 28460365
97. Fossati M, Pizzarelli R, Schmidt ER, Kupferman JV, Stroebel D, Polleux F, et al. SRGAP2 and Its Human-Specific Paralog Co-Regulate the Development of Excitatory and Inhibitory Synapses. *Neuron*. 2016; 91:356–69. <https://doi.org/10.1016/j.neuron.2016.06.013> PMID: 27373832
98. Iascone DM, Li Y, Sümbül U, Doron M, Chen H, Andreu V, et al. Whole-Neuron Synaptic Mapping Reveals Spatially Precise Excitatory/Inhibitory Balance Limiting Dendritic and Somatic Spiking. *Neuron*. 2020;1–13. <https://doi.org/10.1016/j.neuron.2020.02.015> PMID: 32169170
99. Gray EG. Axo-somatic and axo-dendritic synapses of the cerebral cortex. *J Anat*. 1959; 93:420–433. Available from: <https://pubmed.ncbi.nlm.nih.gov/13829103> PMID: 13829103
100. Uchizono K. Characteristics of excitatory and inhibitory synapses in the central nervous system of the cat. *Nature*. 1965; 207: 642–643. Available from: <https://pubmed.ncbi.nlm.nih.gov/5883646> <https://doi.org/10.1038/207642a0> PMID: 5883646
101. Isaacson JS, Scanziani M. How inhibition shapes cortical activity. *Neuron*. 2011; 72:231–43. <https://doi.org/10.1016/j.neuron.2011.09.027> PMID: 22017986
102. Boivin JR, Nedivi E. Functional implications of inhibitory synapse placement on signal processing in pyramidal neuron dendrites. *Curr Opin Neurobiol*. 2018; 51:16–22. <https://doi.org/10.1016/j.conb.2018.01.013> PMID: 29454834
103. Villa KL, Berry KP, Subramanian J, Cha JW, Oh WC, Kwon HB, et al. Inhibitory Synapses Are Repeatedly Assembled and Removed at Persistent Sites In Vivo. *Neuron*. 2016; 89:756–69. <https://doi.org/10.1016/j.neuron.2016.01.010> PMID: 26853302
104. Rall W. Theoretical significance of dendritic trees for neuronal input-output relations. In: Reiss RF, editor. *Neural Theory and Modeling*. Stanford University Press; 1964. p. 73–97.

105. Dayan P, Abbott LF. Theoretical Neuroscience: Computational and Mathematical Modeling of Neural Systems. MIT Press. 2001.
106. Stuart G, Spruston N, Häusser M. Dendrites. Oxford University Press. 2016.
107. Nusser Z, Hájos N, Somogyi P, Mody I. Increased number of synaptic GABA(A) receptors underlies potentiation at hippocampal inhibitory synapses. *Nature*. 1998; 395:172–7. <https://doi.org/10.1038/25999> PMID: 9744275
108. Matsuzaki M, Ellis-Davies GCR, Nemoto T, Miyashita Y, Iino M, Kasai H. Dendritic spine geometry is critical for AMPA receptor expression in hippocampal CA1 pyramidal neurons. *Nat Neurosci*. 2001; 4:1086–92. <https://doi.org/10.1038/nn736> PMID: 11687814
109. Fukazawa Y, Shigemoto R. Intra-synapse-type and inter-synapse-type relationships between synaptic size and AMPAR expression. *Curr Opin Neurobiol*. 2012; 22:446–52. <https://doi.org/10.1016/j.conb.2012.01.006> PMID: 22325858
110. Holler S, Köstinger G, Martin KAC, Schuhknecht GFP, Stratford KJ. Structure and function of a neo-cortical synapse. *Nature*. 2021; 591:111–6. <https://doi.org/10.1038/s41586-020-03134-2> PMID: 33442056
111. Koch C, Segev I. The role of single neurons in information processing. *Nat Neurosci*. 2000; 3:1171–7. <https://doi.org/10.1038/81444> PMID: 11127834
112. Bloodgood BL, Giessel AJ, Sabatini BL. Biphasic Synaptic Ca Influx Arising from Compartmentalized Electrical Signals in Dendritic Spines. In: Stevens CF, editor. *PLoS Biol*. 2009; 7:e1000190. <https://doi.org/10.1371/journal.pbio.1000190> PMID: 19753104
113. Sabatini BL, Oertner TG, Svoboda K. The life cycle of Ca²⁺ ions in dendritic spines. *Neuron*. 2002; 33:439–52. [https://doi.org/10.1016/s0896-6273\(02\)00573-1](https://doi.org/10.1016/s0896-6273(02)00573-1) PMID: 11832230
114. Avermann M, Tomm C, Mateo C, Gerstner W, Petersen CCH. Microcircuits of excitatory and inhibitory neurons in layer 2/3 of mouse barrel cortex. *J Neurophysiol*. 2012; 107:3116–34. <https://doi.org/10.1152/jn.00917.2011> PMID: 22402650
115. Feldmeyer D, Lübke J, Sakmann B. Efficacy and connectivity of intracolumnar pairs of layer 2/3 pyramidal cells in the barrel cortex of juvenile rats. *J Physiol*. 2006; 575:583–602. <https://doi.org/10.1113/jphysiol.2006.105106> PMID: 16793907
116. Frick A, Feldmeyer D, Helmstaedter M, Sakmann B. Monosynaptic connections between pairs of L5A pyramidal neurons in columns of juvenile rat somatosensory cortex. *Cereb Cortex*. 2008; 18:397–406. <https://doi.org/10.1093/cercor/bhm074> PMID: 17548800
117. Lefort S, Tomm C, Floyd Sarria JC, Petersen CCH. The Excitatory Neuronal Network of the C2 Barrel Column in Mouse Primary Somatosensory Cortex. *Neuron*. 2009; 61:301–16. <https://doi.org/10.1016/j.neuron.2008.12.020> PMID: 19186171
118. Scala F, Kobak D, Shan S, Bernaerts Y, Lathurnus S, Cadwell CR, et al. Layer 4 of mouse neocortex differs in cell types and circuit organization between sensory areas. *Nat Commun*. 2019; 10:1–12. <https://doi.org/10.1038/s41467-018-07882-8> PMID: 30602773
119. Hull C, Isaacson JS, Scanziani M. Postsynaptic Mechanisms Govern the Differential Excitation of Cortical Neurons by Thalamic Inputs. *J Neurosci*. 2009; 29:9127–36. <https://doi.org/10.1523/JNEUROSCI.5971-08.2009> PMID: 19605650
120. Hoffmann JHO, Meyer HS, Schmitt AC, Straehle J, Weibrecht T, Sakmann B, et al. Synaptic conductance estimates of the connection between local inhibitor interneurons and pyramidal neurons in layer 2/3 of a cortical column. *Cereb Cortex*. 2015; 25:4415–29. <https://doi.org/10.1093/cercor/bhv039> PMID: 25761638
121. Kobayashi M, Hamada T, Kogo M, Yanagawa Y, Obata K, Kang Y. Developmental profile of GABA-mediated synaptic transmission in pyramidal cells of the somatosensory cortex. *Eur J Neurosci*. 2008; 28:849–61. <https://doi.org/10.1111/j.1460-9568.2008.06401.x> PMID: 18691332
122. Xu H, Jeong HY, Tremblay R, Rudy B. Neocortical Somatostatin-Expressing GABAergic Interneurons Disinhibit the Thalamorecipient Layer 4. *Neuron*. 2013; 77:155–67. <https://doi.org/10.1016/j.neuron.2012.11.004> PMID: 23312523
123. Acker CD, Hoyos E, Loew LM. EPSPs Measured in Proximal Dendritic Spines of Cortical Pyramidal Neurons. *eNeuro*. 2016; 3:1–13. <https://doi.org/10.1523/ENEURO.0050-15.2016> PMID: 27257618
124. Pedregosa F, Varoquaux G, Gramfort A, Michel V, Thirion B, Grisel O, et al. Scikit-Learn: Machine Learning in Python. *J Mach Learn Res*. 2011; 12: 2825–2830. Available from: <http://jmlr.org/papers/v12/pedregosa11a.html>
125. Sabatini BL, Maravall M, Svoboda K. Ca²⁺ Signaling in dendritic spines. *Curr Opin Neurobiol*. 2001; 11:349–56. [https://doi.org/10.1016/s0959-4388\(00\)00218-x](https://doi.org/10.1016/s0959-4388(00)00218-x) PMID: 11399434
126. Higley MJ, Sabatini BL. Calcium signaling in dendritic spines. *Cold Spring Harb Perspect Biol*. 2012; 4. <https://doi.org/10.1101/cshperspect.a005686> PMID: 22338091

127. Efron B, Tibshirani RJ. An Introduction to the Bootstrap. CRC Press. 1994.
128. Koch C, Poggio T, Torre V. Nonlinear interactions in a dendritic tree: localization, timing, and role in information processing. *PNAS* 1983; 80:2799–2802. Available from: <https://pubmed.ncbi.nlm.nih.gov/6573680> <https://doi.org/10.1073/pnas.80.9.2799> PMID: 6573680
129. Chiu CQ, Lur G, Morse TM, Carnevale NT, Ellis-Davies GCR, Higley MJ. Compartmentalization of GABAergic inhibition by dendritic spines. *Science*. 2013; 340:759–62. <https://doi.org/10.1126/science.1234274> PMID: 23661763
130. Charrier C, Joshi K, Coutinho-Budd J, Kim JE, Lambert N, De Marchena J, et al. Inhibition of SRGAP2 function by its human-specific paralogs induces neoteny during spine maturation. *Cell*. 2012; 149:923–35. <https://doi.org/10.1016/j.cell.2012.03.034> PMID: 22559944
131. Sarid L, Bruno R, Sakmann B, Segev I, Feldmeyer D. Modeling a layer 4-to-layer 2/3 module of a single column in rat neocortex: Interweaving in vitro and in vivo experimental observations. *Proc Natl Acad Sci*. 2007; 104:16353–8. <https://doi.org/10.1073/pnas.0707853104> PMID: 17913876
132. Almog M, Korngreen A. A quantitative description of dendritic conductances and its application to dendritic excitation in layer 5 pyramidal neurons. *J Neurosci*. 2014; 34:182–96. <https://doi.org/10.1523/JNEUROSCI.2896-13.2014> PMID: 24381280
133. Müllner FE, Wierenga CJ, Bonhoeffer T. Precision of Inhibition: Dendritic Inhibition by Individual GABAergic Synapses on Hippocampal Pyramidal Cells Is Confined in Space and Time. *Neuron*. 2015; 87:576–89. <https://doi.org/10.1016/j.neuron.2015.07.003> PMID: 26247864
134. Rostaing P, Real E, Siksou L, Lechère JP, Boudier T, Boeckers TM, et al. Analysis of synaptic ultrastructure without fixative using high-pressure freezing and tomography. *Eur J Neurosci*. 2006; 24:3463–74. <https://doi.org/10.1111/j.1460-9568.2006.05234.x> PMID: 17229095
135. Korogod N, Petersen CCH, Knott GW. Ultrastructural analysis of adult mouse neocortex comparing aldehyde perfusion with cryo fixation. *elife*. 2015; 4:1–17. <https://doi.org/10.7554/eLife.05793> PMID: 26259873
136. Kubota Y, Karube F, Nomura M, Kawaguchi Y. The Diversity of Cortical Inhibitory Synapses. *Front Neural Circuits*. 2016; 10:1–15. <https://doi.org/10.3389/fncir.2016.00001> PMID: 26834567
137. Tremblay R, Lee S, Rudy B. GABAergic Interneurons in the Neocortex: From Cellular Properties to Circuits. *Neuron*. 2016; 91:260–92. <https://doi.org/10.1016/j.neuron.2016.06.033> PMID: 27477017
138. Kuljis DA, Park E, Telmer CA, Lee J, Ackerman DS, Bruchez MP, et al. Fluorescence-based quantitative synapse analysis for cell-type specific connectomics. *eNeuro*. 2019. <https://doi.org/10.1523/ENEURO.0193-19.2019> PMID: 31548370
139. Nabavi S, Fox R, Proulx CD, Lin JY, Tsien RY, Malinow R. Engineering a memory with LTD and LTP. *Nature*. 2014; 511:348–52. <https://doi.org/10.1038/nature13294> PMID: 24896183
140. Hayashi-Takagi A, Yagishita S, Nakamura M, Shirai F, Wu YI, Loshbaugh AL, et al. Labelling and optical erasure of synaptic memory traces in the motor cortex. *Nature*. 2015; 525:333–8. <https://doi.org/10.1038/nature15257> PMID: 26352471
141. Segal M. Dendritic spines: Morphological building blocks of memory. *Neurobiol Learn Mem*. 2017; 138:3–9. <https://doi.org/10.1016/j.nlm.2016.06.007> PMID: 27311757
142. Lisman J. A mechanism for the Hebb and the anti-Hebb processes underlying learning and memory. *PNAS*. 1989; 86:9574–8. <https://doi.org/10.1073/pnas.86.23.9574> PMID: 2556718
143. Feldman DE. The Spike-Timing Dependence of Plasticity. *Neuron*. 2012; 75:556–71. <https://doi.org/10.1016/j.neuron.2012.08.001> PMID: 22920249
144. Graupner M, Brunel N. Calcium-based plasticity model explains sensitivity of synaptic changes to spike pattern, rate, and dendritic location. *Proc Natl Acad Sci*. 2012; 109:3991–6. <https://doi.org/10.1073/pnas.1109359109> PMID: 22357758
145. Hayama T, Noguchi J, Watanabe S, Takahashi N, Hayashi-Takagi A, Ellis-Davies GCR, et al. GABA promotes the competitive selection of dendritic spines by controlling local Ca²⁺ signaling. *Nat Neurosci*. 2013; 16:1409–16. <https://doi.org/10.1038/nn.3496> PMID: 23974706
146. Higley MJ. Localized GABAergic inhibition of dendritic Ca²⁺ signalling. *Nat Rev Neurosci*. 2014; 15:567–72. <https://doi.org/10.1038/nrn3803> PMID: 25116141
147. Nakahata Y, Yasuda R. Plasticity of spine structure: Local signaling, translation and cytoskeletal reorganization. *Front Synaptic Neurosci*. 2018; 10:1–13. <https://doi.org/10.3389/fnsyn.2018.00001> PMID: 29445338
148. Gabernet L, Jadhav SP, Feldman DE, Carandini M, Scanziani M. Somatosensory integration controlled by dynamic thalamocortical feed-forward inhibition. *Neuron*. 2005; 48:315–27. <https://doi.org/10.1016/j.neuron.2005.09.022> PMID: 16242411

149. Kimura F, Itami C, Ikezoe K, Tamura H, Fujita I, Yanagawa Y, et al. Fast activation of feedforward inhibitory neurons from thalamic input and its relevance to the regulation of spike sequences in the barrel cortex. *J Physiol*. 2010; 588:2769–87. <https://doi.org/10.1113/jphysiol.2010.188177> PMID: 20530116
150. Wehr M, Zador AM. Balanced inhibition underlies tuning and sharpens spike timing in auditory cortex. *Nature*. 2003; 426:442–6. <https://doi.org/10.1038/nature02116> PMID: 14647382
151. Frenkel MY, Sawtell NB, Diogo ACM, Yoon B, Neve RL, Bear MF. Instructive Effect of Visual Experience in Mouse Visual Cortex. *Neuron*. 2006; 51:339–49. <https://doi.org/10.1016/j.neuron.2006.06.026> PMID: 16880128
152. Markram H, Muller E, Ramaswamy S, Reimann MW, Abdellah M, Sanchez CA, et al. Reconstruction and Simulation of Neocortical Microcircuitry. *Cell*. 2015; 163:456–92. <https://doi.org/10.1016/j.cell.2015.09.029> PMID: 26451489
153. Bhatia A, Moza S, Bhalla US. Precise excitation-inhibition balance controls gain and timing in the hippocampus. *Elife*. 2019; 8:1–29. <https://doi.org/10.7554/eLife.43415> PMID: 31021319
154. Fossati M, Assendorp N, Gemin O, Colasse S, Dingli F, Arras G, et al. Trans-Synaptic Signaling through the Glutamate Receptor Delta-1 Mediates Inhibitory Synapse Formation in Cortical Pyramidal Neurons. *Neuron*. 2019; 104:1081, e7–94. <https://doi.org/10.1016/j.neuron.2019.09.027> PMID: 31704028
155. Deerinck TJ, Bushong EA, Thor A, Ellisman MH. NCMIR Methods for 3D EM: A new protocol for preparation of biological specimens for serial block face scanning electron microscopy. *Nat Cent Microsc Imag Res*. 2010. Available from: http://www.emc.missouri.edu/pdf/Ellisman's_SBFSEM_sampleprep_protocol.pdf
156. Belevich I, Joensuu M, Kumar D, Vihinen H, Jokitalo E. Microscopy Image Browser: A Platform for Segmentation and Analysis of Multidimensional Datasets. *PLoS Biol*. 2016; 14:1–13. <https://doi.org/10.1371/journal.pbio.1002340> PMID: 26727152
157. Kremer JR, Mastronarde DN, McIntosh JR. Computer visualization of three-dimensional image data using IMOD. *J Struct Biol*. 1996; 116:71–6. <https://doi.org/10.1006/jsbi.1996.0013> PMID: 8742726
158. Hines ML, Carnevale NT. NEURON: A tool for neuroscientists. *Neuroscientist*. 2001; 7:123–35. <https://doi.org/10.1177/107385840100700207> PMID: 11496923
159. Barbour B. Analysis of Claims that the Brain Extracellular Impedance Is High and Non-resistive. *Bio-phys J*. 2017; 113:1636–8. <https://doi.org/10.1016/j.bpj.2017.05.054> PMID: 28978453
160. Jahr CE, Stevens CF. A quantitative description of NMDA receptor-channel kinetic behavior. *J Neurosci*. 1990; 10:1830–7. <https://doi.org/10.1523/JNEUROSCI.10-06-01830.1990> PMID: 1693952
161. Brecht M, Roth A, Sakmann B. Dynamic receptive fields of reconstructed pyramidal cells in layers 3 and 2 of rat somatosensory barrel cortex. *J Physiol*. 2003; 553:243–65. <https://doi.org/10.1113/jphysiol.2003.044222> PMID: 12949232
162. Doyon N, Vinay L, Prescott SA, De Y. Chloride Regulation: A Dynamic Equilibrium Crucial for Synaptic Inhibition. *Neuron*. 2016; 89:1157–72. <https://doi.org/10.1016/j.neuron.2016.02.030> PMID: 26985723
163. Boffi JC, Knabbe J, Kaiser M, Kuner T. KCC2-dependent Steady-state Intracellular Chloride Concentration and pH in Cortical Layer 2/3 Neurons of Anesthetized and Awake Mice. *Front Cell Neurosci*. 2018; 12:1–14. <https://doi.org/10.3389/fncel.2018.00001> PMID: 29386999

RÉSUMÉ

La vulnérabilité aux troubles du neuro-développement a augmenté au cours de l'évolution humaine. Pourtant, les voies moléculaires qui relient l'évolution et les maladies du cerveau restent largement inconnues. Nous avons identifié ici la caténine delta-2 (CTNND2) comme partenaire de liaison de SRGAP2C, une protéine spécifique à l'homme qui ralentit la maturation synaptique et augmente la connectivité corticale. CTNND2 est une protéine de liaison à la cadhérine dont les mutations provoquent une déficience intellectuelle dans le syndrome de Cri-du-Chat et un autisme sévère. En utilisant des manipulations in utero de neurones pyramidaux corticaux de couche 2/3, nous démontrons que la déficience de CTNND2 perturbe la coordination excitation/inhibition et augmente l'excitabilité neuronale chez les souris juvéniles, puis conduit à une perte précoce de synapses à l'âge adulte. L'analyse protéomique a mis en évidence un complexe postsynaptique central qui contraint l'activité excitatrice pendant la période de maturation synaptique. Ainsi, CTNND2 est une protéine multifonction au carrefour des troubles du développement neurologique et de l'évolution humaine, dont la perte de fonction entraîne une défaillance de l'homéostasie neuronale et dont l'interaction avec SRGAP2C pourrait contribuer à la néoténie synaptique humaine et à la persistance à long terme.

MOTS CLÉS

Synapse ; Neurone ; Développement

ABSTRACT

Vulnerability to neurodevelopmental disorders increased during human evolution. Yet little is known about the molecular pathways that link evolution and brain diseases. Here we identified catenin delta-2 (CTNND2) as a binding partner of SRGAP2C, a human-specific protein that slows down synaptic maturation and increases cortical connectivity. CTNND2 is a cadherin-binding protein whose mutations cause intellectual disability in the Cri-du-Chat syndrome and severe autism. Using sparse in utero manipulations of layer 2/3 cortical pyramidal neurons, we demonstrate that CTNND2 deficiency disrupts excitation/inhibition coordination and increases neuronal excitability in juvenile mice, and then leads to precocious synapse loss during adulthood. Proteomic analysis highlighted a core postsynaptic complex that constrains excitatory activity during the period of synaptic maturation. Thus, CTNND2 is a multifunctional protein at the crossroads of neurodevelopmental disorders and human evolution, whose loss of function causes a failure of neuronal homeostasis and whose interaction with SRGAP2C might contribute to human synaptic neoteny and long-term persistence.

KEYWORDS

Synapse ; Neuron ; Development